Optimization and Design of Reactive Crystallization Process

Wenjing Liu

Submitted in accordance with the requirements for the degree of

Doctor of Philosophy

The University of Leeds

Institute of Particle Science and Engineering

School of Chemical and Process Engineering

September 2014

The candidate confirms that the work submitted is her own, except where work which has formed part of jointly-authored publications has been included. The contribution of the candidate and the other authors to this work has been explicitly indicated below. The candidate confirms that appropriate credit has been given within the thesis where reference has been made to the work of others. This copy has been supplied on the understanding that it is copyright material and that no quotation from the thesis may be published without proper acknowledgement.

© <2014>"The University of Leeds"<Wenjing Liu>

Acknowledgements

Abstract

Crystallization is an important process used in a wide range of industries, which has made it the main process in the primary manufacturing stage, and thereby the quality of crystals produced has a major impact on downstream processes such as filtration, milling and drying, as well as transport and storage processes. Organic reactive crystallization, which is widely used in the production of active pharmaceutical ingredients (APIs), has many unique features that make it different from cooling or anti-solvent crystallization, even leading to some concepts and methods not directly applicable to this process.

A survey of the literature reveals that previous research on reactive crystallization has mainly been conducted for inorganic materials which are known to be simpler than crystallization of organic materials. For example, it is known that compared with inorganic materials, organic materials tend more to aggregation and form amorphous. In addition, the published literature in this research area is often concerned with laboratory scale crystallization, rather than industrial scale processes.

The focus of this research project is to carry out research on the process design, optimization, simulation and scale-up of organic reactive pharmaceutical crystallization. The objective is to research the process and crystallizer design which takes advantage of the features of the reactive crystallization process and on simulation, optimization and scale-up techniques with the aim of manufacturing high quality products measured by the products' crystallinity, stability, purity, and processability. Process analytical technology (PAT) is used as a supporting tool to achieve the above stated objectives. An off-patent drug, sodium cefuroxime which is considered as a second generation antibiotic, is used as the case study drug.

Firstly, on-line Attenuated Total Reflection-Fourier Transform InfraRed spectroscopy (ATR-FTIR) was used to monitor the change in the supersaturation in order to optimize the flow rate of the anti-solvent during the anti-solvent re-crystallization process of sodium cefuroxime. The solubility of

sodium cefuroxime under various temperatures T, pH values and solvents was measured and correlated in models. The effect of the anti-solvent (95% ethanol) flow rate on crystallinity was examined and the results showed that appropriate anti-solvent flow rate could improve the stability of sodium cefuroxime. The optimized anti-solvent re-crystallization process provided a new method to obtain high-quality seeds of sodium cefuroxime.

Secondly, Process Analytical Technology (PAT) based on Focused Beam Reflectance Measurement (FBRM) was used to optimize the parameters of the reactive synthesis process of sodium cefuroxime, such as the feed order, the reaction temperature, the stirring speed, the feed rate/speed and the amount of seeds. An impinging jet mixer, which could provide rapid mixing effectiveness of reactants, was applied and optimized. After that, the optimized process was scaled-up from 1L to 10L with a volumetric scaling-up factor of 10. The product had superior crystallinity, uniform size distribution, higher stability and purity, which indicated that this optimization methodology and impinging jet mixer design could be applied in other similar reactive crystallization processes.

Finally, Process Analytical Technology (PAT) including Ultraviolet–Visible Spectrometry (UV) and FBRM was used to study the reaction kinetics and the mechanism of crystal growth in the reactive synthesis process of sodium cefuroxime. A process and crystallizer was designed based on the data obtained above. This process provided two reactors in series for conducting a rapid reactive crystallization process of pharmaceutical compounds in continuous mode. It involved a tank reactor with the use of an impinging jet mixer and stirrer to create intensive mixing of the reactants before nucleation and a tubular reactor with suitable length to avoid back mixing of the products. The results showed that by using this process, the product had uniform size distribution, higher stability and superior crystallinity, in both laboratory scale and 50L scaled-up processes.

Table of Contents

List of Tables

List of Figures

Chapter 1

Introduction

1.1 Background and Motivation

Crystallization is an important process used in a wide range of industries including pharmaceutical, biopharmaceutical, agrochemical, healthcare, energy and various personal consumer products. It is reported that over 80% of all forms of pharmaceutical products including tablets, aerosols, capsules, suspensions and suppositories contain crystalline components, making crystallization one of the most important processes in the manufacture of pharmaceuticals. As a primary manufacturing process producing active pharmaceutical ingredients (APIs), the quality of crystals can have a major impact not only on the final product performance, but also on the downstream processes such as filtration, milling and drying, as well as transportation and storage processes (Desikan et al., 2000; Shan et al., 2002).

In the production of an API, crystallization is often used as a purification step after the reactive synthesis of the API is completed. It uses cooling or anti-solvent as a means of reducing the solubility of the API in the solvent, forcing the API compound to come out in a solid crystalline form. In the reactive crystallization process, however, two steps, reactive synthesis of the API and its purification using crystallization, take place in the same vessel (Berry and Ng, 1997). While cooling and anti-solvent crystallization has been well studied, much less work has been done on reactive crystallization. The majority of available literature on this topic focuses on inorganic reactive crystallization which is considered simpler than organic in many aspects (Hirasawa et al., 1997; Kitamura et al., 2002; Tsuge et al., 1996).

Pharmaceutical, or in more general terms, organic compound reactive crystallization has many unique features compared to cooling or anti-solvent crystallization. For example, reactive crystallization is often much faster than

cooling or anti-solvent crystallization, increasing the possibility of forming amorphous materials and impurities (Chen et al., 2013; Michell et al., 2012). In some reactive crystallization processes, the API can be completely insoluble in the solvents, raising such questions as if the concepts widely used in designing and controlling cooling and anti-solvent crystallization are still applicable. For instance, is there still a metastable zone, or can the metastable zone concept still be used for process design and optimization of reactive crystallization in which the supersaturation can be extremely high? Furthermore, due to the complex and fast reaction and the crystallization process, the existing crystallizer designs may not be the most suitable option.

So far, the understanding of the reactive crystallization process is still in a semi-skilled state (Chen et al., 2013; Shimizu and Hirasawa, 2013; Wang and Li, 2012). Under such conditions, process analysis technology (PAT) was proposed to promote the traditional medicine crystallization technology to a modern one (Birch et al., 2005; Munson et al., 2006). Through on-line PAT monitoring, process analysis and studying the impact of key process parameters, the quality of the final product can be controlled and the batch-to-batch variation can be reduced. Using PAT changes drug production from test quality control (quality-by-testing) to design quality control (quality-by-design) (Saleemi et al., 2012a).

Traditionally, there are two main basic vessel types in the existing crystallizer designs: the tank reactor and the pipe or tubular reactor. These two types can further form three main basic reactors: the batch reactor, the continuous stirred-tank reactor and the plug flow reactor. These reactors have two significant drawbacks when being used as a reaction crystallizer for the rapid reactive crystallization process (David J. Am Ende et al., 2003; Lindrud et al., 2001; Midler et al., 1994):

Firstly, the mixing effectiveness is limited, which means that it will need a relatively long time to achieve sufficient mixing that the reaction required. The mixing time is not a major concern in the design of a reactive crystallization

process when the reaction or crystallization kinetics is much slower than the time of mixing. However, in those very rapid reactive crystallization processes occurring under high supersaturation conditions, a lack of rapid mixing can drastically affect the properties of the end product including crystal size distribution, morphology and purity.

Secondly, the residence time of reactants cannot be kept the same. The reactants entering the reactor at the early stage can react sufficiently, resulting in a long residence time and more opportunities to be in contact with the crystal seed for growth. At the same time, the reactants entering the reactor thereafter may still require more residence time to complete the reaction. In addition, besides reducing the product yield, leading to a non-uniform crystal size distribution, for some APIs which are easy to degrade during the production process, in some extreme cases different residence times may lead to degradation of a large percentage of products before downstream processes.

In addition, for batch type operation, periodic downtime is required. The entire production process needs to stop before the product is removed. Besides a waste of time and labor due to the concentration required, solubility and other conditions change with time, the batch-to-batch variation is difficult to avoid.

In our study, synthesis of sodium cefuroxime was chosen as a representative organic reactive crystallization process. Cefuroxime is a valuable broad spectrum antibiotic, which has high activity against a wide range of gram-positive and gram-negative micro-organisms (Gower and Dash, 1977; Greenwood et al., 1976). However, its poor stability has been a cause of widespread concern during industrial production. In the storage and transportation processes, it tends to deepen solid color, reduce solubility and become sticky (Fu et al., 2010; Liu et al., 2014). The aim of this study was to design, optimize and scale-up a process for continuous organic reactive crystallization synthesis of sodium cefuroxime. Process analytical technology (PAT) was used to achieve the above stated objectives. The products were characterized using XRD, the imaging instrument *Morphologi* G3 and SEM. The

ultimate performance of this process was judged by the product's performance in crystallinity, stability, purity and processability.

1.2 Research Objectives

Based on the above observations, the purpose of this study was to research designs of crystallizers for the reactive crystallization process of APIs, and on modeling, optimization and scale-up of this process. More specifically, the work had the following objectives:

- Select a representative and challenging reactive crystallization process for drugs, to study reactor design, modeling, and optimization techniques. The selected drug compound is sodium cefuroxime.

- Investigate new equipment designs for semi-continuous and continuous operation of the reactive crystallization process. The performance of the reactor is judged by the product's performance in crystallinity, stability, purity and processability.

- Study modeling techniques including computational fluid dynamics (CFD) with the aim of improving the process design.

- Research is conducted on crystallizers of different size scales, from laboratory, to pilot plant and industrial scales.

- Process analytical technology (PAT) including on-line ATR-FTIR, FBRM and UV is used as a support tool to achieve the above stated project objectives.

1.3 Structure of the Thesis

The body of the thesis constitutes nine chapters. The current chapter describes the background, motivation and research objectives.

Chapter 2 Literature Review

This chapter first introduces the principles of crystallography, crystal formation methods including nucleation and growth, the internal and external factors affecting crystal morphology, as well as the crystal dissolution, regeneration and the reactive crystallization. Then the re-crystallization process and reactive crystallization process of sodium cefuroxime are reviewed. This chapter also summarizes factors that affect the physical and chemical stability of the drug. In the final section, the optimization progress of the crystallization reactor is described.

Chapter 3 Materials and Experimental Instruments

This chapter presents the profile of raw materials and the experimental facilities as well as the instruments used for measurement and analysis including: Attenuated Total Reflection-Fourier Transform InfraRed Spectroscopy (ATR-FTIR), Focused Beam Reflectance Measurement (FBRM), Scanning Electron Microscope (SEM), *Morphologi* G3 and X-ray Diffraction (XRD).

Chapter 4 Analytical Profile of Sodium Cefuroxime

In this chapter, the sodium cefuroxime samples from different companies were first analyzed. According to the appearance of these samples, the general impression of the drug stability is described. Then, the stability test procedure of sodium cefuroxime is introduced, and on the basis of the physical properties and the stability test results of these sodium cefuroxime samples, the relationship between the drug crystalline state and its stability is generally established.

Chapter 5 Re-crystallization of Sodium Cefuroxime

In this chapter, the anti-solvent re-crystallization process is used to purify the commercial sodium cefuroxime product for seed collection and on-line ATR-FTIR is used to optimize this process. Prior to that, in order to ensure on-line ATR-FTIR can work effectively, the preparatory work such as solubility determination and instrument calibration was completed first.

During this process, the least-squares method was used to construct the predictive model of the solution concentration and the solubility data, which changed with the *pH* values of sodium cefuroxime, was measured first.

Chapter 6 Optimization of Reactive Synthesis Process of Sodium Cefuroxime

In this chapter, PAT based on FBRM was used to optimize the parameters of the reactive crystallization process of sodium cefuroxime, such as the feed order, the reaction temperature, the stirring speed and the feed rate/speed and the amount of seeds.

Chapter 7 Impinging Jet Mixer Probe Design and Scale-up

In the previous chapters (Chapters 5 and 6), the anti-solvent re-crystallization process was optimized for seed collection (Chapter 5), and the parameters of the reactive crystallization process were also determined by a product's performance in stability (Chapter 6). In this chapter, an impinging jet mixer is used to further optimize this reactive crystallization process of sodium cefuroxime according to its characteristics and 10L scaled-up tests are conducted for industrialization.

Chapter 8 Reactor Design of Continuous Reactive Crystallization Process and Scale-up

By using the impinging jet mixer probe and optimized parameters in Chapter 7, the products with satisfied stability have already been obtained. In this chapter, on the basis of the characteristics of the reactive crystallization process of sodium cefuroxime, by studying the reaction kinetics, measuring and simulating the residence time and the fluid flow state, a crystallizer and process are designed. Following this, the experiment was verified and scaled-up (50L). Some constructive suggestions are also provided for the existing industrial instruments.

Chapter 9 Conclusions and Future Work

This final chapter summarizes the key scientific accomplishments achieved in this thesis and the possible future research directions.

Chapter 2
Literature Review

2.1 Principle of Crystallography

2.1.1 Crystals and Amorphous Materials

Crystallography is the science that examines the arrangement of atoms in solids. X-ray crystallography is used to determine the arrangement of atoms. A crystal or crystalline solid is a solid material whose constituent atoms, molecules, or ions are arranged in an ordered pattern extending in all three spatial dimensions. In addition to their microscopic structure, large crystals are usually identifiable by their macroscopic geometrical shape, consisting of flat faces with specific, characteristic orientations (Lehmann, 1900; Riecke, 1900). On the other hand, an amorphous or non-crystalline solid is a solid that lacks the long-range order characteristic of a crystal (Liebig, 1846). A crystal at solid state can be converted to an amorphous particle and vice versa (Fitzgerald, 1902; Hempel and von, 1900; Smith and Holmes, 1902).

There are several properties that can be used to characterize a crystal (Pavlow, 1904; Tsuruta, 1900; Voigt, 1902; Wulff, 1901a):

- Self-limited. In appropriate conditions, crystals can spontaneously form a regular geometric polyhedron.

- Uniformity. Different parts of the same crystal have the same properties, such as the structure.

- Anisotropy. From different orientation, the properties of a crystal are different, such as the conductivity.

- Symmetry. The same part (crystal face, crystal edges and corners) and properties (physical and chemical properties) of a crystal are regularly repeated in different directions or positions.

- Stability. In the same thermodynamic conditions, with the same chemical composition, comparing to the amorphous state, the crystalline state is more stable, which is because the minimum internal energy.

2.1.2 Crystal Formation Method

A crystal can be formed by five different methods:

- Crystallization of gas condensate, such as the snowflake which formed by water vapour cooling (Seligman, 1937; Simpson, 1937).
- Crystallization of super-cooling, such as the ice which formed by water below the freezing point (Leaf, 1908).
- Crystallization of supersaturated solution, such as the salt crystal formed through precipitation (Lehmann, 1915; Lunde, 1926).
- Crystallization of amorphous, such as the quartz or feldspar ceramic formed by volcanic glass (Kruger, 1904; Pishch et al., 1986).
- Solid state crystalline phase transition, for example, at appropriate pressure and temperature conditions, diamond can be transformed into graphite (Schleicher, 1923; Vogel and Tammann, 1909).

2.1.2.1 Crystal Nucleation

Nuclei are the crystalline phase particles that precipitate from a medium, and have particle sizes greater than a certain critical size for their continuously growing. Nucleation is a process of the formation of crystalline phase particles (Barus, 1902). The rate at which the nucleation takes place is considered as deterministic of the final crystal size distribution. It is suggested that nucleation occurs by several mechanisms spontaneously, from the existence of foreign agents in solution, reactor-wall scratching to the pre-existence of crystals of the

self-assembly of solute molecules in an ideal situation (Rodebush and Clarke, 1958; Thiessen, 1929).

The excess of free energy associated with the degree of supersaturation (the solute concentration menus the solubility) leads to the formation of nuclei by an addition mechanism:

$$A + A = A_2; \tag{2.1}$$

$$A_2 + A = A_3; \tag{2.2}$$

$$A_{n-1} + A = A_n \tag{2.3}$$
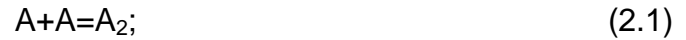
where *A* means the excess of free energy and subscripts mean the number of addition times.

1. Homogeneous nucleation

The theory of nucleation explains that in homogeneous nucleation (Buckle, 1961), the overall free energy, ΔG, between the small solid particle of radius *r* and the solute in solution is equal to the addition of the excess free energy between the particle surface and the bulk of the particle (surface excess free energy), ΔG_s, and the excess free energy between every large particle and solute in solution, ΔG_v. $\Delta G_s \propto r^2$ with positive values, whilst $\Delta G_v \propto r^3$ which is negative in saturated solutions. Then, it follows that

$$\Delta G = \Delta G_s + \Delta G_v = 4\pi r^2 \gamma + \frac{4}{3}\pi r^3 \Delta G_v \tag{2.4}$$

where ΔG_v is the free energy change of the transformation per unit volume, and γ is the interfacial tension, or surface energy, between the developing crystalline surface and the solution. The free energy of formation needs to reach a maximum, ΔG_c that corresponds to the required free energy for a spherical cluster of radius r_c to become stable (Figure 2.1).
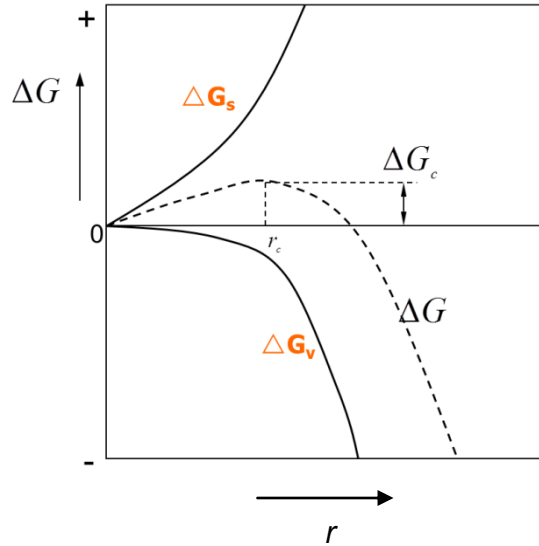
Figure 2.1 Free energy diagram for nucleation-formation of the critical nucleus (Buckle, 1961).

The values of ΔG_c and r_c are obtained when $d\Delta G/dr = 0$. This leads to the expression

$$r_c = -\frac{2\gamma}{\Delta G_v} \tag{2.5}$$

and with equation (2.4)

$$\Delta G_c = \frac{16\pi\gamma^3}{3(\Delta G_v)^2} = \frac{4\pi\gamma r_c^2}{3} \tag{2.6}$$

The growth of the clusters is described by the Gibbs-Thompson equation (Luckhaus and Modica, 1989)

$$\ln\frac{c}{c^*} = \ln S = \frac{2\gamma v}{kTr} \tag{2.7}$$

where k is the Boltzmann constant and v is the molecular volume.

Using the Arrhenius equation to express the rate of nucleation, J, ΔG_c and J can be expressed in the following terms (Fleischmann and Michaelis, 1907):

$$\Delta G_c = \frac{16\pi\gamma^3 v^2}{3(kT\ln S)^2} \tag{2.8}$$

$$J = A \exp[-\frac{16\pi\gamma^3 v^2}{3k^3T^3(\ln S)^2}] \tag{2.9}$$

11

where *A* is the pre-exponential factor. This equation shows that supersaturation, *S*, interfacial tension, *γ*, temperature, *T*, and molecular volume, *v*, can affect the rate of nucleation.

Equation (2.9) shows that the rate of nucleation increases with supersaturation and temperature and it decreases with the increase of interfacial tension.

2. Heterogeneous nucleation

Heterogeneous nucleation, nucleation with the nucleus at a surface, is much more common than homogeneous nucleation. Heterogeneous nucleation is typically much faster than homogeneous nucleation because the nucleation barrier ΔG* is much lower at a surface. This is because the nucleation barrier comes from the positive term in the free energy ΔG, which is the surface term. For homogeneous nucleation the nucleus is approximated by a sphere and so has a free energy equal to the surface area of a sphere, $4\pi r^2$, times the surface tension *σ*. However, as we can see in the schematic of macroscopic droplets (Figure 2.2), droplets on surfaces are not complete spheres and so the area of the interface between the droplet and the surrounding fluid is less than $4\pi r^2$. This geometrical factor reduces the interfacial area and so the interfacial free energy, which in turn reduces the nucleation barrier (Sear, 2007).
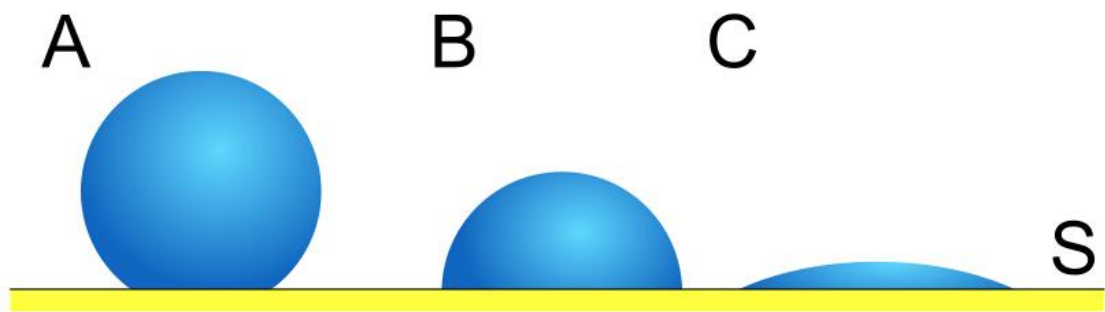
Figure 2.2 Three droplets on a surface, illustrating decreasing contact angles (Sear, 2007).

In Figure 2.2, the contact angle between the droplet surface and the surface (S) increases from left to right (A to C), and we see that the surface area of the droplet increases as the contact angle increases. This geometrical effect reduces the barrier and hence results in faster nucleation on surfaces with

smaller contact angles. Also, if instead of the surface being flat it curves towards fluid, then this also reduces the interfacial area and so the nucleation barrier. There are expressions for this reduction for simple surface geometries (Sholl and Fletcher, 1970). In practice, this means we expect nucleation to be fastest on pits or cracks in surfaces made of material such that the nucleus forms a small contact angle on its surface.

2.1.2.2 Basic Theory of Crystal Growth

1. Layer growth theory (Bunn and Emmett, 1949; Goldstein and Rosenhead, 1936)

Layer growth theory refers that when the growth of a layer of atoms happens on the smooth surface of the nuclei, the best "seat" for the atom at the interface which wants to go into the lattice is a position on three sides' concave angle. It can be seen in Figure 2.3, position 3 is the general position, position 2 has two surface concave angles and position 1 has a three sides' concave angle. In the ideal case, the crystal growth begins with the first rank, followed by the adjacent ranks, and then a layer of atoms covers one surface. The crystal grows layer by layer, surface by surface.
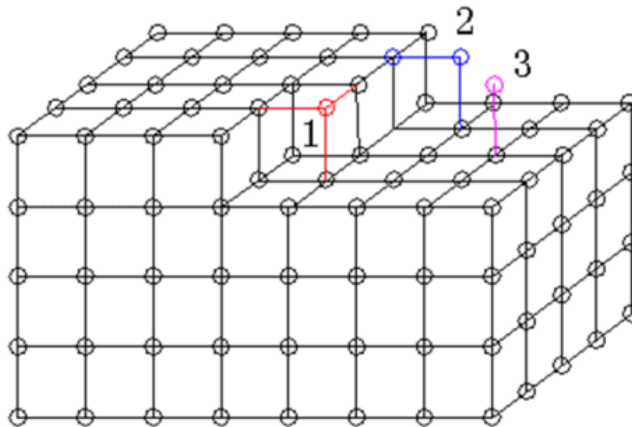
Figure 2.3 Schematic for the Layer growth theory (Bunn and Emmett, 1949).

Some of the growth phenomena could be interpreted as follows:

- The surface of crystal often grows in flat or straight polyhedron shape.

- In the process of crystal growth, the environment may change, resulting in that the properties of crystals (such as color) and composition may subtly change with different times. Therefore, the band structure can be often seen in the cross-section of the crystal.

2. Spiral growth theory (Castle, 1934; Preston, 1948)

Based on the screw dislocation of the crystal structure, spiral growth theory was proposed. On the crystal growth interface, the spiral concave corner emerges on the screw dislocation. The extension of this corner, which is formed by two concave surfaces, is the source of the crystal growth, promoting the growth of the surface.

The formation of screw dislocation (Figure 2.4) can be described as follows: In the crystal growth process, due to the impurities or the non-uniform distribution of the thermal stress, the internal stress of a surface can be generated. When this internal stress exceeds a certain limit, relative shear (AD to BC) along this surface will occur, resulting in that a dislocation will be formed at the end of this relative shear, which is the spiral concave corner.
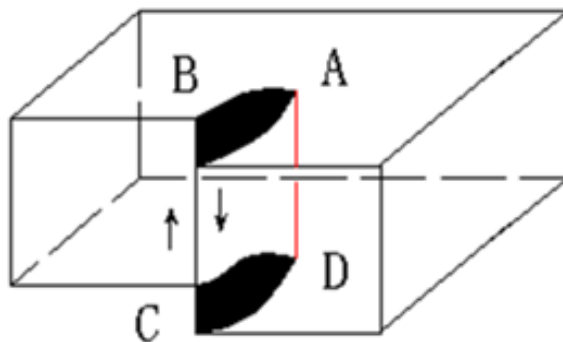
Figure 2.4 Schematic for the Spiral growth theory-1 (Castle, 1934).

The emergence of the dislocation on the crystal surface provides sources (the concave corner) that never disappear. From Figure 2.5, it can be seen that: (a): Molecule falls on the concave corner first; (b)-(e): With the crystal growth, the concave corner cannot disappear with the accumulation of molecules, only the

concave angle continuous spiral with molecule accumulation, leading to the crystal surface layer growth (f).
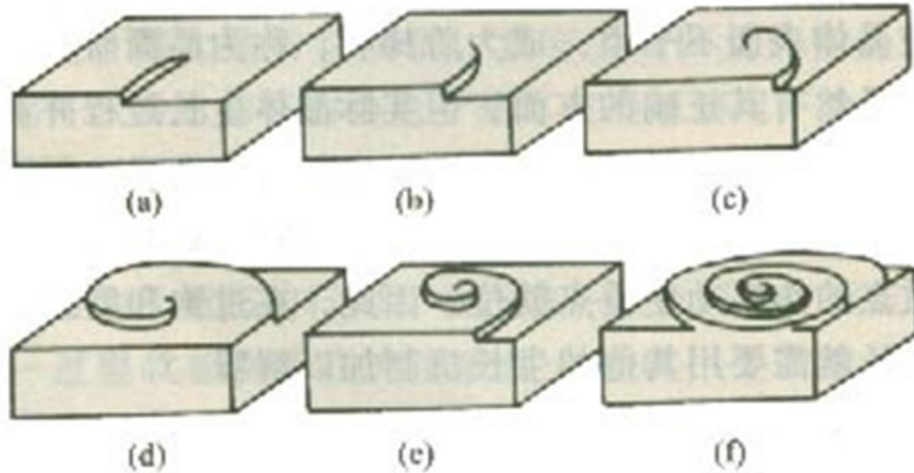
Figure 2.5 Schematic for the Spiral growth theory-2 (Castle, 1934).

2.1.2.3 Growth Rate of Crystal Surfaces

The growth rate of crystal face can be defined as the length of a crystal face grows along its normal direction in a unit time, which is closely related to the size of the crystal surface (Parvov and Shubniko.Av, 1964; Smythe, 1967). Form Figure 2.6, it can be seen that if the growth rate of a crystal face is slower than the adjacent crystal faces, this crystal surface is always gradually expanded during the crystal growth process (AB with the growth rate of h_1 and CD with the growth rate of h_3). However, if a crystal face grows faster than the adjacent crystal faces, this crystal surface may be gradually reduced during the growth process and even eventually completely "submerged" and disappeared (BC with the growth rate of h_2). This phenomenon is known as crystal surface "overlap" (Figure 2.6). It is noteworthy that when the angle between two adjacent crystal faces is an acute angle, the slower growing surface will not overlap the faster one.
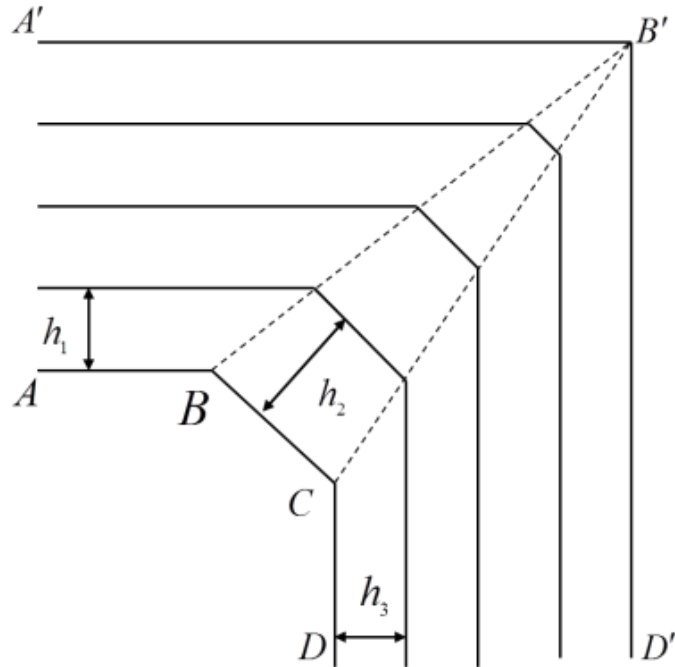
Figure 2.6 Schematic for the crystal surface overlap.

Very commonly when the supersaturation (or degree of supercooling) is high and sometimes even when it is not high, growth kinetics may be diffusion-controlled (Burshtei.Ai and Tsvetkov, 1974; Nielsen, 1959). Under such conditions, the polyhedral crystal form will be unstable; it will sprout protrusions at its corners and edges where the degree of supersaturation is at its highest level. The tips of these protrusions will clearly be the points of highest supersaturation. It is generally believed that the protrusion will become longer (and thinner at the tip) until the effect of interfacial free energy in raising the chemical potential slows the tip growth and maintains a constant value for the tip thickness.

2.1.3 Internal and External Factors of Crystal Morphology

2.1.3.1 Internal Factors of Crystal Morphology

1. Bravis theory (van Uven, 1914)

The actual crystal surfaces are often parallel to the surface that has the density lattice net (Figure 2.7). The larger the density of the surface is, the greater the

importance of the corresponding crystal surface is. In a crystal, the relative growth rate of the crystal face is inversely proportional to the density of its own net. That is, the larger the density of the surface is, the slower the surface grows (the growth rate: 1 (BC) > 3 (AB) > 2 (CD)).
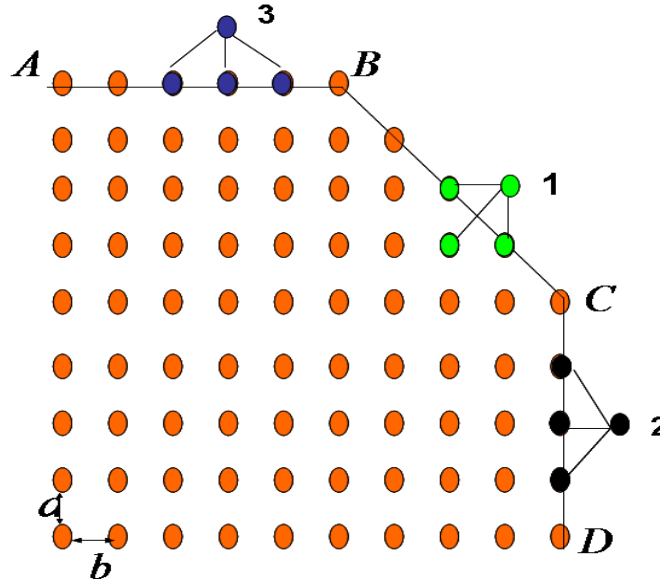
Figure 2.7 Schematic of Bravis theory (b > a) (van Uven, 1914).

2. Wulff theory (Wulff, 1901a)

In equilibrium conditions, the change between two phases is to ensure that the total surface energy is minimal. That is, the equilibrium shape of crystal should have the minimum surface energy. This principle can be expressed as follows:

When both the temperature, *T*, and the crystal volume, *V*, are constant:

$$\sum \gamma_i A_i = \text{Minimun} \tag{2.10}$$

where γ_i and A_i are the surface energy and area of the *i* th face, respectively.

For the equilibrium shape, the normal distance from the crystal centre to the crystal surface is proportional to the surface energy itself. Therefore, the growth rate of the crystal surface is proportional to the crystal surface energy.

2.1.3.2 External Factors of Crystal Morphology

1. Environment (Kunchur, 1965; Lasko, 1961)

At ideal conditions, the environment for the crystal growth (temperature and supersaturation) should be uniform in all directions. Therefore, the growth rate of same surface of crystals can remain unchanged. However, in practical conditions, the environment for the crystal growth is often non-uniform which dramatically affects the crystal morphology.

2. Temperature (Boswell and Iler, 1936; Bridgman, 1933)

Temperature had a direct result of the change of supersaturation or over-cooling degree, which leads to the corresponding change of the surface energy and relative growth rate of different crystal surfaces, hence affecting the crystal morphology.

3. Impurity (Bocek et al., 1962; Bube and Thomsen, 1955; Johnston, 1962)

Impurities in solution often selectively absorb on a crystal surface. The presence of impurities can change the crystal surface energy, so its relative growth rate changes resulting in the crystal morphology changing.

4. Viscosity (Chigrinov and Grebenkin, 1975; Falco et al., 1974)

The increase of solvent's viscosity would prevent the generation of eddy, so the crystal can generate under uniform conditions. Since parts of the crystal's edge are more easily to contact the solute than centres, it grows fast. In contrast, the centre of the crystal grows slowly, or even stops resulting in forming the skeletal crystal.

5. Crystallization rate (Ebian et al., 1975; Lusena and Cook, 1954; Moustafa et al., 1975)

When the crystallization rate is small, the crystal can grow big. Crystallization rate also affects the purity of crystal. The crystal obtained from rapid crystallization tends to wrap a lot of impurities.

2.1.4 Crystal Dissolution and Regeneration

Dissolution is the process by which a solute forms a solution in a solvent. The solute, in the case of solids, has its crystalline structure disintegrated as separate ions, atoms, and molecules form. For liquids and gases, the molecules must be adaptable with those of the solvent for a solution to form. The outcome of the process of dissolution is governed by the thermodynamic energies involved, such as the heat of solution and entropy of solution, but the dissolution itself (a kinetic process) is not. Overall the free energy must be negative for net dissolution to occur. In turn, those energies are controlled by the way in which different chemical bond types interact with those in the solvent (Wulff, 1901b). As the corners and edges of crystals have more opportunities to contact with the solvent, these areas dissolve faster, leading to approximate spherical crystals during dissolution processes.

For dissolved (or partially dissolved) crystals, the crystal polyhedral shape can be restored under a suitable environment, which is referred to the regeneration of the crystal. Dissolution and regeneration are not simply the opposite phenomenon (Valeton, 1923, 1924a, b).

- For crystal dissolution, the dissolution rate changes gradually with the direction of the crystal. This can force the crystal dissolving to a nearly sphere. For crystal regeneration, the growth rate also changes greatly with the direction. Therefore, they can revert to the stable polyhedron shape.
- During the growth process, the surface with large density can be easily maintained. In contrast, in the dissolution process, the surface with larger density becomes more unstable.

2.1.5 Reactive crystallization

Crystallization process is a physical process. Reactive crystallization process puts chemical reactions into this process which makes it more complex. The researchers have made many contributions on the single crystallization process

(cooling or anti-solvent crystallization process) or the chemical reaction kinetics (reaction kinetics), but the study of these two processes combination is still immature, even been involved, most are mainly focused on the inorganic reactive crystallization process.

Tsuge et al (Tsuge et al., 1987) studied reactive crystallization of calcium carbonate by liquid-liquid reaction. Crystallization experiments with calcium carbonate by three liquid-liquid reaction systems from a continuous mixed-suspension mixed-product removal (MSMPR) crystallizer were conducted to make clear the characteristics of reactive crystallization kinetics. Momonaga (Momonaga et al., 1992) studied reactive crystallization of methyl α-mwthoxyimino acetoacetate, they believed that both the chemical reaction and crystallization rates can affect the crystal purity. Betty and Ng (Berry and Ng, 1997) studied the synthesis of reactive crystallization processes. A systematic method was presented to synthesize reactive crystallization processes. It showed how to selectively crystallize a desired solid product(s) after a reaction step and how to use compound formation to effect separation of a mixture. Kelkar and Ng (Kelkar and Ng, 1999) studied the design of reactive crystallization systems incorporating kinetics and mass-transfer effects. A coherent approach for the design of reactive crystallization systems was presented by incorporating reaction and crystallization kinetics, and mass transfer, into an existing equilibrium-based conceptual design method. Mandare and Pangarkar (Mandare and Pangarkar, 2003) studied the effect of mixing parameters on crystal size using semi-batch reactive crystallization of sodium perborate tetrahydrate. They found that secondary nucleation played a dominant role in deciding the final crystal size. Chen (Chen et al., 2004) used a size-independent agglomeration model to interpret a CO_2–$BaCl_2$–H_2O gas–liquid reactive crystallization system. Purwins (Purwins et al., 2007; Purwins et al., 2006) studied the kinetics of the reactive crystallization of $CuInSe_2$ and $CuGaSe_2$ chalcopyrite films for solar cell applications. Guo (Guo et al., 2006) studied the effect of ultrasound on the homogeneous nucleation of $BaSO_4$ during reactive crystallization. Sarkar (Sarkar et al., 2007) proposed that the

determination of the optimal feed profiles for a reactive crystallizer was an important dynamic optimization problem, as the feed profiles offered a significant control over the quality of the product crystals.

These literatures indicated that reactive crystallization had very wide range of application and is worthy to study. They also revealed that the mixing effectiveness and the operation parameters had dramatically effect on the performance of the product such as the crystal size distribution, purity and morphology. In fact, most main active pharmaceutical ingredients are obtained through the rapid organic reactive crystallization process in pharmaceutical industry. Reactive crystallization has many unique features that make them different from cooling or anti-solvent crystallization, even leading to some concepts and methods not directly applicable to the former. Firstly, the metastable zone theory cannot be used anymore because the generated product is insoluble in organic solvents. If the solubility is almost zero, the supersaturation is infinity and the metastable zone does not exist. Secondly, under this great supersaturation, a large amount of secondary nucleation will generate, which may create the agglomeration replace the interface growth to become an important driving force of crystallization grow.

In order to obtain satisfied product, researchers began to monitor even to control the crystallization process despite still stayed in the study of the inorganic material without reaction. Alatalo (Alatalo et al., 2008) studied the utilization of attenuated total reflectance–Fourier transformed infrared (ATR–FTIR) and Raman spectroscopy to investigate isothermal semi-batch precipitation of a model compound, L-glutamic acid. ATR–FTIR spectroscopy was mainly used for in-line monitoring of the solution phase and Raman spectroscopy for analysis of the solid phase (Alatalo et al., 2010a; Alatalo et al., 2010b; Hatakka et al., 2010). Ma and Wang (Ma and Wang, 2012) designed a closed-loop control system on a real crystallization process to produce the desired shape for rod-like crystals based on the principle that it is possible to exercise closed-loop control over the particle shape of the crystals produced from cooling crystallization processes through tracking an optimum temperature

or supersaturation profile which can be obtained through optimisation using a morphological population balance (M-PB) model.

2.2 Sodium Cefuroxime

2.2.1 Introduction

Cefuroxime is a valuable broad spectrum antibiotic, which has high activity against a wide range of gram-positive and gram-negative micro-organisms (Gower and Dash, 1977; Greenwood et al., 1976). The sodium salt of cefuroxime, a non-toxic derivative, is well suited to administration on injection because of good solubility in water (Cook et al., 1976a). As one of the second-generation cephalosporin, due to its superior lactamase stability, even beyond cefoperazone, the third-generation, sodium cefuroxime always plays an important role in clinical practice. Since developed by Glaxo in 1976 (Cook et al., 1976b), sodium cefuroxime has been widely used for decades. However, its poor stability has been widespread concerned during industrial production. In the storage and transportation processes, it tends to deepen solid color, solubility and liquidity is reduced, and it becomes sticky (Fu et al., 2010).

Although sodium cefuroxime has only one crystalline state according to Pharmacopoeia, in a fast reactive process, it exists in a number of different crystallinity with varying degrees of solid stability and purity and with differing physical and chemical characteristics. It has proved in practice that it is difficult to manufacture sodium cefuroxime industrially in a total crystalline form having a combination of suitable properties such as solid state stability, purity, particle size, and filtration and drying characteristics (Stables, 1981).

2.2.2 Physical Profile

The formula of sodium cefuroxime is $C_{16}H_{15}N_4NaO_8S$ (Monosodium (6R, 7R)-3-carbamoyloxymethyl-7-[(Z)-2-furan-2-yl-2-(methoxyimino) acetylamino]-8-oxo-5-thia-1-azabicyclo [4.2.0] oct-2-ene-2-carboxylate) with a molecular weight of 446.37 (Greenwood et al., 1976). The molecular structure can be seen in Figure

2.8. Sodium cefuroxime is a white to light yellowish white crystals or crystalline powder. It is freely soluble in water, soluble in methanol, and very slightly soluble in ethanol (95 %). Fourier transform infrared spectrum and powder x-ray diffraction pattern of sodium cefuroxime are shown in Table 2.1, Figure 2.9 and Figure 2.10.

Table 2.1 Infrared Band Assignments of sodium cefuroxime.

Wavenumber, cm^{-1}	Infrared Assignment
3500	NH stretch of amide, H-bonded
3368,3254	NH stretches, symmetric and antisymmetric of carbamate NH_2
3063,3000	6-H,7-H stretches in β-lactam ring
2961	CH asymmetric stretch in CH_3
2937,2926	CH asymmetric stretch in CH_3
2906	CH asymmetric atretch in OCH_3
2879	CH symmetric atretch in CH_3
2856	CH asymmetric atretch in CH_2
2820	CH deformation, overtone, CH_3
1758	C=O stretch, β-lactam
1699	C=O stretch, carbamate
1667	C=O stretch, amide I
1642	C=N, oxime
1627,1412	C=O stretches, asymmetric and symmetric, in CO_2
1560,1546	NH deformations; also amide II in syn-CH_3O oximes
1603,1483,1402	Ring bands in 2-substituted furans
1461	CH_3 deformation in CH_3O
1335	NH_2 bend, in carbamate
1083	C-O stretch, in CH_3O
1063,1048	C-O and N-O stretches, in CH_2O of carbamate and oxime
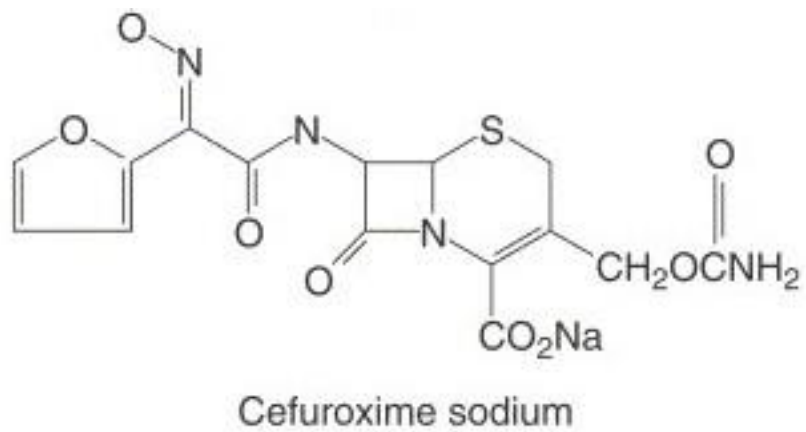
Cefuroxime sodium

Figure 2.8 The molecular structure of sodium cefuroxime.
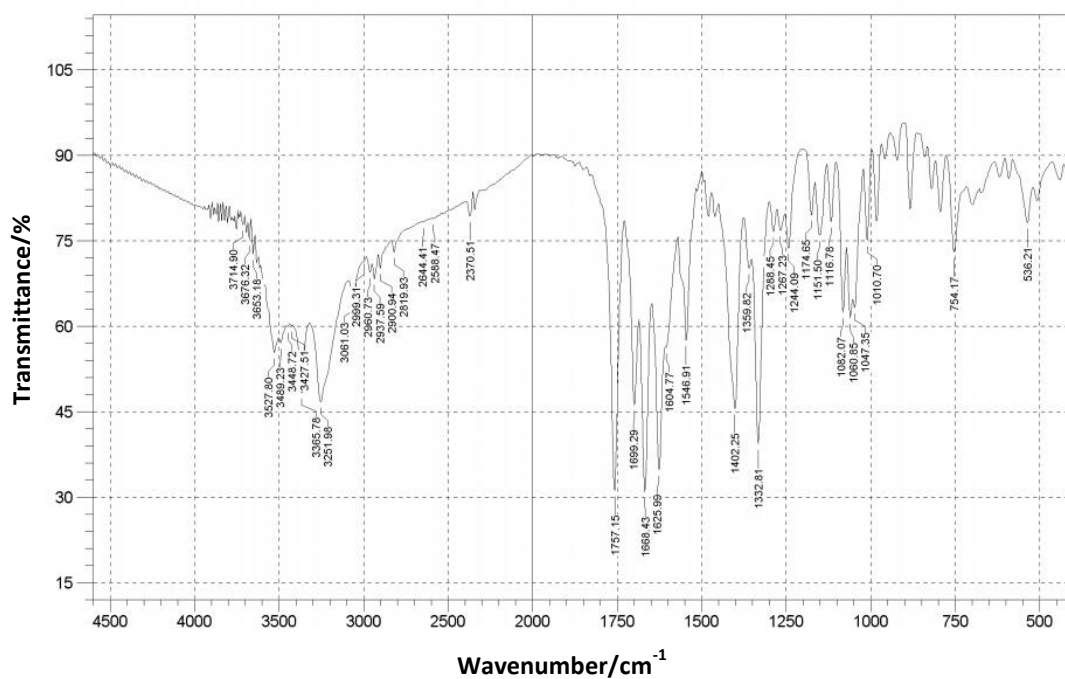
Figure 2.9 Infrared spectrum of sodium cefuroxime.
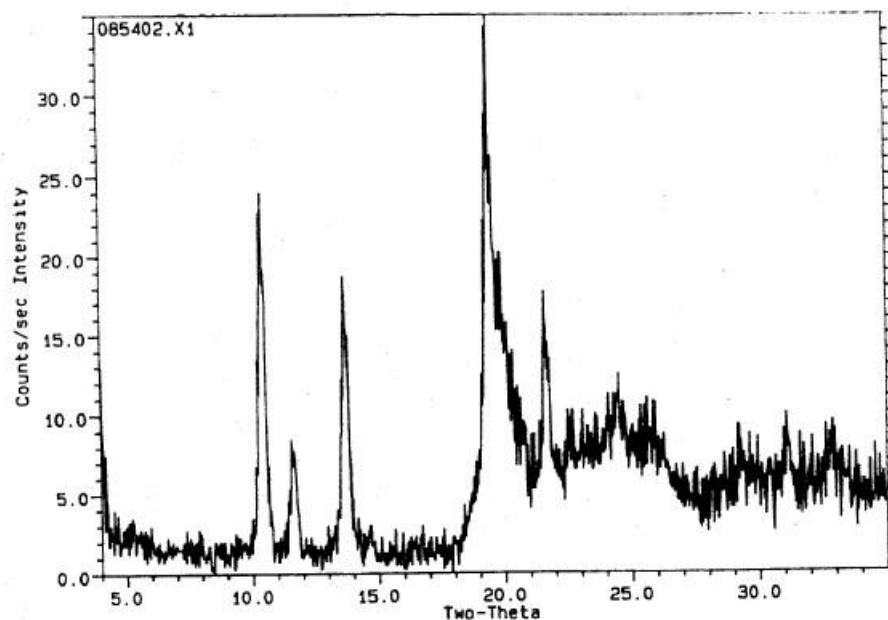
Figure 2.10 Power x-ray diffraction pattern of sodium cefuroxime (Mixture of crystalline and amorphous) (Wozniak and Hicks, 1991).

2.2.3 Overview of the Synthetic Process

At present, there are four main methods of sodium cefuroxime production:

- Acid cefuroxime is dissolved in the mixed solvent of water and acetone, then active carbon is added into the solvent mixture for bleaching. After filtration, sodium salt (sodium lactate, sodium acetate, and sodium ethylhexanoate) is added for crystallization to produce sodium cefuroxime (Cabri et al., 2003; Humber et al., 1981; Thompson and Baalham, 1981; White et al., 1988).

- By adding acetonitrile, acid cefuroxime forms a solvent compound firstly, then follows method (a) (Zheng et al., 2011; Zhou and Fu, 2010).

- By adding N, N-benzyl acetamide, acid cefuroxime forms salt firstly, and then sodium salt is added to the mixture of acetone, methanol, acetonitrile and tetrahydrofuran to precipitate out sodium cefuroxime (Cook et al., 1976a, b).

- Crude sodium cefuroxime is dissolved in water firstly, then active carbon is added into the solvent mixture for bleaching. After filtration, water

miscible organic solvent (acetone, isopropanol and ethanol) is dropped to precipitate out sodium cefuroxime (Cai et al., 2007; Hu et al., 2011; Stables, 1981).

The first three methods use different reaction paths, reaction conditions or solvents to improve the process. The last one is a method for purification by re-crystallization process. In these patents (Cabri et al., 2003; Cai et al., 2007; Cook et al., 1976a, b; Hu et al., 2011; Stables, 1981; Thompson and Baalham, 1981; White et al., 1988; Zheng et al., 2011; Zhou and Fu, 2010), most researchers focused on the purity or the yield of this drug, stability test is only mentioned as a detection means, few of them concerned about the impact of various process parameters on stability, not to mention the crystallinity (Crisp et al., 1991a; Crisp et al., 1991b). In fact, the stability of drugs in their amorphous form is usually lower than crystalline form, because of the higher free energy level. Therefore, increase the crystallinity of the drug can further improve its stability.

2.2.3.1 Reactive Synthesis of Sodium Cefuroxime

Cefuroxime Acid

at 10°C to 15°C for 5 mins

anhydrous sodium acetate (5 g)

pH had risen to 7.2   filter

washed with methanol (23 ml) containing dichloromethane (10 ml)

warmed to 25°C   →   1.5 hrs   washed with THF → Sodium Cefuroxime
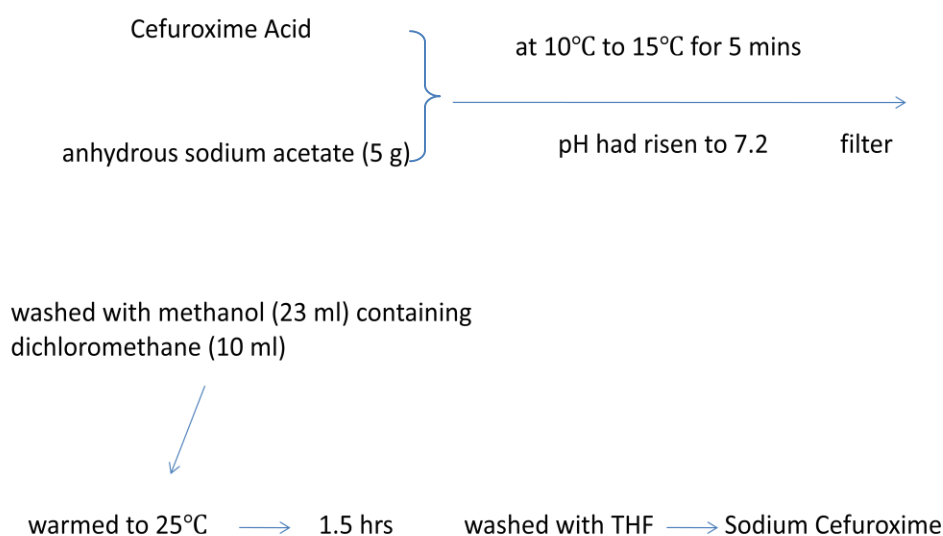
Figure 2.11 Reactive synthesis of sodium cefuroxime 1.

Cefuroxime Acid 20°C

sodium 2-ethylhexanoate (338 g) in a mixture of methyl acetate and water (40 ml) was added over 20 minutes

pH of 5.5

10 mins

filtered

washed with methyl acetate
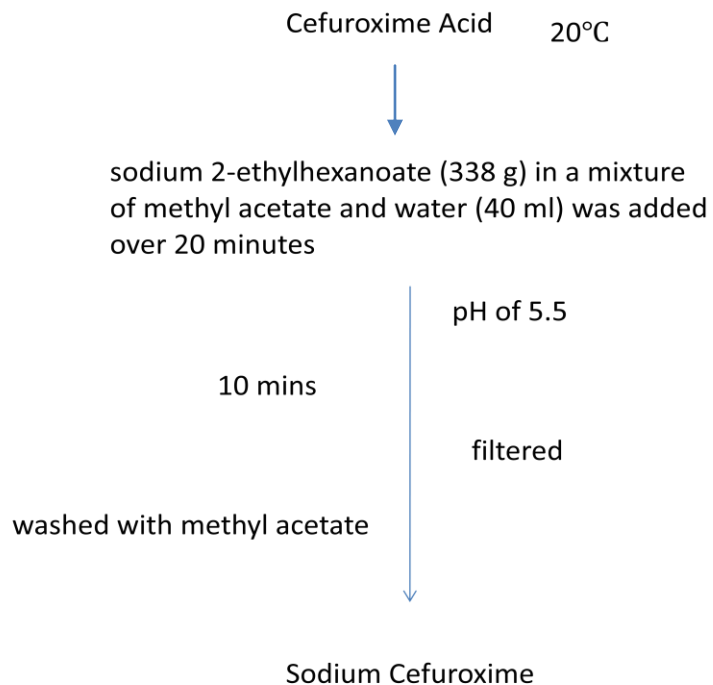
Sodium Cefuroxime

Figure 2.12 Reactive synthesis of sodium cefuroxime 2.

water(4ml)

ethanol(25ml,95%)

acetone(120ml)   Charcoal (0.6g)   filtered

citric acid (0.35g)

cefuroxime acid(10g)   stirred 30mins   acetone

ethanol(50ml)
                                    40°C
acetone(10ml)
                                                Sodium Cefuroxime
sodium lactate(5g,70%)   stirred 30mins
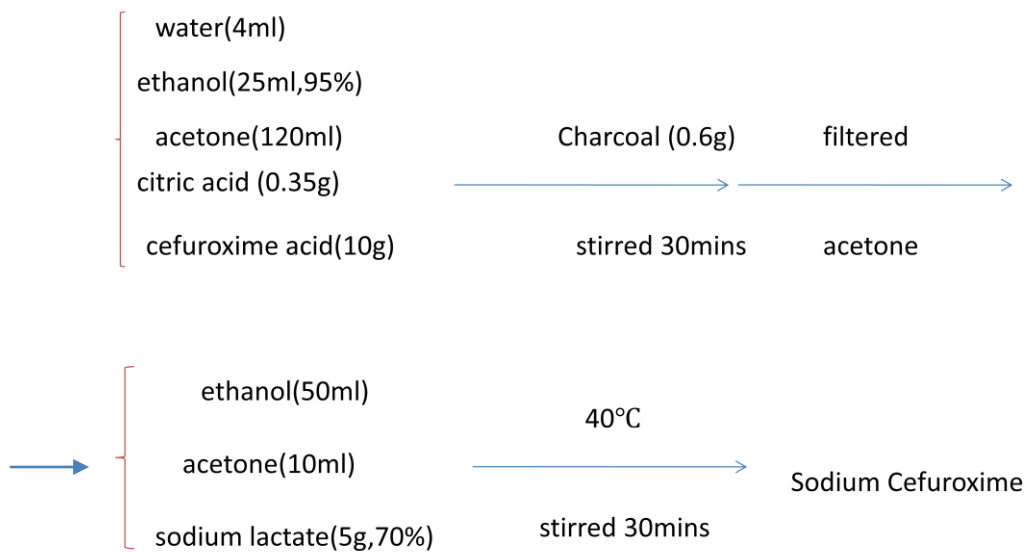
Figure 2.13 Reactive synthesis of sodium cefuroxime 3.

water(50ml)

acetone(400ml)

cefuroxime acid(50.9g)

25℃ ~26℃

Charcoal (5g)

filtered

sodium lactate(0.27g)
methanol(250ml)
sodium ethylhexanoate(39.5g)

stirred 30mins

Sodium Cefuroxime

20℃
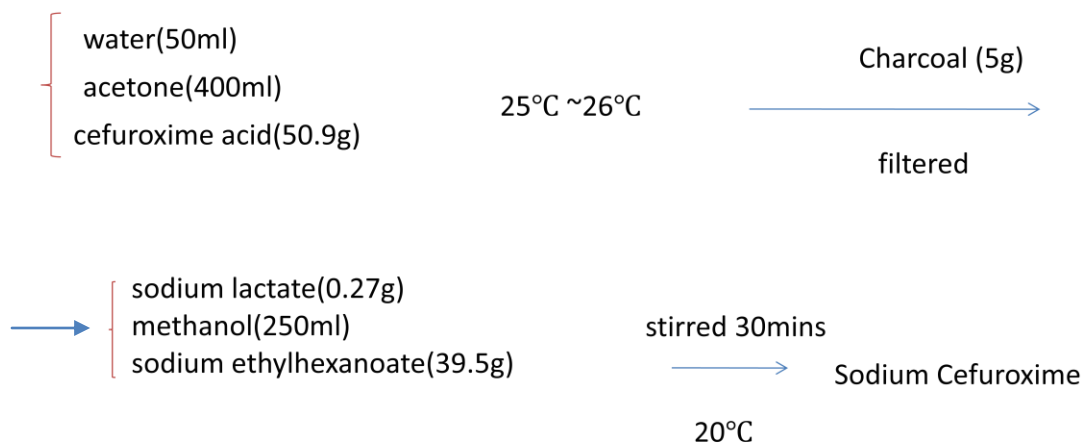
Figure 2.14 Reactive synthesis of sodium cefuroxime 4.

water(30ml)

acetone(200ml)

cefuroxime acid(40g)

Charcoal (4g)

filtered

25℃ ~30℃

sodium lactate
sodium acetate
sodium ethylhexanoate

stirred 15mins

acetone(600ml)

stirred 30mins
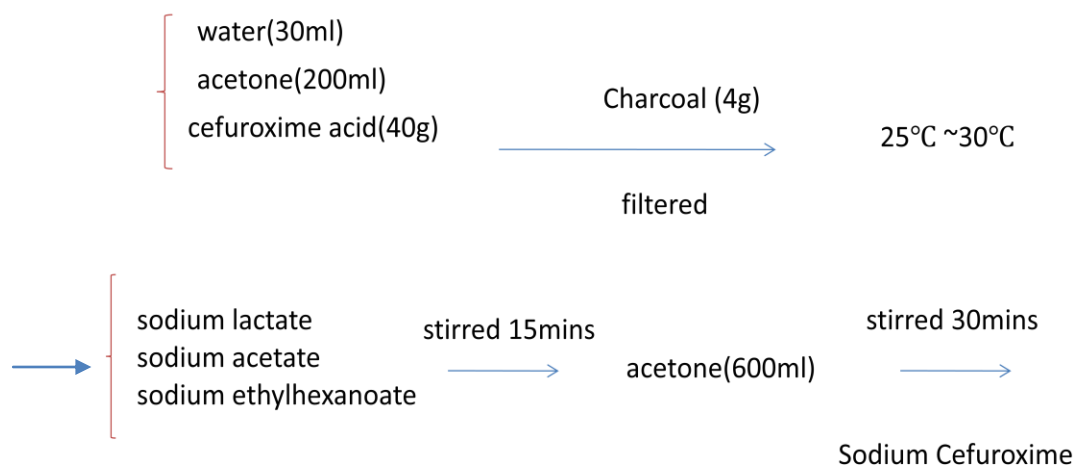
Sodium Cefuroxime

Figure 2.15 Reactive synthesis of sodium cefuroxime 5.

2.2.3.2 Re-crystallization of Sodium Cefuroxime

Sodium cefuroxime (10 g)   Charcoal (1 g)

in water (60ml) at 25℃-30℃   ————————————————→   filtered

stirred for 30 mins

added at 20° to stirred slurry of
sodium cefuroxime (Form II;0.1 g)
in 25% w/v sodium lactate aqueous   aqueous solution of 50% w/v
solution (20ml) maintained at 50℃   sodium lactate (70 ml) at 20℃
over 3 hours

————————————————————————→

cooled to 5℃   Sodium Cefuroxime
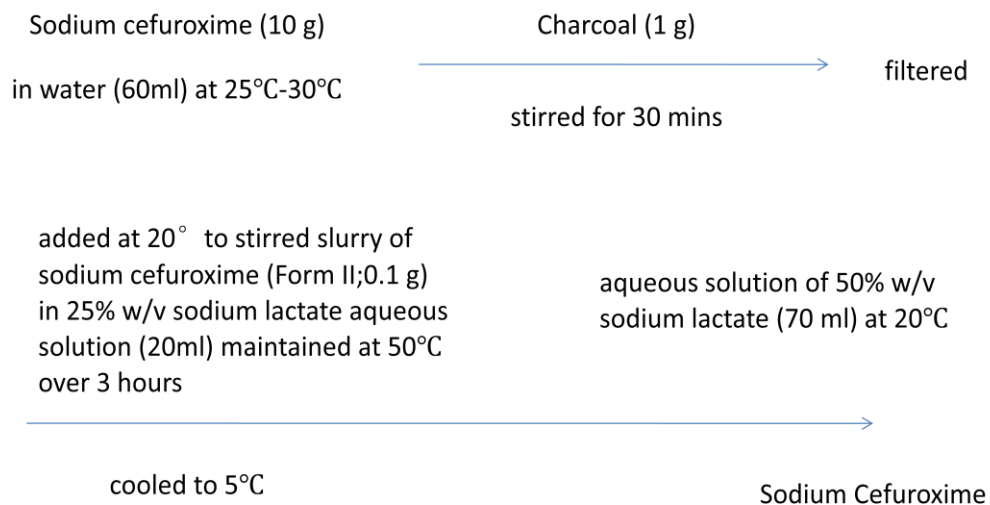
Figure 2.16 Re-crystallization of sodium cefuroxime 1.

Sodium cefuroxime (10 g)   Charcoal (1 g)   25℃

water (100ml)   ————————————————→   filtered

stirred for 30 mins

5℃
————————→   –   acetone(2000ml) ————→   stirred for 30 mins

1hr

30 mins
————→   Sodium Cefuroxime
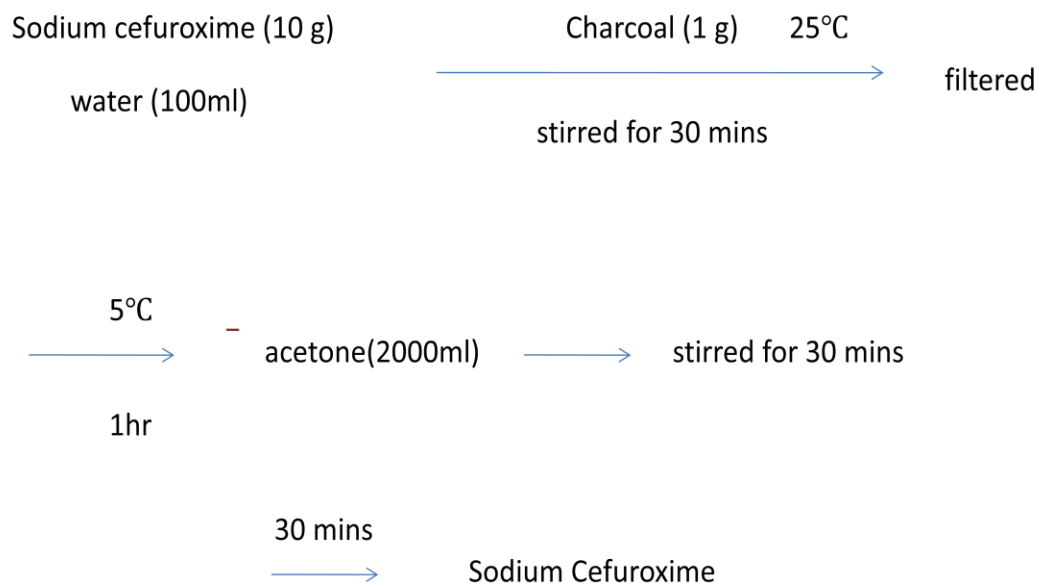
Figure 2.17 Re-crystallization of sodium cefuroxime 2.

Sodium cefuroxime (35 g) Charcoal (1.1 g) 15℃ 10% Acetic acid, pH-6.5

water (200ml)

stirred for 30 mins filtered

methanol(48ml) 10 ℃ ~15℃ acetone(560ml)

acetone(967ml)

3℃ ~ 5℃ Sodium Cefuroxime

1hr
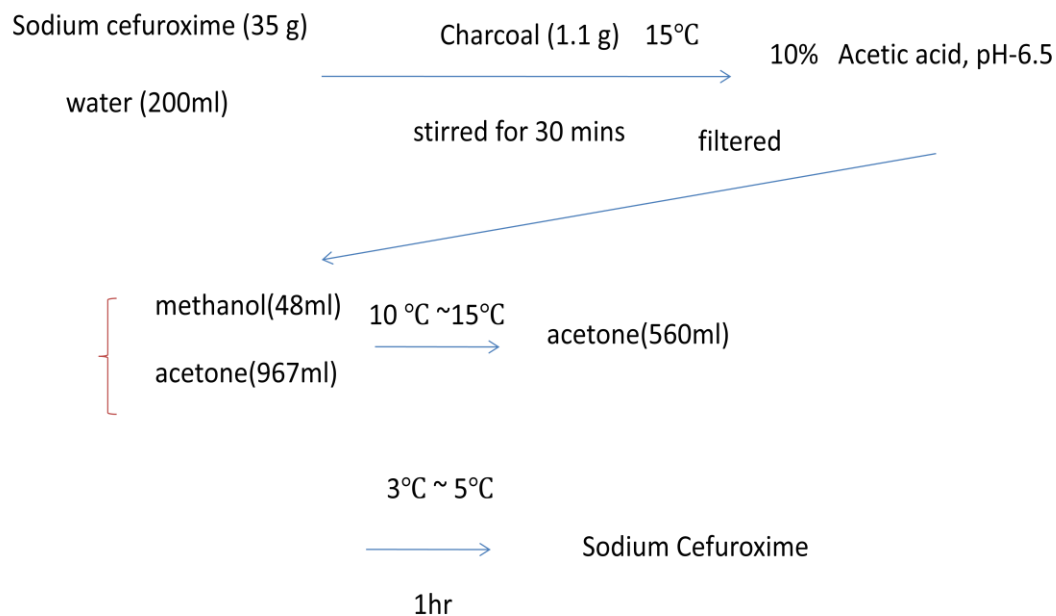
Figure 2.18 Re-crystallization of sodium cefuroxime 3.

2.2.3.3 Motivation

As a drug produced through either the reaction crystallization process or a re-crystallization process, the change of the crystalline form can not only affect the drug external appearance without altering its internal structure, but also reduce its effectiveness, or even endanger the safety of the drug consumers. This is because the stability of drugs in their amorphous form is generally lower than that of drugs in their crystalline form, due to the higher free-energy level of the amorphous state. For example, the relationship between degradation rate and crystallinity determined from heats of dissolution for ß-lactam antibiotics such as sodium cefazolin indicates that a drug with low crystallinity tends to have decreased chemical stability (Pikal et al., 1978; Siviero et al., 2002). Thus, since sodium cefuroxime is described as a predominantly amorphous martial in Pharmacopoeia, it indicates that increase of its crystallinity would likely improve its stability.

2.3 Stability of Drugs

2.3.1 Introduction

The stability of a drug includes chemical stability and physical stability. Due to the difference of molecular structures, under certain conditions, some drugs are easy for chemical degradation. Likewise, with the changes of the physical conditions, some drugs are also easy for physical degradation. Chemical degradation and physical degradation of drug substances may change their pharmacological effects, resulting in altered efficacy therapeutic as well as toxicological consequences (Kisbye and Schou, 1951). Because pharmaceuticals are used therapeutically based on their efficacy and safety, they should be stable and maintain their quality until the time of usage or until their expiration date. The quality should be maintained under the various conditions that pharmaceuticals encounter, during production, storage in warehouses, transportation, and storage in hospital and community pharmacies, as well as in the home. Therefore, understanding the factors that alter the stability of pharmaceuticals and identifying ways to guarantee their stability are critical (Schou, 1951; Schou and Rhodes, 1951a, b).

2.3.2 Chemical Stability

2.3.2.1 Introduction

The easiest way to study drug instability is to understand the effect of drug loss, which results in a reduction of effectiveness, through chemical reactions. The effectiveness loss often happens due to the poor quality of a drug. The drug effectiveness loss can be caused by:

- Drugs may change to the toxic substances because of degradation. Therefore, it is important not only to understand how much time drugs loss will cost, but also its degradation products. In some situations, the degradation products may be known as toxicity (Ellin and Wills, 1964; Sokoloski et al., 1977).

- Degradation of drugs may make the product esthetical unacceptable. If a significant feature changes such as the color or the odour of drugs, the consumer will refuse even though its effectiveness did not reduce (Gosselin et al., 1996b; Hoener et al., 1974).

- Even though a drug may be stabilized in its intended formulation, the formulator must show that the drug is also stable under the *pH* conditions found in the gastrointestinal tract, if the drug is intended for oral use. Most drug substances are fairly stable at the neutral pH values found in the small intestine (disregarding enzymatic degradation) but can be unstable at *pH* values found in the stomach (Anderson et al., 1988; Gosselin et al., 1996a; Nightingale, 1976).

2.3.2.2 Pathways of Chemical Degradation

As pharmaceutical drugs have different molecular structures, various degradation pathways exist, including hydrolysis, dehydration, isomerisation and racemisation, elimination and oxidation. It will be very useful if the chemical stability can be predicted from the molecular structure of the drug. It will also help both in the design of stability and in the early stages of drug development to determine the drug formula in order to minimize chemical degradation.

For most injection products, the drug needs to contact with water, even in solid dosage forms, the water often exists, though at very low levels. Therefore, hydrolysis is one of the most common reactions associated with drug degradation. Many researchers have widely reported on the drug hydrolysis, such as the hydrolysis of procaine (Higuchi et al., 1950; Marcus and Baron, 1959), aspirin (Edwards, 1950; Garrett, 1957), chloramphenicol (Lusena and Cook, 1954). Hydrolysis is often the main degradation pathway for drugs having ester and amide functional groups in their molecular structures.

Sodium cefuroxime, known as a kind of β-lactam antibiotics, has ester and amide functional groups within its molecular structure. It means hydrolysis of ester bond and amide bond become the main cause of chemical degradation.

2.3.3 Physical Stability

2.3.3.1 Introduction

Most studies on drug stability have focused on the chemical stability of drugs. However, the physical stability of drugs must also be studied. The physical state of a drug determines the physical properties such as solubility. Because these properties affect the efficacy and the safety of a drug, changes in the physical state of a drug need to be noticed. Traditionally, changes in physical state can be detected by differential scanning calorimeter and X-ray diffraction analysis.

2.3.3.2. Physical Degradation

1. Crystalline state and Polymorphism

The chemical stability of drugs is affected by the crystalline state of the drug. Drugs with the crystalline state have lower free energy, hence resulting in slower degradation reactivity.

Many drugs have different polymorphism. Each crystalline state has different free energy level and different chemical reactivity. For example, ramified crystals of 5-nitroacetylsalicylic acid are more susceptible to hydrolysis than the column-shaped crystals (Okamura et al., 1980). Solid-state hydrolysis of carbamazepine from needle-shaped crystals with a higher crystalline order is faster than that of beam-shaped and prismatic forms (Luckhaus and Modica, 1989). Reactivity of carbamazepine to light also depends on the crystalline form of the drug (Matsuda et al., 1994). Differences in reactivity among different crystalline forms have also been reported for photodegradation of furosemide (Devilliers et al., 1992).

The stability of drugs in their amorphous form is usually lower than crystalline form, because of the higher free energy level. For example, the study of β-lactam antibiotic sodium cefuroxime indicates that a drug with low crystallinity tends to have lower chemical stability (M. J. Pikal et al., 1978).

2. Moisture adsorption

Moisture adsorption is very important for solid drugs. Moisture adsorption during storage can affect the physical stability of drugs. Moisture adsorption is controlled by the physical properties of the drug. For example, the adsorption of moisture by aspirin crystals is increased by adding hydrophilic excipients (Mitrevej and Hollenbeck, 1983).

It has reported that the moisture adsorption rate, W', for water-soluble drugs can be represented by the following equation, based on a heat-transport control model (Vancampen et al., 1983a, b, c):

$$W' = (C + F)ln\frac{RH_i}{RH_0} \qquad (2.11)$$

RH_i and RH_0 are relative humidity and critical relative humidity, respectively, and C and F are the conductive coefficient and the radiative coefficient, respectively.

2.3.4 Factors Affecting Stability

Factors, which affect the stability of drugs, include internal factors such as the molecular structure and external factors such as the temperature, *pH* value, light, oxygen and moisture. In addition, mechanical forces such as pressure may also affect the drug chemical and physical stability.

2.3.4.1 Temperature

Temperature is one of the main factors affecting drug stability. The relationship between rate constant and temperature has been described by the Arrhenius equation,

$$k = Aexp(\frac{-Ea}{RT}) \qquad (2.12)$$

where *Ea* is the activation energy and *A* is the frequency factor.

2.3.4.2 The *pH* value

The second most important parameter affecting drug stability is *pH* value. Many

researchers have studied the effect of *pH* value on degradation rates of drug substances in aqueous solutions (Adams, 1969; Brodersen, 1947; Tiselius, 1981).

The effect of *pH* value on degradation rate can be explained by the catalytic effects that hydronium or hydroxide ions can have on various chemical reactions. Effectively, a catalyst is a species that does not change the free energy of the reactants and products. It lowers the energy barrier to reaction. By definition, a true catalyst is not consumed as a result of the reaction.

When a reaction depends on constant *pH* value, it usually follows pseudo-first-order kinetics, which can be described by first-order rate constant k_{obs}. A reaction in which hydronium ion, hydroxide ion, and water catalysis are observed can be described by

$$k_{obs} = k_{H^+}\alpha_{H^+} + k_{H_2O} + k_{OH^-}\alpha_{OH^-} \qquad (2.13)$$

Where k_{obs} is the sum of the specific rate constants and activities for each parallel pathway, and a_{H+} and a_{OH-} are the activities of hydronium and hydroxide ion, respectively.

2.4 Crystallizer

2.4.1 Introduction

There are a couple main basic vessel types:

- A tank
- A pipe or tubular reactor (laminar flow reactor(LFR))

Both types can be used as continuous reactors or batch reactors. Most commonly, reactors are run at steady-state, but can also be operated in a transient state. When a reactor is first brought back into operation, it would be considered to be in a transient state, where key process variables change with time. Both types of reactors may also accommodate one or more solids

(reagents, catalyst, or inert materials), but the reagents and products are typically liquids and gases (Burton et al., 1948; Cohen, 1954).

There are three main basic models used to estimate the most important process variables of different chemical reactors:

- batch reactor model (batch)

- continuous stirred-tank reactor model (CSTR)

- plug flow reactor model (PFR)

2.4.2 Continuous Stirred-Tank Reactor (CSTR)

In a CSTR (Figure 2.19), one or more fluid reagents are introduced into a tank reactor equipped with an impeller while the reactor effluent is removed.
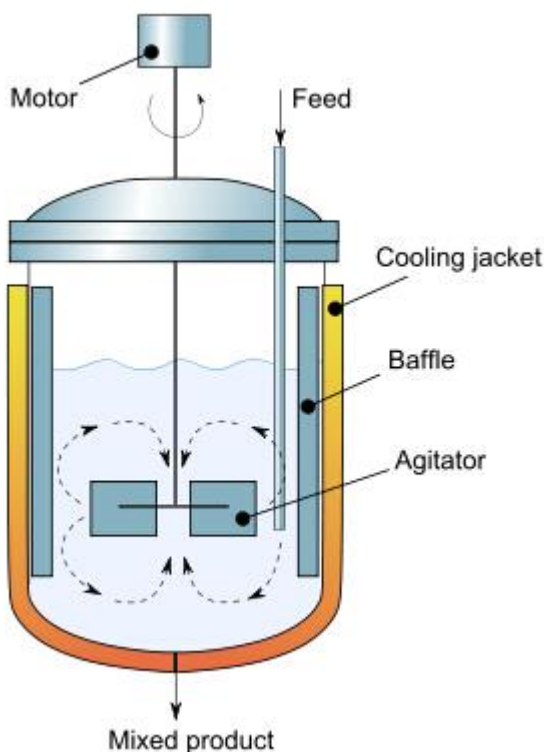
Figure 2.19 Cross-sectional diagram of Continuous flow stirred-tank reactor (Schmidt and Dauenhauer, 2007).

CSTR is widely used in crystallization studies. Leubner (Leubner, 1998) proposed a new steady state theory of crystallization in the continuous stirred tank reactor (CSTR). This theory was developed based on a dynamic balance between growth and nucleation. Lucas (Lucas et al., 2007) modeled an entire poly(ethylene terephthalate) (PET) solid-state polymerization (SSP) process with precrystallizers, crystallizers, SSP reactors, and dryers using a unified cell approach. This approach built complex unit-operation models using individual cells and continuous-stirred-tank reactor (CSTR) models. Akindeju (Akindeju et al., 2010) studied a phenomenological spinning disc continuous stir tank and settler reactor (SDCSTR) for continuous synthesis of titania from its chloride precursor and water in which the desired polymorph, particle size, and distribution were controlled by the characteristics of the atomized inlet reagents, disc, and tank stir rate. Steyer (Steyer et al., 2010) investigated the influence of detailed thermodynamically well formulated activity coefficient models on the particle size distributions (PSDs) in a one-dimensional population balance model of a semibatch continuous stirred-tank reactor (CSTR). Zhang (Zhang et al., 2013) reported the theoretical derivation of a kinetic model for the prediction of average block structures such as number-average blocks, average block length, and average number of linkage points per chain, etc., in chain shuttling polymerization in the presence of dual catalysts based on the proposed mechanism. They further investigated how the chain shuttling rate constant and virgin chain shuttling agent (CSA) feed rate affected the average block structures predicted by this theoretical model for polymers produced in a continuous stirred tank reactor (CSTR).

2.4.3 Plug Flow Reactor (PFR)

In a PFR, one or more fluid reagents are pumped through a pipe or tube (Figure 2.20). The chemical reaction proceeds as the reagents travel through the PFR. In this type of reactor, the changing reaction rate creates a gradient with respect to distance traversed; at the inlet to the PFR the rate is very high, but as the

concentrations of the reagents decrease and the concentration of the product(s) increases the reaction rate slows.
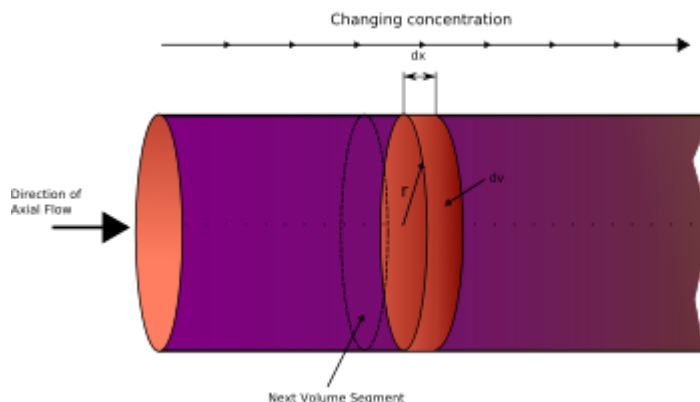
Figure 2.20 Simple diagram illustrating plug flow reactor model (McComas and Eckert, 1965).

Stoller' (Stoller et al., 2005) work dealt with the use of a compartmental model to interpret the change of the performances of a draft-tube baffled (DTB) crystallizer due to progressive scaling. The examined case was the reaction - crystallization of sodium perborate tetrahydrate. First of all, a model based on both MSMPR and PFR compartments was developed. The model was then applied to evaluate the reduction of the flow rate of the circulation stream through the draft-tube due to progressive scaling, and to predict the relevant crystallizer performances. Finally, the possibility of estimating the scaling extent in the crystallizer from the crystal size distribution (CSD) measured along the run time was shown. Johnson (Johnson et al., 2012) studied a fully continuous process including an asymmetric hydrogenation reaction operating at 70 bar hydrogen, aqueous extraction, and crystallization at pilot scale. The main safety advantages of running the hydrogenation reaction continuous rather than batch were that the flow reactor was smaller for the same throughput and, more importantly, the tubular hydrogenation reactor ran 95% liquid filled at steady state.

2.5 Final Remarks

In this chapter, the principles of crystallography, crystal formation method including nucleation and growth, the internal and external factors affecting crystal morphology, as well as the crystal dissolution, regeneration and the reactive crystallization were first introduced. Then the re-crystallization process and reactive crystallization process of sodium cefuroxime were reviewed. This chapter also summarized the factors that affect the physical and chemical stability of the drug. In the final section, the optimization progress of the crystallization reactor was described.

Chapter 3
Materials and Experimental Instruments

3.1 Materials

In traditional processing methods, 7-ACA (3-(Acetyloxymethyl)-7-amino-8-oxo-5-thia-1-azabicyclo [4.2.0]oct-2-ene-2- carboxylic acid) was used as the reactant for the production of sodium cefuroxime. However, 7-ACA needs strong alkali such as sodium hydroxide to break the acetyl bond, which leads to more side reactions hence affecting product quality. Therefore, a replaced reactant, D-7-ACA (Deacetyl 7-ACA) was used in this study, which is more environment-friendly and can further improve the recovery ratio of the product (Liu et al., 2014). The reaction stoichiometric equation can be seen as follows:
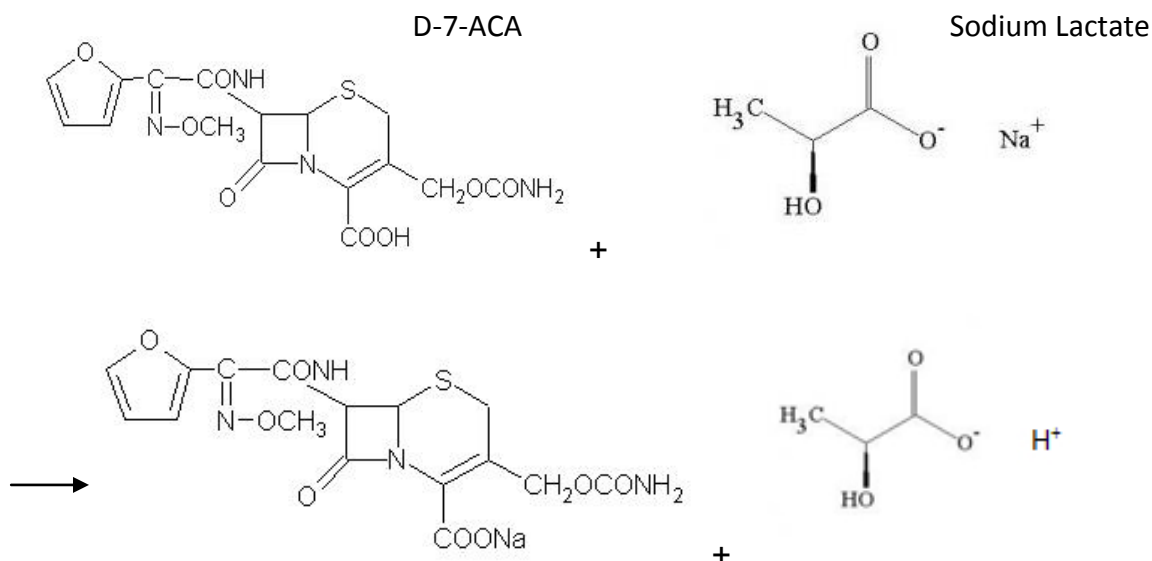
Its physical profile can be seen in Table 3.1 and Figure 3.1.

Table 3.1 Physical profile of acid cefuroxime.

Analysis	Specifications
Description	White or almost white crystalline powder
Solubility	Soluble in N,N-dimethylacetamide, very slightly soluble in ethanol, practically insoluble in water
PH	2.5-3.5
Water	1.0%
Specific optical rotation	$+62^{o}$--$+68^{o}$
Absorbance (450nm)	0.20
Assay	98.5%
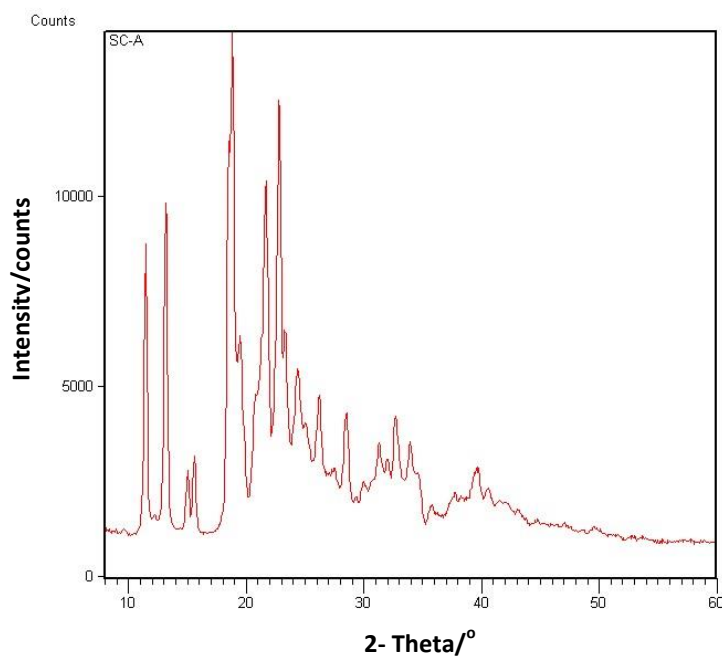
Figure 3.1 The XRD pattern of acid cefuroxime.

The preparation of the reaction solution can be described as follows: At first, 9.0 g 60 % w/w sodium lactate aqueous solution (Fisher Scientific UK Ltd) was dissolved in the mixed solvent of 40 mL acetone and 50 mL 95 % ethanol at 20 - 25 $^{\circ}$C. The mixture was then filtered and washed with 10 mL 95 % ethanol into a beaker. Next, 10 g acid cefuroxime was dissolved in the mixed solvent of 246 mL acetone and 124 mL 95 % ethanol. The activated carbon was added in the acid cefuroxime solution and this mixture was stirred for 10 - 15 minutes at 38 - 42 $^{\circ}$C, then filtered and the activated carbon needed to be washed with 30 mL acetone. After that, put the sodium lactate solution in the tank crystallizer first with 0.3 g sodium cefuroxime crystals added as seeds. Then the acid cefuroxime solution was added into the reactor with 4 mL·min^{-1} feed rate at 25 - 28 $^{\circ}$C, and the reaction took place immediately at a stirring speed of 80 - 100 rpm. Because sodium cefuroxime is insoluble in the solvent, the solution became turbid quickly. Finally, the reaction products, sodium cefuroxime, needed to be filtered and washed by the mixture of acetone and 95 % ethanol (1.8 : 1) until the pH valve reached 8.0. After 24 hours vacuum drying in the DZF-6030B vacuum oven, the final product can be obtained. The seeds, sodium cefuroxime crystals ($C_{16}H_{15}N_4NaO_8S$, 446.37 kg·mol^{-1}, > 92 %, water content < 0.24 %), was produced by an anti-solvent re-crystallization process (Liu et al., 2014). Ethanol (95 % v/v) and activated carbon were obtained from Fisher Scientific UK Ltd, acetone was obtained from Sigma, and the distilled water produced in our own laboratory was also used in the process.

3.2 Experimental Instruments

3.2.1 Pump and Vacuum Oven

3.2.1.1 Diaphragm Pump

A diaphragm pump is a positive displacement pump that uses a combination of the reciprocating action of a rubber, thermoplastic or teflon diaphragm and suitable valves either side of the diaphragm to pump a fluid.
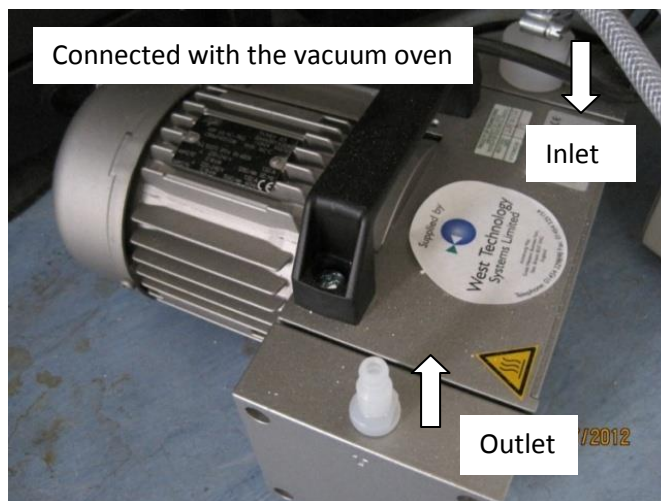
Figure 3.2 The diagram of diaphragm pump.

The diaphragm pump (Figure 3.2) consists of a pump body and a drive motor. The pump casing contains the drive unit and two pump heads. Each pump head contains a diaphragm and the work valves. Both pump heads are arranged opposite each other. It is for the vacuum oven.

3.2.1.2 Peristaltic Pump

The peristaltic pump used in this study (Figure 3.3) is a liquid delivery device for controlling the flow rate. It usually makes the contents of the tube moving towards a certain direction by periodically compressing the elastic tube at an even rate. The flow rate is determined by the diameter of the pipe and compression speed.
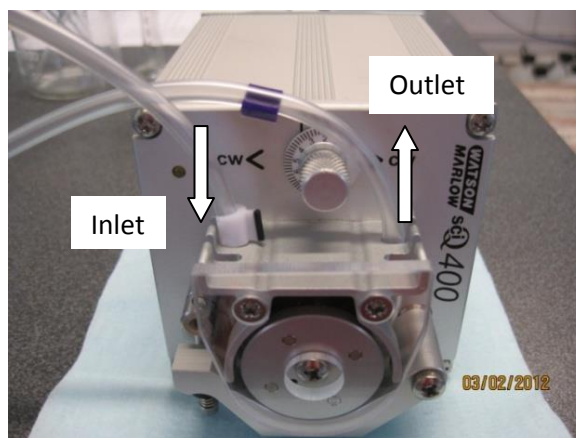
Figure 3.3 The diagram of peristaltic pump.

3.2.1.3 Vacuum oven

Vacuum oven (Figure 3.4) is designed especially for drying materials, which is thermo-sensitive or decompounded and oxidative easily. It can be filled with inert gases, which is especially in a rapid drying of some compound material.
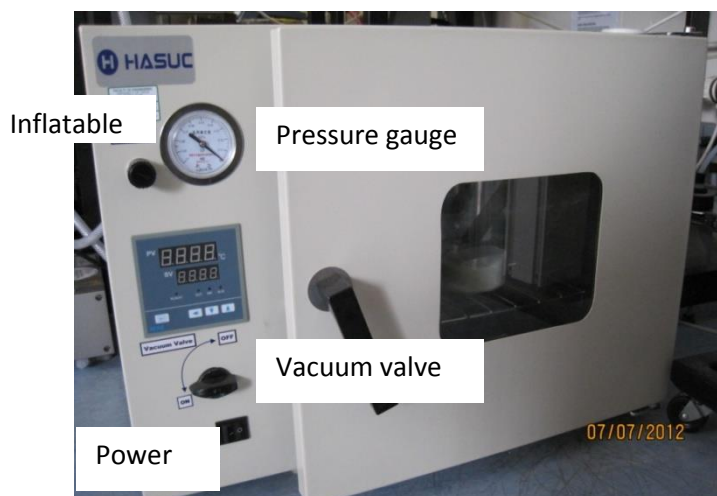
Figure 3.4 The diagram of vacuum oven.

3.2.2 Attenuated Total Reflection-Fourier Transform InfraRed (ATR-FTIR) Spectroscopy

The core part of Fourier Transform Infrared Spectrometer (Figure 3.5) is a Michelson interferometer. Before the sample reaches the detector, certain frequencies of infrared light absorption happen, this makes the interference light intensity change, resulting in different interference pattern of the different samples. The interference pattern of light curve changes with the moving distance of the moving mirror. The use of the Fourier transform function can produce intensity versus frequency spectrum figures.

Figure 3.5 Attenuated Total Reflection-Fourier Transform InfraRed (ATR-FTIR) spectroscopy (Ma et al., 2010).

ATR-FTIR is widely used for measurement of concentration and supersaturation during the crystallization process. Dunuwila and Berglund (Dunuwila and Berglund, 1997) used Attenuated Total Reflection (ATR) Fourier transform infrared (FTIR) spectroscopy for the in situ measurement of supersaturation in crystallization processes. Lewiner (Lewiner et al., 2001) proposed that the monitoring of supersaturation using on-line FTIR was a valuable method for an improved analysis of key phenomena involved during crystallization processes (primary and secondary nucleation. agglomeration, phase transition, seeding, etc.). Pollanen (Pollanen et al., 2005) presented a stable PLS calibration for solute concentration measurement in batch cooling crystallization processes using ATR-FTIR, which meant that ATR-FTIR can be used to predict the concentration during the crystallization process. Borissova (Borissova et al., 2009) then assessed the in situ measurement of solution supersaturation associated with the batch cooling crystallization of L-glutamic acid (LGA) at 500 mL and 20 L scale sizes via ATR-FTIR spectroscopy. Recently, ATR-FTIR was used for studying APIs frequently. Wang (Wang et al., 2013) studied the anti-solvent co-crystallization process of carbamazepine and

saccharin using on-line ATR-FTIR and Felipe Soares and Carneiro (Felipe Soares and Carneiro, 2014) studied co-former crystals in ibuprofen-nicotinamide co-crystals also using on-line ATR-FTIR.

3.2.2.1 IR Principle

Infrared spectroscopy (IR spectroscopy) is a spectroscopy that deals with the infrared region of the electromagnetic spectrum, that is light with a longer wavelength and lower frequency than visible light (Elert et al., 1998). The infrared portion of the electromagnetic spectrum is usually divided into three regions; the near-, mid- and far- infrared, named for their relation to the visible spectrum (Figure 3.6).
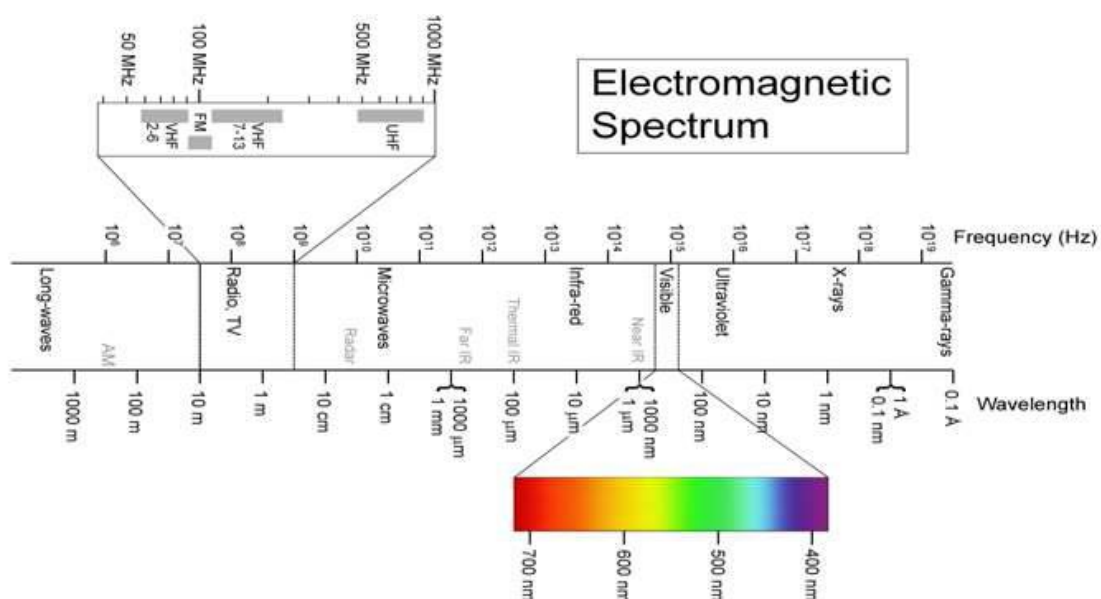
Figure 3.6 The whole range of ElectroMagnetic (EM) spectrum, Infrared light lies between the visible and microwave wavelengths (Ma et al., 2010).

The higher-energy near-IR, approximately $14000 \sim 4000$ cm^{-1} ($0.8 \sim 2.5$ µm wavelength) can excite overtone or harmonic vibrations. The mid-infrared, approximately $4000 \sim 400$ cm^{-1} ($2.5 \sim 25$ µm) may be used to study the fundamental vibrations and associated rotational-vibrational structure. The far-infrared, approximately $400 \sim 10$ cm^{-1} ($25 \sim 1000$ µm), lying adjacent to the microwave region, has low energy and may be used for rotational spectroscopy.

The names and classifications of these subregions are conventions, and are only loosely based on the relative molecular or electromagnetic properties.

In order to be "IR active", it must be associated with changes in the dipole. A permanent dipole is not necessary, as the rule requires only a change of the dipole in moment. A molecule can vibrate in many ways, and each way is called a vibrational mode. For molecules with N number of atoms, linear molecules have $3N - 5$ degrees of vibrational modes, whereas nonlinear molecules have $3N - 6$ degrees of vibrational modes (also called vibration degrees of freedom). For example, H_2O, a non-linear molecule, have $3 \times 3 - 6 = 3$ degrees of vibrational freedom, or modes.

Simple diatomic molecules have only one bond and only one vibrational band. If the molecule is symmetrical, e.g. N_2, the band is not observed in the IR spectrum, but only in the Raman spectrum. Asymmetrical diatomic molecules, e.g. CO, absorb in the IR spectrum. More complex molecules have many bonds, and their vibrational spectra are correspondingly more complex, i.e. big molecules have many peaks in their IR spectra.

Vibrations fall into the two main categories of stretching and bending. Stretching means change in inter-atomic distance along bond axis, and bending means change in angle between two bonds. There are four types of bending: rocking, scissoring, wagging and twisting.

In addition to the vibrations mentioned above, interaction between vibrations can occur (coupling) if the vibrating bonds are joined to a single, central atom. Vibrational coupling is influenced by a number of factors:

- Strong coupling of stretching vibrations occurs when there is a common atom between the two vibrating bonds.
- Coupling of bending vibrations occurs when there is a common bond between vibrating groups.
- Coupling between a stretching vibration and a bending vibration occurs if the stretching bond is one side of an angle varied by bending vibration.

- Coupling is greatest when the coupled groups have approximately equal energies.
- No coupling is seen between groups separated by two or more bond.

When a certain wavelength of infrared go through a group molecule of material and the vibration frequency or the rotational frequency of this group molecule happens to have the same frequency with the infrared light, the molecules can absorb energy to transit from the ground state energy level to a higher energy level. Therefore, infrared spectroscopy method is essentially a way to determine the substance of molecular structure according to the relative vibration and rotation between the molecules inside atom. Organic molecules exist in different energy states that can absorb corresponding infrared wavelengths (Richard et al., 2005). It is actually the energy state of a molecule which allows us to perform a measurement with IR in the wavelength regions as shown in Figure 3.7 (absorption bands at different wavelengths).
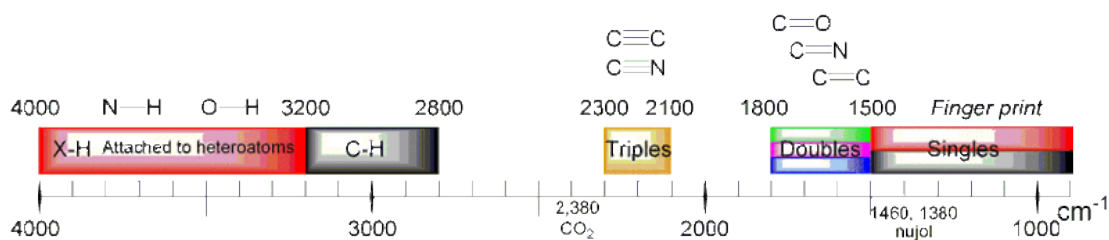
Figure 3.7 The chemical absorptions bands of infrared spectrum between 1000 – 4000 cm^{-1} (Ma et al., 2010).

The law of absorption gives the first quantitative unit for spectral measurements. A relationship must be derived between the concentration of a substance and the absorption it causes (Brugel, 1965a, b). Equation shows the relationship between the concentration and the absorbance famously known as the Bouguer-Lambert-Beer law

$$A = \varepsilon bc \qquad (3.1)$$

where A is absorbance; ε is the extinction coefficient; b is path length; c is concentration.

3.2.2.2 IR Techniques

A common laboratory instrument that uses this technique is a Fourier transform infrared (FTIR) spectrometer. FTIR spectroscopy is a measurement technique that allows one to record infrared spectra. Infrared light is guided through an interferometer and then through the sample (or vice versa). A moving mirror inside the apparatus alters the distribution of infrared light that passes through the interferometer. The signal directly recorded, called an "interferogram", represents light output as a function of mirror position. A data-processing technique called Fourier transform turns this raw data into the desired result (the sample's spectrum): Light output as a function of infrared wavelength (or equivalently, wavenumber).

The design of the ATR-FTIR probe, instrument and the procedure for its use in experimental process is shown in Figure 3.8. In experimental operational practice, the top part of the probe was inserted into the solution to meausure its concentration. The process of how ReactIR works will be explained briefly. As illustrated in Figure 3.8, ReactIR is probe based Attenuated Total Reflection mid-FTIR spectroscopy. The evanescent penetration depth of the infrared light into the processing medium at the probe tip is limited to 1-2 micrometers which enables selective detection of molecules in solution for either homogeneous or heterogeneous systems. The detected infrared absorbance is a function of solution concentration and solution temperature, which is the basis for solution concentration measurement using ReactIR.

Internal Reflection (ATR)

from source
4000~650 cm^{-1}

Liquid-Solid Slurry

ATR crystal

to detector

Beer's Law: A = abc

1~2 μm

A – absorbance
a – absorptivity, molar absorption or extinction coefficient; a = a (I,T,type)
b – optical path length into the sample (cm); b = b (I,T,RI) in ATR
c – solute molar concentration (mol/L)

(a)

49

(b)   (c)
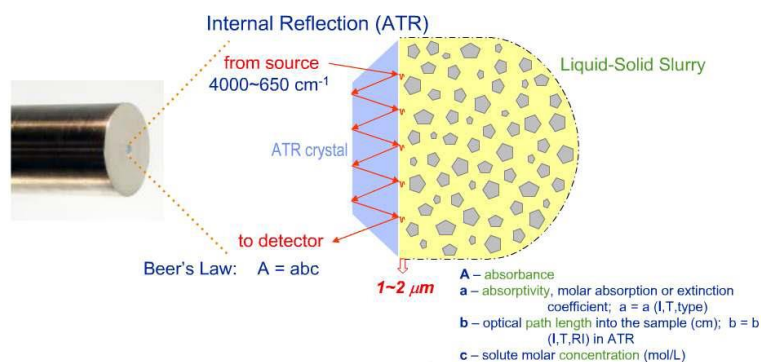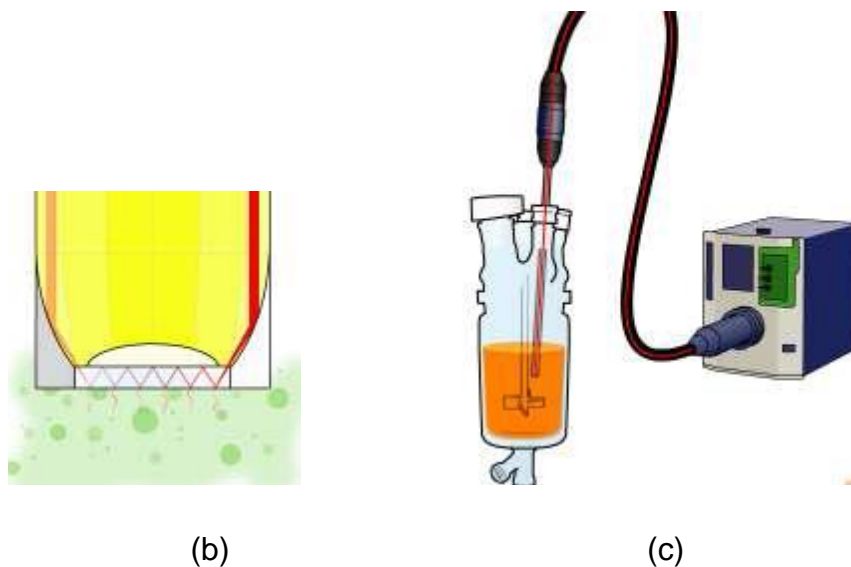
Figure 3.8 (a) The probe tip of the instrument (b) The probe tip in the solution (c) Straight connection between probe and fibre (Ma et al., 2010).

After the measurement of the spectra, the data was transferred to the connected PC and the corresponding IC IR software will manage the data and show it on the interface in real-time (Figure 3.9).
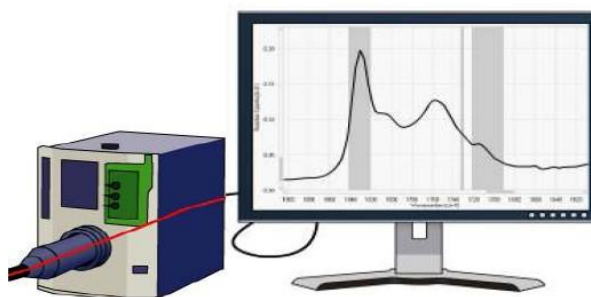
Figure 3.9 The spectra connected to a PC and the real-time measurement of the spectrum (Ma et al., 2010).

3.2.3 Focused Beam Reflectance Measurement (FBRM)

The basic measurement principle of the FBRM technique is a relatively simple concept. This cutaway schematic in Figure 3.10 illustrates the key internal components of each probe-based instrument. A solid-state laser light source provides a continuous beam of monochromatic light that is launched down

FBRM probe. An intricate set of lenses focuses the laser light onto a small spot. This focal spot is carefully calibrated to be positioned at the interface between the probe window and the actual process. It measures the chord length distribution (CLD), which is a relevant function of the crystal size distribution, and also provides the count number, which is a relevant function of the seed number.
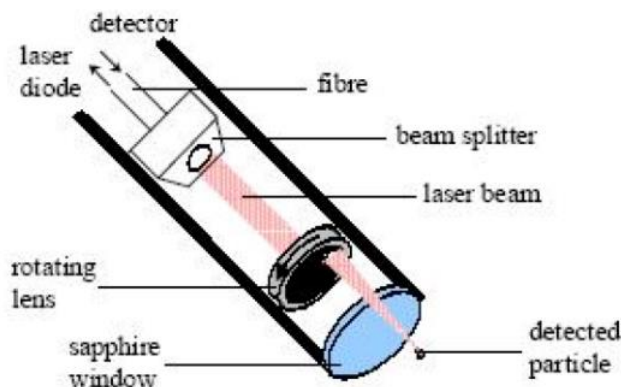
Figure 3.10 Schematic of the focused beam reflectance measurement (Braatz, 2002).

The FBRM technique provides on-line and in-situ information about the chord length distribution of a population of particles in dispersion. This is rather promising for applications such as crystal size distribution control in crystallization processes. Ruf's (Ruf et al., 2000) study deepened the understanding of the characteristics of the FBRM measurement. On the one hand, a model was presented, which allowed in principle to transform particle size distributions (PSD) into chord length distributions (CLD). On the other hand, measurements with particles in suspension showed the critical dependence of the measurement on the optical properties of the system. Yu (Yu et al., 2008) examined the relationship among total counts of chord lengths, statistics of chord length distribution, particle number and average particle size in simulated crystallization, which involved selective introduction of predetermined particle populations into a suspension so as to simulate the occurrence of nucleation and crystal growth as detected by the FBRM. Hermanto (Hermanto et al., 2010) achieved batch-to-batch product quality consistency in terms of crystal size distribution (CSD) in un-seeded anti-solvent crystallization using FBRM.

During the manufacturing of active pharmaceutical ingredients crystalline products in the purest forms are required. Quite often multiple components are present during crystallization, which requires their continuous monitoring and finally separation. Saleemi (Saleemi et al., 2012c) demonstrated the application of ATR-UV/vis spectroscopy with suitable calibration model together with FBRM for the monitoring of a multi-component crystallization system including both cooling and anti-solvent operations. Luo (Luo et al., 2013) used In-situ ATR-FTIR, FBRM and particle video microscope (PVM) simultaneously to monitor the concentration, supersaturation, chord length distribution, and crystal habit, respectively, during a cooling crystallization process of Methyprednisolone Hemisuccinate (MPHS) from ethanol system.

3.2.3.1 FBRM Principle

FBRM is used for the optimization experiment of the amount of seed. The basic measurement principle of the FBRM technique is a relatively simple concept. This cutaway schematic in Figure 3.11 illustrates the key internal components of each probe-based instrument. The probe of the FBRM instrument is cylindrical, which is good for being fixed when measuring. The laser which is emitted by the laser diode inside the probe forms laser beam in the beam splitter via optical fibres. The laser beam is directed down the probe and focused at a focal point near the probe window. As the optics is rotating around an axis parallel to the probe at a constant speed, the laser beam can have a circular pathway. When a particle passes near the probe window, it can be scanned across by the laser beam. The particle can scatter light back to the probe. The light is then collected inside the probe for the analysis. When the laser beam crosses the particle, it traces a chord along the particle profile.
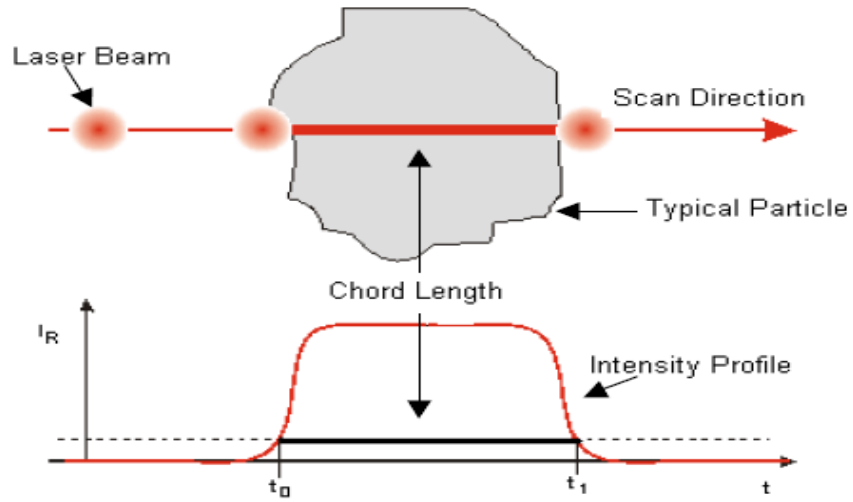
Figure 3.11 The principle of measuring the chord length by FBRM.

This chord length distribution (CLD) can be calculated by the duration of the reflection, which is a relevant function of the crystal size distribution, and FBRM can also provide the count number, which is a relevant function of the seeds number. The principle of measuring the chord length is shown in Figure 3.11.

The laser beam, which runs at a speed of V_b, is reflected to the FBRM probe partially at the point when it first touches the crystal. The duration of the reflection is measured as t_0. The laser beam then traces along the particle profile and reflected partially at the point when it leaves the crystal. The duration of this reflection is measured as t_1. The chord length, S, can be calculated by V_b, t_0 and t_1:

$$S = V_b \times (t_1 - t_0) \tag{3.2}$$

The times of chord length measured can be added up to form Figure 3.12.
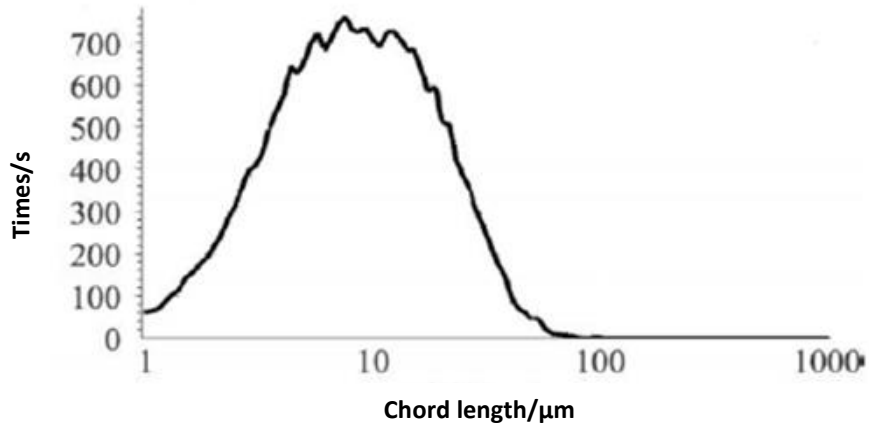
Figure 3.12 The chord length distribution.

3.2.4 Scanning Electron Microscope (SEM)

Scanning electron microscope (SEM) (Figure 3.13) is commonly used for material analysis. Scanning electron microscopy is used to observe the surface structure of the samples. Its working principle is that using a bunch of very fine electron beam to stimulate the secondary electrons from the sample surface, which are collected by the probe, where change the scintillator into optical signals. Then the optical signals are converted into electrical signals by the photomultiplier tube and amplifier to control the strength of the electron beam on the screen, showing synchronized with the electron beam scanning images. The image reflects the surface structure of the sample. In order to let the sample surface to emit secondary electrons, the sample after fixation, dehydration, will spray on a layer of heavy metal particles, issued under the electron beam bombardment secondary electron signal.
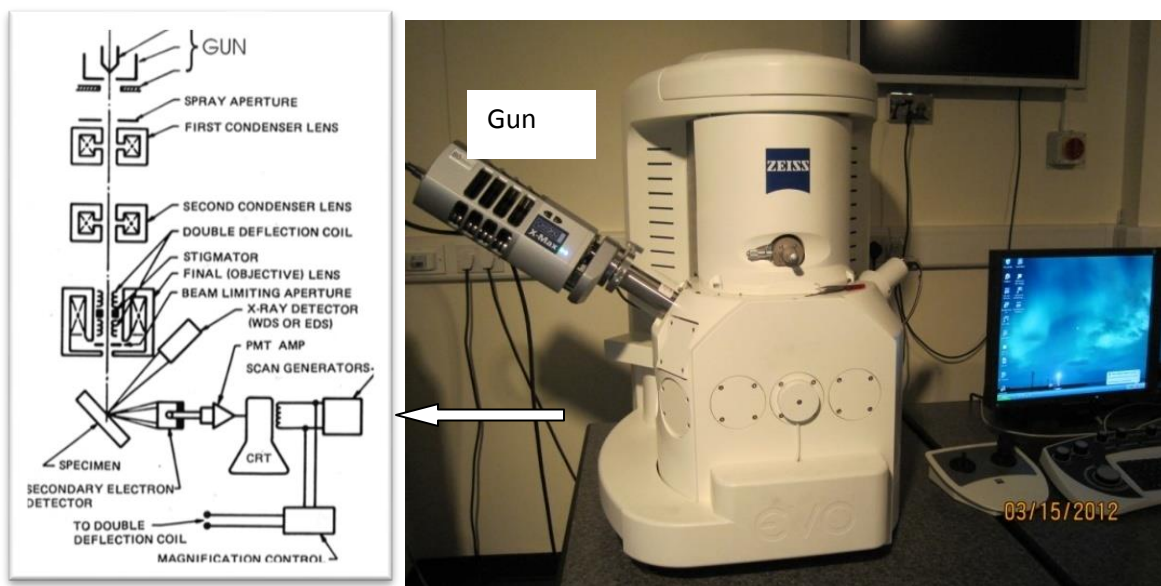
Figure 3.13 The diagram of scanning electron microscope (Zhao et al., 2013).

3.2.5 *Morphologi* G3

The *Morphologi* G3 (Figure 3.14) measures the size and shape of particles using the technique of static image analysis. Fully automation with integrated dry sample preparation makes it the ideal replacement for costly and time-consuming manual microscopy measurements. The main features are summarised as follows:

- Automated SOP control for unattended operation and reproducible results boosting productivity

- Excellent quality microscope images ensuring accurate characterization

- Integrated dry powder dispersion with accurate pressure control automates sample preparation for consistent measurements

- Advanced manual microscope control mode providing increased value as a shared laboratory resource

- Rapid automatic particle counting on membrane filters

- Powerful and intuitive software interface making both visual and statistical interpretation of your data easier than ever.
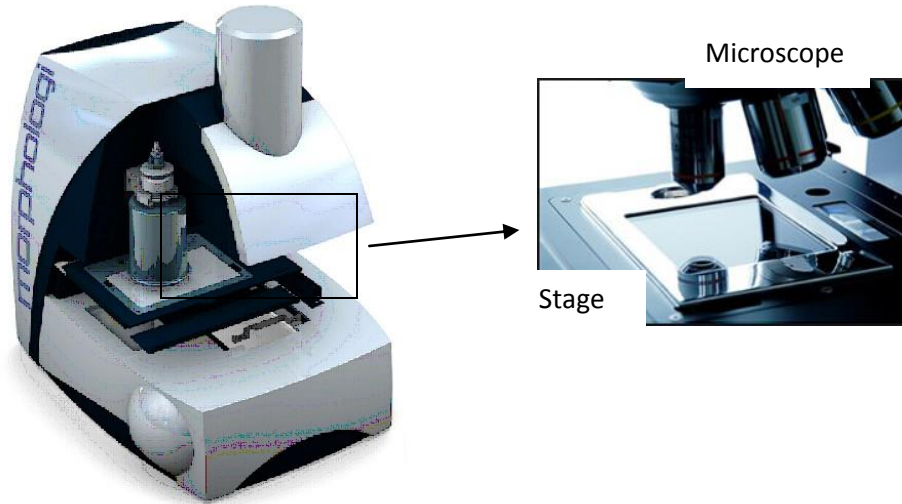
Figure 3.14 The diagram of *Morphologi* G3 (Zhao et al., 2013).

3.2.6 X-ray Diffraction (XRD)

XRD (Figure 3.15) is short for X-ray diffraction. The crystal can be used as the X-ray grating to enhance or diminish the intensity of the X-ray coherent scattering light, interference effect will occur. The maximum intensity of the beam is called the X-ray diffraction line due to the large number of atomic scattering wave superposition ((Benedict et al., 1979; Brusewitz, 1982; Huang et al., 1981).
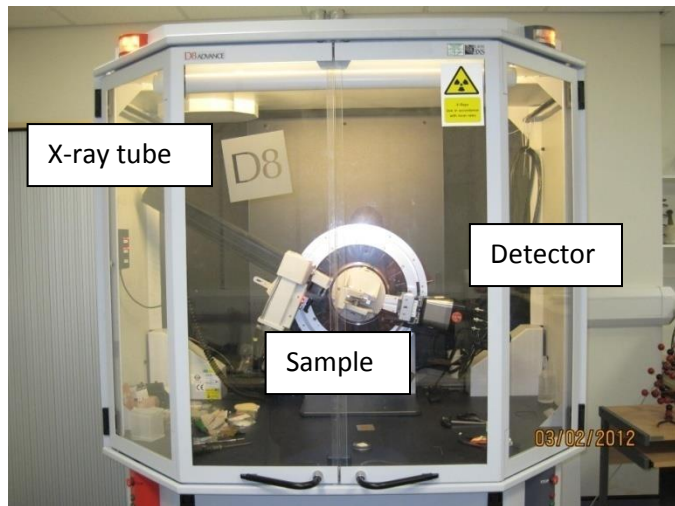
Figure 3.15 The diagram of X-ray diffraction.

Consider a set of equidistant atomic planes of spacing *d*, and a monochromatic plane X-wave falling on it at an angle *θ* (Figure 3.16). It is assumed that each atomic plane reflects a very small fraction of the incident amplitude, small enough so that the weakening effect of this reflection on the incident amplitude may be neglected throughout the crystal. Under most angles of incidence, θ, the waves reflected from neighbouring planes will show a phase difference, and where all the reflected waves come together at great distance from the crystal, the superposition of these waves of systematically increasing phases will lead to a cancellation of amplitudes and to optical field zero. There exists, then, only the transmitted wave. If, however, the phases of all the reflected waves arrive within less than one half wave-length phase difference, then all reflected amplitudes will build up together to an optical field in the direction of reflection, without any actual cancellations of contributions (Hubbard et al., 1983; Pierron et al., 1967; Sargent et al., 1979).

$$2d \sin \theta = n\lambda \qquad\qquad (3.3)$$
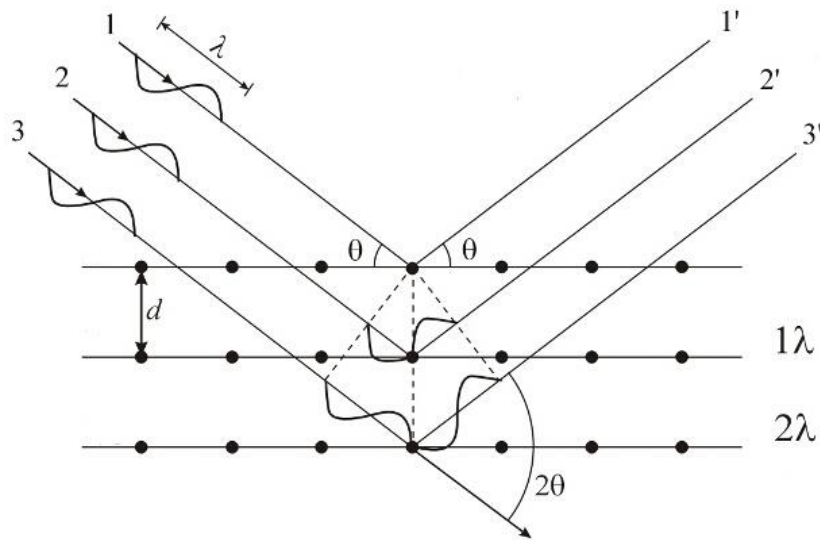
Figure 3.16 Bragg diffraction schematic (Bragg, 1912).

Application of a known wavelength X-ray to measure the angle *θ*, to calculate the interlinear spacing *d*, is used for X-ray structure analysis. Another application is using known *d* crystal to measure the angle *θ*, in order to

calculate the characteristic X-ray wavelength, and thus can be detected in the existing data elements contained in the sample.

An X-ray beam impinging on a crystal will be scattered in all directions by the atoms of the crystal. In some directions, an increased intensity is observed due to the constructive interference of the scattered waves. The conditions for constructive interference are easily derived from the simple geometrical picture for the scattering of an X-ray beam by planes of atoms in a crystal, shown in Figure 3.16. From Figure 3.16, it is clear that diffraction from a set of planes will only occur if the normal to these planes is bisecting the angle between the incident and the scattered beam (Schumann and Nagel, 1982; Steele and Wertz, 1977; Wong et al., 1983), which means that diffraction occurs only when the distance travelled by the parallel X-rays are an integer of the wavelength. There are three X-ray methods for quantitative phase analyses:

- External standard method – compare the experimental line intensity from the mixture to a line from a pure phase.
- Direct comparison method – compare the experimental line intensity from the mixture to a line from another phase in the mixture.
- Internal standard method – compare the experimental line intensity from the mixture to a foreign material mixed with the sample.

X-ray diffraction can also be used for crystallinity determination (Adnadjevic et al., 1990; Foner and Adan, 1983; Gundy, 1987; Pikal et al, 1978; Teeaar et al., 1987). For a mixture of crystalline and non-crystalline (sodium cefazolin), the X-ray diffraction cannot form a perfect interference peak, which leads to the X-ray diffuse scattering. The both pattern will overlap each other (Figure 3.17). The degree of the crystallinity can be determined by the ratio of the crystalline and non-crystalline pattern area. Our product, sodium cefuroxime, is a mixture of crystal and amorphous which can be seen in Figure 3.18. Three sharp peaks of the XRD pattern of sodium cefuroxime were observed at 2θ values of 9° to 10.5^o, 10.5^o to 13° and 14° to 15°. The peak intensity and peak width at half height of peak between 9° to 10.5^o were chosen to present the crystallinity of

sodium cefuroxime for quantification in this thesis. Our aim is to increase the crystallinity of our product.
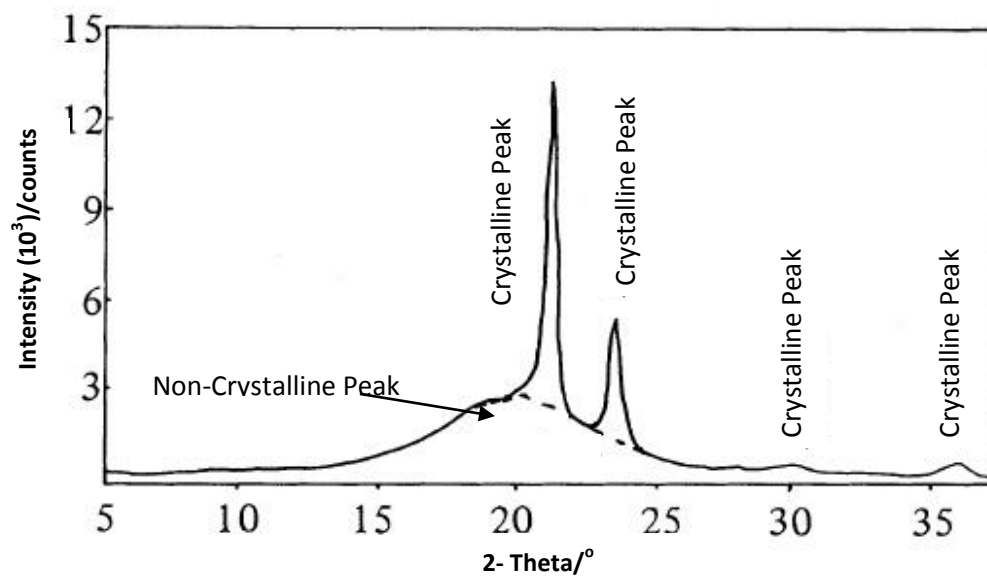
Figure 3.17 The XRD pattern of the mixture of crystalline and non-crystalline of sodium cefazolin (Pikal et al, 1978).
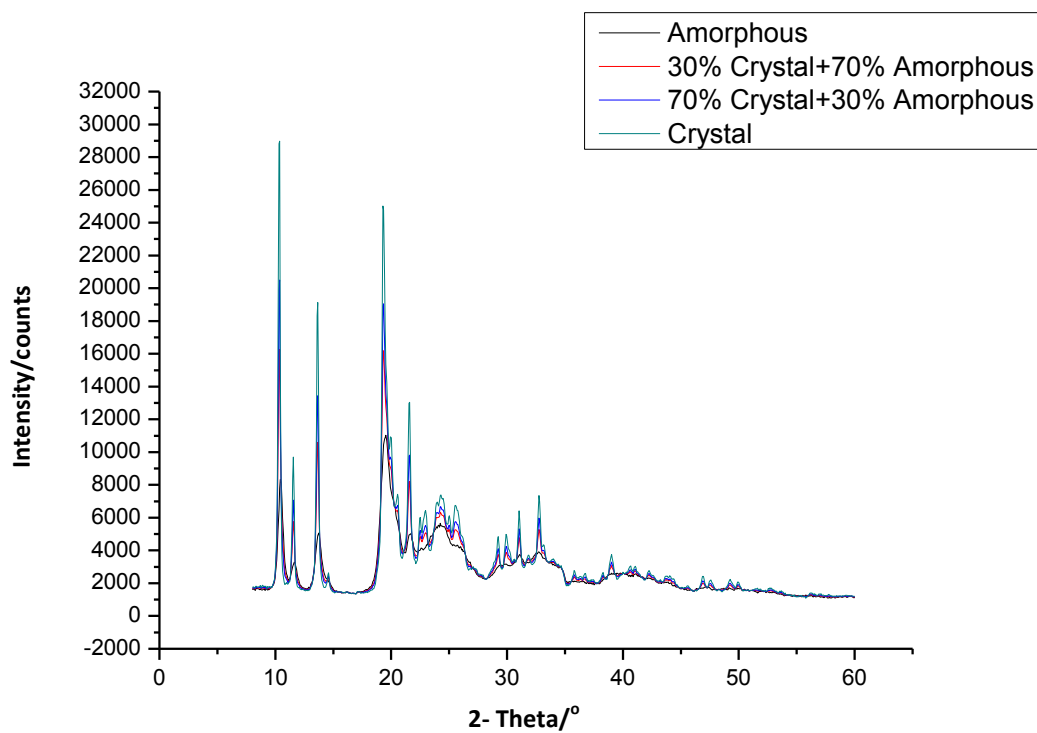
Figure 3.18 The XRD pattern of the mixture of crystal and amorphous of sodium cefuroxime.

The XRD peak intensity is correlated with the morphology of the crystal (Inoue and Hirasawa, 2013). Our product, sodium cefuroxime, has only one polymorph and morphology (Wozniak and Hicks, 1991) which means that the XRD peak intensity could only be affected by the crystallinity of the product. Since the pure crystal of sodium cefuroxime cannot be obtained by any means, the crystalline sample used in this XRD experiment (Figure 3.18) was the sample with best stability which, generally considered, should contain more crystal. From the XRD result, it can be seen that the intensities of peaks increased with the increase of the amount of the crystalline sample, which indicated that the XRD results can be used for crystallinity determination in this study.

3.2.7 1L Equipment for Anti-Solvent Re-Crystallization Process

The equipment used for the anti-solvent re-crystallization process is illustrated in Figure 3.19, which was originally set-up by Dr. Chaoyang Ma in 2010. The *pH* meter and the feed pump were installed in this study. Considering the size of the reactor (1 L), the experimental programme was that: 150 g commercial sodium cefuroxime (Sample 1) was dissolved in 550 g distilled water, and then filtered into the reactor with the stirring speed between 80 to 100 rpm, and then 550 g 95 % (v/v) ethanol was added by means of a WATSON MARLOW SCI 400 peristaltic pump for the flow rate control.
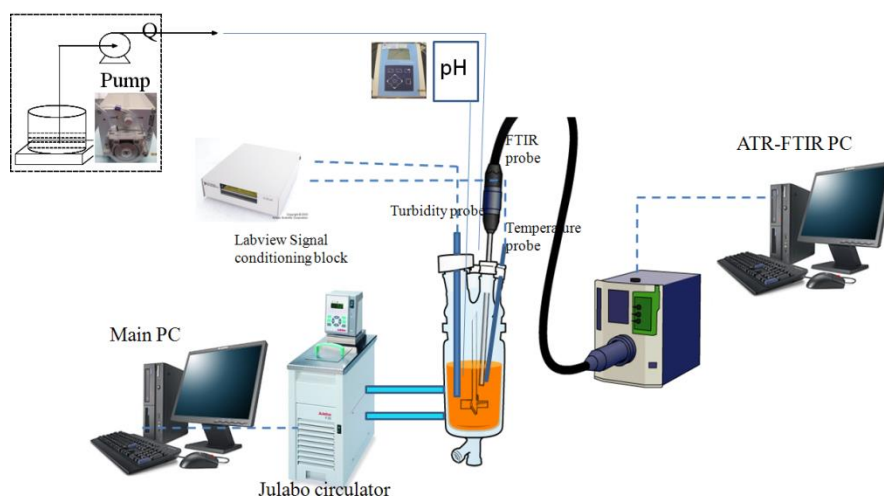
Figure 3.19 The equipment of the anti-solvent re-crystallization process (Ma et al., 2010).

ReactIR™ 4000 (Mettler Toledo Co., Ltd, is an FTIR-based in situ reaction analysis system designed specifically for the organic process); a turbidimeter, a thermostat Julabo circulator, and a pH meter (JENWAY 3510) were used to monitor this process. After this re-crystallization process, the product was washed using 95 % (v/v) ethanol until the *pH* value reached 8 and was then dried in the DZF-6030B vacuum oven for 24 hours.

3.2.8 1L Equipment for Reactive Crystallization Process Optimization

The 1L rigs used for reactive crystallization process optimization are illustrated in Figures 3.20. The 1L rig was also used to prepare seeds using the anti-solvent re-crystallization process, by only replacing the focused beam reflectance measurement (FBRM) probe (Saleemi et al., 2012c; Yu et al., 2004) with an attenuated total reflectance-Fourier transform infrared (ATR-FTIR) probe (Groen and Roberts, 1999). In the anti-solvent re-crystallization process, ATR-FTIR was used for monitoring the supersaturation. In the reactive crystallization process, FBRM was used to monitor crystallization processes and to provide qualitative and quantitative information about nucleation and crystal growth (Doki et al., 2004; Saleemi et al., 2012b).
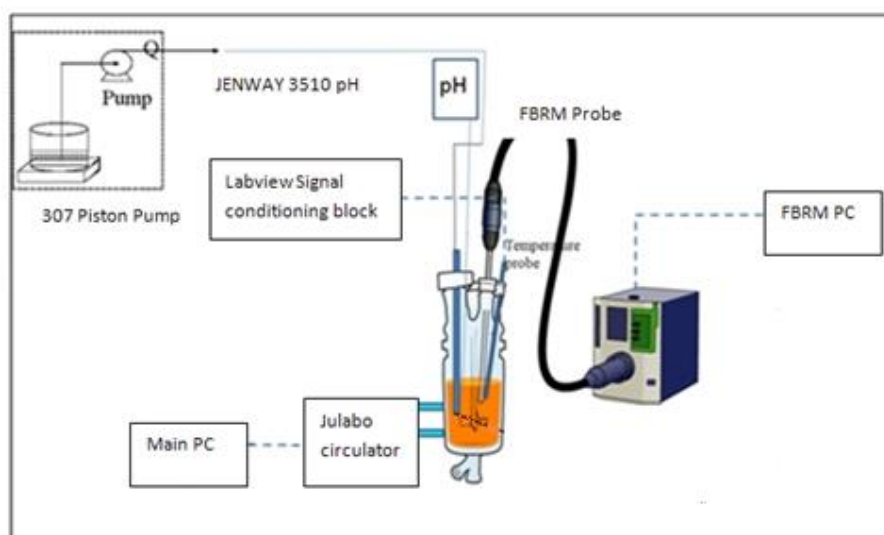
Figure 3.20 The 1L rig that was used for both seeds preparation and reactive crystallization (Ma et al., 2010).

The 1L rig is cylindrical in shape with a jacket to control the reaction temperature by water circulator. The diameter and height of the 1L reactor are 10 cm and 12 cm, respectively. The impeller in the 1L reactor is 45° pitched blade impeller with the diameter and height of 5 cm and 2 cm, respectively.

3.2.9 1L and 50L Equipment for Continuous Crystallization Process

The 1L and 50L continuous crystallizer for crystallization of sodium cefuroxime can be seen in Figure 3.21, which were designed and set-up with the help of Dr. Caiyun Ma and Mr. Steve Caddick from mechanical workshop. The reaction temperature (controlled by a Julabo circulator) was around 25 ^{o}C. The stirring speed (controlled by an IKA EUROSTAR digital stirrer) was kept around 80 rpm. The feed speeding was 10 m·s^{-1} (controlled by 307 Piston Pumps) by using the impinging jet mixer.

(a) 1L continuous crystallizer
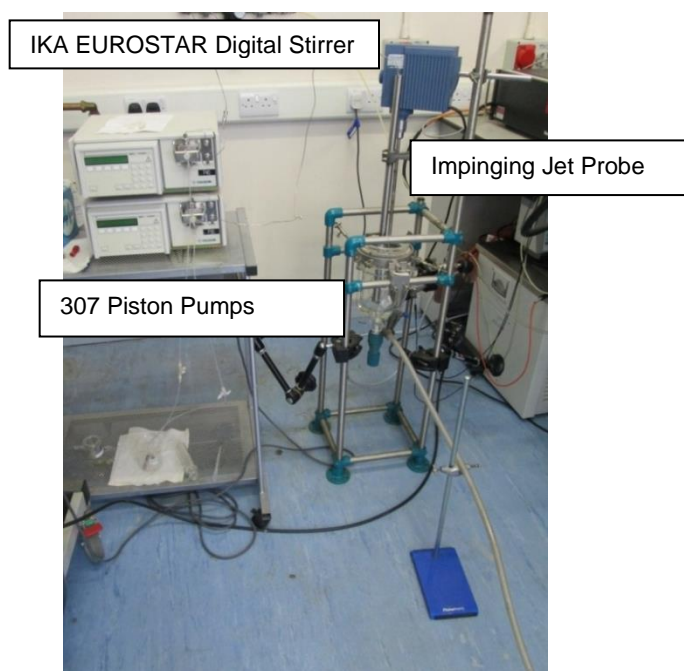
IKA EUROSTAR Digital Stirrer

(b) 50L continuous crystallizer

Figure 3.21 1L and 50L crystallizer set-up for reactive crystallization of sodium cefuroxime (Set-up with the help of Dr.Caiyun Ma and Mr. Steve Caddick).

3.2.10 Computational Fluid Dynamics (CFD)

Computational Fluid Dynamics (CFD) is the combination of modern fluid mechanics, numerical mathematics and computer science. Using a variety of discrete mathematical methods, CFD can solve various practical issues through hydrodynamics numerical experiments and computer simulations.

CFD has been developed quickly for last 20 years. In addition to the development of computer hardware which provides a solid material foundation, it is mainly because both analysis methods and experimental methods have great restrictions, such as the complexity of the problem, neither for analysis solution, nor for experiments. However, in contrast, the advantages of CFD method are clear. After a certain assessment, CFD software can broaden the range of experimental studies and reduce the expensive cost of experiments.

FLUENT software is designed based on the group idea of CFD software. Using different formats and discrete numerical methods, FLUENT software can achieve the best combination of accuracy, stability and computational speed. Thereby complex flow fields' issues can be solved efficiently. FLUENT can simulate fluid flow, heat and mass transfer, chemical reactions and other complex physical phenomena by many models.

The flow pattern of our system should be characterised as liquid-solid multiphase flow. There are two approaches in CFD for the numerical calculation of multiphase flows: the Eulerian-Lagrangian approach and the Eulerian-Eulerian approach. The former uses the Navier-Stokes equations to calculate the dynamics of the fluid phase and solves the dispersed solid phase by tracking a large number of particles through calculated flow field. This approach is more concerned with the movement of particles than the flow pattern, and computationally expensive. The Eulerian-Eulerian approach, on the other hand, adopts the concept of phase volume fraction and treats each phase as one interpenetrating continua, which is more suitable for our process.

In FLUENT, three different Euler-Euler multiphase models are available: the volume of fluid (VOF) model, the mixture model, and the Eulerian model. The Eulerian model is the most complex of the multiphase models in FLUENT. It solves a set of n momentum and continuity equations for each phase. Coupling is achieved through the pressure and interphase exchange coefficients. The description of multiphase flow as interpenetrating continua incorporates the concept of phasic volume fractions, denoted here by α_q. The volume of the phase q, V_q, is defined by

$$V_q = \int_V \alpha_q \, dV \qquad (3.4)$$

where

$$\sum_{q=1}^{n} \alpha_q = 1 \qquad (3.5)$$

The flow pattern of the system in this study should be characterised as liquid-solid multiphase turbulence flow. The governing equations for the Eulerian-Eulerian multiphase model are listed as follows (Chen et al., 2011; Ma et al., 2014):

1. The Continuity Equation

The continuity equation for phase q is

$$\frac{\partial}{\partial t}\left(\alpha_q \rho_q\right) + \nabla \cdot \left(\alpha_q \rho_q \vec{v}_q\right) = \sum_{p=1}^{n}(\dot{m}_{pq} - \dot{m}_{qp}) + S_q \qquad (3.6)$$

where ρ_q is the physical density of phase q, $\vec{v}_q$ is the velocity of phase q and $\dot{m}_{pq}$ characterizes the mass transfer from the pth to q^{th} phase, and $\dot{m}_{qp}$ characterizes the mass transfer from phase q to phase p. By default, the source term S_q is zero, but the user-defined mass source can be used for each phase.

2. The Momentum Balance Equation

The momentum balance for phase q yields

$$\frac{\partial}{\partial t}\left(\alpha_q \rho_q \vec{v}_q\right) + \nabla \cdot \left(\alpha_q \rho_q \vec{v}_q \vec{v}_q\right) = -\alpha_q \nabla p + \nabla \cdot \bar{\bar{\tau}}_q + \alpha_q \rho_q \vec{g} +$$

$$\sum_{p=1}^{n}(\vec{R}_{pq} + \dot{m}_{pq}\vec{v}_{pq} - \dot{m}_{qp}\vec{v}_{qp}) + (\vec{F}_q + \vec{F}_{lift,q} + \vec{F}_{vm,q}) \qquad (3.7)$$

where $\bar{\bar{\tau}}_q$ is the qth phase stress-strain tensor

$$\bar{\bar{\tau}}_q = \alpha_q \mu_q \left(\nabla \vec{v}_q + \nabla \vec{v}_q^{\,T}\right) + \alpha_q (\lambda_q - \frac{2}{3}\mu_q)\nabla \cdot \vec{v}_q \bar{\bar{I}} \qquad (3.8)$$

here μ_q and λ_q are the shear and bulk viscosity of phase q, $\vec{F}_q$ is an external body force, $\vec{F}_{lift,q}$ is a lift force (not included by default because the lift force is insignificant compared to the drag force in our case), $\vec{F}_{vm,q}$ is a virtual mass force (not included by default because the virtual mass effect is significant when the secondary phase density is much smaller than the primary phase density which is not exist in our case), $\vec{R}_{pq}$ is an interaction force between phases, and p is the pressure shared by all phases. $\vec{v}_{pq}$ is the interphase velocity, defined as

follows. If $\dot{m}_{pq} > 0$ (i.e., phase p mass is being transferred to phase q), $\vec{v}_{pq} = \vec{v}_p$; if $\dot{m}_{pq} < 0$ (i.e., phase q mass is being transferred to phase p), $\vec{v}_{pq} = \vec{v}_q$.

The solution of Equation (3.4)-(3.8) for one phase, along with the theory that the sum of phase volume fractions is equal to one, allows for the calculation of the volume fraction of another phase.

3. Energy Balance Equation

To describe the conservation of energy in Eulerian multiphase applications, a separate enthalpy equation can be written for each phase:

$$\frac{\partial}{\partial t}(\alpha_q \rho_q h_q) + \nabla \cdot (\alpha_q \rho_q \vec{v}_q h_q) = -\alpha_q \frac{\partial \rho_q}{\partial t} + \bar{\bar{\tau}}_q : \nabla \vec{v}_q - \nabla \cdot \vec{q}_q + \sum_{p=1}^{n}(Q_{pq} +$$
$$\dot{m}_{pq} h_{pq} - \dot{m}_{qp} h_{qp}) \tag{3.9}$$

where h_q is the specific enthalpy of the qth phase, $\vec{q}_q$ is the heat flux, Q_{pq} is the intensity of heat exchange between the pth and q^{th} phase, and h_{pq} is the interphase enthalpy. The heat exchange between phases must comply with the local balance conditions $Q_{pq} = -Q_{qp}$ and $Q_{qq} = 0$.

4. The Turbulence Model

In comparison to single-phase flows, modelling turbulence in multiphase system is much more complex due to the addition of large quantity of momentum equations of all phases. Among the several turbulence models available in FLUENT (zero-/one-equation, two-equation (k - ε, $k - \omega$, and the variations), Reynolds stress models (RSM)), the standard $k - \varepsilon$ model with the standard wall function for near-wall treatment is most commonly used to model turbulence because of lower computational consuming. When designing a new reactor, the reference data need to be obtain through a relatively simple and quick mode, therefore, the standard $k - \varepsilon$ model was chosen to model turbulence in our process.

The turbulence kinetic energy k and its rate of dissipation ε are obtained from the following transport equations:

$$\frac{\partial}{\partial t}(\rho k) + \frac{\partial}{\partial x_i}(\rho k u_i) = \frac{\partial}{\partial x_j}\left[\left(\mu + \frac{\mu_t}{\sigma_k}\right)\frac{\partial k}{\partial x_j}\right] + G_K + G_b - \rho\varepsilon - Y_M \qquad (3.10)$$

and

$$\frac{\partial}{\partial t}(\rho\varepsilon) + \frac{\partial}{\partial x_i}(\rho\varepsilon u_i) = \frac{\partial}{\partial x_j}\left[\left(\mu + \frac{\mu_t}{\sigma_k}\right)\frac{\partial\varepsilon}{\partial x_j}\right] + C_{1\varepsilon}\frac{\varepsilon}{k}(G_K + C_{3\varepsilon}G_b) - C_{2\varepsilon}\rho\frac{\varepsilon^2}{k} \qquad (3.11)$$

where G_K represents the generation of turbulence kinetic energy due to the mean velocity gradients, G_b is the generation of turbulence kinetic energy due to buoyancy, Y_M represents the contribution of the fluctuating dilatation in compressible turbulence to the overall dissipation rate, $C_{1\varepsilon}$, $C_{2\varepsilon}$, and $C_{3\varepsilon}$ are constants, σ_k and σ_ε are the turbulent Prandtl numbers for k and ε.

The turbulent viscosity μ_t is computed by combining k and ε as follows:

$$\mu_t = \rho C_\mu \frac{k^2}{\varepsilon} \qquad (3.12)$$

where C_μ is a constant.

The model constants $C_{1\varepsilon}$, $C_{2\varepsilon}$, C_μ, σ_k, and σ_ε have the following default values:

$$C_{1\varepsilon}=1.44, \ C_{2\varepsilon}=1.92, \ C_\mu=0.09, \ \sigma_k=1.0, \ \sigma_\varepsilon=1.3$$

They have been found to work fairly well for a wide range of wall-bounded and free shear flows.

The computational domain of this crystallizer with discretised cells was produced by Gambit 2.4 software. Pure single-phase flow simulation approach for the impinging jet design was carried out first with the results being compared with the previous experimental data. The Eulerian-Eulerian two-phase flow simulation approach was then conducted for the determination of residence time and residence time distribution of this process.

3.3 Analytical characterization

X-ray diffraction data were collected using Bruker D8 advance (CuKα1, λ = 1.540598Å). Yttria (Y_2O_3) was used as standard for the estimation of instrumental peak broadening. The size distribution data were collected using *Morphologi* G3 Particle Size and Particle Shape Analyzer from Malvern. The *Morphologi* G3 measures the size and shape of particles using the technique of static image analysis. Fully automation with integrated dry sample preparation makes it the ideal replacement for costly and time-consuming manual microscopy measurements. After 24 hours vacuum drying in the vacuum oven, the same amount of samples was used for each XRD measurement and *Morphologi* G3 analysis.

Chapter 4
Analytical Profile of Sodium Cefuroxime

4.1 Introduction

As a commonly used injectable broad-spectrum antibiotic, the stability issues of sodium cefuroxime should be given very serious consideration. For its metamorphic, many external factors that may affect its stability have been thought of for many years. For example, high temperature, strong light and damp will accelerate its decomposition which indicates this drug should be kept in a cool, dark and dry place. In addition, because of the production process, this drug often has residual water and organic solvent, which may also result in difficulties preserving and ease to metamorphose during the transportation and storage processes.

Besides these external factors, there is another important neglected factor, its crystalline state. It is well known that most of the organic antibiotics are composed in the crystalline and amorphous states. For the solid drug, more crystal, which means lower internal free energy, can make the drug more stable. But for an injectable drug, amorphous, which means that it is more easily dissolved, is also an important necessary composition. So now, the problem is, in order to keep its stability as well as its solubility, it needs to find the balance of the crystalline state and amorphous state of the drug. In view of the fact that sodium cefuroxime is a sodium salt, whose solubility in water is guaranteed, we needed to focus on its crystalline state to improve its stability.

Generally, low crystallinity, non-uniform crystal size distribution and aggregation phenomenon are the main factors affecting the stability of the drug. In this chapter, the samples from different companies were studied using crystallographic analysis tools in order to find the relationship between the stability and the crystalline state as well as the mean size and size distribution. Meanwhile, the results of these stability studies were used for evaluating the

following process optimization and the reactor and process design. The samples analyzed in this study were: Sample 1 from GSK, Samples 2 - 6 from Weiqida with different shelf-lives (Sample 2 has the shortest shelf-life followed by Sample 3, Sample 4, Sample 5 and Sample 6 has the longest shelf-life).

4.2 Stability Analysis

4.2.1 Appearance

For drug consumers, the easiest way to judge whether this drug has metamorphosed or not is from its appearance. Figure 4.1 shows three typical states of sodium cefuroxime: (a) Qualification - the main features are the white appearance, smaller particles with uniform size distribution, creamy feel and higher solubility; (b) Onset of deterioration - the color of the particles starts to turn yellow and the size of the particles becomes larger, maybe because of the aggregation; (c) Serious deterioration - the main features are the yellow appearance, larger particles with non-uniform size distribution, rough feel and lower solubility. Only state (a) can be used safely for injection.

     (a) Qualification   (b) Onset of deterioration   (c) Serious deterioration
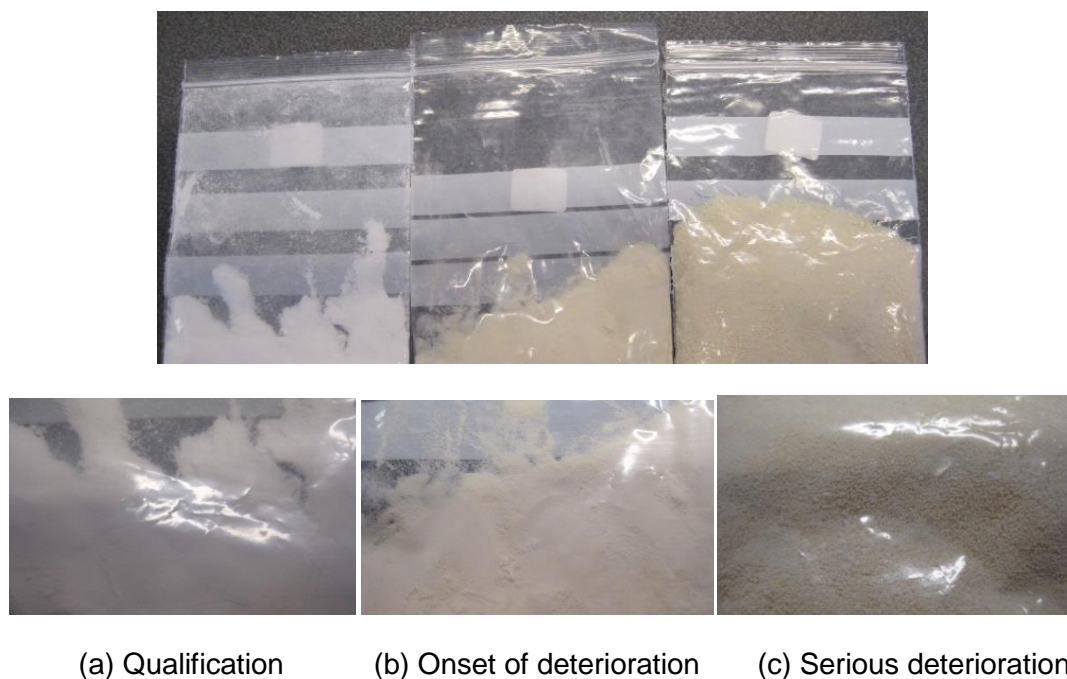
Figure 4.1 Three typical states of sodium cefuroxime: (a) Qualification; (b) Onset of deterioration; (c) Serious deterioration.

4.2.2 Stability Determination Method

Although the drug metamorphic can be judged though the changes in appearance, it cannot provide specific information on drug stability, such as the shelf-life. Obviously, longer shelf-life means that the drug is more stable, so how to know the shelf-life, as the drug metamorphic, is the major concern of both producers and consumers. Therefore, the drug stability test is used to give specific information about judgement of the shelf-life.

For our samples, the detailed stability test operation was as follows: the sealed sodium cefuroxime samples were placed in the stability chamber at 40 $^{\circ}$C/60 $^{\circ}$C without light. After a fixed number of days (3 days, 5 days, 7 days, 10 days 14 days and 20 days), a 0.6 g sample was taken out and dissolved in 5 mL distilled water, and then compared with the standard solution to decide the level by use of a UV instrument.

The standard solution has ten levels Y-1 #~Y~10 # (Figure 4.2), and lower level means higher quality, longer shelf-life and higher stability.

(a) 3 days   (b) 5 days
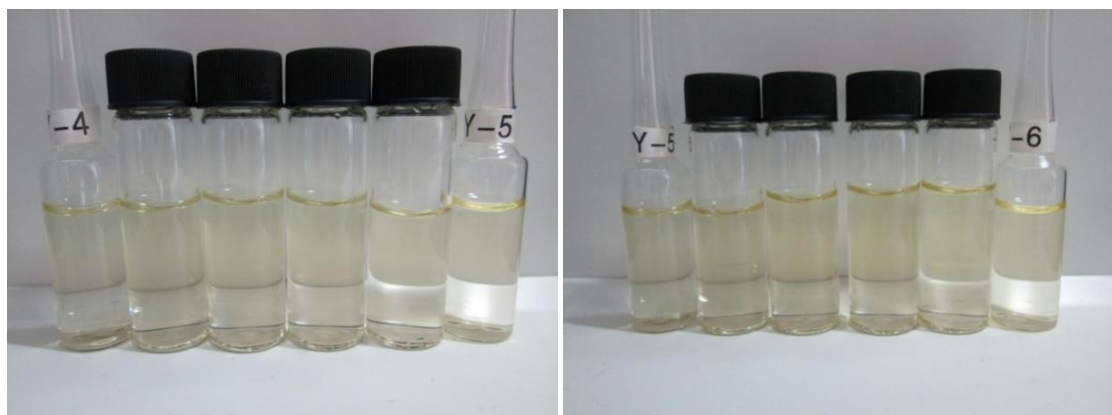
(c) 7 days   (d) 10 days
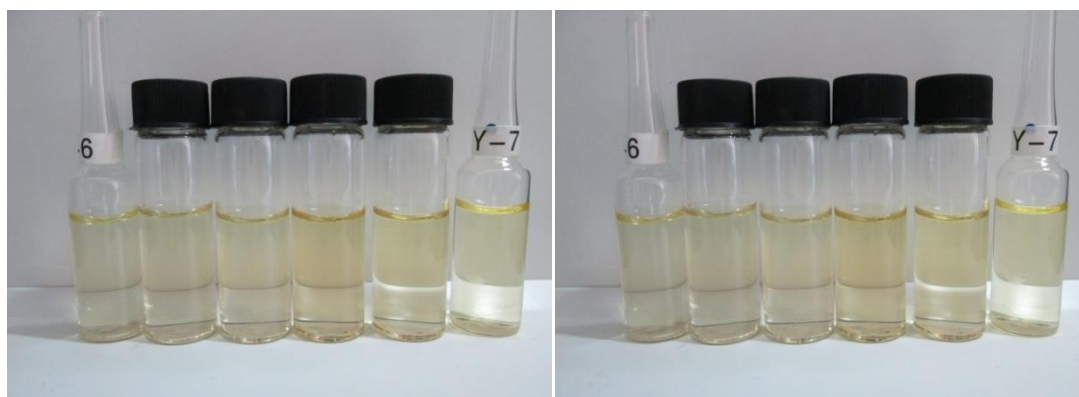
(e) 14 days   (f) 20 days

Figure 4.2 The solution of sodium cefuroxime compared with the standard solution.

The samples from different companies were analysed using the stability test measurements. Table 4.1 and Table 4.2 present the basic physical data (provided by the companies) and stability test data about these samples. Y means the color grade yellow. The water content should be less than 0.3% and the sodium cefuroxime content should be more than 90 %. In these samples, Sample 1 had the highest stability, followed by Sample 6, Sample 5, Sample 4 and Sample 3. Sample 2 showed the lowest stability.

Table 4.1 Physical data of samples from different companies (GSK and Weiqida).

Batch No.	Water (%)	Color Grade	Specific Volume($m^3 \cdot kg^{-1}$)	Content Measured by HPLC (%)
Sample 1	0.239	<Y-2#	--	92.22
Sample 2	0.239	<Y-2#	1.8	94.96
Sample 3	0.229	<Y-2#	1.8	94.36
Sample 4	0.219	<Y-2#	1.6	92.15
Sample 5	0.214	<Y-2#	1.6	93.05
Sample 6	0.222	<Y-2#	1.8	93.47

Table 4.2 Stability test data of samples from different companies (GSK and Weiqida).*

Batch number	Color grade (40 ^{o}C)			
	0 day	5 days	7 days	10 days
Sample 1	⟨Y-2#	--	⟨Y-5#	⟨Y-6#
Sample 2	⟨Y-2#	⟨Y-7#	⟨Y-7#	⟨Y-8#
Sample 3	⟨Y-2#	⟨Y-5#	⟨Y-7#	⟨Y-7#
Sample 4	⟨Y-2#	--	--	⟨Y-7#
Sample 5	⟨Y-2#	--	⟨Y-6#	⟨Y-6#
Sample 6	⟨Y-2#	--	⟨Y-6#	⟨Y-6#

* Y means the color grade yellow.

The solution of sodium cefuroxime would turn yellow in a short time for many reasons. Therefore, contrast work must be completed within a minute. It is generally believed that in the water environment sodium cefuroxime would decompose into cefuroxime amino compounds (yellow), which can also be proved by the ammonia odour from the metamorphosed solid samples.

4.3 Physical Properties Analysis

The stability test data (Table 4.2) indicated that even though these samples were all qualified, they had different shelf-lives. In order to discover the relationship between the drug stability and the crystalline state, it was necessary to find a method to judge the stability combined with the crystalline state. Three analytical tools were used in this study: SEM was used for the collection of crystalline images; *Morphologi* G3 was used for the measurement of the crystal mean size and size distribution; XRD was used for the measurement of the crystalline state.

4.3.1 SEM (Scanning Electron Microscope)
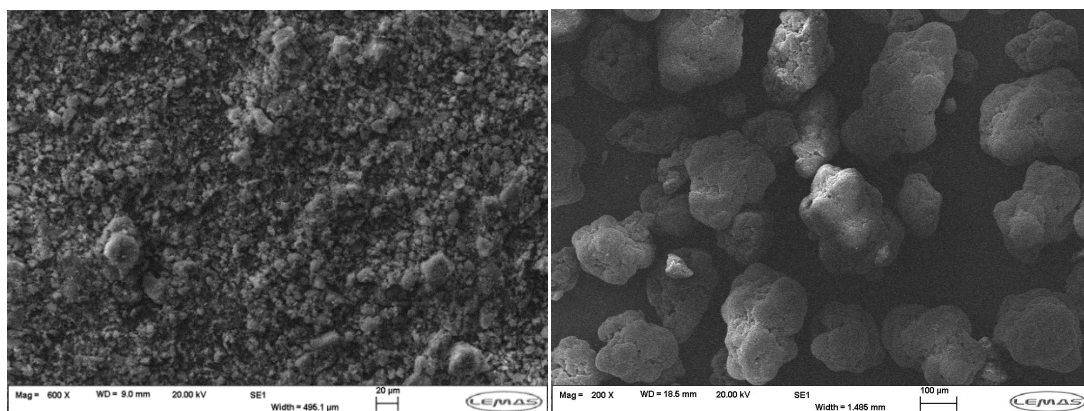
(a) Sample 1   (b) Sample 2
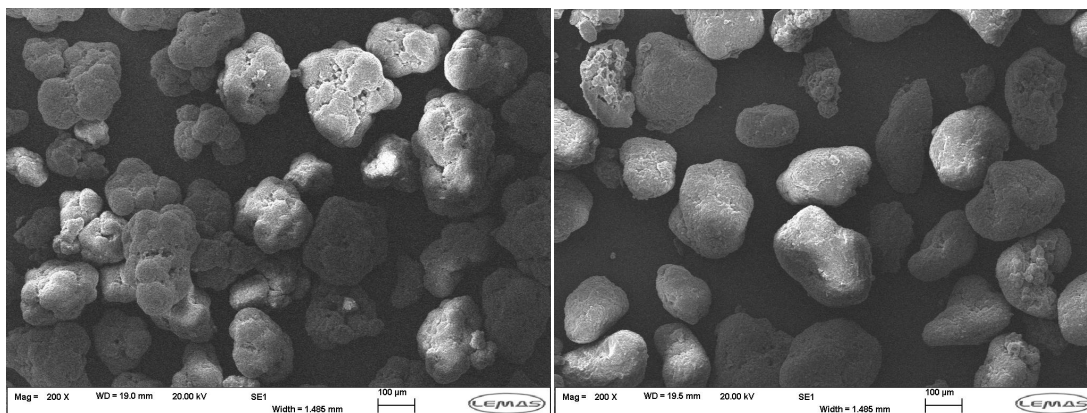
(c) Sample 3   (d) Sample 4
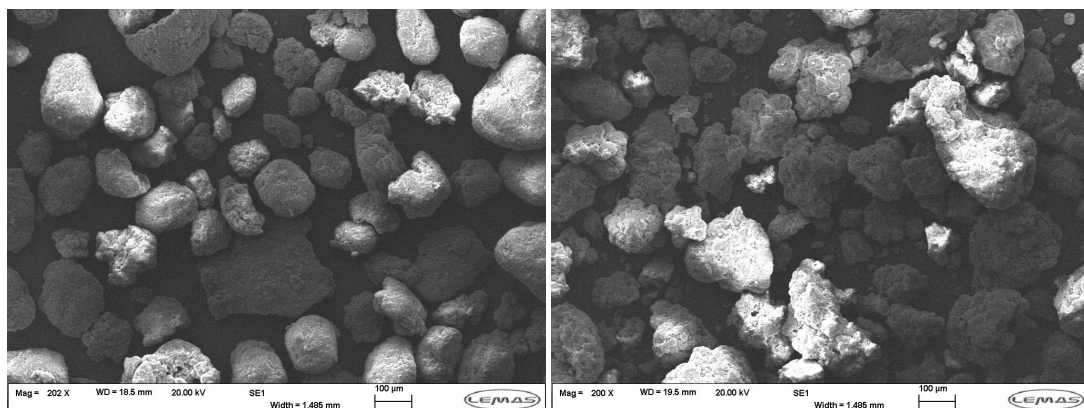
(e) Sample 5   (f) Sample 6

Figure 4.3 The SEM results of samples from different companies.

It can be seen from Figure 4.3 that the sample of good quality had a smaller particle size. In addition, the good stability samples also had a rough surface. This may be because in the cleaning and drying processes, these particles can be cleaned and dehydrated more thoroughly, thus the stability of the products increased.

From these sodium cefuroxime samples, it is hard to find a single crystal of sodium cefuroxime, because these samples have undergone a number of downstream processes. Therefore, we decided to use an ultrasonic instrument to disperse these samples in a liquid environment in order to find the single crystalline structure.

0.1 g Sample 1 (the best) was added in 5 mL 95% ethanol (insoluble), then the ultrasonic instrument was used to disperse them at different times (0s, 30s, 60s, 120s). After that, three drops of these solutions of sodium cefuroxime were taken out and placed on the sample stage until dry and coated by gold, and then SEM was used to observe.

As can be seen from Figure 4.4, the different dispersion times caused significant changes in the samples. (a) the sample was not dispersed. Only the edge became rough because of the erosion of the solvent. (b) the sample experienced part of the dispersion. It can be seen that its monocrystalline was a flat cuboid with an approximate length of 2 μm and a width of 0.5 μm. They constituted the entire particle by lamellar structure. (c) the sample experienced longer time dispersion. The lamellar structure was destroyed and disintegrated into many small balls with different diameters. (d) the sample experienced quite long time dispersion. It had lost its fixed shape, and was randomly distributed in the sample stage. This phenomenon indicated that the sodium cefuroxime crystalline structure was very fragile and easily broken.
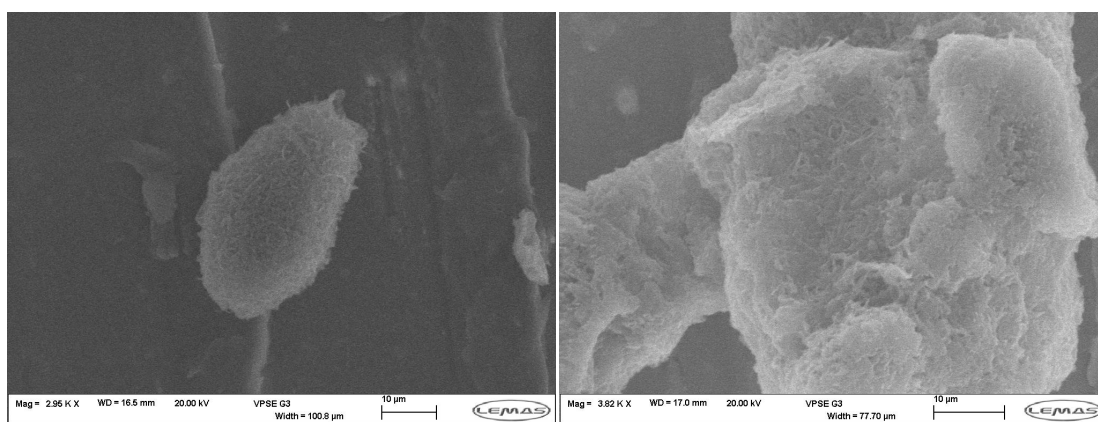
(a) 0 s   (b) 30 s
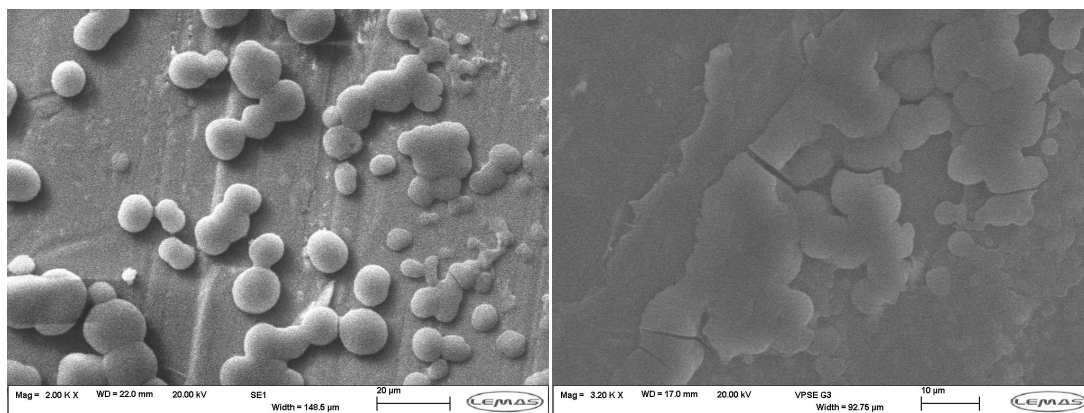
(c) 60 s   (d) 120 s

Figure 4.4 The SEM results of sodium cefuroxime after different dispersion times using ultrasonic instrument: (a) 0 s; (b) 30 s; (c) 60 s; (d) 120 s.

4.3.2 *Morphologi* G3
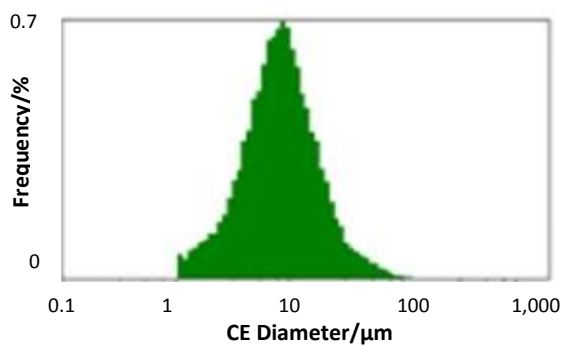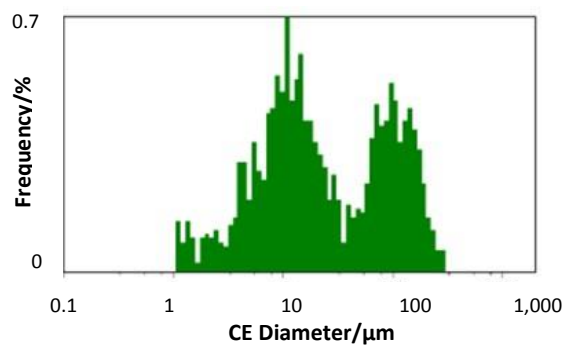
(a) Sample 1 (8.4μm)   (b) Sample 2 (18.4μm)
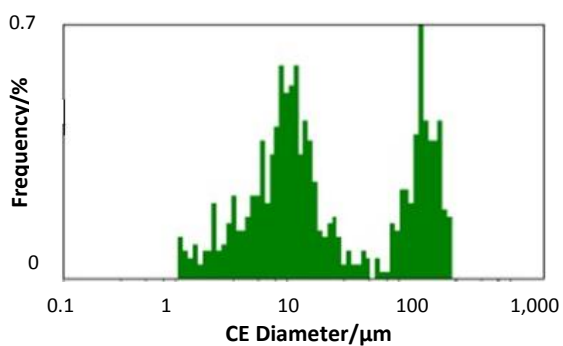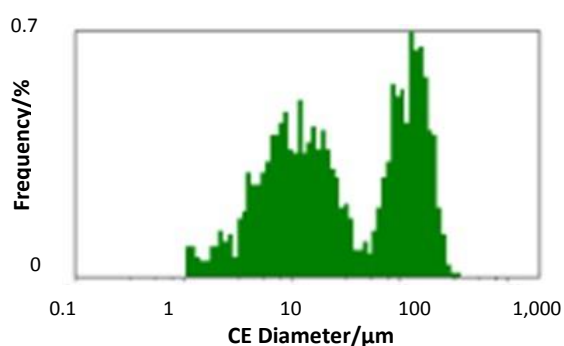
(c) Sample 3 (14.2 μm)   (d) Sample 4 (23.7 μm)
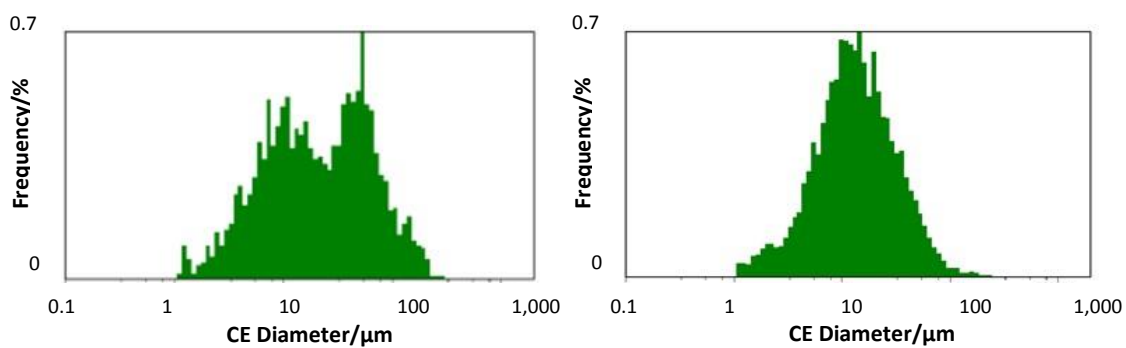
(e) Sample 5 (20.8 µm)　　　　　(f) Sample 6 (10.2 µm)

Figure 4.5 *Morphologi* **G3 results of samples from different companies**

As can be seen from Figure 4.5, the particle of the best stability sample (Sample 1) had the smallest mean particle size and a narrow particle size distribution.

The results of *Morphologi* G3 gave further evidence of the conclusion obtained from SEM that the sample of good quality had a smaller particle size. Besides the relatively large mean particle size, the particle size distributions of the poor quality products also had a bi-modal phenomenon. The particle size distributions of Sample 6 and Sample 1 were the closest, and the stability of Sample 6 was following Sample 1 based on the stability test data.

4.3.3 XRD (X-Ray Diffraction)

The XRD pattern of sodium cefuroxime obtained from different samples indicated that it was a mixture of crystal and amorphous state. Three sharp peaks were observed at 2θ values of 9° to 10.5^{o} (the main peak), 10.5^{o} to 13° and 14° to 15°.

As can be seen from Figure 4.6, the good stability samples (Sample 1) had the higher peak intensity. It indicated that better crystalline state may lead to higher stability.
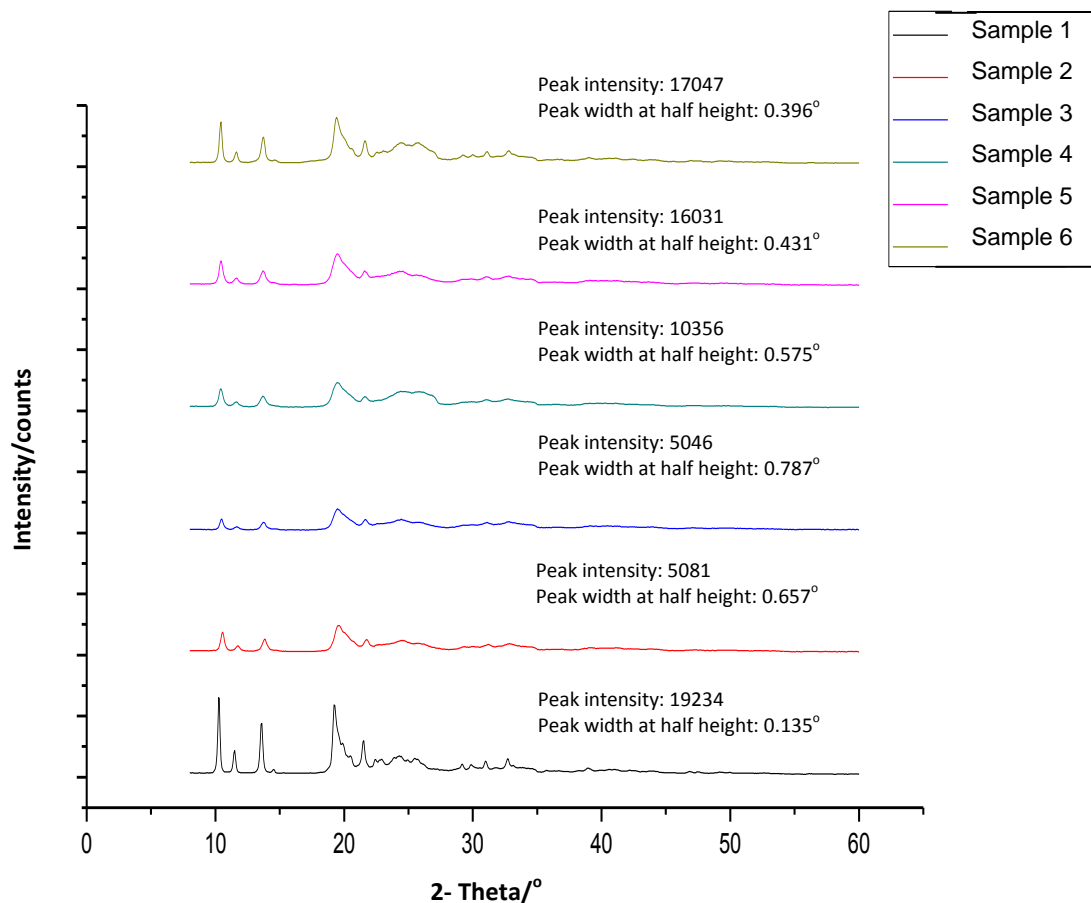
Figure 4.6 The XRD pattern of samples from different companies (peak intensity and peak width at half height of peak between 9° to 10.5^o were chosen to present the crystallinity).

4.4 Final Remarks

As can be seen from the above physical properties analysis, many factors can lead to the instability of sodium cefuroxime. Although it was still not certain, the general conclusions were: low temperature, the smaller particle size, narrow particle size distribution and more perfect crystal structure can improve the stability of sodium cefuroxime. The following are some more detailed conclusion.

As can be seen from the above physical properties analysis, many factors can lead to the instability of sodium cefuroxime. Although it was still not certain, the general conclusions were: at low temperature, the smaller the particle size, narrow particle size distribution and more perfect crystal structure can improve

the stability of sodium cefuroxime. The following are some more detailed conclusions.

1. The SEM results showed that the cleaning and drying process had influence on the stability of the product. The cleaning process, in addition to making sure the impurities were removed more thoroughly, more importantly, it needed to clean the product to weakly alkaline (pH > 8), which meant removing the un-reacted acid cefuroxime from the generated sodium cefuroxime. That is because acid cefuroxime was much easier to degradate than sodium cefuroxime and if too much remained it would not only affect the product color, but also affect the potency of the drug. The drying process, in addition to the solvent (ethanol and acetone) being removed, it was also necessary to evaporate the residual water (should be < 0.3 %). The residual solvent would cause the user damage and too much water remaining would lead to the product's accelerated deterioration. This is due to the ester and amide functional groups within the molecular structure of sodium cefuroxime degrading more quickly in the presence of water.

2. The SEM and *Morphologi* G3 results showed that the mean particle size and particle size distribution also had a great influence on the stability of a product. Too large or too small a mean particle size would make the quality of products worse. If this inappropriate mean size happened to meet the residual water, it would make the sodium cefuroxime easily aggregate, and then affect the solubility of the product. If the mean size of the particle was in the appropriate range, but the particle size distribution was non-uniform, the quality of the product would also be compromised. So, in the future, under the premise of the mean size guarantee, more uniform size distribution was also the aim.

3. The XRD pattern showed that the crystalline state was also essential for product stability. The physical properties of cefuroxime sodium showed that it was a mixture of crystal and amorphous state, thus the goal of optimization was to make the crystal structure more perfect, with fewer defects. An amorphous state could shorten the dissolution time, but in the preservation process,

amorphous, due to the greater hygroscopic capacity than the crystal, was unpopular. Even though the residual water was qualified, if the product contained more amorphous, it would absorb moisture from the air and make the product degrade in a relatively short period of time. In addition, the crystal itself had a slower rate of degradation because of lower free energy. Therefore, to improve the crystal structure of the product was definitely conducive to its stability.

4. Since many factors may affect the stability of the product and the focus of this study was to improve the crystallinity, XRD was chosen as the main approach for the general rough judgment of the results. It can provide more immediate results than the other methods concerning the crystal structure with a small amount of sample in a short time. Therefore, in the following chapters, XRD pattern was used to make a distinction between high stability and low stability, which would guide the direction of the following process optimization and reactor and process design.

Chapter 5

Re-crystallization of Sodium Cefuroxime

5.1 Introduction

Re-crystallization of solids is a valuable technique because it is often used for purification of products. Other techniques for purifying solids such as sublimation, extraction and chromatography, are more complicated. The process of re-crystallization involves dissolution of the solid in an appropriate solvent and the subsequent re-formation of the crystals upon cooling or anti-solvent, so that any impurities will remain in solution. Even though the re-crystallization process cannot remove all impurities, it can help to mend the defective crystalline structure.

The re-crystallization process is seldom used in the organic laboratory because the crystals often form a viscous oily substance containing impurities, as a result of which it is difficult to separate the desired pure solid (Thompson and Baalham, 1981). Therefore, supersaturation monitoring seems to be indispensable because both nucleation and growth of crystals are driven thermodynamically by supersaturation. Infrared spectroscopy is now established as a simple and reliable technique for dynamic measurement of solution concentration. Specifically, Attenuated Total Reflection-Fourier Transform InfraRed (ATR-FTIR) spectroscopy has been successfully used in on-line solution concentration and supersaturation monitoring (Borissova et al., 2009).

In this chapter, re-crystallization was used to purify the commercial sodium cefuroxime products and Attenuated Total Reflection-Fourier Transform InfraRed (ATR-FTIR) Spectroscopy was used to optimize this process. Before that, in order to ensure that ATR-FTIR can work properly and provide accurate data, the preparatory work such as solubility determination and instrument calibration were completed first.

5.2 Solubility

5.2.1 Solubility and Solution Supersaturation

When a liquid (solvent) and a solid (solute) are brought into contact, the attractive forces of the liquid tend to break apart the surface of the solid and to disperse its ions into the liquid in the form of discrete units. This process is called dissolution. The limit to which the solute dissolves is defined as its solubility. The solubility of a substance fundamentally depends on the used solvent as well as on temperature and pressure. The limit of the solubility of a substance in a specific solvent is measured as the saturation concentration, where adding more solute does not increase the concentration of the solution.

Under certain conditions this equilibrium-limit value of solution concentration may be exceeded, leading to supersaturation. Several different types of units are used to describe supersaturation. All of these require that the actual solution concentration be known along with the saturation (solubility) concentration of the solution at certain conditions. Supersaturation is often expressed as the difference between concentration units and therefore, has the same units as those used for concentration. Supersaturation can be defined as

$$\Delta c = c - c^* \qquad (5.1)$$

where Δc is the solute supersaturation in concentration units, c is the actual solute concentration and c^* is the solute saturation concentration. The value reported will, obviously, vary with the type of concentration units used. A commonly used unit for supersaturation is the solute supersaturation ratio, defined as

$$S = \frac{c}{c^*} \qquad (5.2)$$

This ratio is always a number greater than one for a supersaturated solution. A related unit, the relative supersaturation σ, is defined as

$$\sigma = \frac{c - c^*}{c^*} \qquad (5.3)$$

and is related to the solute supersaturation ratio as follows:

$$\sigma = s - 1 \tag{5.4}$$

It is important to note that these definitions of supersaturation assume an ideal solution, having an activity coefficient of one. It is a common practice to ignore activity coefficients in most cases and employ concentrations in expressions for supersaturations. However, in very non ideal solutions and in precise studies of crystal growth and nucleation, activity coefficients are often used. In crystallization, supersaturation, a concentration gradient, is the driving force for crystal nucleation and growth. There are four main methods to create supersaturation:

- Temperature change;
- Evaporation of solvent;
- Changing the solvent composition;
- Chemical reaction.

5.2.2 Solubility of Organic Drug

Unlike the solubility of inorganic substance only affected by temperature and pressure, the factors that affect the solubility of the organic drug are more complex. There are eight main factors:

- The drug molecular structure. The solubility of the drug in the solvent is the result of the interaction between the drug molecules and the solvent molecules. According to the "Like Dissolves Like", the polarity of the drug has a great influence on its solubility, and the molecular structure decides the drug polarity.
- Solvent. By reducing the attraction between the drug molecules or ions, the solvent changes them to solvate and then dissolves them. The polar solvent allows the salts and polar drug to become solvate and dissolve; the polar groups in weak polar drug molecules form the hydrogen bonds with water and dissolve; non-polar drug molecules form induced dipole-

induced dipole with non-polar solvent molecules and dissolve; semi-polar drug molecules form induced dipole - permanent dipole with non-polar solvent molecules and dissolve.

- Temperature. The influence of temperature on the solubility depends on the dissolution process is endothermic or exothermic. If the drug needs extra heat to dissolve, its solubility usually increases with the increase of the temperature. The vast majority of the drug dissolution processes are endothermic, so their solubility increases with the increase of the temperature.

- Particle size. Under a certain temperature, the solubility and dissolution rate of the drug is proportional to its surface area. That is, the smaller particles have a greater solubility, while the larger particles have a smaller solubility.

- Polymorph. Polymorphs are different lattice arrangement crystals with the same chemical molecular but obtain under different crystallization conditions such as solvent, temperature, cooling rate. Polymorphs are widespread in organic drug. Different crystalline forms result different lattice energy and different melting point, dissolution rate and solubility. Polymorph with the smallest lattice energy is the most stable one, called stable type, which has the smallest solubility and dissolution rate.

- Solvate. In the crystallization process, the crystal lattice of the drug will change due to the added solvent molecules, the obtained crystals known as solvates. If the solvent is water, is called a hydrate. Solvate and non-solvate have different solubility and dissolution rate, in most cases.

- *pH* value. Most drugs are weak organic acid, weak base or salts. The solubility of these drugs is huge influenced by the *pH* value. Weakly acidic drug solubility increases with the *pH* value increase and weakly basic drug solubility increases with the *pH* value decrease. The amphoteric drug has its minimum solubility when its isoelectric point is equal to the *pH* value.

- Common ion effect. If the dissociation type or salt type of the drug is the restricted dissolved components, the ion concentration in the solution will be the determinant to this drug solubility. Usually, to a saturated solution of soluble salts, by adding a compound containing the same ion, its solubility will decrease. Such as the hydrochloride salts has a lower solubility in physiological saline or diluted hydrochloric acid than in the water.

For our samples, from the Pharmacopoeia, sodium cefuroxime is freely soluble in water and buffered solutions; soluble in methanol; very slightly soluble in ethyl acetate, diethyl ether, octanol, benzene and chloroform. So the main factors that affect the solubility are the solvent type, temperature and the *pH* value (sodium cefuroxime only has one polymorph). The more solubility data are shown in Table 5.1.

Table 5.1 Solubility data of sodium cefuroxime.

Solvent	Solubility (mg/mL)	USP Solubility
Water	≥100.0	Freely Soluble
Buffer-pH 7.0	≥100.0	Freely Soluble
Buffer-pH 4.5	≥100.0	Freely Soluble
Buffer-pH 1.2	≥100.0	Freely Soluble
Methanol	≥50.0-<100.0	Soluble
Ethyl acetate	<0.5	Very Slightly Soluble
Diethyl ether	<0.5	Very Slightly Soluble
Octanol	<0.5	Very Slightly Soluble
Benzene	<0.5	Very Slightly Soluble
Chloroform	<0.5	Very Slightly Soluble

5.2.3 IR Spectra of Water, Ethanol and Acetone

Since ATR-FTIR is based on the absorption spectra of the different functional groups in the organic substance to establish the concentration relationship, the presence of interference peaks will bring a lot of errors, or even lead to the instrument cannot be used. Figure 5.5 illustrates the absorption curves of water, acetone and ethanol (the wavenumber range: 1500 – 2000 cm^{-1}, because the characteristic peak of sodium cefuroxime is 1758 cm^{-1} (C=O stretch, β-lactam)).

(a) Water

(b) Ethanol

87
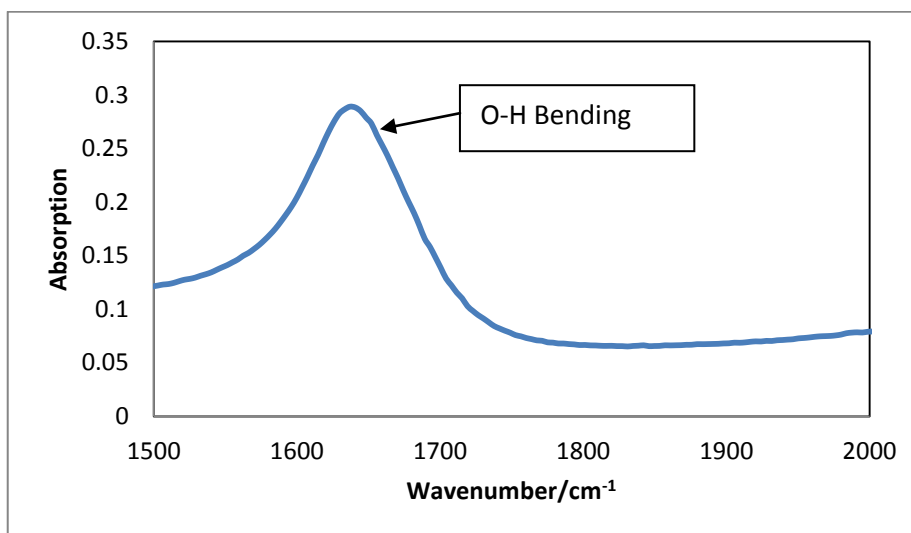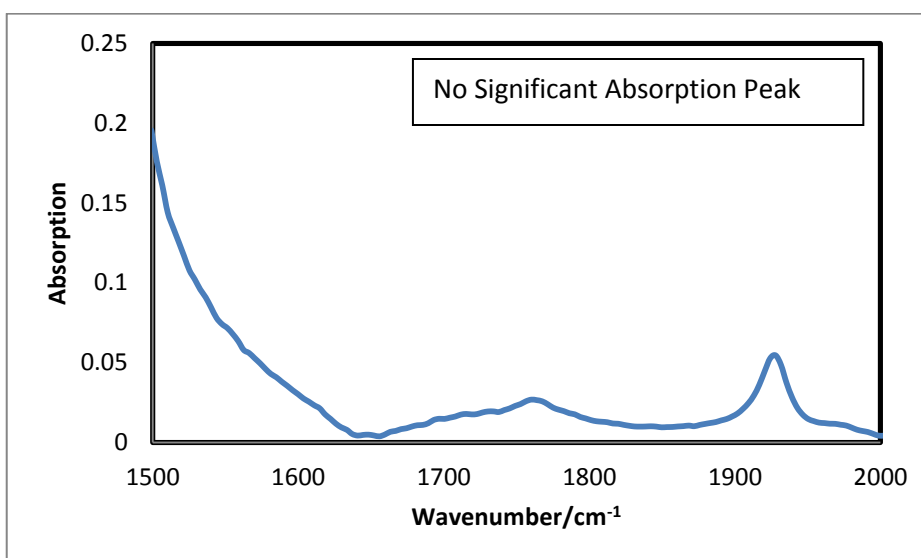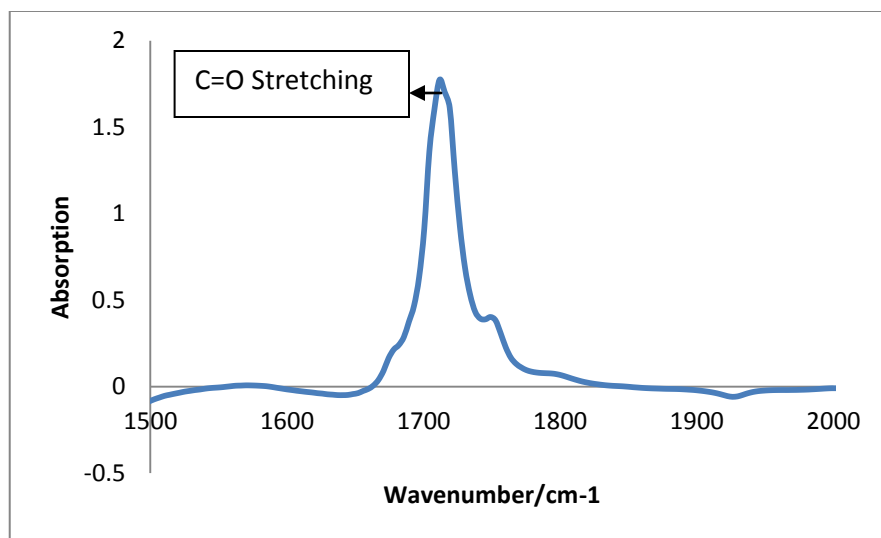
(c) Acetone

Figure 5.1 The absorption curves of the water, ethanol and acetone.

5.3 Methods

5.3.1 Solubility Determination

The gravimetric method was used for measuring the solubility of sodium cefuroxime in solvents. It involved the following steps. First, the solubility of sodium cefuroxime in water was measured and correlated, and then solubility of sodium cefuroxime in ethanol was also measured and correlated under the same temperature and *pH* conditions. To estimate the solubility of sodium cefuroxime in a mixture of water and ethanol, the Jouyban-Acree model (Acree, 1992), was employed since it was considered as one of the most accurate models to represent the solubility of a drugs in amixed solvent. In the Jouyban-Acree model, there are three constants that need to be determined. Therefore experiments were also conducted to obtaining solubility data in mixtures of water and ethanol of diffident ratios, at varied temperatures and *pH* values.

Commercial sodium cefuroxime was dissolved in one solvent, and then filtering the mixture through Whatman Qualitative Circles FDH-300-130T using a Vacuubrand MZ 2C+2AK vacuum pump. The clear solution was evaporated to

dryness in a DZF-6030B vacuum oven at approximate 35 $^{\circ}$C with ABF 63/4c-7RQ vacuum pump within half an hour (to prevent sodium cefuroxime from degradation), and the remaining solid was weighed using AND GX-200 balance. Each measurement was weighed twice at 5 minutes interval. If the two measurements give the same weight, it indicated that the sample was dry. Then the solution solubility was calculated using the following equation:

$$x = \frac{W_1/\text{kg} - W_2/\text{kg}}{W_3/\text{kg} - W_4/\text{kg}} \tag{5.5}$$

where x is the solubility of the solute in mass solid per weigh of solvent, W_1 is the total weight of the dry residue and sampling bottle, W_2 is the weight of the sampling bottle, W_3 is the total weight of the sampling bottle and solution (after filtering), and W_4 is the weight of the sampling bottle plus dry residue.

The relative standard uncertainty u_r can be calculated using the following equation:

$$u_r(x) = \frac{u(x)}{|x|}, for\ x \neq 0 \tag{5.6}$$

To minimize the uncertainty in obtaining the experimental data of solubility, at a given temperature T and pH value, for a given solvent (water, ethanol, or mixture of water and ethanol at a defined ratio), solubility of sodium cefuroxime was measured in three parallel experiments conducted in parallel. The averaged value of the three parallel experiments was regarded as the solubility at that T and pH value and in that solvent. It was found that the maximum error for every three parallel experiments was $u_r(x) = 0.03$.

The above described procedure of measuring the solubility of sodium cefuroxime has assumed that the precipitates were only sodium cefuroxime without containing precipitate of acid cefuroxime. When a salt dissolves in aqueous solution, dissociation equilibrium between the ionized and the non-ionized species is attained (Stahl and Wermuth, 2002). It is therefore important to make sure that in the pH range studied in the present work (pH 5-7), the solid that precipitated out from the process is a pure salt, rather than a mixture of the

salt and the free acid (sodium cefuroxime and acid cefuroxime). According to Wozniak and Hicks's work (Wozniak and Hicks, 1992), sodium cefuroxime is freely soluble in buffer solvents of $pH = 7.0$, 4.5 and 1.2. To further confirm that there no free acid in the precipitated solids, we have also performed XRD analysis of the precipitate (Figure 5.2). The XRD pattern of the precipitate did not show any sign of containing acid cefuroxime. For example, the two peaks of acid cefuroxime (blue line) between the 2θ values of 15° to 17° did not show any appearance in the precipitate XRD pattern. (The characteristic peaks of sodium cefuroxime crystals were observed at 2θ values of 9° to 10.5^o (the main peak), 10.5^o to 13° and 14° to 15°).
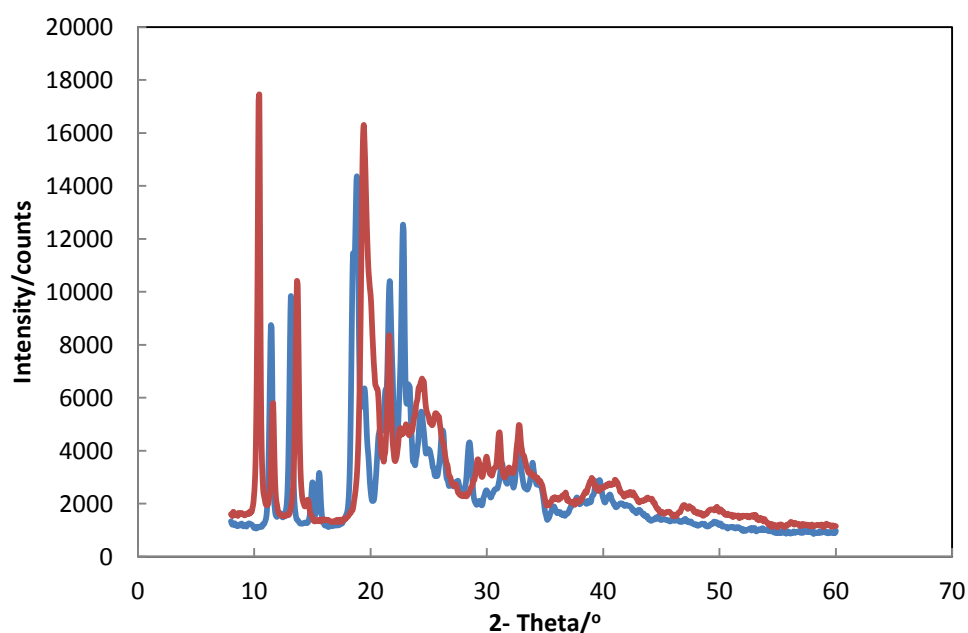
Figure 5.2 The XRD pattern of sodium cefuroxime (red line) and acid cefuroxime (blue line).

The Jouyban-Acree model (Jouyban and Acree, 2006) is expressed as:

$$\log(10^3 x_3) = \varphi_1 \log(10^3 x_1) + \varphi_2 \log(10^3 x_2) + \varphi_1 \varphi_2 \sum_{i=0}^{2} \frac{J_i(\varphi_1 - \varphi_2)^i}{T/K} \qquad (5.7)$$

where x_1, x_2, and x_3 are the solubility of the solute in water, co-solvent and solvent mixture at a fixed temperature. J_i is the model constant. φ_1 and φ_2 refer to the volume fraction of water and co-solvent in the binary solvents without solute.

5.4 Results and Discussion

5.4.1 Solubility of Sodium Cefuroxime

In Pharmacopeia, sodium cefuroxime is freely soluble in water and buffer solvent (*pH* 7.0, *pH* 4.5 and *pH* 1.2) (Wozniak and Hicks, 1992), soluble in methanol and very slightly soluble in ethyl acetate, diethyl ether, octanol, benzene and chloroform. Therefore, water was chosen to be one of the solvents. However, there was research focused on neither the influence of *pH* value on solubility of sodium cefuroxime nor provided any data. In order to investigate the effect of both temperature and *pH* value on the solubility of sodium cefuroxime, on the basis of the conditions of industrial production, the test temperature range was set to be 24 to 35 ^{o}C, and the test *pH* value range was 5 to 7. Acetic acid was used to adjust the *pH* value because it showed no effect on sodium cefuroxime.

It can be seen from Figure 5.3 that for 10 ^{o}C of temperature change, the solubility varied about 6 % and for one *pH* value change, solubility changed around 2 %. The solubility of sodium cefuroxime decreased with the decrease of temperature, but the extent of decrease was relatively limited, indicating that the cooling crystallization process was not suitable for the re-crystallization of sodium cefuroxime. On the other hand, the solubility of sodium cefuroxime reduced with the increase of *pH* values indicating that it was a weak basic drug. Therefore, it was not feasible to re-crystallise sodium cefuroxime by changing *pH* because a weak basic drug is unstable in the acidic environment. Based on the fact that the solubility of sodium cefuroxime is sensitive to the different solvents, the anti-solvent method was found to be the best for the re-crystallization purification process.
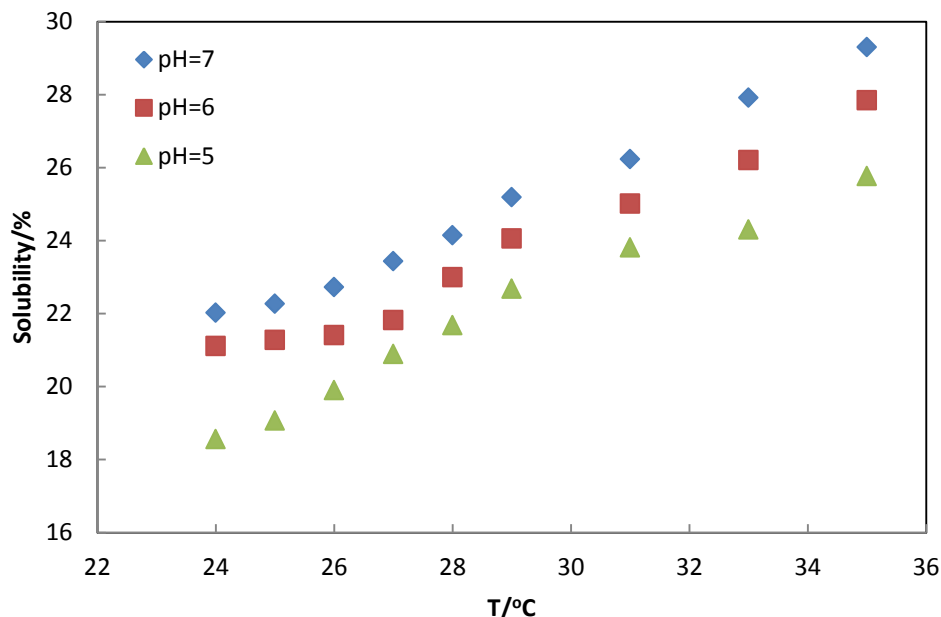
Figure 5.3 The solubility profiles of sodium cefuroxime in water under different temperatures.

Subsequently, the solubility of sodium cefuroxime in 95 % ethanol was investigated under the same conditions. It was found that sodium cefuroxime was slightly soluble in pure ethanol (0.05 %), but the solubility in 95 % ethanol was 1.14 g / 100 g solvent, at 25 ^{o}C and *pH* 7. It was found from the experiments that the solubility in 95 % ethanol had little change with the temperature and *pH* values in 95 % ethanol, so compared with the solubility in the water, the change can be ignored. The solubility of sodium cefuroxime in 100 g 95 % ethanol was treated as a constant of 1.14 g in the following formula fitting.

5.4.2 Solubility of Sodium Cefuroxime in Binary Solvent

Zhao (Zhao et al., 2012; Zhao et al., 2010) studied the thermodynamics and kinetics of sodium cefuroxime in binary solvents during anti-solvent crystallization processes. The anti-solvents they used were acetone, ethanol and propan-2-ol, but acetone was selected as the preferred anti-solvent because the hydrogen bond between solvents enhanced its solubility, leading to the maximum yield being obtained. However, besides the solubility and yield, the influence of an anti-solvent on the final product quality was also a very

important factor affecting the selection of an anti-solvent. Acetone has already been found not to be an ideal choice because it can deepen the color of the final product (Hu et al., 2011). According to the data provided by Zhao and the color requirement of the product, ethanol was found to be more appropriate. The use of 95 % ethanol instead of pure ethanol was due to the fact that 95 % ethanol was much cheaper and more easily obtained in the industrial production.

The method to determine the solubility of sodium cefuroxime in the solvent mixture by the Jouyban-Acree model only gave us the correlation among the temperature, the solvent ratio and the solubility. However, in the present study, due to the solubility of sodium cefuroxime being strongly influenced by *pH* value and the environmental *pH* value was changed by the amount of acid cefuroxime, the process also required the *pH* value effect. Therefore, the solubility data under different *pH* values were measured for fitting corresponding formula (as shown in Figure 5.4). The test temperature range was 24 to 29 ^{o}C.
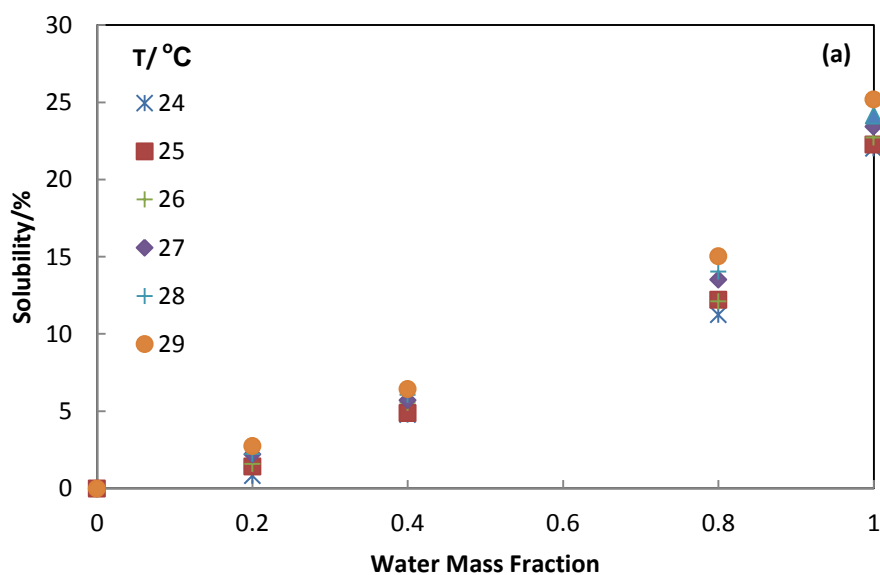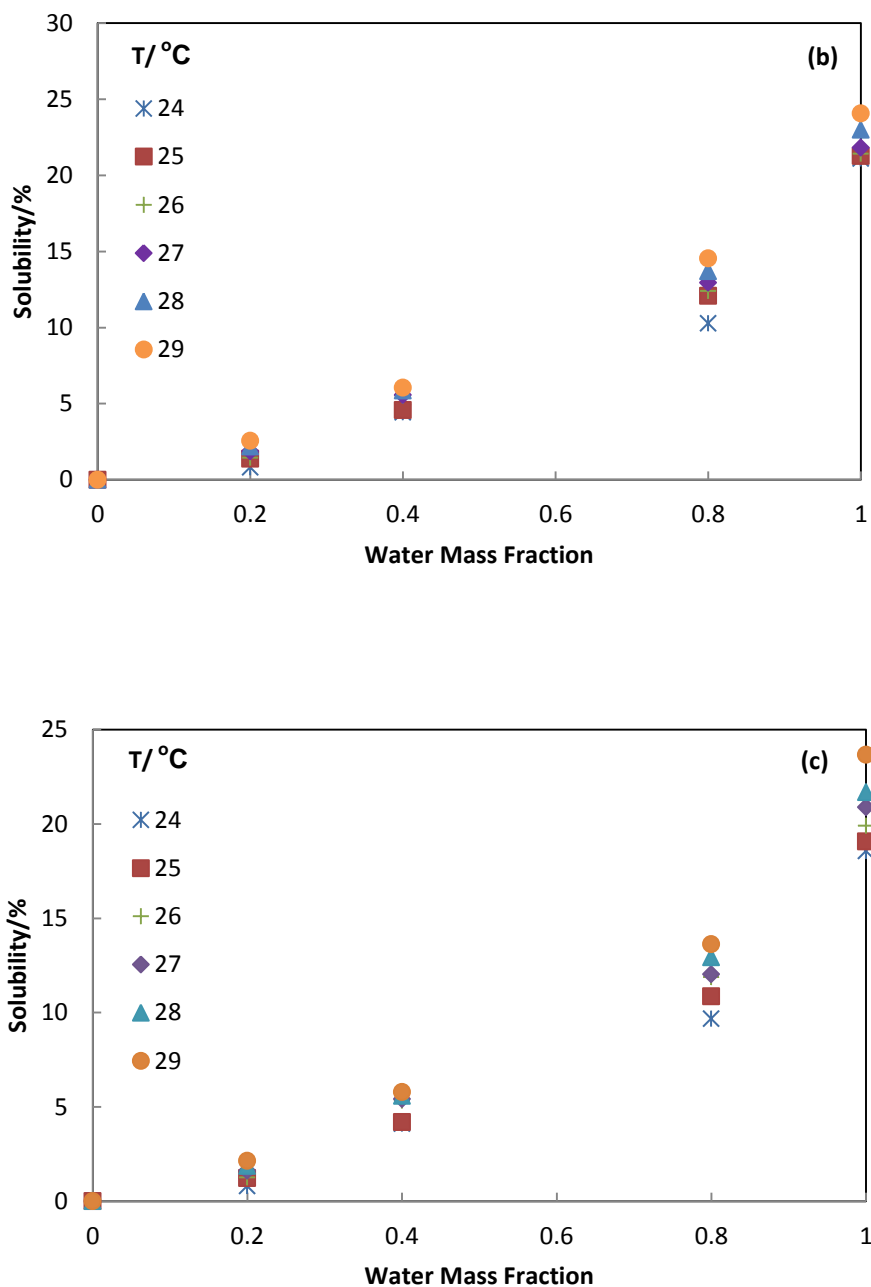
Figure 5.4 The experimental solubility profiles of sodium cefuroxime in binary solvent (ethanol and water): (a) *pH*=7; (b) *pH*=6; (c) *pH*=5.

The results showed that with the increase in the percentage of water in the mixed solvent, the solubility of sodium cefuroxime increased at different degrees. When the percentage of water was less than 0.5, the lower solvent polarity was and the slower solubility increased. When the percentage of water

was greater than 0.5, the polarity of the solvent enhanced together with the accelerated performance of hydrogen bonds in a water-rich environment, solubility grew rapidly. On the other hand, with the decreasing *pH* value, the growing trend of solubility became less obvious, which possibly resulted from: (a) the decline of the *pH* value making the solubility decline overall; (b) the decreasing *pH* value led to the ammonia being protonated and unable to form hydrogen bonds due to the existence of amino hydrogen in the sodium cefuroxime molecule.

The least-squares method (first described by Carl Friedrich Gauss around 1794) was used to construct the predictive model:

$$\beta = (X^T X)^{-1} X^T Y \tag{5.8}$$

where *β* is a matrix of coefficients, *X* is a matrix of predictors and *Y* is a matrix of responses.

Table 5.2 showed the fitting results using Equation (5.8). To verify the accuracy of the fitting, three contrasts can be seen in Figure 5.5. The results showed that most of the simulation data were located around the experimental data which meant that the model worked effectively, especially for the percentage of water lower than 0.5.

Table 5.2 The fitting results of the Jouyban-Acree model.

pH	J_0	J_1	J_2
7	68.8	472.5	1156.4
6	65.4	484.8	1136
5	73.3	510.1	1213.7
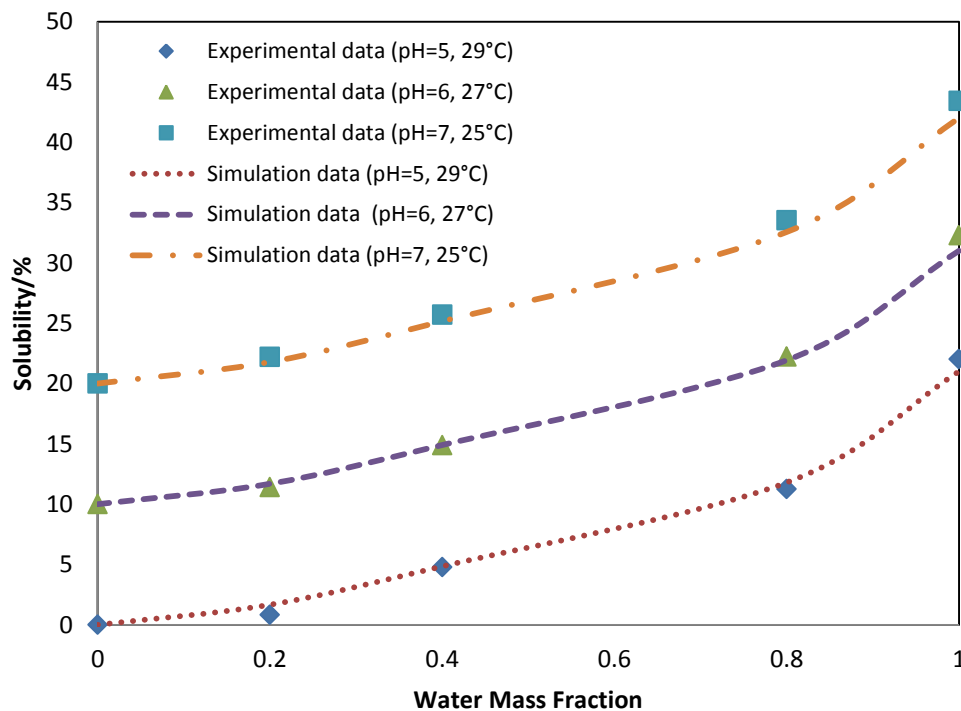
Figure 5.5 The contrast diagram of sodium cefuroxime solubility in binary solvent between experimental and simulation data.

5.4.3 Calibration Experiment of on-line ATR-FTIR

The calibration data used in this work contained 38 spectra (Table 5.3), which included spectra from: solutions with different proportions (100 % to 50 %) and the concentration ranged from 0 g to the solubility of sodium cefuroxime in the corresponding solvent. The selection of 50 % as the lower limit was due to the fact that the re-crystallization process took a long time and during this period, sodium cefuroxime degraded easily in water. If the proportion of the anti-solvent is too high, the unstable sodium cefuroxime will be crystallized, hence affecting the product quality.

Table 5.3 The spectrum data for ATR-FTIR calibration.[*]

Solvent	Sodium Cefuroxime (g)									
Water										
100 %	0	0.5	1.0	1.5	2.0	2.5	3.0	3.5	4.0	4.4
90 %	0	0.5	1.0	1.5	2.0	2.5	2.8			
80 %	0	0.5	1.0	1.5	2.0	2.5				
70 %	0	0.5	1.0	1.5	2.0	2.2				
60 %	0	0.5	1.0	1.5	1.9					
50 %	0	0.5	1.0	1.5						

*Note: (1) For each solution made, three spectra were taken, and the average of the three measurements was regarded as the spectrum at that concentration. (2) Data points highlighted were used for training the model, while data points with clear background were used for test the model.

As the other characteristic peaks were not in the measurement range of our ATR-FTIR instrument, the characteristic peak, wave number 1758 cm^{-1} (C=O stretch, β-lactam) was selected to perform the calibration. Figure 5.6 provided the absorption curves of sodium cefuroxime in pure water and 50 % water at 25 ^{o}C and *pH* 7. It can be seen that the absorption of IR spectra at the wave number 1758 cm^{-1} was proportional to the value of solution concentration.
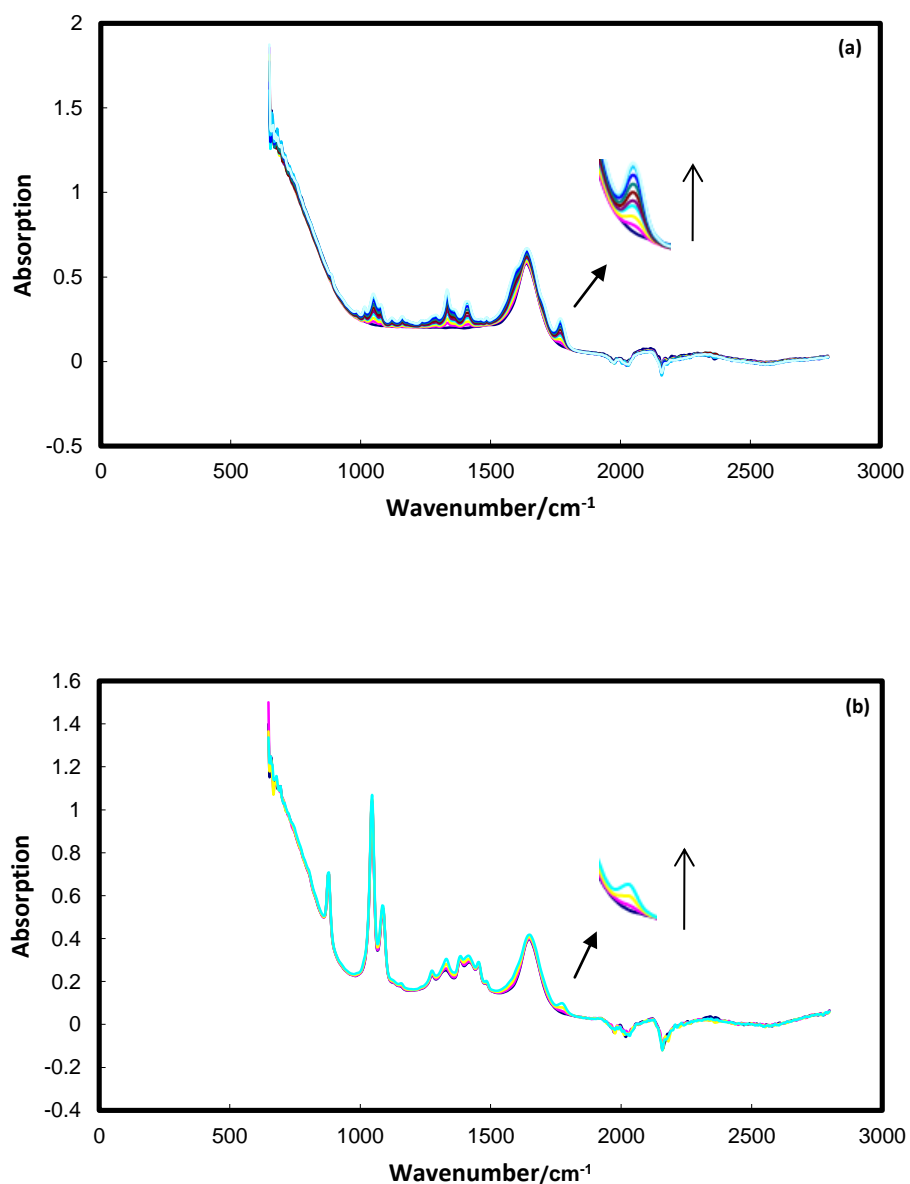
Figure 5.6 The ATR-FTIR absorption spectra of sodium cefuroxime at 25 ^{o}C and *pH* 7 (pure water (a): solution concentrations of 0.0, 2.5, 5.0, 7.5, 10.0, 13.0, 15.0, 17.5, 20.0 and 22.2 %; binary solvent with 50 % water (b): solution concentrations of 0.0, 2.5, 5.0 and 7.5 %).

Subsequently, the IR absorption spectra of sodium cefuroxime in other different proportions were done under the same conditions. In Table 5.3, the spectra data highlighted were used to construct the ATR-FTIR calibration model and the rest of the data in Table 5.3 were used for the model validation. The

concentration of sodium cefuroxime during the re-crystallization process was then calculated with the model.

The partial least squares regression method (PLS) (Abbasi et al., 2013; Zhai et al., 2013) was used to construct this predictive model. The general underlying model of multivariate PLS is:

$$X = LP^T + E \tag{5.9}$$

$$Y = LQ^T + F \tag{5.10}$$

where X is an $n{\times}m$ matrix of predictors, Y is an $n{\times}p$ matrix of responses, L is an $n{\times}l$ matrix, P and Q are, respectively, $m{\times}l$ and $p{\times}l$ loading matrices, and matrices E and F are the error terms.

The prediction results of the test data were plotted in Figure 5.7. The actual values were compared with the predicted ones, with the diagonal line being the ideal prediction. It can be concluded that most of the predicted data were located around the diagonal which meant that the model works effectively.
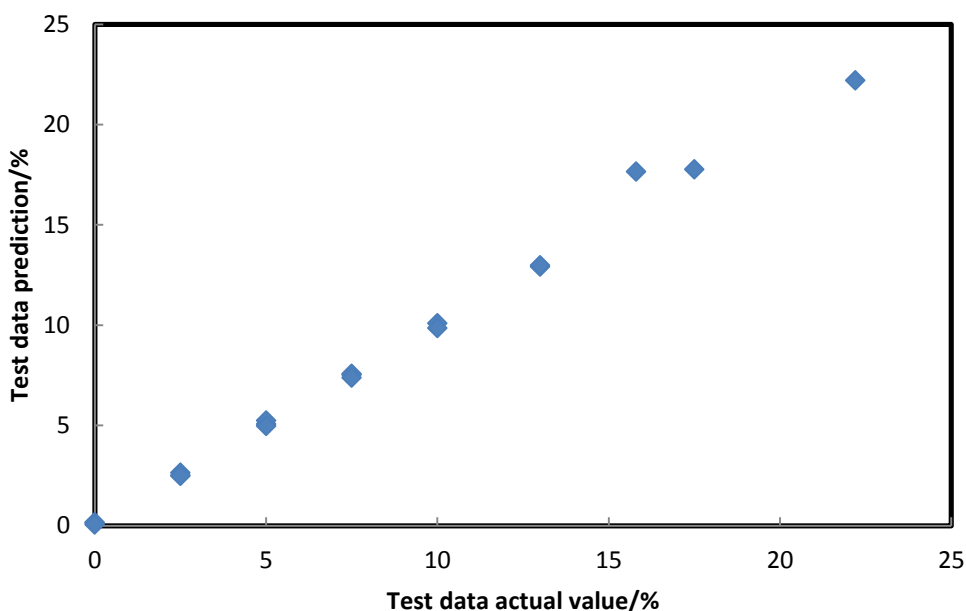
Figure 5.7The Calibration model of on-line ATR-FTIR prediction performance.

5.4.4 Monitoring the Anti-solvent Re-crystallization Process

The solubility prediction model (Equation 5.8) was used to predict the solubility of sodium cefuroxime during the re-crystallization process, and the ATR-FTIR calibration models (Equation 5.10 and 5.11) were used to calculate the concentration of sodium cefuroxime during the re-crystallization process. In the following work, supersaturation was used to optimize the re-crystallization process.

As the temperature did not vary very much in the anti-solvent re-crystallization processes, the anti-solvent flow rate became the main focus of our investigations such as 2 mL·min^{-1} for Sample 2 and 8 mL·min^{-1} for Sample 3. The selection of different flow rates was a dilemma. On one hand, lower flow rate could make the crystal grow slowly, thereby reducing the crystal defect and the chance of impurity intrusion. However, on the other hand, if the flow rate is too slow, the residence time of sodium cefuroxime in water will be long, which increases the risk of the degradation of product quality.

From Figure 5.8, it can be seen that under both flow rates, the results showed most similar phenomenon during the whole re-crystallization process except the supersaturation, which will be further discussed in the next paragraph. The temperature had the smallest fluctuation, the concentration and solubility decreased with the increase of ethanol in the various degrees. However, the supersaturation experienced first an increasing and then a decreasing process. At the start, with the increase of the anti-solvent, the concentration of the solution remained unchanged，while the solubility decreased rapidly until it was less than the concentration, resulting in the generation of the supersaturation. Due to the decline rate of solubility being greater than the decline rate of the concentration, the supersaturation started to increase. However, because of the metastable zone, where spontaneous crystallization was improbable, the turbidity remained the same, which indicated no crystal generation, and the supersaturation continued rising. Once the crystal began to precipitate, the turbidity began to decline and the supersaturation, as the driving force

promoting the continuation of this precipitation, also began to decline after a period of time, where the inflection point appeared. After experiencing a continuous decline to a certain extent, the supersaturation entered into the metastable zone again. When the anti-solvent was stopped, due to the slow deposition rate, we considered that the crystal stopped precipitation. The result showed that this process was not an obviously endothermic or exothermic process and the inflection point of the supersaturation was the key to the effect of the crystallinity on the product.
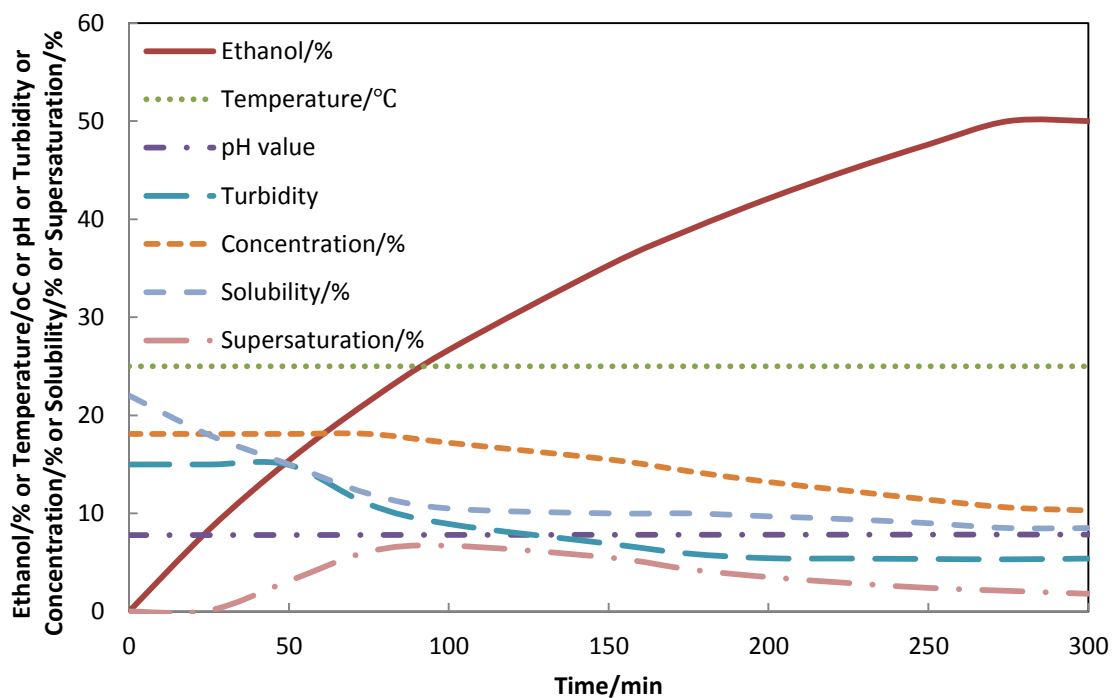
(a) Parameter monitoring in a slow anti-solvent experiment (2 mL·min^{-1})
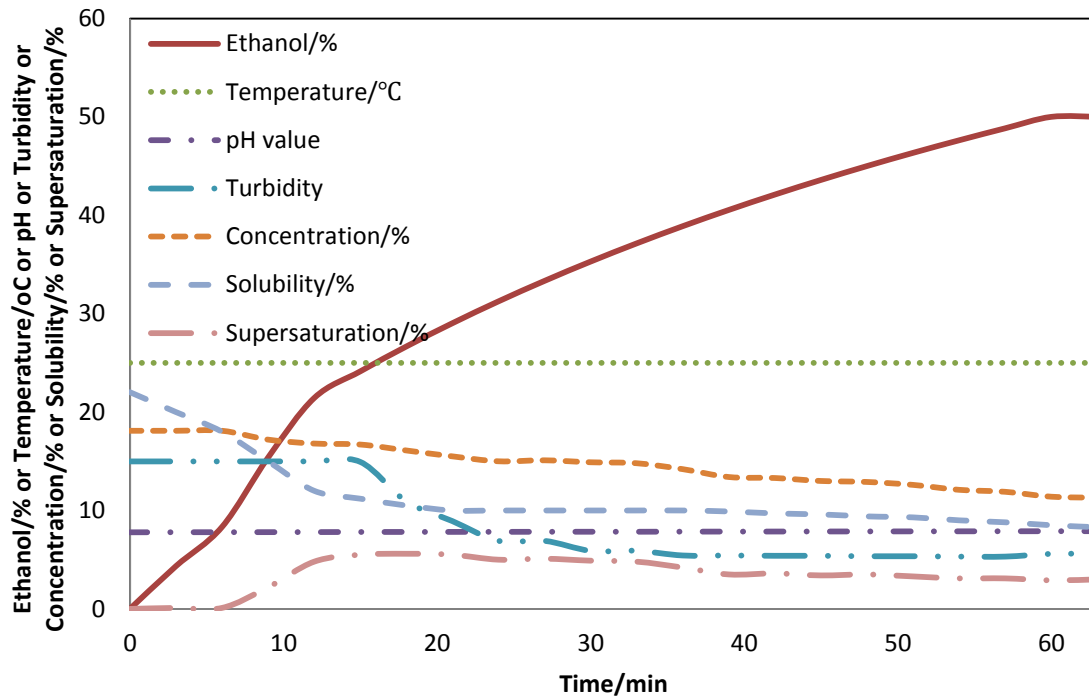
(b) Parameter monitoring in a rapid anti-solvent experiment (8 mL·min^{-1})

Figure 5.8 Profiles of variables in anti-solvent re-crystallization experiment: ethanol (*E*), temperature (*T*), turbidity (*TU*), *pH*, solution concentration (*C*), solubility (*S*) and supersaturation (*Δc*= concentration *C* – solubility *S*) during the anti-solvent re-crystallization process; (a) Parameter monitoring in a slow anti-solvent experiment (2 mL·min^{-1}); (b) Parameter monitoring in a rapid anti-solvent experiment (8 mL·min^{-1}).

From Figure 5.9, the difference between these two flow rates on the supersaturation curves can be more clearly seen. The rapid flow rate made the inflection point of supersaturate appear and reduce earlier. This was because it caused the distribution of the supersaturation to be non-uniform, resulting in the partial excessive supersaturation which caused the first crystal precipitation. Once the crystal generated, the supersaturation began to decline. In contrast, the shower flow rate can produce not only a higher inflection point, but also a fewer fluctuations, which meant the crystal can be produced in a more uniform environment, therefore better crystal structure and size distribution can be obtained. The idea that the sodium cefuroxime precipitates as soon as possible

to prevent degradation in water would only lead to more crystal structure defects.
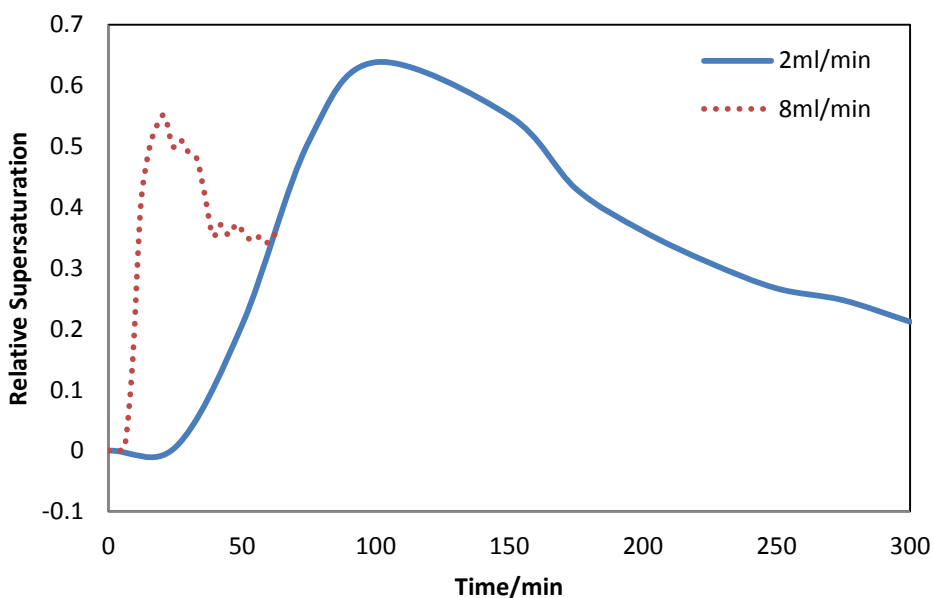
Figure 5.9 The diagram of relative supersaturation diagram with different anti-solvent feed rate.

5.4.5 Physical Properties Analyses

As indicated by Yoshioka and Stella in their book (Yoshioka and Stella, 2002), the factors that affect a crystalline drug's stability can include crystallinity, impurity, water content, purity, size distribution, shape etc. Some of these factors are often correlated. The general view is that increased crystallinity often meant higher purity and lower impurity content and leading to improved stability.

The crystalline state of these three samples (Table 5.4) was characterised using XRD and compared (Figure 5.10). The results showed that the crystalline state of Sample 2 was much higher than that of Sample 3, which meant that the rapid flow rate did little good to the product quality. However, both of them were higher than the original batch (Sample 1), which meant that even if the samples were obtained under a relatively rapid re-crystallization process, the purpose of reducing the impurities and mending the crystal structure during this anti-solvent re-crystallization process can also be partly achieved.

Table 5.4 The operating conditions of samples in anti-solvent process.

Batch No	Operating Conditions
Sample 1	Before anti-solvent process, obtained from Weiqida
Sample 2	After anti-solvent process, anti-solvent feed rate: 2 mL/min
Sample 3	After anti-solvent process, anti-solvent feed rate: 8 mL/min

Peak intensity: 22012
Peak width at half height: 0.165^o
(a)

Peak intensity: 22100
Peak width at half height: 0.155^o
(b)

Peak intensity: 6130
Peak width at half height: 0.632^o
(c)

2- Theta/^{o}
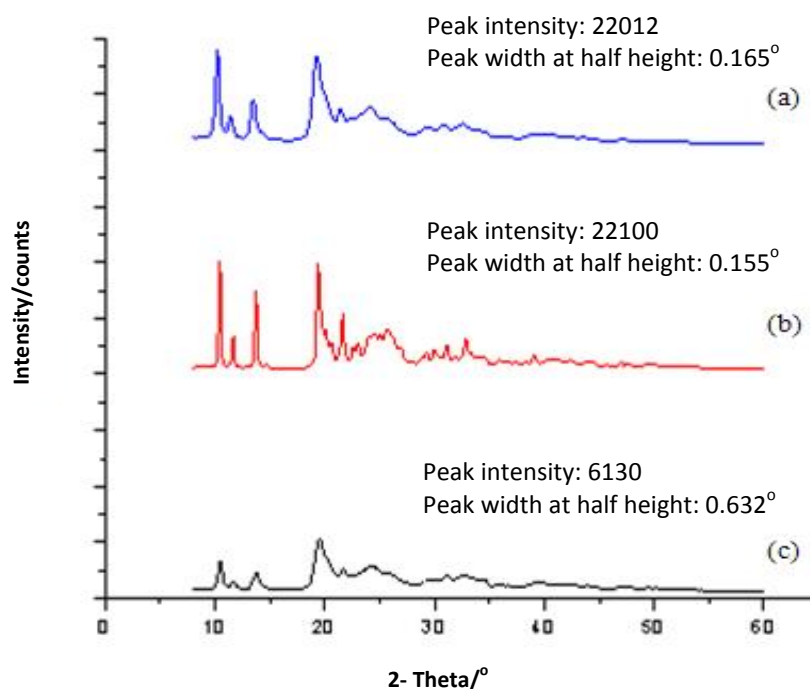
Figure 5.10 The XRD pattern of sodium cefuroxime: Sample 3 ((a) blue line) and Sample 2 ((b) red line) are obtained via re-crystallization process which shows better crystallinity than Sample 1 ((c) black line) which was the crystals used in the re-crystallization process (peak intensity and peak width at half height of peak between 9° to 10.5^o were chosen to present the crystallinity).

The SEM results (Figure 5.11) showed that sodium cefuroxime had serious aggregation phenomenon. As is well known, serious aggregation is usually considered as a significant problem for rapid crystallization. Like ceftriaxone sodium (Zhang et al., 2010), as a result of the lamellar habit, it was hard to completely avoid aggregation in this anti-solvent re-crystallization process.

However, after this re-crystallization process, Sample 2 had a smaller mean particle size and more uniform size distribution. Appropriate mean size and uniform size distribution are also important for higher stability (Hiwalea et al., 2009). Compared with Sample 1, the rapid crystallization rate can only lead to a non-uniform crystal size distribution.
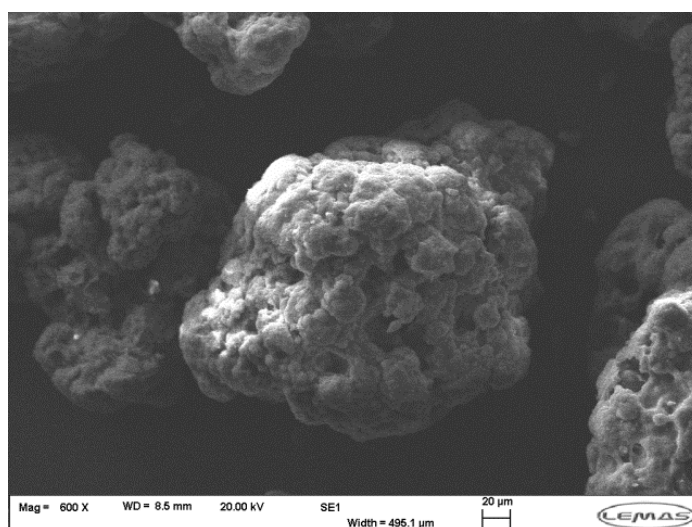
(a) Sample 1(184.5 µm)
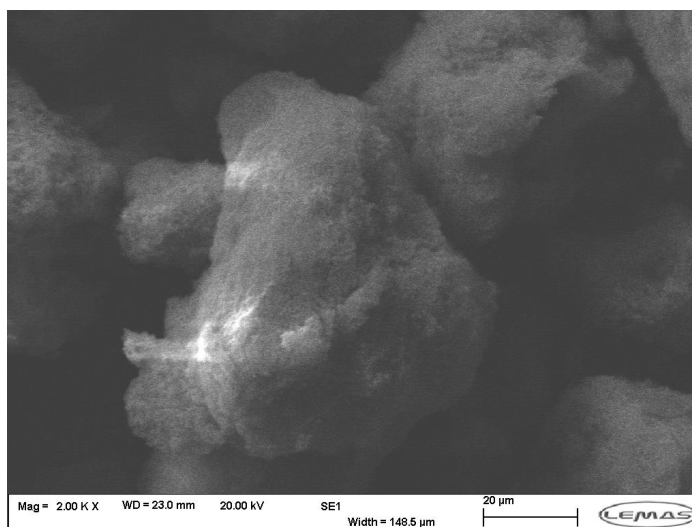
(b) Sample 2 (77.4 µm)

Figure 5.11 The SEM images of sodium cefuroxime: (a) Sample 1 (184.5 µm); (b) Sample 2 (77.4 µm).

Other physical properties were also analysed to further verify the product stability. As can be seen in Table 5.5, the water content was reduced and the

content of sodium cefuroxime was increased in Sample 2, which meant that the impurity decreased in sodium cefuroxime crystals after the re-crystallization process. These changes further proved that the crystallinity has been improved. Better crystallinity can reduce the defect of the crystal and reduce the moisture and impurities wrapped in the crystal growth process as well. The stability test data results (Table 5.6) proved that the stability improved in Sample 2, indicating that a good crystalline state can improve the stability of the product. The anti-solvent re-crystallization method can produce the desired product quality, so it is an ideal method for high quality seed production.

Table 5.5 Physical data of sodium cefuroxime.[*]

Batch No	Water (%)	Color Grade	Specific Volume $(m^3 \cdot kg^{-1})$	Content Measured by HPLC (%)
Sample 1	0.239	< Y-2#	1.8	94.96
Sample 2	0.226	< Y-2#	3	95.23

Table 5.6 Stability test data of sodium cefuroxime.[*]

Batch No	Color Grade (40 ^{o}C)			
	0 day	3 days	6 days	10 days
Sample 1	< Y-2#	< Y-7#	< Y-7#	< Y-8#
Sample 2	< Y-2#	< Y-4#	< Y-5#	< Y-5#

* **(1) Y means the color grade yellow; (2) Sample 1 refers to the original crystals that are used in re-crystallization, Sample 2 refers crystals obtained from re-crystallization.**

5.5 Final Remarks

In this chapter, based on the solubility measurement and calibration model construction, ATR-FTIR was applied on monitoring the re-crystallization process of cefuroxime sodium. Through this process, the crystalline state of the product was improved, and the seeds with high quality for the next reaction process optimization and reactor design were obtained. The following are some more detailed remarks:

1. The investigation of the solubility of sodium cefuroxime showed that, on the one hand, it was less affected by temperature, which meant the cooling re-crystallization of sodium cefuroxime cannot be used; on the other hand, it was affected by *pH* value, which indicated that sodium cefuroxime is weakly basic compound and easily degraded in an acidic environment, so changing *pH* value for re-crystallization of sodium cefuroxime cannot be used either. Due to its different solubility in different solvents, alternately, the anti-solvent re-crystallization process was used for improving the crystalline state of the product.

2. The solubility and calibration model construction indicated that multiple linear least squares method was an effective approach for model building. But when it comes to the real application, there are still some operational details that need attention. First of all, taking the background of the spectrum is quite important and the background does have very serious impact on the results. Before using the probe, maintaining a good contrast peak (higher than the value of 20000) is the sufficient condition to get better spectrum results. Secondly, the purge system is quite important in the IR measurement. It is important to make sure that the air drying system works 24 hours longer before taking spectra in the crystallization experiments.

3. In this system, ATR-FTIR was used for concentration measurement which was based on the IR absorption spectra of different substances. However, the absorption spectrum of sodium cefuroxime and acetone were overlapped. Thus, although there were two solvents mentioned before can be chosen for re-

crystallization process, only one of them can be achieved, that was ethanol. Furthermore, the absorption spectra of sodium lactate, acid cefuroxime and sodium cefuroxime were also overlapping, which indicated that ATR-FTIR cannot be used to monitor the reactive synthesis process.

4. Just as mentioned in the literature, the re-crystallization method can indeed reduce the content of impurities and defects in the crystal, so that the crystal can be more perfect. Although due to the low yield cannot be large-scale industrialized, re-crystallization provided a new method to obtain high-quality seeds, and proved that a perfect crystalline state can improve the stability of the drugs.

Chapter 6

Optimization of Reactive Synthesis Process of Sodium Cefuroxime

6.1 Introduction

Sodium cefuroxime synthesized by the reaction is somewhat different with that re-crystallized by anti-solvent process in chapter 5. Although sodium cefuroxime has only one crystalline state according to Pharmacopoeia and literatures, in a rapid reactive process, it exists in a number of different crystallinity with varying degrees of solid stability and purity and with differing physical and chemical characteristics. It has proved in practice that it is difficult to manufacture sodium cefuroxime industrially in a total crystalline form having a combination of suitable properties such as solid state stability, purity, particle size, and filtration and drying characteristics.

In order to synthesize more stable sodium cefuroxime, many methods have been tried in laboratory, some of which have already been summarized in literature review. But they all have some obvious disadvantages, such as the use of organic solvents are excessive or toxic which makes downstream difficult, the harsh reaction conditions are difficult to be used in industrial scale, excessive water consumption during the reaction lead to the water residue unqualified, or the particles obtained is too small to filter and difficult to dry. And so far, most of them are still in a semi-skilled state, which means it can be influenced by many factors, especially the process parameters.

Despite facing these problems, many excellent efforts have been done to optimize laboratory operating conditions for industrial production application and there are many methods have already been widely used for commercial production. And in this chapter, in order to further improve the crystallinity of sodium cefuroxime produced by reactive synthesis process without changing its

filtration and drying characteristics, we chose one industrial synthesis method now being used to optimize, it might not be the best method of synthesis, but it is the least toxic process with the simplest operation and highest stability.

The original operation for industrial application of sodium cefuroxime synthesis process was: putting the sodium lactate solution in the reactor first with 0.3 g sodium cefuroxime added as seeds, and the acid cefuroxime solution was added to the reactor with 4 - 6 mL·min^{-1} feed rate at 25~28 ^{o}C, and the reaction took place immediately with stirring. Therefore, the main parameters in this study were: the feed order, the amount of activated carbon, the drying time, the reaction temperature, the stirring speed, the feed rate, and the amount of seeds.

In this study, increasing the crystallinity of the product, hence improving the stability, was the main purpose. As the XRD pattern are directly relevant to the perfection level of crystal structure, the pattern results was used to judge the crystallinity. This is attributed to the fact that our product exists as a mixture of crystal and amorphous state. Furthermore, comparing with the stability test (3 days, 5 days, 7 days, 10 days, 14 days and 20 days), XRD pattern can be measured quickly and gives the direct evidence for the process optimization. The procedure of the analytical characterization (XRD, *Morphologi* G3 and SEM) were the same which can be seen in chapter 5.

6.2 Optimization of reaction conditions

6.2.1 Determination of Feed Order

As mentioned before, the industrial feed order was that the sodium lactate solution was first added and followed the cefuroxime acid solution. In order to increase the product yield, that is, to make the acid cefuroxime reaction completed, it was necessary to ensure the sodium lactated excess. The other reason that chose sodium lactate first was that sodium cefuroxime was unstable under the acidic condition and if the acid cefuroxime solution was added first into the reactor, it would cause that most of the reaction process was carried out under acidic condition, which was not conducive to the product quality.

Two methods were compared (Figure 6.3): (a) 2 mL sodium lactate solution was put in the reactor first, and then added 2 mL acid cefuroxime solution; (b) 2mL acid cefuroxime solution was put in the reactor first, then added 2 mL sodium lactate solution. The results can be seen in Figure 6.3. The smaller crystal was obtained from the first one (a). The particles obtained from the second method (b) were relatively large and have obvious agglomeration phenomenon. Besides the *pH* environment of process (a) was more conducive to the product stability, so adding sodium lactate solution first (a) was used in the future optimization trials.
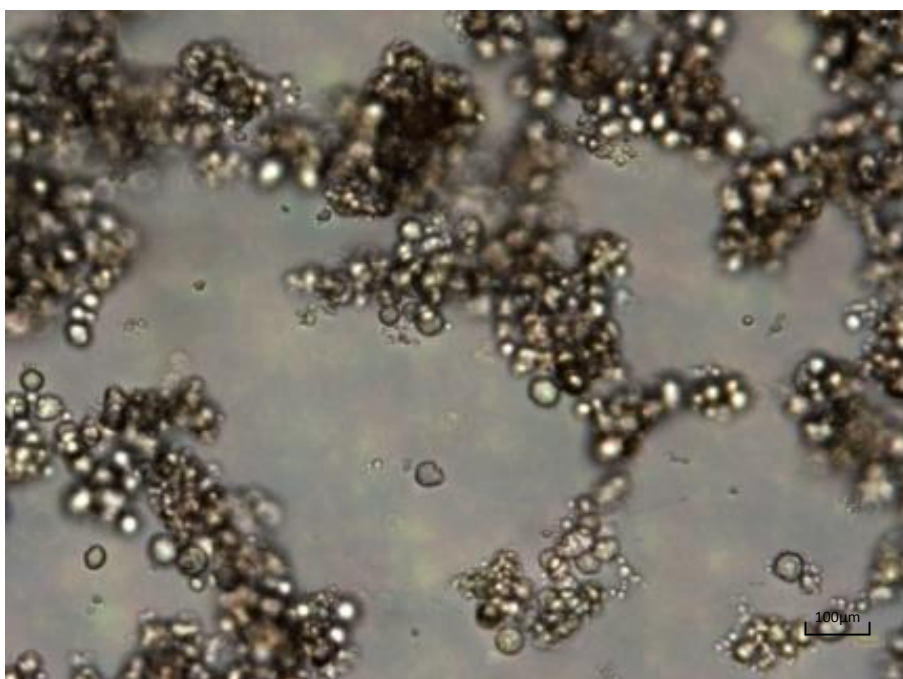
(a) 2 mL sodium lactate solution was put in the reactor first, and then added 2 mL acid cefuroxime solution
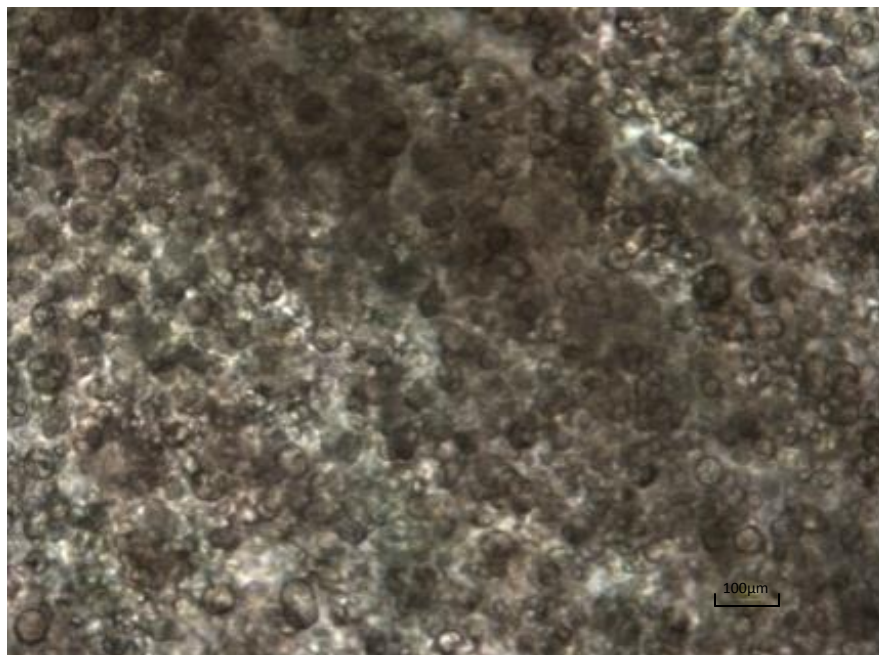
(b) 2mL acid cefuroxime solution was put in the reactor first, then added 2 mL sodium lactate solution.

Figure 6.1 The optical microscope results of the reactive synthesis process of sodium cefuroxime (25 $^{\circ}$C).

6.2.2 The Impact of Raw Material

Many experiments were done on the basis of the first batch of raw material, but no matter how we changed the reaction temperature, the amount of activated carbon or the feed rate, the results were always unsatisfactory and the color of the product kept yellow, even though the products stored at the low temperature also would deepen the color level soon. Then, based on the principle of the degradation of acid cefuroxime, it was speculated that maybe because the raw material degraded quickly when stored at the room temperature or exposed to the air, thereby, to some extent, affected the quality of the product. So the quality of acid cefuroxime must improve, especially the color grade requirements, and both the raw material and the product should be stored at the low temperature and sealed.

6.2.3 The Impact of Activated Carbon, Drying Process

Many processes of the pharmaceutical technology used the activated carbon for decolorization. The greater the amount of activated carbon used, the more easily the decoloration process is. But it also brought along the difficulties of filtering and resulted that the activated carbon residue would affect the clarity and purity of the product. Experimental results suggested that: the best mass ratio of the amount of activated carbon and the acid cefuroxime was 0.1:1. Decolorization time also had effect on the product, so to the experimental scale, the appropriate decolorization time was 15 – 20 min.

In the drying process of the product, it was found that the oxidation was another factor that caused the product degradation. If the product was dried naturally at room temperature, the apparent color of the product would soon turn yellow. In some literature, using nitrogen purge filter press could improve the apparent color of the product. However, due to the big energy and time consumption, it was difficult to use in the laboratory experiment. Instead, we used the vacuum oven at a room temperature or a lower temperature for our product drying. However, in industrial operation the drying process may take the nitrogen purge filter press.

Table 6.1 Operation Parameters of the Optimization Experiments in 1L rig.*

Reaction temperature (^{o}C)	Feed rate (mL·min^{-1})	Stirring speed (rpm)	Amount of seeds (g)
20 (A)	2 (E)	80 (I)	None (M)
25 (B)	4 (F)	100 (J)	0.3 (N)
30 (C)	6 (G)	150 (K)	
35 (D)	8 (H)	200 (L)	

* **The letters A B and C will be used in Figure 6.2 6.3 and 6.4 to denote the designs.**

In the following optimization experiments for operation parameters, letters were used to denote the designs for clear (Table 6.1).

6.2.4 Determination of Temperature

At a higher temperature, the increasing Brownian motion can make the dispersion rate of a solute in a solvent much larger than that at a lower temperature. Therefore, high temperature condition can promote the forward reaction. If the other conditions are kept the same, the time required to reach equilibrium is inversely proportional to the temperature increase, i.e., as the temperature increases, the time spent on reaching equilibrium can be rapidly shortened. As a result, it seems that when possible, a higher reaction temperature should be used during a reaction process. However, at the same time, the reaction temperature is also one of the important factors that affect the quality of the final product; in particular, the impact on the product color grade is very significant. In chapter 2, it motioned that sodium cefuroxime is known as a kind of β-lactam antibiotics, which has ester and amide functional groups within its molecular structure. This means that the hydrolysis of ester bond and amide bond becomes the main factor to cause chemical degradation. Under higher temperature, this chemical degradation can be more severe, hence resulting in lower product stability. In our studies, it was found that the mother liquor color grade at the end of the reaction could become yellower even by visual observation after filtration if the reaction temperature was too high. In addition, the product obtained from higher temperature reaction was often caked or hardened, which was not conducive to the drying and milling processes (Thompson and Baalham, 1981).

In order to investigate the influence of reaction temperature on the crystallization process, the test reaction temperatures were 20 ^{o}C (AEIN), 25 ^{o}C (BFIN), 30 ^{o}C (CFIN), and 35 ^{o}C (DFIN). The XRD pattern results (Figure 6.2) showed that the reaction temperature within the tested temperature range had little effect on the crystalline state. Therefore, the optimization tests were performed at room temperature (20 ^{o}C - 25 ^{o}C).
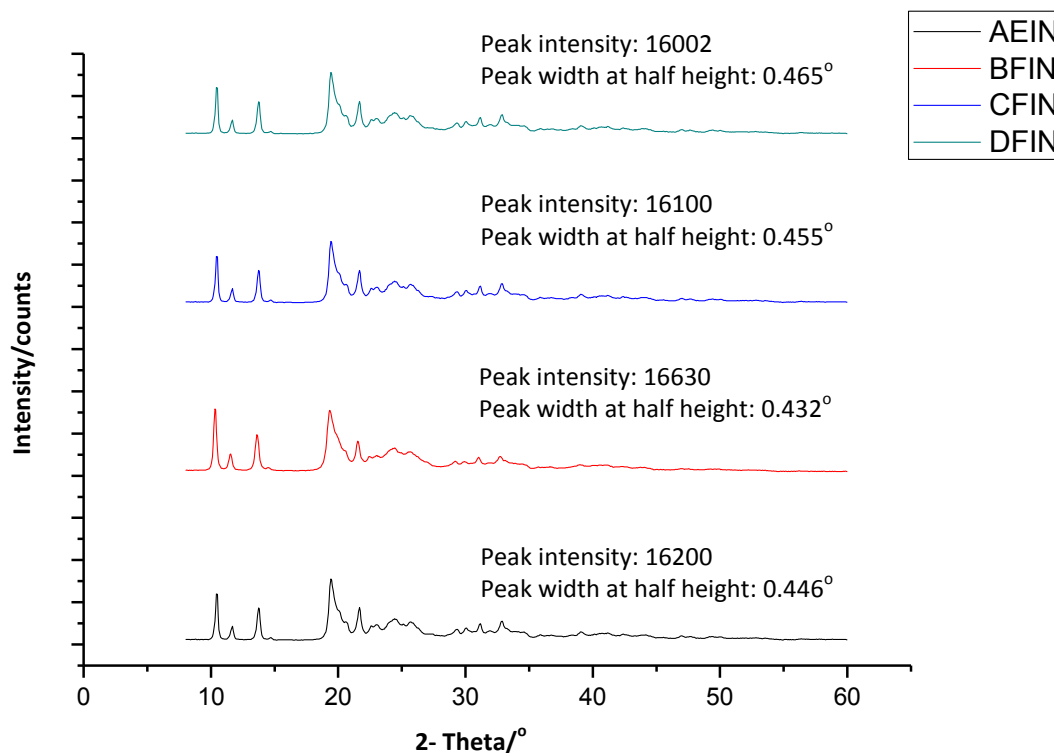
Figure 6.2 The XRD pattern of sodium cefuroxime obtained from the 1L crystallizer for determination of the reaction temperature (peak intensity and peak width at half height of peak between 9° to 10.5° were chosen to present the crystallinity) (the meaning of the monogram in the label table on the right side can be seen in Table 6.1, e.g. AEIN means the reaction temperature is 20 °C (A), the feed rate is 2 mL·min⁻¹ (E), the stirring speed is 80 rpm (I) and the amount of seeds is 0.3 g (N)).

6.2.5 Determination of Feed Rate

For the reactive process, the feed rate has a direct impact on the reaction rate. Generally, very fast feed rate would make the reactants react insufficiently, hence leading to the final products mixing with the unreacted reactants. For the crystallization process, fast feed rate would make local supersaturation increase rapidly, in particular, in larger-scale crystallizers, which is more likely to cause non-uniform supersaturation distribution, hence resulting in low crystallinity of the product. On the contrary, slow feed rate is conducive to the growth of crystals, but it might not be a desirable operating condition because it would lengthen the production time.

On the basis of the industrial feed time, several test feed rates were used in the current studies: 2 mL·min^{-1} (BEIN), 4 mL·min^{-1} (BFIN), 6 mL·min^{-1} (BGIN) and 8 mL·min^{-1} (BHIN). The XRD pattern results (Figure 6.3) showed that the feed rates of 2 mL·min^{-1} and 4 mL·min^{-1} produced the crystals with higher crystallinity, which meant that the slow feed rate was more conducive for sodium cefuroxime crystalline formation.
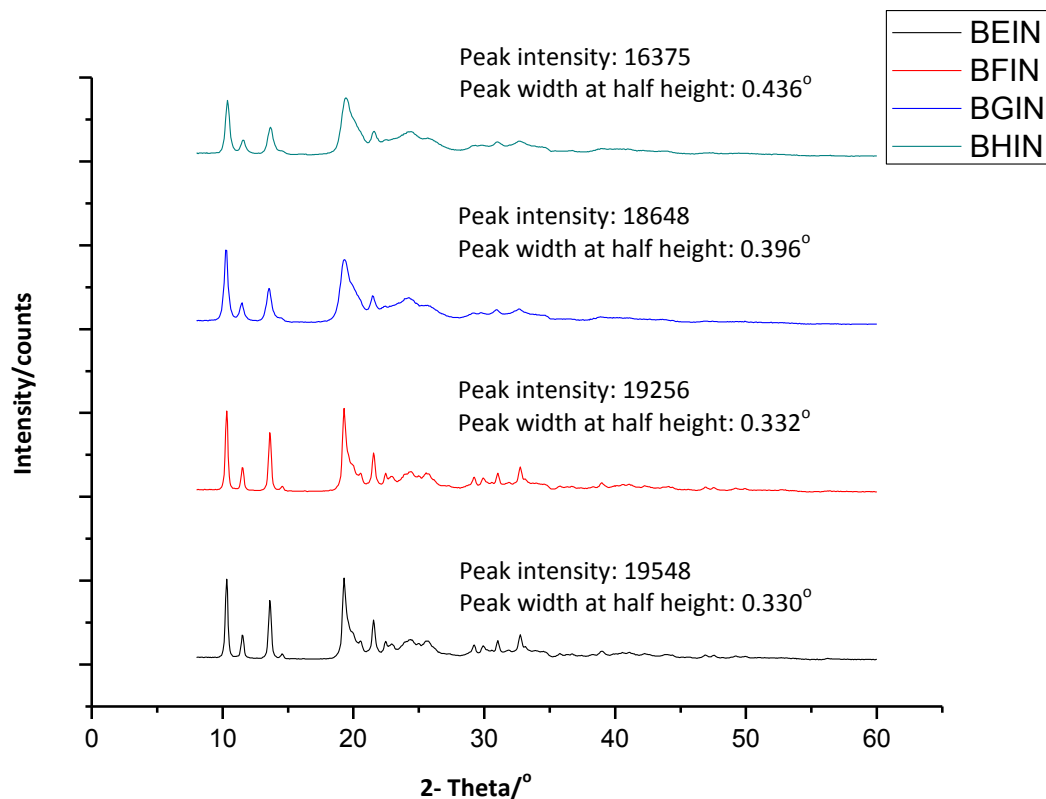
Figure 6.3 The XRD pattern of sodium cefuroxime obtained from the 1L crystallizer for determination of the feed rate(peak intensity and peak width at half height of peak between 9° to 10.5^{o} were chosen to present the crystallinity) (the meaning of the monogram in the label table on the right side can be seen in Table 6.1).

6.2.6 Determination of Stirring Speed

In a crystallization process, stirring can keep the solution concentration in a more uniform state, hence leading to the corresponding supersaturation on the crystal interface more uniform. The use of stirring can also cause the crystals to collide with each other and to influence the local environment and temperature distributions for the crystals to grow up. However, a higher stirring speed also

produces large horizontal shear force, which can break the formed crystals. Therefore, the determination of a suitable stirring speed is one of the necessary conditions for producing high quality crystals from reactive crystallization processes under the current investigation.

On the basis of the industrial operating parameters, the tested stirring speeds were: 80 rpm (BFIN), 100 rpm (BFJN), 150 rpm (BFKN) and 200 rpm (BFLN). The XRD pattern results (Figure 6.4) showed that an appropriate stirring speed within a range of 80 - 100 rpm provided proper collision opportunities for crystal growth and also maintained the solution concentration uniform.
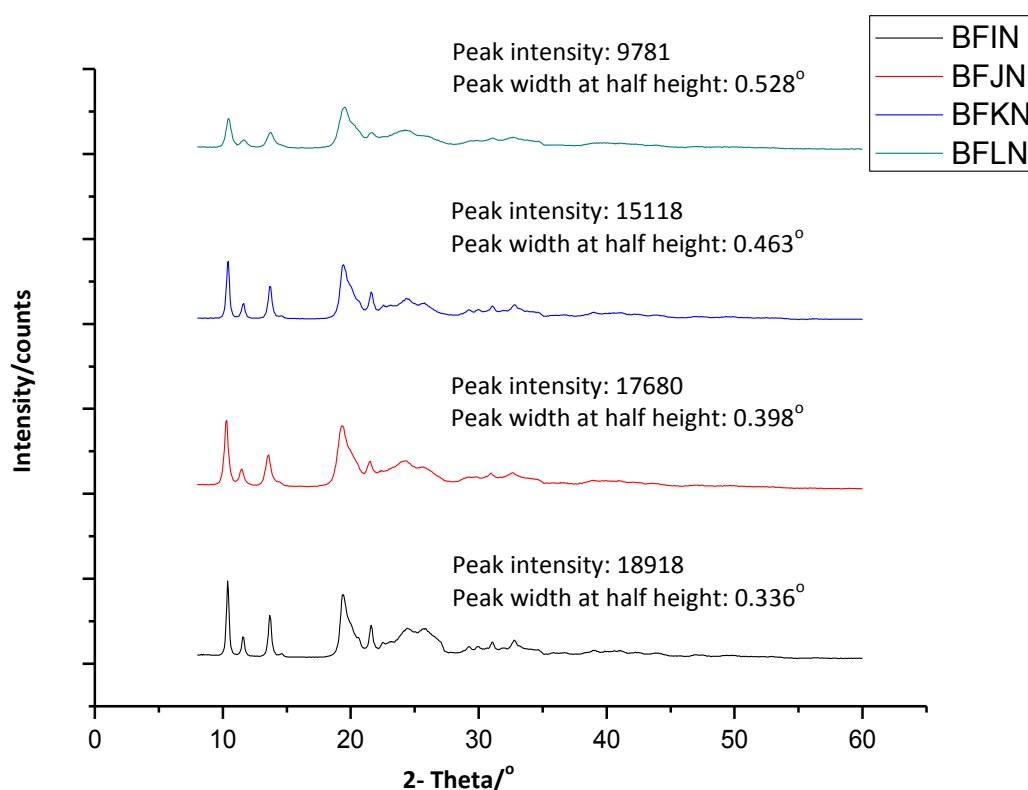
Figure 6.4 The XRD pattern of sodium cefuroxime obtained from the 1L crystallizer for determination of the stirring speed rate (peak intensity and peak width at half height of peak between 9° to 10.5^o were chosen to present the crystallinity) (the meaning of the monogram in the label table on the right side can be seen in Table 6.1).

The *Morphologi* G3 results also showed that an appropriate stirring speed (such as 80 -100 rpm) was able to produce more narrow particle size distribution (Figure 6.5 (a, b)). However, if the stirring speed was set to be too

high (such as 150 - 200 rpm), the crystals subjected to greater shear force would be broken into small particles, hence not only resulting in the number of particles being increased and a less narrow particle size distribution (Figure 6.5 (c, d), ever bimodal distribution (d)), but also leading to more amorphous particles in the final products. The *Morphologi* G3 results (Figure 6.5) indicated that the fluid stresses were sufficient to break the crystal that grew following an aggregation mechanism. This may be the main cause for a bimodal CSD.

(a) BFIN (6.7 μm)

(b) BFJN (6.1 μm)

(c) BFKN (6.0 μm)

(d) BFLN (4.1 μm)
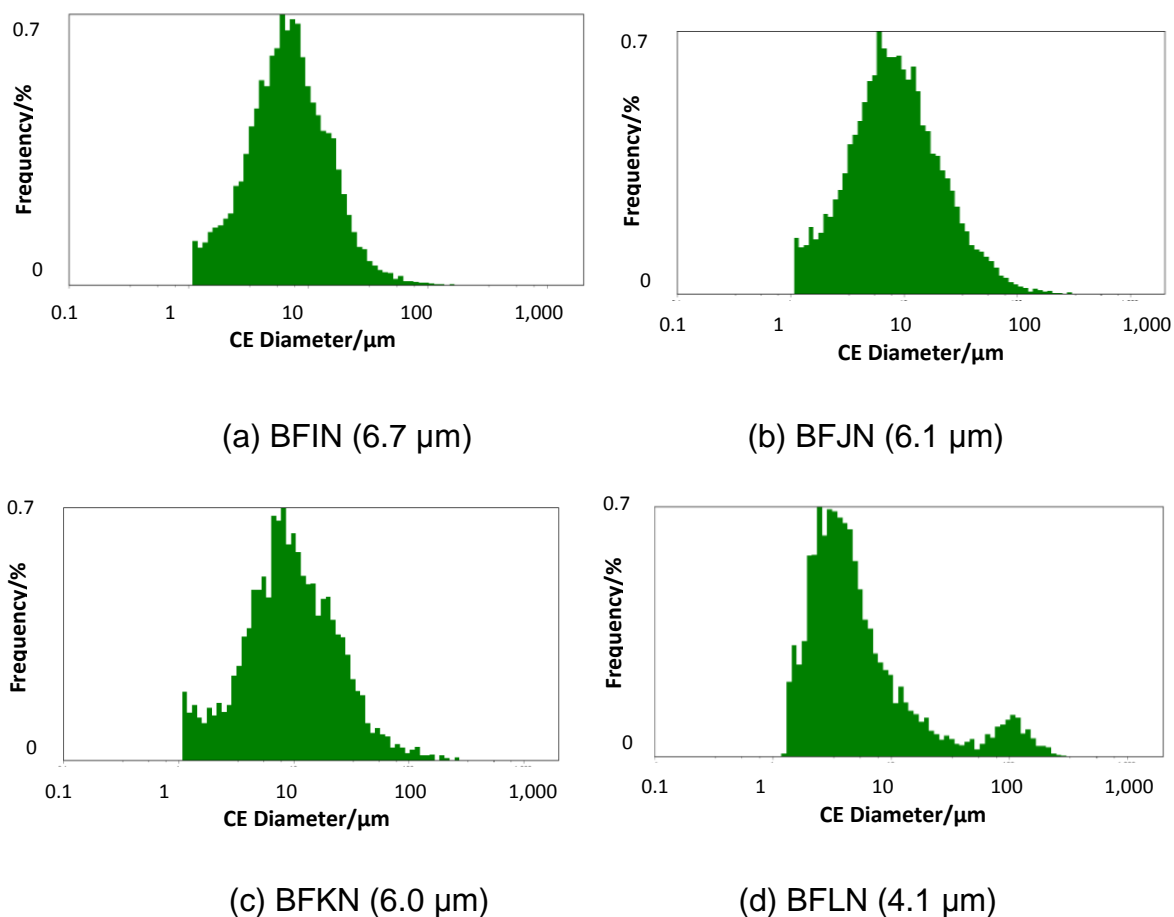
Figure 6.5 The *Morphologi* G3 results of sodium cefuroxime obtained from the 1L crystallizer for determination of the stirring speed during the optimization of reactive crystallization process: (a) BFIN (80 rpm); (b) BFJN (100 rpm); (c) BFKN (150 rpm); (d) BFLN (200 rpm).

In addition, there were still two noteworthy issues: a) for the reactive crystallization process, the sufficiently mixing of the reactants was conducive to the reaction procedure, and helpful to keep the uniform distribution of supersaturation at the same time. Generally, it was believed that increasing the

stirring speed could make mixing better, but for some relatively fragile crystals, a higher stirring speed would break the crystals with higher possibilities. b) The optimum stirring speed was only targeted with the laboratory crystallizer configurations and the type of the stirring paddle used in the current study. If the crystallizer configuration or the paddle type is changed, the similar procedure can be used to obtain the corresponding optimum stirring speed.

6.2.7 Determination of Amount of Seeds

6.2.7.1 Amount of Seeds

Different amount of seeds provides different final products. Too few seeds cannot help to suppress the secondary nucleation, while too many seeds may lead to tiny crystals. A simplified method was generally used to estimate the appropriate amount of seeds in the industry (Inoue et al., 1984). The load of the seed can be predicted from the amount of the solute dissolved in the solvent, the size of the seed and the desired size of the final product. For a crystallization process that only has crystal growth and the formation of nuclei can be ignored, the number of product crystals should be equal to the number of seeded crystals as described in the following formula,

$$\frac{M_P}{K_V \rho V_P} = \frac{M_S}{K_V \rho V_S} \tag{6.1}$$

where M_p and M_s are the mass of the product crystals and the seed crystals, respectively, g; K_v is the volume shape factor; V_p and V_s are the average volume of the product crystals and the seed crystals, respectively.

Obviously, this is only a simplified approach. The expression of the average size of the product crystals and seeded crystals is far less accurate. For almost all of the crystallization processes, secondary nucleation is inevitable. However, this approach can provide a reference for further research. Using this method, the optimal amount of the required seeds was found to be 0.3 g in the current study.

To further confirm the amount of seeds, FBRM (Focused Beam Reflectance Measurement, LASENTEC, S400A Controller, PI-14/206 PROBE) was used in this un-seeded reaction. As the FBRM could detect the counts number of crystals in the crystallizer (Barrett and Glennon, 1999; Heath et al., 2002), the plan was to take a quick initial feed rate to produce different numbers of seeds, and then slow down the feed rate to avoid secondary nucleation. Two different initial feed rates, 4 mL·min^{-1} (Sample 1) and 10 mL·min^{-1} (Sample 2), were selected, corresponding to the slower and faster feed rates, respectively (Table 6.2). In order to prevent excessive feed which would lead to the generation of too many seed crystals, the feed pump was opened one minute every five minutes. The feed rate was changed only in the experiments for the determination of the amount of seeds. In other experiments either for operation parameters optimization or for impinging jet design, the feed pump operated during the entire reactive crystallization process with the optimized feed rate (4 mL·min^{-1}) for the reactant feed.

Table 6.2 The operating conditions of samples for seed determination.

Batch No	Operating Conditions
Sample 1	Temperature: 20 - 25 °C, The initial feed rate: 4 mL·min^{-1}, The stirring speed: 80 rpm, no seed
Sample 2	Temperature: 20 - 25 °C, The initial feed rate: 10 mL·min^{-1}, The stirring speed: 80 rpm, no seed

Faster feed can produce larger number of crystals. Therefore, in our study, the faster feed was only used for a higher degree of supersaturation to ensure different amounts of seeds can be generated quickly at the very beginning of the entire reactive crystallization process. After that, a slower feed was used to reduce the degree of supersaturation to inhibit secondary nucleation. Besides, the present of appropriate number of seeds can also lower the degree of supersaturation in the solution which could further inhibit secondary nucleation.

Here, secondary nucleation meant the nucleation that happened after the seeds were added.

The results (Figure 6.6 (a) and (b)) showed that when the feed amount reached 40 mL - 70 mL, the seed crystals generated could be obviously detected. The number of each sized crystals generated by faster initial feed rate was significantly less than that generated by a slower initial rate, which meant that the faster initial rate quickly made enough seeds to suppress secondary nucleation. The final total counts numbers were 35,000 and 25,000, respectively. It also revealed that in the case of a certain amount of product, the crystal size obtained with the faster initial feed rate (10 mL·min^{-1}) was bigger than that with the slower one (4 mL·min^{-1}) because of the lower total counts number, which could make the filtration process more easily and quickly. Two repeat experiments were then conducted following the same conditions with Sample 1 and Sample 2, respectively. The results (Figure 6.6 (c)) showed that when using 10 mL·min^{-1} as the initial feed rate (Sample 2), the growth rate of the total counts was significantly slower during the time period between 50 – 90 minutes, which further confirmed that the appropriate number of seeds can inhibit the secondary nucleation during the reactive crystallization process, hence confining the nucleation process and promoting the growth process.
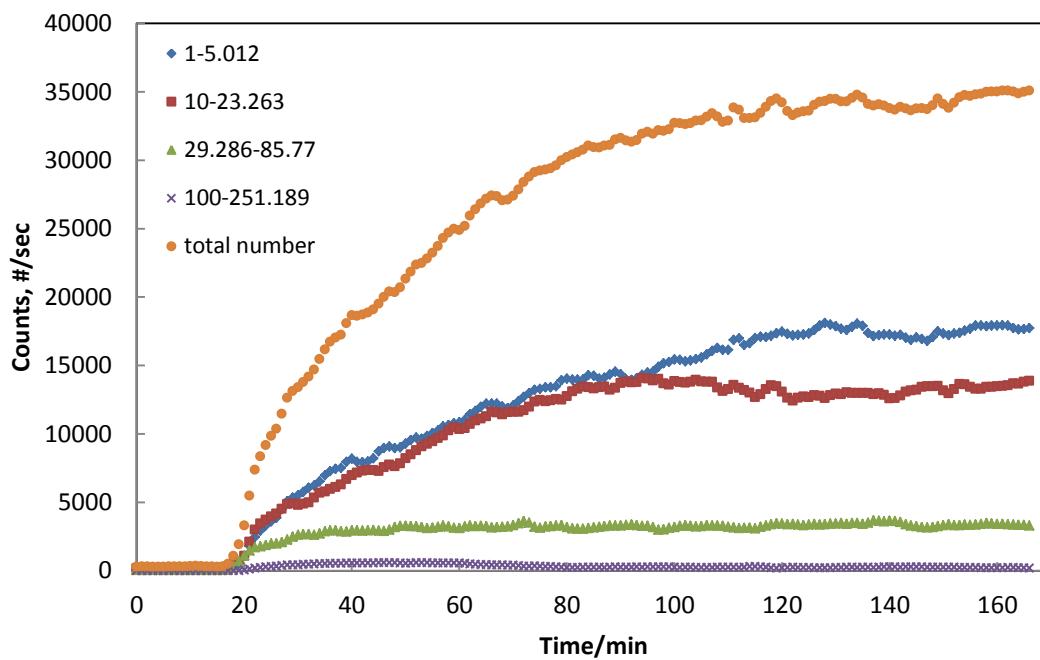
(a) Sample 1: 4 mL·min^{-1} + 4 mL·min^{-1}
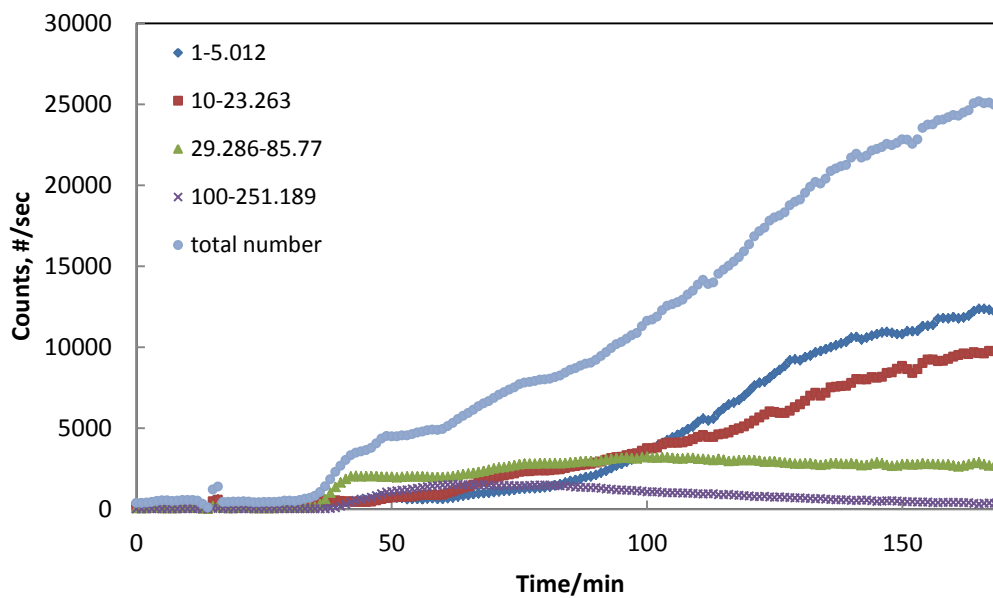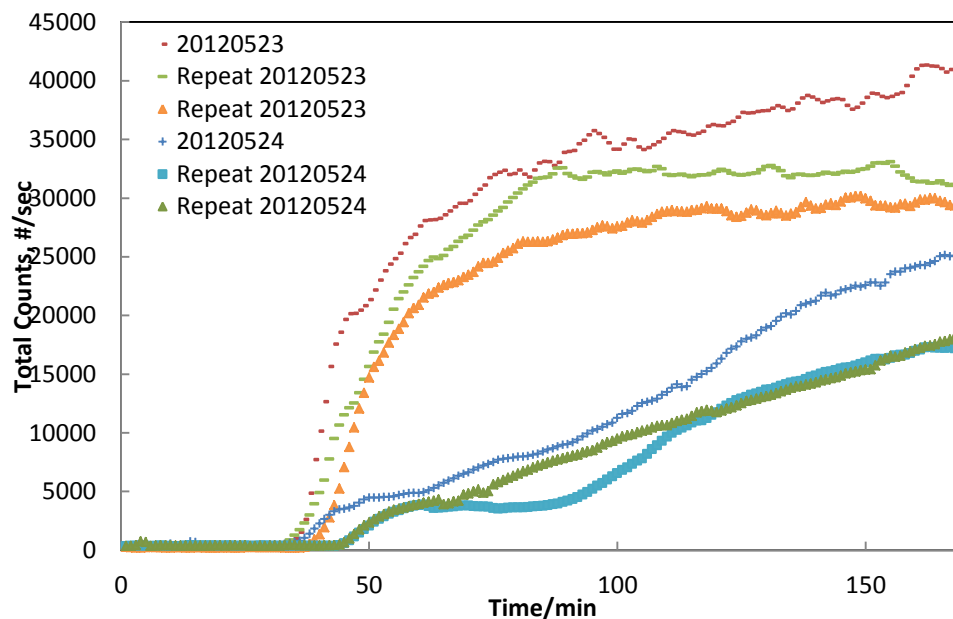
(b) Sample 2: 10 mL·min^{-1} + 4 mL·min^{-1}

(c) two repeat experiments following the same conditions with Sample 1 and
Sample 2, respectively

Figure 6.6 The FBRM results of 1L un-seeded experiments for determination of the seed loading
(the range of sizes for the FBRM counts is μm): (a) Sample 1: 4 mL·min^{-1} + 4 mL·min^{-1}; (b) Sample 2:
10 mL·min^{-1} + 4 mL·min^{-1}; (c) two repeat experiments following the same conditions with Sample 1
and Sample 2, respectively.

The un-seeded tests demonstrated the influence of the initial amount of seed
crystals on the final product (Figure 6.7). As can be seen from the XRD pattern
results, if the feed rate was changed from 10 mL·min^{-1} to 4 mL·min^{-1} when the
total counts number reached 5000, the crystallinity of the product was better.
Therefore, in order to get the appropriate amount of seeds, in the following
experiments, the seeds obtained from the anti-solvent re-crystallization method
were added into the crystallizer directly and the reactants feed only began when
the total counts number reached 3000 - 5000, then the change of the weight
was weighed to obtain the optimum amount of seeds. When using this method,
the seed obtained by anti-solvent re-crystallization method was assumed to be
the same as the seeds produced by itself during the beginning of reactive
crystallization process, because it was difficult to obtain the profile of the seeds
produced using faster feed rate at the beginning of the reactive crystallization

when the FBRM counts reach 5000 #/s. Two repeat experiments were carried out to further verify that the seed amount obtain from this replacement process (using the seeds obtained from anti-solvent re-crystallization to replace the seeds produced by the reaction itself) under this assumption could produce high quality product.
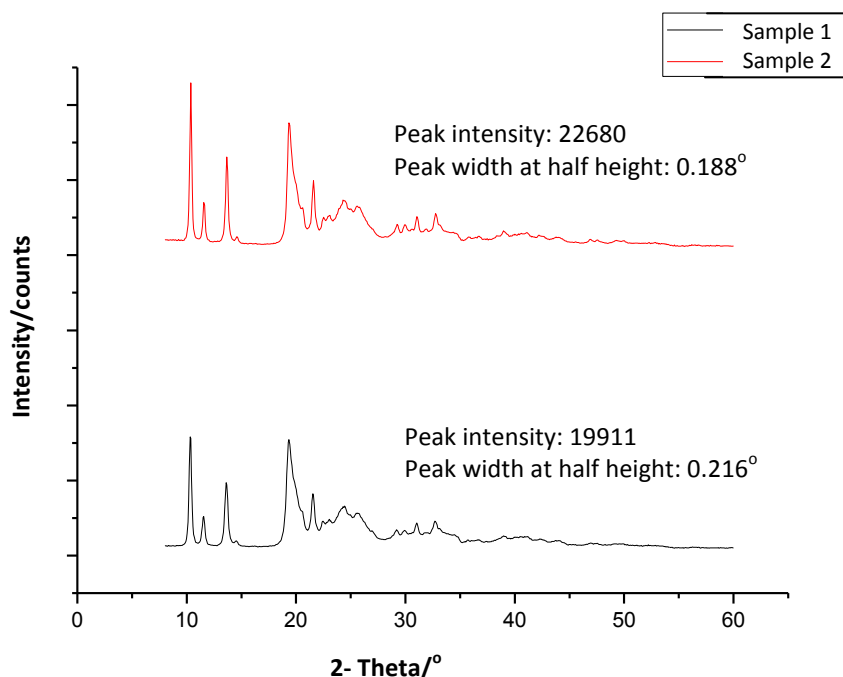
Figure 6.7 The XRD pattern of 1L un-seeded experiments for determination of the seed loading during the optimization of reactive crystallization process: black line – Sample 1: 4 mL·min^{-1} + 4 mL·min^{-1}; red line – Sample 2: 10 mL·min^{-1} + 4 mL·min^{-1} (peak intensity and peak width at half height of peak between 9° to 10.5^{o} were chosen to present the crystallinity).

As can be seen from the results of the seeded tests (Figure 6.8), total counts number were controlled below 30000 for all cases, and the optimal seed amount by weighing method was 0.407 g. Compared with 0.3 g of seeds calculated by Equation (6.1) in the previous discussion, this big different amount of seeds showed that secondary nucleation phenomena cannot be ignored in reaction crystallization processes of sodium cefuroxime. In fact, for such a rapid crystallization process, it was difficult to completely avoid secondary nucleation

phenomena. Even manipulating and optimizing the amount of seeds to be used can only play a supporting role.
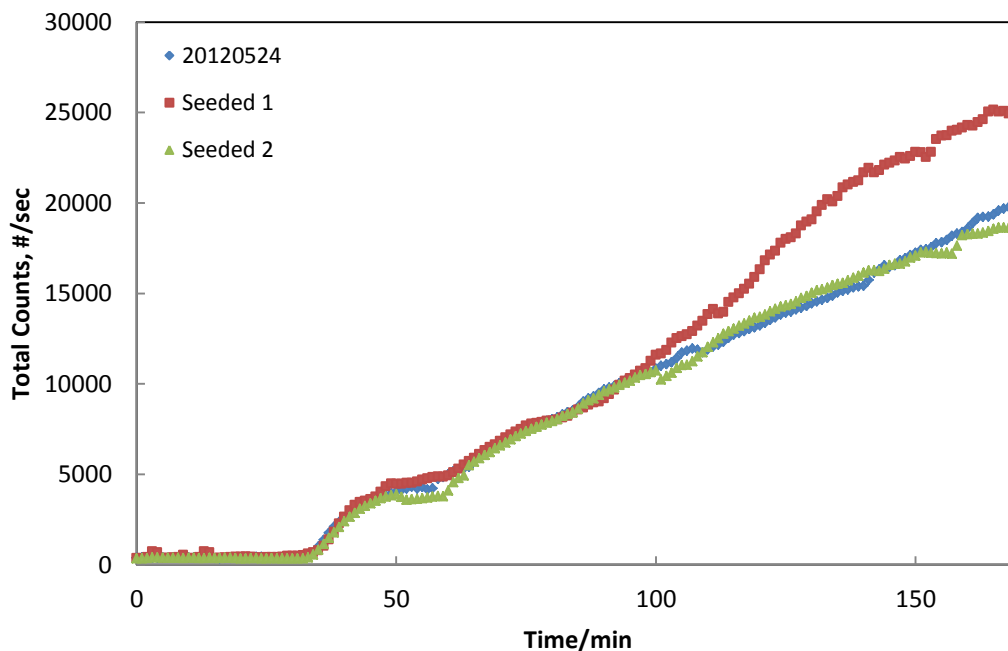
Figure 6.8 The FBRM results of two 1L seeded reactive crystallization processes comparing with Sample 2 (10 mL·min^{-1} + 4 mL·min^{-1}, un-seeded experiment) for determination of the seed loading during the optimization of reactive crystallization process.

6.3 Product Analytical Profile

After the above optimization experiments, the optimized operating conditions were:

- Temperature: 20 - 25 °C
- The feed rate: 4 mL·min^{-1}
- The stirring speed: 80 rpm
- Seeds: 0.407 g obtained from the anti-solvent re-crystallization process

Then, these optimized operating conditions were used to do three repeated tests (Sample 3, Sample 4 and Sample 5) (Table 6.3), and the test samples

were analyzed by XRD (Figure 6.9), *Morphologi* G3 (Figure 6.10) and SEM (Figure 6.11).

Table 6.3 The operating conditions of samples for parameter optimization in 1L reactor.

Batch No	Operating Conditions
Sample 3	Temperature: 20 - 25 °C, The feed rate: 4 mL·min^{-1}, The stirring speed: 80 rpm, the amount of seeds:0.407 g
Sample 4	Temperature: 20 - 25 °C, The feed rate: 4 mL·min^{-1}, The stirring speed: 80 rpm, the amount of seeds:0.407 g
Sample 5	Temperature: 20 - 25 °C, The feed rate: 4 mL·min^{-1}, The stirring speed: 80 rpm, the amount of seeds:0.407 g
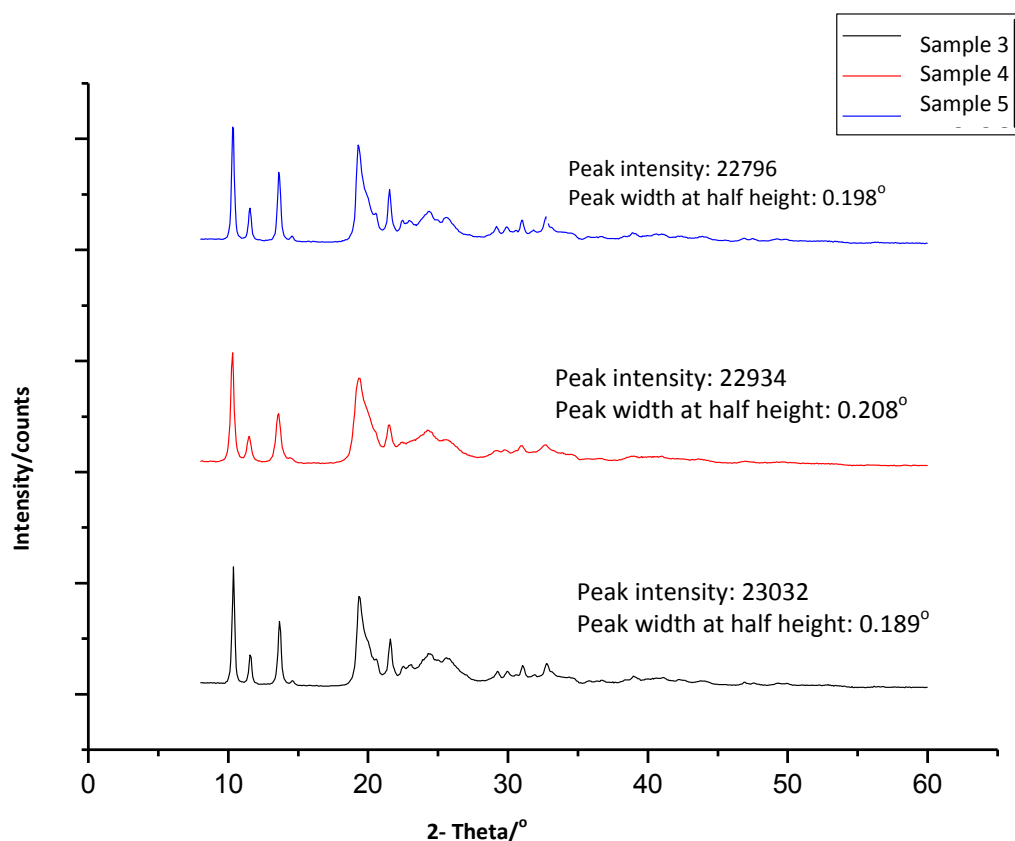
Figure 6.9 The XRD pattern of 1L repeated optimization experiments (peak intensity and peak width at half height of peak between 9° to 10.5° were chosen to present the crystallinity).

(a) Sample 3 (8.5 μm)   (b) Sample 4 (8.4 μm)

(c) Sample 5 (8.6 μm)
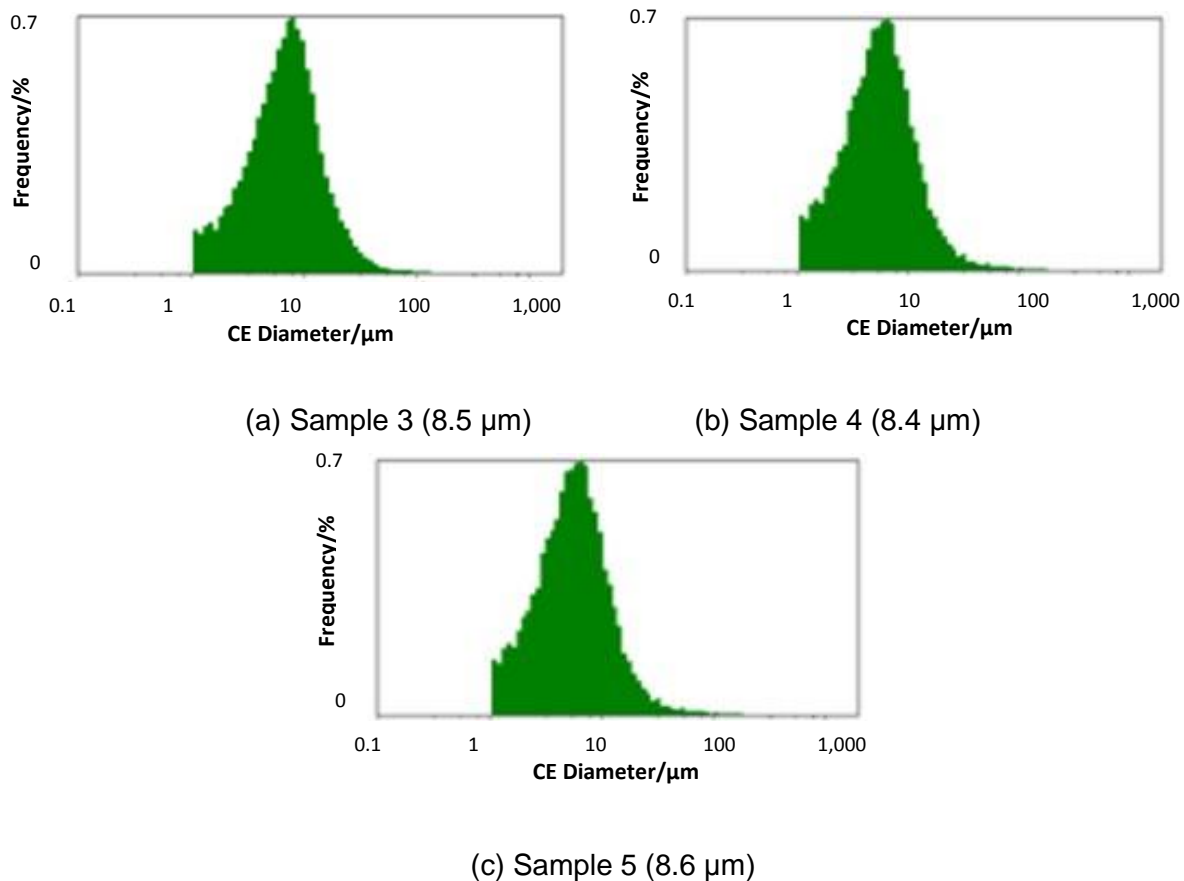
Figure 6.10 The *Morphologi* G3 of 1L repeated optimization experiments.
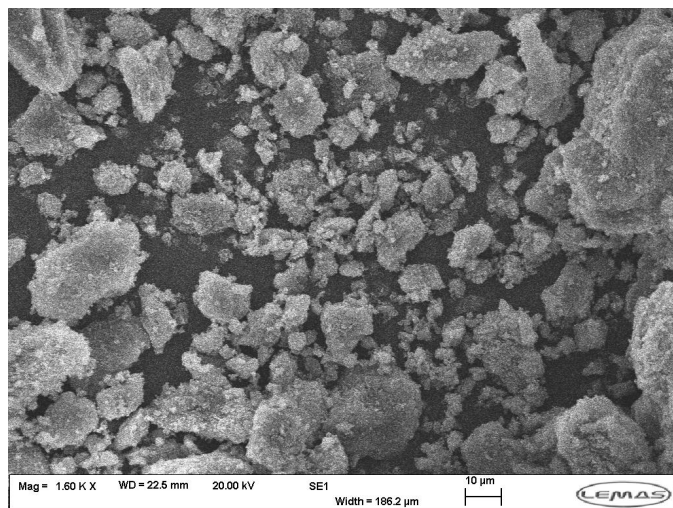
Sample 3

Figure 6.11 The SEM of 1L repeated optimization experiments (the optimized operating conditions were: temperature: 20 - 25 °C; the feed rate: 4 mL·min^{-1}; the stirring speed: 80 rpm; seeds: 0.407 g obtained from the anti-solvent re-crystallization process).

As can be seen from the results of the *Morphologi* G3 (Figure 6.10) and SEM (Figure 6.11), the product still had aggregation phenomena, but the mean size and size distribution were improved. The XRD pattern (Figure 6.9) showed the improvement of the crystallinity of the product. It can be concluded that simple changes of the operating parameters had limited effect on the product quality.

6.4 Final Remarks

1. The size of the product obtained by the reactive crystallization was larger than that obtained by the anti-solvent re-crystallization process. This improvement was conducive to the downstream processes.

2. For the reactive crystallization, the rapid crystallization process, serious aggregation phenomenon and secondary nucleation phenomena are inevitable. Therefore, some traditional theory, also includes the reactor established based on it, cannot work well. In order to further improve the crystallinity, in the following chapters, the reactor and process were designed and scaled-up.

3. The optimized operating parameters were not exactly the best parameters but the most suitable parameters for industrial production. After considering multi-conditions, only the parameters which were most favourable to the industrial scale were chosen for scale-up.

Chapter 7

Impinging Jet Feed Probe Design and Scale-up

7.1 Introduction

The conventional reactor and the feed mode designed for the slow crystallization process is widely used in the purification of APIs. The advantage of this type reactor is easy to operate, while it is also a process for producing large, low surface area particles. However, if the compounds require high surface area because of high bioavailability, this slow crystallization process must require subsequent high intensity milling, which may result in yield loss, noise and dust generation, as well as unwanted personnel exposure. Furthermore, the mixing effect of this conventional reactor is poor. It will need a relative long time to achieve the sufficient mixing to allow the reaction to complete. The mixing time is not a major concern in the design of a precipitation process when the precipitation kinetics are much slower than the time scale of mixing. However, in those very rapid and occur under high supersaturation conditions precipitation process, a lack of rapid mixing in the reactor can drastically effect the properties of the end product including crystal size distribution, morphology and purity. Obviously, the traditional reactor has limited the product further improvement.

The organic reactive synthesis process has higher requirements for the mixing time. This is because the bonding forces in organic crystal lattices generate a much higher frequency of amorphous than those found in highly ionic inorganic solid, "oiling out" of supersaturated material is not uncommon, and such oils often solidify without structure. So we need to find a new method to achieve high intensity micromixing of fluids so as to form a homogeneous composition prior to the start of nucleation.

As a result, mixing models for reactive crystallization processes have been the subject of studies in literature (Garside and Tavare, 1985; Pohorecki and Baldyga, 1983). A very promising technique to shortening the mixing time in a reactive crystallizer is a design using jet mixers (Careno et al., 2012; David J. Am Ende et al., 2003; Hacherl et al., 2003; Lindrud et al., 2001; Liu et al., 1990; Midler et al., 1989; Midler et al., 1994; Tamir and Kitron, 1987). In the design, two liquid streams of reactants form narrow, coplanar jets at high velocities impinging upon each other within a small mixing zone. Study on jet mixing as a technique for reactive crystallization was still limited, in particular for crystallization of pharmaceuticals. Midler et al. (Midler et al., 1989; Midler et al., 1994) tested a jet mixer for rapid precipitation of several pharmaceutical compounds. They found that the mixing intensity in the jet mixer was helpful in rapidly achieving good mixing and uniformly high supersaturation environment, which led to a high quality final product with superior crystallinity and purity. Mahajan and Kirwan (Mahajan and Kirwan, 1996) reported that the use of a two-impinging-jets precipitator could deliver rapid micromixing and the level of micromixing in the precipitator affected the crystal size distribution of the precipitated product (Lovastatin). By adding a sonication probe closed to the impinging point, Lindrud (Lindrud et al., 2001) produced submicron-sized crystals of several pharmaceutical compounds which had great stability and purity. After that, David J. Am Ende (David J. Am Ende et al., 2003) and Hacherl (Hacherl et al., 2003) proposed that using impinging-jet crystallization could produce the product with desired particle size characteristics. Woo (Woo et al., 2009, 2011) also simulated the crystal size distribution in a confined impinging jet crystallizer by computational fluid dynamics method to provide further understanding of this process.

In the previous experiments (chapters 5 and 6), we have already selected a suitable method for production of the seed, and we also optimized the reactive crystallization process parameters (operating conditions and the amount of seeds). In this chapter, the impinging jet mixer was used and scaled-up to

further optimize this reactive crystallization process according to its characteristics.

7.2 Methods and Apparatus

7.2.1 Reactive Crystallization Process

Reactive crystallization of sodium cefuroxime has three main features that have dictated our design of the process: the rapid reaction rate, very low solubility of sodium cefuroxime in the solution, and the huge supersaturation as a result of the above two factors. In addition, in the reactor design, other factors also need to be taken into account such as the time scales of crystal growth and reactions, i.e., crystal growth is not as fast a process as the reaction, and crystal growth mechanisms in the process, i.e., the crystal growth is likely to follow an aggregation mechanism rather than a surface growth model or a combination of the two mechanisms. Based on these considerations, a design of a combination of an impinging jet mixer and a stirred tank crystallizer was proposed and optimized in this study, and further scaled-up from 1L to 10L scales. The impinging jet mixer can achieve high intensity micromixing of fluids so as to form a homogeneous compound prior to the start of nucleation. This technology permits direct crystallization of the high surface area particles with high purity and great stability under high supersaturation, which is favoured by reactive crystallization processes (David J. Am Ende et al., 2003; Lindrud et al., 2001; Midler et al., 1994).

As mentioned before, it is believed that both mechanisms, i.e. the seed crystals grow in the supersaturated solution and also aggregate with freshly nucleated material, affect the increase of particle size. In this study, it is assumed that the crystal growth is likely to follow an aggregation mechanism rather than a surface growth model. The injection nozzles should be placed as close as possible to the stirrer of the stirred tank crystallizer, the logic behind this proposal is that the formed nuclei or the small particles can be immediately dispersed in the slurries of the stirred tank crystallizer where crystals are

growing so that these nuclei or small particles leaving the jet nozzles will move to and grow on the surfaces of the growing crystals, rather than the nuclei and small particles themselves further aggregate. The mixture stays in the tank crystallizer for a desirable time period under well-mixing conditions to allow crystals to grow (or aggregates).

The impinging jet mixer and 10L rig used for reactive crystallization process optimization and scale-up are illustrated in Figures 7.1 and 7.2. The 1L rig was the same as the one used to prepare seeds using the anti-solvent re-crystallization process, by only replacing the focused beam reflectance measurement (FBRM) probe (Saleemi et al., 2012c; Yu et al., 2004) with an attenuated total reflectance-Fourier transform infrared (ATR-FTIR) probe (Groen and Roberts, 1999). In the anti-solvent re-crystallization process, ATR-FTIR was used for monitoring the supersaturation. In the reactive crystallization process, FBRM was used to monitor crystallization processes and to provide qualitative and quantitative information about nucleation and crystal growth (Doki et al., 2004; Saleemi et al., 2012b).

The 1L and 10L tank reactors were both cylindrical in shape with a jacket to control the reaction temperature by water/oil circulator. The diameter and height of the 1L reactor were 10 cm and 12 cm, respectively. The impeller in the 1L reactor was 45° pitched blade impeller with the diameter and height of 5 cm and 2 cm, respectively. The diameter and height of the 10L reactor were 20 cm and 30 cm, respectively. The impeller in the 10L reactor was radial - flow blade turbine impeller with the diameter and height of 14 cm and 5.5 cm, respectively. The impinging jet probe was set-up with the help of Dr.Caiyun Ma and Mr. Steve Caddick (70 % works including the drawing and set-up). The determination of the tube diameter and the selection of the pump were done by me (in section 7.2.2)
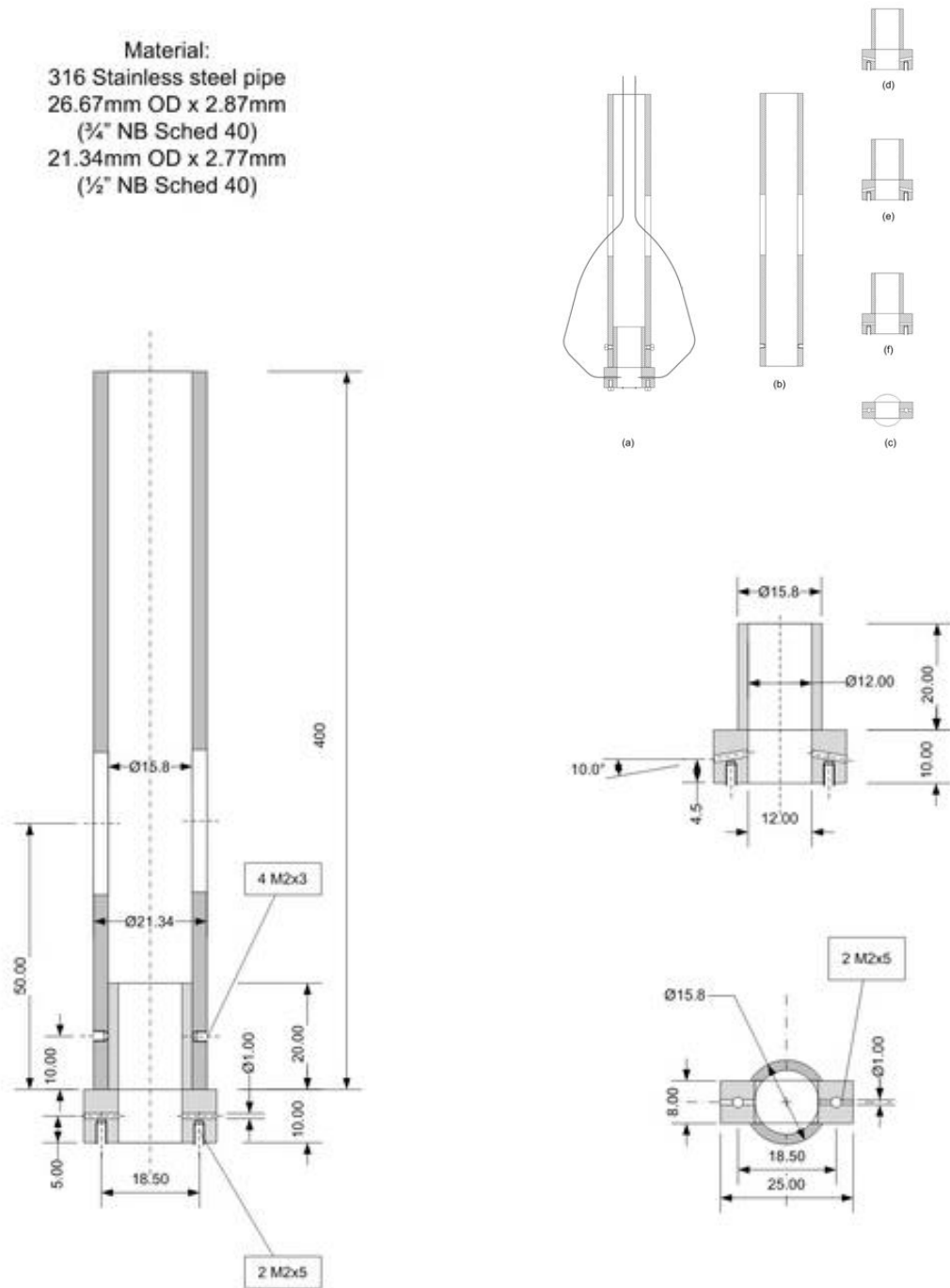
Figure 7.1 The schematic diagram of the impinging jet mixer: (a) the schematic structure of the impinging jet mixer; (b) the schematic structure of the probe tube; (c) the schematic structure of the bottom block holder; (d) 10° downward jets; (e) 10° upward jets; (f) parallel jets (Set-up with the help of Dr.Caiyun Ma and Mr. Steve Caddick).
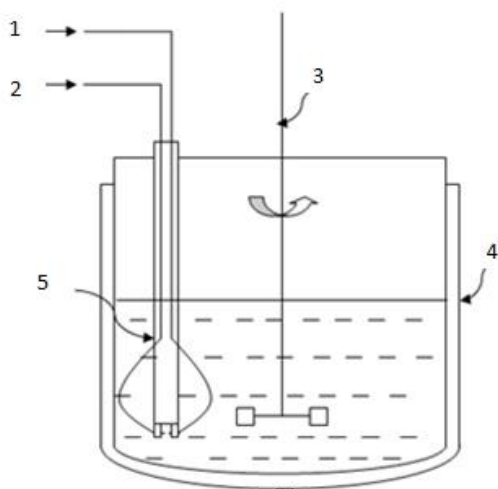
(a)

(b)

Figure 7.2 The 10L rig: (a) the schematic diagram (1 – the sodium lactate solution feeding; 2 – the acid cefuroxime solution feeding; 3 – the IKA EUROSTAR digital stirrer; 4 – the 10L tank reactor with a jacket; 5 – the impinging jet mixer); (b) the impinging jet mixer (Set-up with the help of Dr.Caiyun Ma and Mr. Steve Caddick).

7.2.2 Pressure Drop

In the design of an impinging jet mixer probe, the pressure drop was the main parameter for the selection of the pump and the determination of the nozzle

diameter (Beggs and Parker, 1971). The pressure drop was composed of pipe friction pressure drop, static pressure drop and velocity pressure drop. The formula is as follows,

$$\Delta P = (Z_2 - Z_1)\rho g * 10^{-3} + \frac{(u_2^2 - u_1^2)}{2}\rho * 10^{-3} + \sum h_f(\rho * 10^{-3}) \qquad (7.1)$$

$$\sum h_f = \lambda \frac{(L + \sum L_e)}{D} \frac{u^2}{2} \qquad (7.2)$$

or

$$\Delta P = \Delta P_S + \Delta P_N + \Delta P_f \qquad (7.3)$$

where ΔP is the total pressure drop of the piping system, kPa; ΔP_S is the static pressure drop, kPa; ΔP_N is the velocity pressure drop, kPa; ΔP_f is the friction pressure drop, kPa; Z_1 is the height of the pipeline beginning, m; Z_2 is the height of the pipeline ending, m; g is the gravity acceleration, 9.81 m·s^{-2}; u_1 is the fluid flow rate of the pipeline beginning, m·s^{-1}; u_2 is the fluid flow rate of the pipeline ending, m·s^{-1}; ρ is the fluid density, kg·m^{-3}; h_f is the friction energy loss, J·kg^{-1}; L is the pipe length, m; L_e is the equivalent length of fittings, m, and D is the pipe inner diameter, m.

The flow pattern in the pipeline also had a significant impact on the pressure drop. The flow pattern involves the laminar flow and the turbulent flow, the criteria for determining the fluid flow pattern is Reynolds number. The formula is as follows,

$$Re = \frac{Du\rho}{\mu} \qquad (7.4)$$

where Re is Reynolds number and μ is fluid viscosity, mPa·s.

The friction coefficient (λ) in Equation (7.2) is a function of the Reynolds number and the pipe relative roughness. The formula is as follows,

$$\lambda = \frac{64}{Re} \qquad (7.5)$$

The formula of pipe friction pressure drop is as follows,

$$\Delta P_f = \frac{32 \mu u L}{D^2} \tag{7.6}$$

The formula of the static pressure drop is as follows,

$$\Delta P_S = (Z_2 - Z_1)\rho g * 10^{-3} \tag{7.7}$$

The formula of the velocity pressure drop is as follows,

$$\Delta P_N = \frac{(u_2^2 - u_1^2)}{2}\rho * 10^{-3} \tag{7.8}$$

According to the desired flow rate (4 mL/min for acid cefuroxime and 1 mL/min for sodium lactate in 1L crystallizer, and 40 mL/min for acid cefuroxime and 10 mL/min for sodium lactate in 10L crystallizer) and feed speed (10 m/s), based on the equation (7.9),

$$Q = \pi r^2 v \tag{7.9}$$

where r is the diameters of the nozzle, v is the feed speed and Q is the flow rate, the diameters of two nozzles were 0.13 mm and 0.065 mm in the 1L crystallizer, 0.3 mm and 0.15 mm in the 10L crystallizer, and the theoretical pressure drops in the tubes with an identical tube length of 500 mm were roughly 9.5 MPa and 38 MPa in the 1L crystallizer, 1.8 MPa and 7.1 MPa in the 10L crystallizer, respectively. To meet the required high pressure drops and also the flow rates, the 307 Piston Pump with a high pressure limit of 60 MPa was selected.

7.3 Design of Impinging Jet Mixer Nozzles

Midler (Midler et al., 1994) suggested that the nozzles of the impinging jet mixer could have a slight downward angle of about 10° To decide the best angle and spacing of the nozzles, three angles and two spacing (6.78 mm, 11.76 mm) were chosen as shown in Table 7.1. Taking into account the working range of the pumps, the feed speeds of 10 m·s⁻¹, 15 m·s⁻¹, 20 m·s⁻¹ were selected as the feed speed tests (Table 7.1).

Table 7.1 Design Parameters of the Impinging Jet Mixers.[*]

Angle	Spacing (mm)	Amount of Seed (g)	Feed Speed (m·s^{-1})
10° Upward (A)	6.87 (D)	None (F)	10 (H)
Parallel (B)	11.76 (E)	0.407g (G)	15 (I)
10° Downward (C)			20 (J)

[*] **The letters A B and C will be used in Figure 7.3 7.4 and 7.5 to denote the designs. The diameters of two nozzles were 0.13 mm and 0.065 mm in the 1L crystallizer, 0.3 mm and 0.15 mm in the 10L crystallizer.**

7.3.1 10° Upward Jets

The nozzle arrangements of 10° upward jets were tested in this study with two spacing distances. As can be seen from Figure 7.3, from an overall point of view, the product crystallinity with a wider spacing was higher than the narrow one. This might be due to that the wider spacing increased the location of the collision point of the two fluids, hence resulting in more liquid to have the opportunity to collide with the upper part of the mixer probe and then mix with each other when flowing downward. Furthermore, regardless of the spacing size, basically, the product with a slower feed speed had a better degree of crystallinity, and the seeded case was better than the un-seeded one.
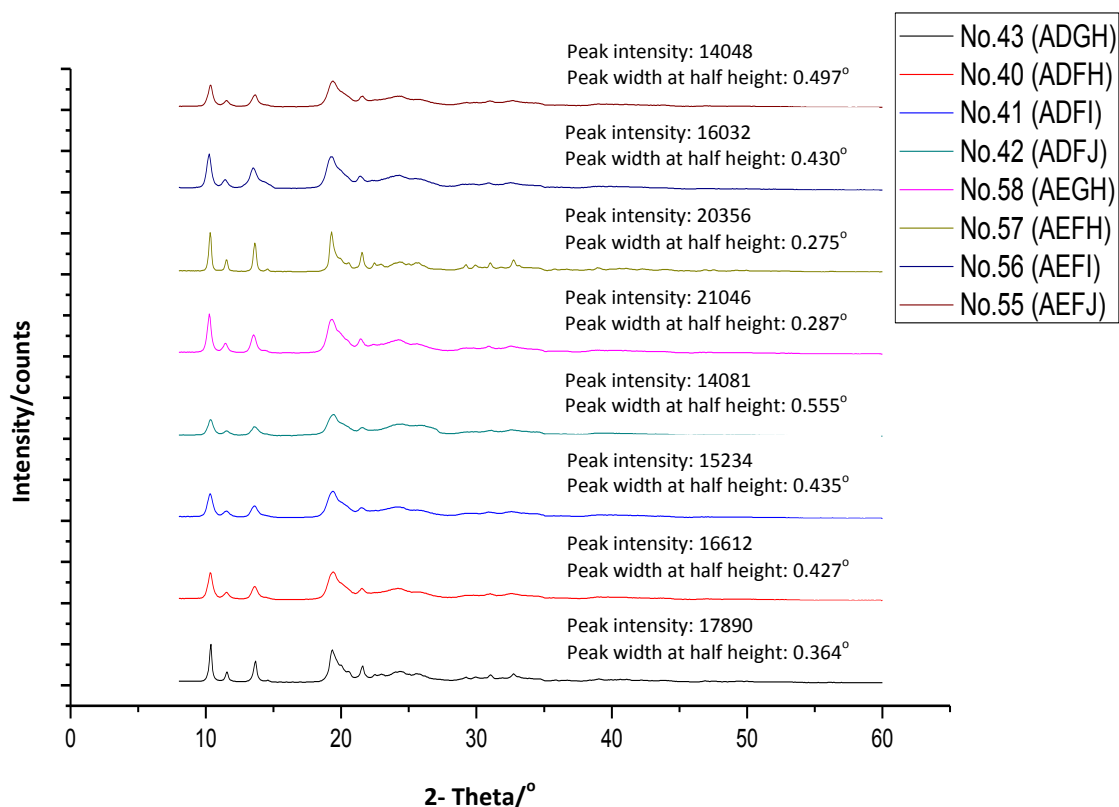
Figure 7.3 The XRD pattern of sodium cefuroxime obtained from the 1L crystallizer with 10° upward jets(peak intensity and peak width at half height of peak between 9° to 10.5^o were chosen to present the crystallinity) (the meaning of the monogram in the label table on the right side can be seen in Table 7.1, e.g. ADGH means the angel of the nozzles is 10° upward (A), the spacing between the two nozzles is 6.87 mm (D), the amount of seeds is 0.407 g (G), and the feed speed is 10 m·s^{-1} (H)).

7.3.2 Parallel Jets

Parallel jets were introduced by many researchers in literature, and also used in many experimental processes (David J. Am Ende et al., 2003; Lindrud et al., 2001; Woo et al., 2009). Theoretically, this feed method can guarantee the two jet fluids to have a frontal collision with their maximum speeds, hence resulting in, possibly, the best mixing effectiveness. However, for the synthesis process of sodium cefuroxime or other drugs, the biggest drawback of this jet configuration is that the parallel jets are very easy to cause product accumulated at the outlet of one nozzle with smaller diameter. The main reason was that the two jets did not have equal feed amounts of the two fluids in this

study. Since the feed volume ratio of the two fluids was 1 : 4 (sodium lactate solution: acid cefuroxime solution), under the same feed speed, the momentum of the less amount fluid feed was half of the larger one, which caused the collision point of two jet streams gradually to be moved to the tube outlet of a fluid with the smaller diameter and less feed amount (the tube for feed sodium lactate solution), eventually leading to the product accumulated slowly at this tube outlet.
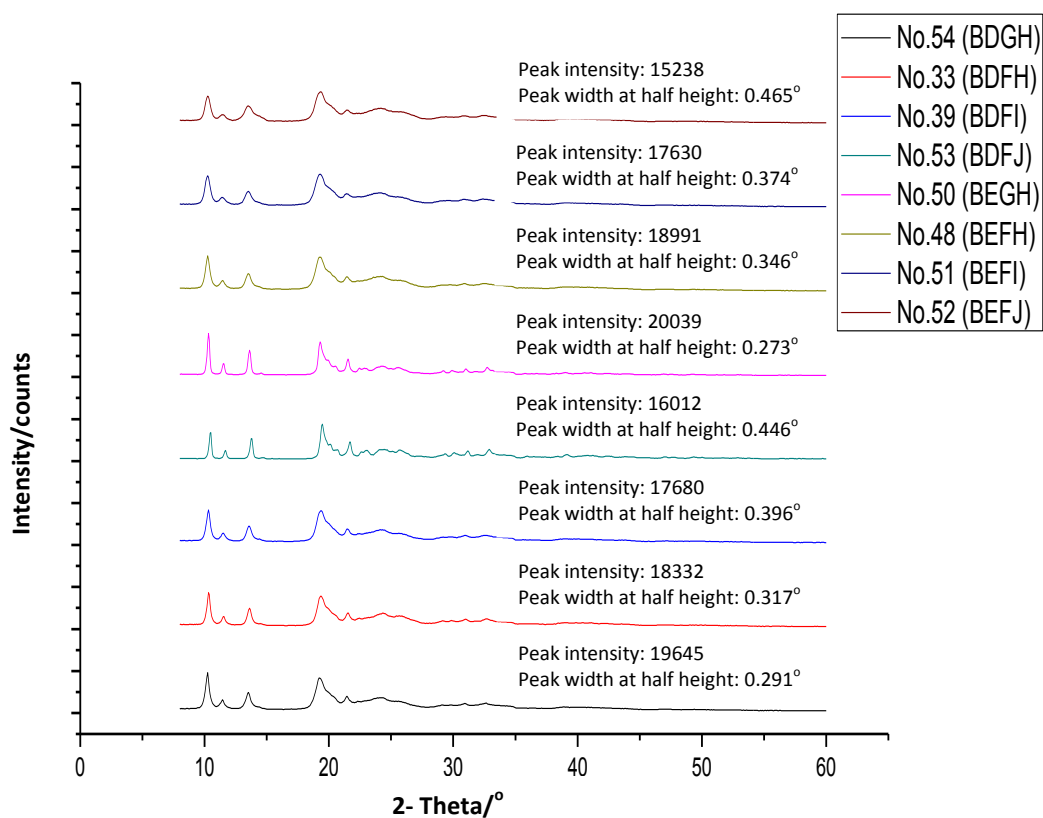
Figure 7.4 The XRD pattern of sodium cefuroxime obtained from the 1L crystallizer with parallel jets (peak intensity and peak width at half height of peak between 9° to 10.5^o were chosen to present the crystallinity) (the meaning of the monogram in the label table on the right side can be seen in Table 7.1).

The XRD pattern of the products obtained from the parallel jets configuration were almost as the same as those obtained with the 10° upward jets (Figure 7.4). The crystallization process with wide spacing produced almost identical product crystallinity when the process had a narrow spacing. For parallel jets,

the impact of mixing was only related to the feed speed, so in the case of high feed speed, the change of spacing had little effect on the experimental results. Furthermore, the product with the slower feed speed also had a better degree of crystallinity, and the seeded case was, again, better than the un-seeded one.

7.3.3 10° Downward Jets

To avoid clogging, a design with 10° downward feed jets was selected in most of the literature (Choo and Kang, 2007; Dehkordi et al., 2009; Li and Ashgriz, 2007; Saien and Moradi, 2012). This feed method can avoid the two fluids from directly frontal collision. Although the collision rate would decline, when the momentum difference between the two fluids was large, it could avoid one fluid stream pushing the collision point of the two streams to the other stream.

The XRD pattern with 10° downward jets were better than that with the 10° upward and parallel jets (Figure 7.5). The product crystallinity of crystals obtained with a narrow spacing was better than that with the wide one. This may be due to that the jets are submersed in the liquid, thus the wide spacing might cause the encountering speeds of the two fluids to be decreased because of the liquid resistance in the crystallizer. This feed method was neither like 10° upward jets that had the upper part of the mixer probe for collision to increase mixing, nor like the parallel jets that provided a frontal collision. Therefore, the collision effect had a significant effect on mixing effectiveness. Meanwhile, the product with a slower feed speed still had a better degree of crystallinity, and the seeded case was still better than the un-seeded one.
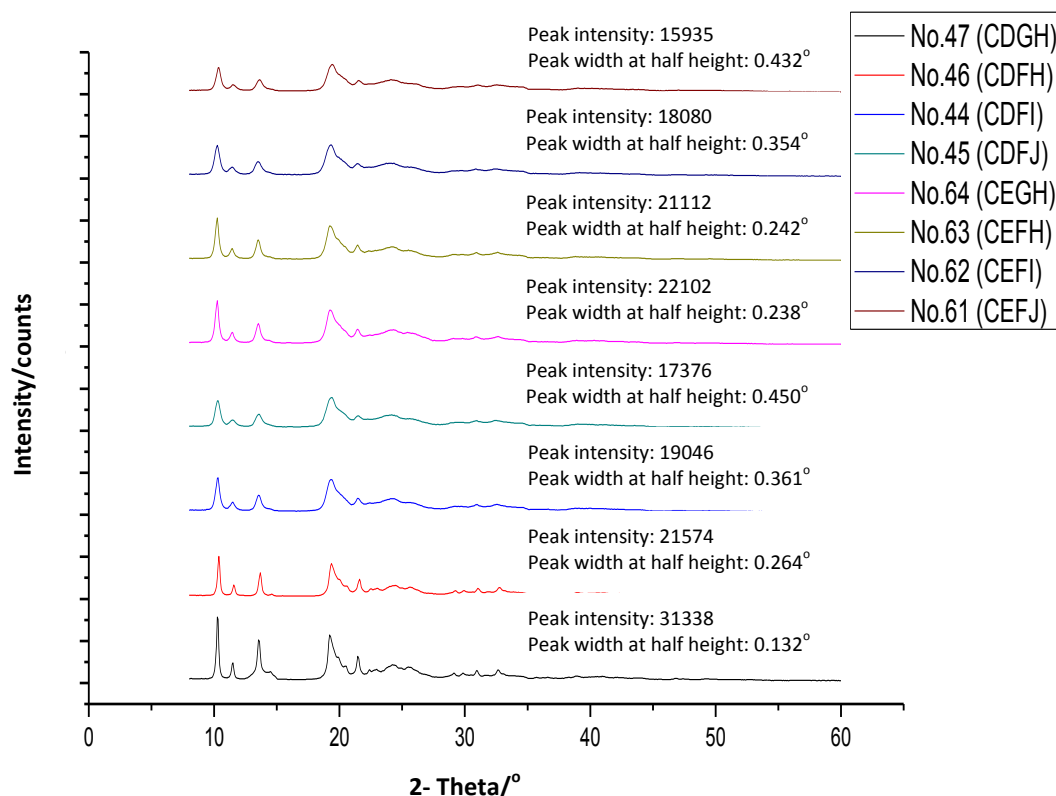
Figure 7.5 The XRD pattern of sodium cefuroxime obtained from the 1L crystallizer with 10° downward jets(peak intensity and peak width at half height of peak between 9° to 10.5^o were chosen to present the crystallinity) (the meaning of the monogram in the label table on the right side can be seen in Table 7.1).

7.3.4 Product Characterization

As mentioned in literature (Dehkordi and Ebrahimi, 2009; Mahajan and Kirwan, 1996), a high linear velocity could produce crystals with higher crystallinity. However, our conclusion was that a slower feed speed was a better choice for obtaining crystals with higher crystallinity, which might be because that the mechanism of sodium cefuroxime crystal growth is different. Several theories have been proposed to explain the mechanism of crystal growth (Kossel, 1934). The diffusion-reaction theory suggested that once an ordered crystal structure is formed by nucleation, the growth units (atoms, ions or molecules) can diffuse from the surrounding supersaturated solution to the surface of the nucleus and resulting in crystal growth. Based on the adsorption layer theory, particle growth

happens on pre-existing layers of atoms or molecules that adsorbed on crystals faces. Besides these theories, another phenomenon that causes the size increasing is called aggregation (Lu and Wang, 2006; Morgan et al., 2005). Solution hydrodynamics, static forces, and particle structures may all have effects on crystal aggregation. Meanwhile, aggregation can mainly happen in supersaturated solutions as it requires high levels of supersaturation to build the bonding between particles.

Sodium cefuroxime synthesis process, the combination of the reaction process and the crystallization process, is such a process which conducts under high levels of supersaturation. The huge supersaturation was firstly generated by the reaction because the product cannot be dissolved in solvents completely, and then the nuclei were generated, and further the growth process happened when the nuclei met the crystal seeds in the crystallizer. Besides the competition between the nucleation process and the growth process during this crystallization process, the kinetic of the reaction itself also directly affects the whole process by varying the supersaturation. In a traditional stirred tank crystallizer, the nucleation and growth processes were carried out at the same time and the same place. The impinging jet mixer designed in this study was to avoid the simultaneous existence of nucleation and growth processes by confining the nucleation process and the growth process within the corresponding nucleation area and the growth area. In the nucleation area, the impinging jet mixer was used to achieve fully mixing of reactants for reaction and to generate small nuclei. Then the impeller drove these small nuclei from the nucleation area to the growth area where the nuclei contact with the crystal seeds in the crystallizer for growth.

A very fast feed speed could force the two reactants to leave the nucleation area and enter the growth area before sufficient reaction happened, which leads to both the nucleation and growth processes took place in the same place just like the conventional crystallizers. Obviously, in order to use this newly-devised impinging jet mixer probe for obtaining high quality crystals, the

selection of a suitable feed speed is very important. Both the mixing effectiveness and the reaction kinetics should be considered. As long as it ensured that the reaction could be finished in the nucleation area, the faster the feed speed was, the better the product crystallinity obtained.

In addition, we also tested the configuration with the impinging jets being located above the liquid level of the stirred tank crystallizer, but unlike what was found by Hacherl (Hacherl et al., 2003) for calcium oxalate model system, the crystallinity of the obtained product was not satisfied which might be because that without the solvent resistance to the jet streams, the feed speed was too high to produce sufficient reaction.

7.4 10L Scale-Up

7.4.1 10L Scale-Up Experiments

In order to achieve industrialization, the scale-up process becomes one of the important final steps. Scale-up is to use the successfully optimized process in the laboratory small-scale reactor under the industrial production conditions, to verify the feasibility of this original process after amplification of reactor size, capacity etc. and to ensure the consistency of the processes. Therefore the scale-up process studies can verify, review and improve the laboratory process results, and provide the reliable production data, as well as the material quality and consumption for industrial production, and also resolve the problem failed to solve or have not yet been discovered at the laboratory stage.

Since a single pump cannot reach the required feed rate, three pumps have joined forces for the acid cefuroxime solution feeding. At beginning, the scale-up was based on the same feed velocity (10 m·s^{-1}) in the 1L crystallizer with a volumetric scaling-up factor of 10 while keeping all other operation parameters the same. The 10L scale-up experiments were conducted at room temperature and the parameters were as follows：

- Feed rate: 40 mL·min^{-1} for acid cefuroxime solution and 10 mL·min^{-1} for

> sodium lactate solution (10 times bigger than the 1L crystallizer based on the volume)

- Stirring speed: 80 - 100 rpm (the same as the 1L crystallizer)

- Feed speed: 10 m·s^{-1} (the same as the 1L crystallizer)

- Seed preparation: anti-solvent re-crystallization process (the same as the 1L crystallizer)

- Amount of seed: 4.07 g (10 times bigger than the 1L crystallizer based on the volume)

- Probe: 10° downward jets with 6.78 mm spacing (the same as the 1L crystallizer)

- The reactant ratio was enlarged tenfold.

Followed the above operating conditions, the crystalline state and crystal size distribution from the obtained crystals (Sample 1) was not as good as expected (Figure 7.6 and Figure 7.7). The biggest difference between the 1L and 10L crystallizers might be the paddle, which was much bigger in the 10L crystallizer. That meant that the paddle might have forced the reactants to leave the nucleation area too early, hence a sufficient reaction did not achieve. Therefore, a reduced stirring speed of 50 rpm was used to increase the residence time of the reactants in the nucleation area. With the reduced stirring speed, the results from experiment Sample 2 showed good crystalline state. The same operating conditions as experiment Sample 2 were repeated in experiments Sample 3, Sample 4 and Sample 5 with satisfactory results being obtained (Figure 7.6, 7.7 and 7.8).

Table 7.2 The operating conditions of samples for 10L scale-up experiments.

Batch No	Operating Conditions
Sample 1	Temperature: 20 - 25 °C, The feed rate: 40 mL·min^{-1}, Feed speed: 10 m·s^{-1}, The stirring speed: 80-100 rpm, the amount of seeds:4.07 g, with impinging jet probe
Sample 2	Temperature: 20 - 25 °C, The feed rate: 40 mL·min^{-1}, Feed speed: 10 m·s^{-1}, The stirring speed: 50 rpm, the amount of seeds:4.07 g, with impinging jet probe
Sample 3	Temperature: 20 - 25 °C, The feed rate: 40 mL·min^{-1}, Feed speed: 10 m·s^{-1}, The stirring speed: 50 rpm, the amount of seeds:4.07 g, with impinging jet probe
Sample 4	Temperature: 20 - 25 °C, The feed rate: 40 mL·min^{-1}, Feed speed: 10 m·s^{-1}, The stirring speed: 50 rpm, the amount of seeds:4.07 g, with impinging jet probe
Sample 5	Temperature: 20 - 25 °C, The feed rate: 40 mL·min^{-1}, Feed speed: 10 m·s^{-1}, The stirring speed: 50 rpm, the amount of seeds:4.07 g, with impinging jet probe

Peak intensity: 19984
Peak width at half height: 0.142°

Peak intensity: 21112
Peak width at half height: 0.131°

Peak intensity: 21376
Peak width at half height: 0.150°

Peak intensity: 21574
Peak width at half height: 0.124°

Peak intensity: 18338
Peak width at half height: 0.345°
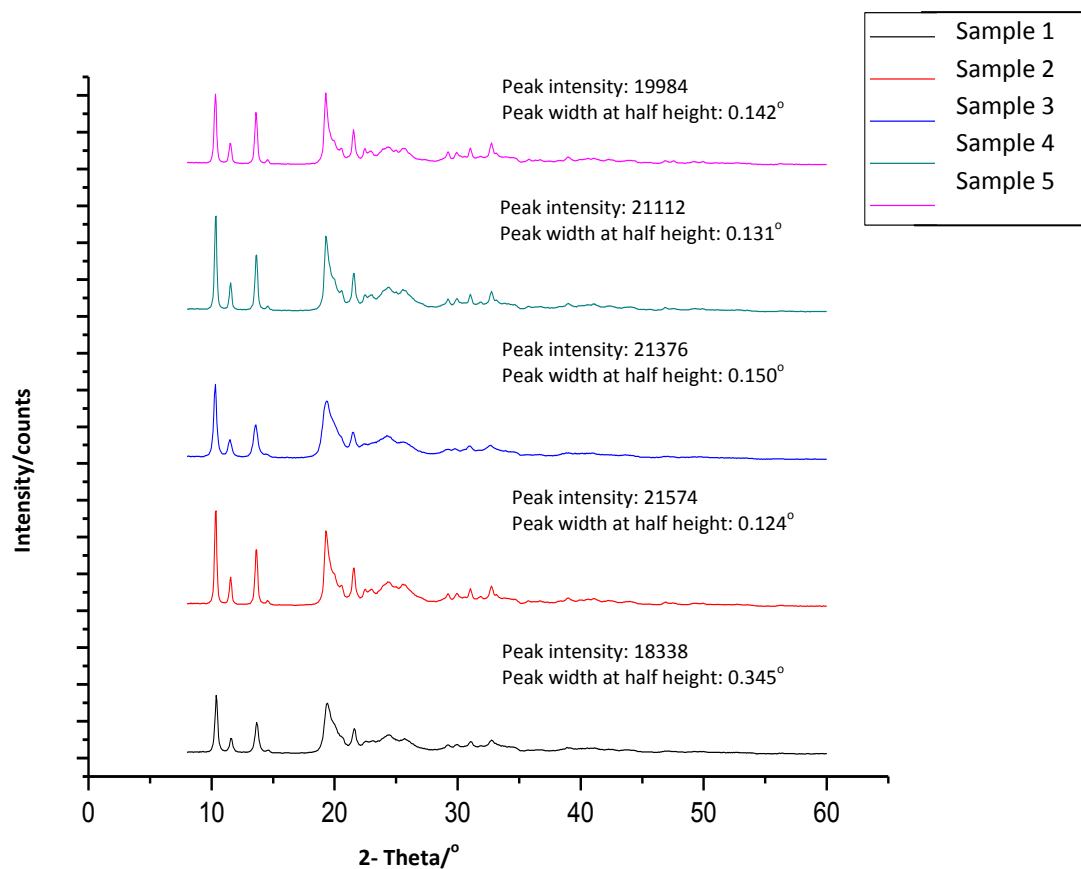
Figure 7.6 The XRD pattern for optimization of the 10L crystallizer (peak intensity and peak width at half height of peak between 9° to 10.5° were chosen to present the crystallinity).
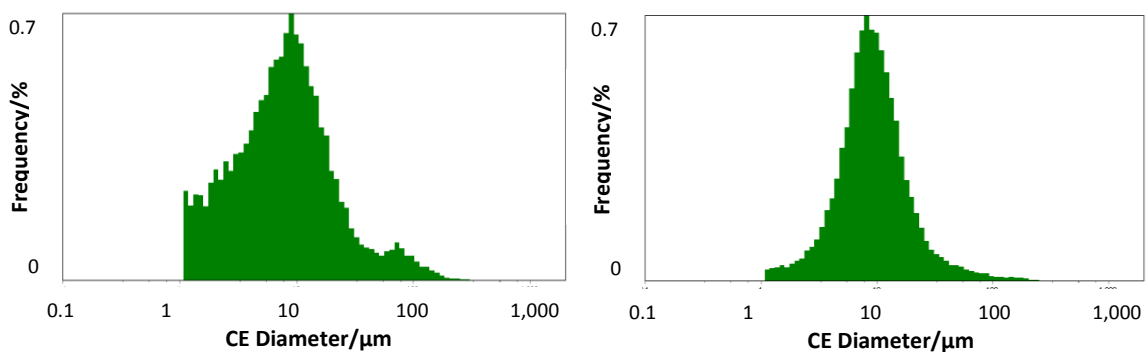
(a) Sample 1 (8.1 μm)　　　　　　　(b) Sample 2 (8.8 μm)
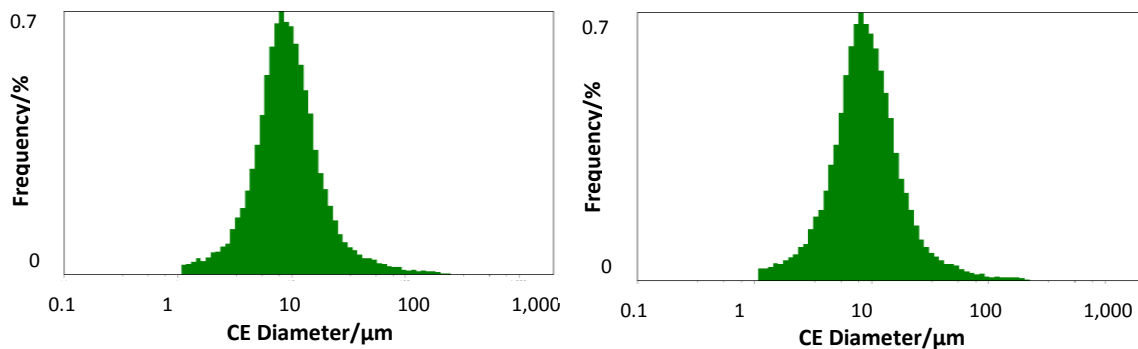
(c) Sample 3 (8.8 μm)　　　　　　(d) Sample 4 (8.7 μm)
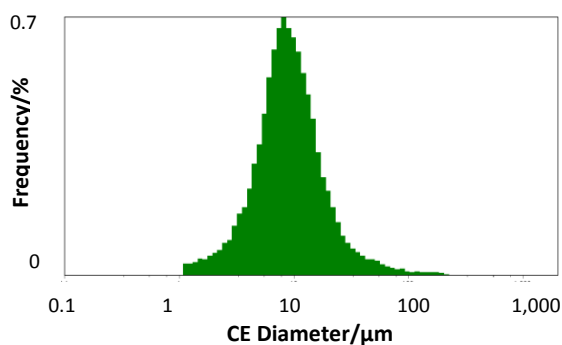
(e) Sample 5 (8.7 μm)

Figure 7.7 The *Morphologi* G3 results of sodium cefuroxime obtained from the 10L crystallizer: (a) Sample 1 (80 rpm); (b) Sample 2 (50 rpm); (c) Sample 3 (50 rpm); (d) Sample 4 (50 rpm); (e) Sample 5 (50 rpm).
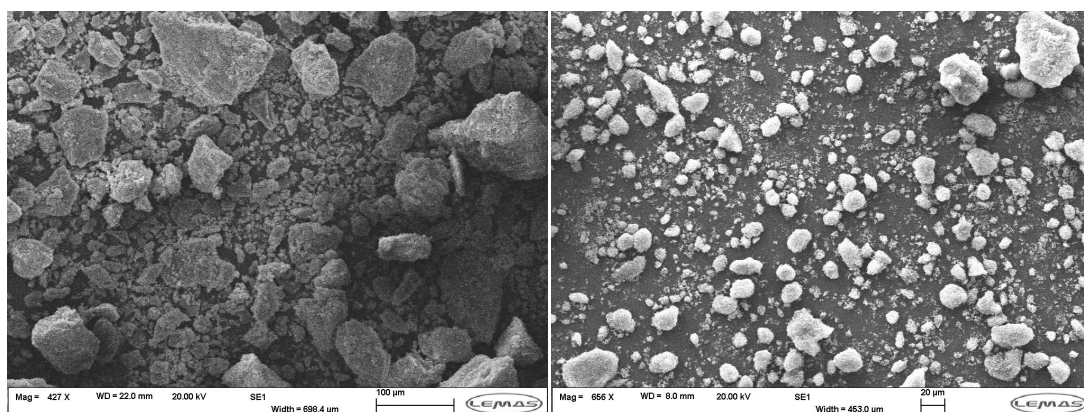
(a) Sample 1　　　　　　　　　(b) Sample 5

Figure 7.8The SEM images of sodium cefuroxime obtained from the 10L scale-up experiments: (a) Sample 1; (b) Sample 5.

7.4.2 Product Analytical Profile

From the *Morphologi* G3 results (Figure 7.7), it can be seen that the crystal size distribution of experiment No.88 was the widest one with the smallest mean crystal size and bimodal phenomenon. After reducing the stirring speed in experiments Sample 2, Sample 3, Sample 4 and Sample 5, narrow crystal size distributions, bigger mean crystal size and single peak could be obtained.

From Table 7.3, it can be seen that the products obtained with the impinging jet mixer probe, compared with the comparative one obtained from the industrial process (Sample 1), had lower water and impurity content. Sample 1 is a representative sample selected by the company. The amount of impurity content was less than the sum of impurity contents from both the raw material and the seeding crystals. These verified that the crystallinity was improved by using this new feed mode. Better crystal structure, besides reducing the defect of the crystal, could reduce the possibility of the moisture and impurities to be wrapped in crystals during the crystal growth process.

Table 7.3 Analysis Result of Sodium Cefuroxime Obtained from the 10L Scale-Up Experiments.*

Batch No	Water (%)	Color Grade	Content Measured by HPLC (%)
Sample 1	0.220	<Y-2#	94.43
Sample 2	0.203	<Y-2#	92.00
Sample 3	0.060	<Y-2#	94.36
Sample 4	0.189	<Y-2#	93.60
Sample 5	0.069	<Y-2#	93.19

* (1) Y means the color grade yellow

As can be seen from the stability results (Table 7.4), Under the condition of 60 $^{\circ}$C, the color grades obtained were at least two levels lower than the comparative one (lower color grade means more stability of the product).

Table 7.4 Stability Test Data of Sodium Cefuroxime Obtained from the 10L Scale-Up Experiments.*

Batch No	Color Grade (60℃)				
	0 day	3 days	5 days	7 days	10 days
Sample 1	<Y-2#	<Y-9#	<Y-10#	>Y-10#	>Y-10#
Sample 2	<Y-2#	<Y-5#	<Y-7#	<Y-8#	<Y-9#
Sample 3	<Y-2#	<Y-5#	<Y-8#	<Y-8#	<Y-9#
Sample 4	<Y-2#	<Y-5#	<Y-8#	<Y-8#	<Y-9#
Sample 5	<Y-2#	<Y-5#	<Y-7#	<Y-8#	<Y-9#

* (1) Y means the color grade yellow

7.5 Final Remarks

1. In the calculation of the pressure drop, it should be noted that the liquid flow pattern was laminar or turbulent. Flow pattern changes greatly affected the pressure generating manner, and thus affected the pressure drop.

2. During these scale-up experiments, the drying process has always been the key process affecting the product quality. In the old industrial process, the drying time was typically 2 hours, but after these tests, it was found that the drying time should be at least 5 hours to ensure that the product was completely dry. So that is, to the following industrial production, the more advanced drying equipment was needed or the drying time needed to be extended.

3. Although the crystallinity and stability of the product has improved after using the impinging jet feed probe, there should be a lot of room for progress. Not

only increasing the degree of crystallinity can improve the product quality, if the downstream can be enhanced, as well as the product packaging, the product quality should be further improved.

Chapter 8

Reactor Design of Continuous Reactive Crystallization Process and Scale-up

8.1 Introduction

In previous chapters, we have mentioned that the batch stirred-tank crystallizer had two significant drawbacks when used as a reaction crystallizer for rapid organic reactive crystallization processes (David J. Am Ende et al., 2003; Lindrud et al., 2001; Midler et al., 1994): Firstly, the mixing effectiveness is limited and, secondly, for batch type operation, periodic downtime is required.

These drawbacks made the optimization of the existing reaction crystallizer more valuable in many research areas. Tavare (Tavare, 1994, 2000) studied a process involving the elementary chemical reaction between two reactant species (Ng and Rippin) and subsequent crystallization of the product in a continuous crystallizer with pre-mixed feeds at the entry. Yin (Yin et al., 2000; Yin et al., 2001) also researched a reactive precipitation process in a continuous isothermal mixed suspension-mixed product removal crystallizer. For industrialization, Schoenecker (Schoenecker et al., 2013) implemented a comprehensive scale-up procedure for amine-functionalized UiO-66, which led to the development of a flow-through metal-organic framework synthesis process. They scaled up a continuous-flow reactive crystallization process by using a draft-tube-type reactor to optimize this process and powder XRD was used to examine the crystal quality. Compared with the batch type operation, the advantages of the continuous operation are apparent: firstly, the same amount of feed compound can be crystallized in significantly less volume via a continuous process rather than using a batch by batch method. Secondly, the continuous process enhances reproducibility of results because all the material crystallizes under consistent conditions.

By using process analytical technology (PAT) based on focused beam reflectance measurement (FBRM) and a stirred-tank crystallizer combined with a designed impinging jet mixer probe, synthesis of sodium cefuroxime was optimized and scaled up to 10L successfully. However, this improvement was still restricted in the conventional batch stirred-tank crystallizer which is not suitable for the rapid organic reactive crystallization process.

In this study, we developed a continuous process for organic reactive crystallization synthesis. Firstly, by using process analytical technology (PAT) including an ultraviolet–visible spectrometer (UV) and focused beam reflectance measurement (FBRM), the chemical reaction kinetics and the residence time distribution (RTD) of the reaction and crystal growth during the synthesis of sodium cefuroxime were determined. Then, with the help of computational fluid dynamics (CFD), a crystallizer was designed and verified based on the basic data obtained above. Finally, the experiments were carried out in 1L and 50L rigs to further test and verify the performance of this process, in particular, under scaled-up operating conditions. The products were characterized using XRD, SEM and the imaging instrument *Morphologi* G3. The procedure of the analytical characterization (XRD, *Morphologi* G3 and SEM) was the same which can be seen in chapter 5. The ultimate performance of this process was judged by the stability and processability of the products obtained using different size scales.

8.2 Reactor Design concept and methods

8.2.1 Design Concept

Midler (Midler et al., 1994) tested a jet mixer for rapid precipitation of several pharmaceutical compounds. They found that the mixing intensity in the jet mixer was helpful in rapidly achieving good mixing and a uniformly high supersaturation environment, which led to a high quality final product with superior crystallinity and purity. He provided a method of impinging fluid jet

streams in a continuous crystallization process to achieve high intensity micromixing of fluids so as to form a homogeneous compound prior to the start of nucleation. This process permitted direct crystallization of the high surface area particles with great stability. Lindrud (Lindrud et al., 2001) and David J. Am Ende (David J. Am Ende et al., 2003) described an apparatus and process for crystallizing submicron-sized particles with the introduction of a sonic probe with impinging jets. The obvious drawback of these inventions was that the reaction process and crystal growth process took place in the same vessel, and/or mentioned the mixture could flow from the outline but still resulted in flowing into another stirred vessel. Besides, they only mentioned that the nozzles of the impinging jet mixer could have a slight downward angle of about 10° from the horizontal to help the flowing material move down and the linear velocity at the jet nozzles should be at least 5 m·s^{-1} with the most preferable one being between about 20 to 25 m·s^{-1}. However, there was no data or experimental results to support the selection. For different reactive crystallization processes, these structural parameters obviously might be varied slightly. Therefore, it is necessary to investigate the impact of design parameters of the impinging jet mixer on crystal structure of the product.

The crystallizer proposed in this study related to a tank reactor (forming reaction/nucleation area) along with an impinging jet mixer to achieve intensity mixing of reactants so as to form a homogeneous compound before nucleation and a tubular reactor (forming crystal growth area) with suitable length to meet the required crystal growth time so as to form uniform crystal size distribution in a continuous reactive crystallization process.

According to the specific attributes and requirements of nucleation and crystal growth mechanism in a reactive crystallization process, the continuous crystallization system has integrated the reactors, a tank reactor and a tubular reactor. For nucleation, which is a faster process compared with the crystal growth process, the mixed flow is favoured in order to prevent aggregation. The driving force, supersaturation, produced by reaction requires thorough mixing of

the reactants. Tank reactor with an impinging jet mixer, in which two liquid streams in the form of narrow, coplanar jets at high velocities impinge upon each other, provides perfect prerequisites to form a homogeneous compound before nucleation. For crystal growth process, which is relative slow, the plug flow is preferred. The flow pattern in a plug flow, no back mixing, means that crystals grow under uniform conditions, and the consistent residence time and uniform crystal size distribution. The continuous process enhances reproducibility of products because all the material crystallizes under consistent conditions. Such uniformity is not possible when using batch methods in which concentration, solubility and other parameters may change with time.
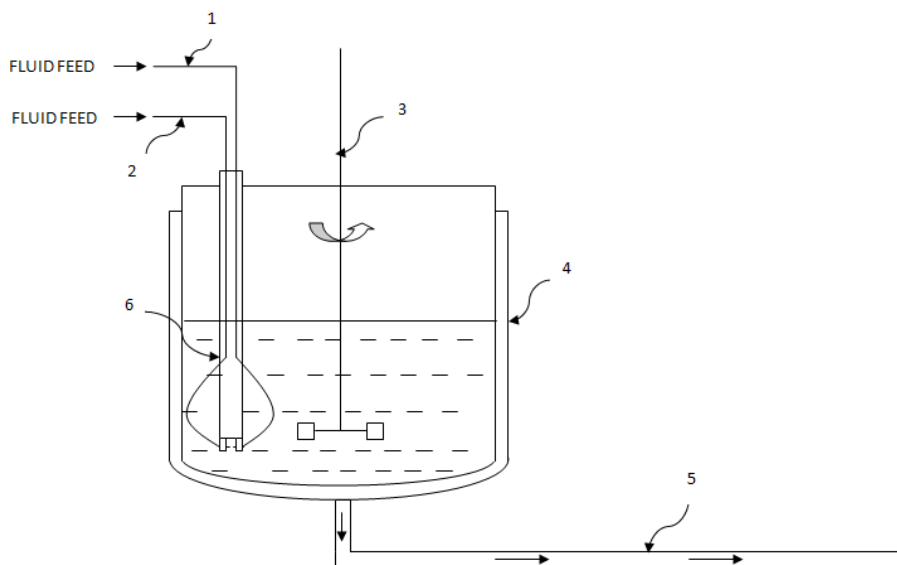
Figure 8.1 Embodiment of the invention with one pair impinging jet: 1 – fluid feed 1; 2 – fluid feed 2; 3 – stirrer; 4 - tank reactor; 5 - tubular reactor; 6 - impinging jet mixer.

We have applied a patent for this design (Wang et al., 2014). Figure 8.1 shows one embodiment of this invention with one pair impinging jet 6 immersed in the liquid and one stirrer 3. The two jet nozzles are preferably held with block so that they can keep the appropriate angle and position under high-speed liquid impact. Fluids 1 and 2 enter the tank reactor 4 where mixing, reaction and nucleation take place, the stirrer 3 make the nuclei flow out the reaction area immediately and create a uniform environment for following nucleation or seed

contact. After nucleation in the tank reactor 4, the material leaves the tank reactor, and then travels into a tubular reactor 5 (the crystal growth area).

8.2.2 Design Methods

Momonaga (Momonaga et al., 1992) studied the reactive crystallization process of methyl alpha-methoxyimino acetoacetate. They investigated the effect of agitation on the chemical reaction rate and crystal quality by considering the mechanisms in reactive crystallization process and proposed that the crystal purity was influenced remarkably by both the chemical reaction and crystallization rates. In order to ensure this crystallizer can not only guarantee the reaction fully completed, but also provide the same residence time for crystal growth, the scales of the tank reactor should be designed by both the reaction kinetics and the production handling capacity, while the scale of the tubular reactor needs to be determined by the crystal growth residence time demand. However, to the best of our knowledge, there are no current research articles covering the reaction and crystallization kinetics study of synthesis of sodium cefuroxime. Therefore, by experiments and simulation methods, the reaction kinetics and the mechanism of crystal growth should be obtained first. The following are the theories and models:

8.2.2.1 Residence Time and Residence Time Distribution

Residence time and residence time distribution has been widely used in chemical engineering, earth science, environmental engineering, pharmaceutical engineering, biology and other fields for nearly a century.

Residence time is the average amount of time that a fluid spends in a particular system. Residence time begins from the moment that the fluid of a particular substance enters the system and ends at the moment that the same fluid of that substance leaves the system. If the size of the system is changed, the residence time of the system will be changed as well. The larger the system, then larger the residence time, assuming the inflow and outflow rates are held

constant. Inflow and outflow will also have an effect on the residence time of a system. If the inflow and outflow rates are increased, the residence time of the system will be shorter. It is assumed that the concentration of the substance in the system and the size of the system remain constant and steady-state conditions (Danckwerts, 1953, 1958; Danckwerts et al., 1954). The base definition for residence time is as follows:

$$t = \frac{\text{System capacity to hold a substance}}{\text{Flow rate of the substance through the system}} \qquad (8.1)$$

The generic variable form of Equation (8.1) is as follows:

$$t = \frac{V}{q} \qquad (8.2)$$

where t is used as the variable for residence time, min; V is the capacity of the system, mL; and q is the flow rate for the system, mL·min^{-1}.

Residence time distribution (RTD) of a reactor is a probability distribution function that describes the amount of time a fluid element could spend inside the reactor. The RTD is widely used to characterize the mixing and flow within reactors and to compare the behaviour of real reactors to their ideal models (Debaun and Katz, 1961; Rietema, 1958; Vandevusse, 1959). The distribution of residence times is represented by an exit age distribution, E (t). The function E (t) has the units of time^{-1} and is defined as follows:

$$\int_0^\infty E(t)dt = 1 \qquad (8.3)$$

The mean residence time is given as follows:

$$\bar{t} = \int_0^\infty t \cdot E(t)dt \qquad (8.4)$$

The degree of dispersion around the mean residence time, the variance σ^2, is as follows:

$$\sigma^2 = \int_0^\infty (t - \bar{t})^2 \cdot E(t)dt \qquad (8.5)$$

The residence time distribution of a reactor can be used to compare its behaviour to that of two ideal reactor models: a) Plug flow reactors. In an ideal plug-flow reactor, there is no axial mixing hence the fluid elements leave from the reactor in the same order as they enter into the reactor. Therefore, the variance of an ideal plug-flow reactor is zero. b) Mixed flow reactors. An ideal continuous stirred-tank reactor is based on the assumption that the flow at the inlet is completely and instantly mixed into the bulk of the reactor. The reactor and the outlet fluid have identical, homogeneous compositions at all times. Therefore, the variance of an ideal mixed-flow reactor is one (Spalding, 1958; Wood, 1962; Yagi and Kunii, 1961). The RTD of a real reactor deviate from that of an ideal reactor, depending on the hydrodynamics within the vessel.

8.2.2.2 Reaction Kinetics

Reaction kinetics, also known as chemical kinetics, is the study of rates of chemical processes. Chemical kinetics includes the investigation of how different experimental conditions can influence the speed of a chemical reaction and yield information about the reaction's mechanism and transition states, as well as the construction of mathematical models that can describe the characteristics of a chemical reaction (Juttner, 1909; Orloff, 1912; Rakowski, 1906). The rate equations of common reaction can be seen in Table 8.1, and k is the reaction rate constant. After integration, it is easy to find out that the key point is to know the relationship between the concentration (*[A]*) and the reaction time (*t*). If *[A]* versus time is a straight line, the reaction is zero-order reaction. If ln (*[A]*) versus time is a straight line, the reaction is first-order reaction. If reciprocal of *A* versus time is a straight line, the reaction is second-order reaction.

Table 8.1 Reaction Rate Equation

	Zero-order reaction	First-order reaction	Second-order reaction
Differential Equation	$-\dfrac{d[A]}{dt} = k$	$-\dfrac{d[A]}{dt} = k[A]$	$-\dfrac{d[A]}{dt} = k[A]^2$
Integral Equation	$[A] = [A]_0 - kt$	$[A] = [A]_0 e^{-kt}$	$\dfrac{1}{[A]} = \dfrac{1}{[A]_0} + kt$
Linear Relationship	$[A] - t$	$\ln([A]) - t$	$\dfrac{1}{[A]} - t$

The main factors that influence the reaction rate are the physical state of the reactants, the concentrations of the reactants, the temperature at which the reaction occurs, and whether or not any catalysts are present in the reaction. For a certain reaction, temperature usually has a major effect on the rate of a chemical reaction. The Arrhenius equation, which gives the quantitative basis of the relationship between the activation energy and the reaction rate constant (Fairclough and Hinshelwood, 1937; Polissar, 1932), is as follows:

$$k = \mathrm{A}e^{-Ea/RT} \tag{8.6}$$

Where A is the pre-exponential factor; Ea is the activation energy, J; T is the reaction temperature, K; and R is the gas constant. The values for A and Ea are dependent on the reaction.

8.3 Determination of Reactor parameters

8.3.1 Ultraviolet–Visible spectrometer (UV) Measurement for Reaction Kinetics

8.3.1.1 Principle of Ultraviolet-Visible Absorption

Molecules containing π-electrons or non-bonding electrons (n-electrons) can absorb the energy in the form of ultraviolet or visible light to excite these electrons to higher anti-bonding molecular orbitals. The more easily excited the electrons (i.e. lower energy gap between the HOMO and the LUMO), the longer the wavelength of light it can absorb. Varieties of substances have their different molecules and atoms with different spatial structure, which absorbs different light energy. Therefore, each substance will have its unique fixed absorption spectrum curve. According to certain features of absorption spectrum, ultraviolet–visible spectrometer can be used to measure the level of the substance content, which is also the basis of qualitative and quantitative spectrophotometric. Like ATR-FTIR spectrometer, the Bouguer-Lambert-Beer law is used to show the relationship between the concentration and the absorbance.

8.3.1.2 Calibration Experiment of UV

An Ultraviolet–visible spectrometer was used to measure the concentration of acid cefuroxime because the absorbance of a solution is directly proportional to the concentration of the absorbing substances in the solution. The characteristic absorption peak of acid cefuroxime is 274 nm (Wozniak and Hicks, 1991). In the ultraviolet and visible spectrum range, ethanol has no absorption, but acetone showed absorption interference. So the mixed solvent of ethanol and acetone with the same proportion of the reaction solvent was selected as the background solvent for the baseline collection. The standard solution of acid cefuroxime (C_1) used for calibration included spectra from 0 mol·L^{-1} to 0.2 mol·L^{-1} (every 0.02 mol·L^{-1}), which covered the entire range of the reaction concentration change. The calibration results can be seen in Figure 8.2. A straight line indicated that this method worked effectively.
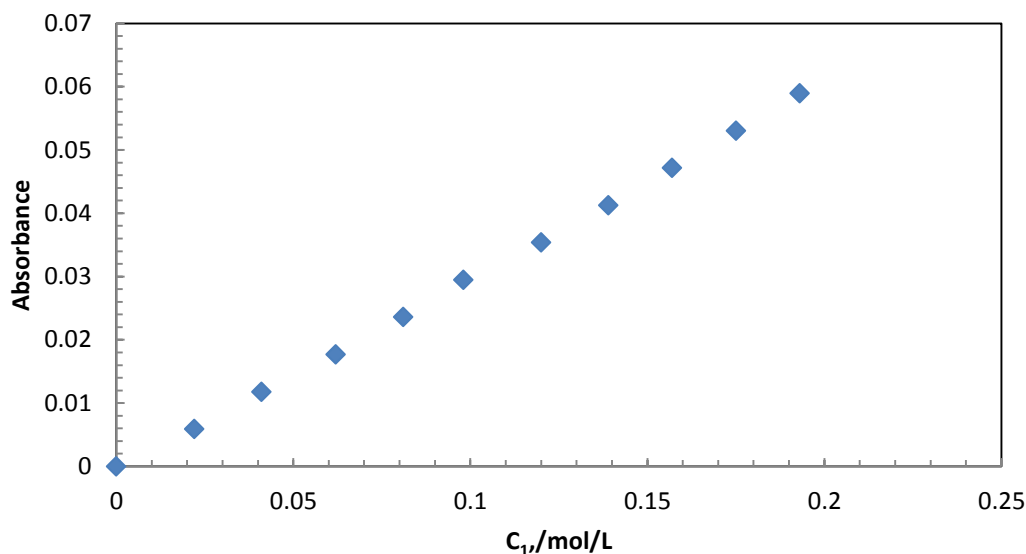
Figure 8.2 Ultraviolet–visible spectrometer calibration curve of acid cefuroxime (C_1) from 0 mol·L^{-1} to 0.2 mol·L^{-1}.

8.3.1.3 Determination of the Reaction Parameters

After calibration, the UV spectrometer was used to measure the concentration of acid cefuroxime for reaction kinetic determination. According to the reactant ratio, the two reactants were put into the UV spectroscopy cell at the same time. However, two issues were revealed: a) as the reaction occurred, the solution rapidly became turbid. The particles generated had a significant impact on UV measurement. b) There was no stirrer in the UV spectroscopy cell, so the reactants cannot achieve full mixing, which was different from the actual reaction conditions.

To solve these issues, the beaker was used to replace the UV spectrometer cell where the reaction was carried out. A magnetic stirrer was put into a beaker first, then the reactants were poured into the beaker at one minute intervals. The clear supernatant solution was drawn out by a pipette and injected into the spectrometer cell for measurement. When the measurement was completed (about 10 seconds), the solution was put back into the beaker. This approach can not only avoid the effect of particles on measurement accuracy, but also

make sure the process is close to the actual operation. Five parallel tests were conducted, Table 8.2 and Figure 8.3 present the relationship of the mean concentration values versus the reaction time.

Table 8.2 Five parallel UV tests.

Time	Run 1	Run 2	Run 3	Run 4	Run 5
0 min	0.058 mol/L	0.058 mol/L	0.059 mol/L	0.057 mol/L	0.058 mol/L
1 min	0.035 mol/L	0.034 mol/L	0.035 mol/L	0.035 mol/L	0.036 mol/L
2 min	0.026 mol/L	0.025 mol/L	0.026 mol/L	0.027 mol/L	0.026 mol/L
3 min	0.019 mol/L	0.019 mol/L	0.018 mol/L	0.018 mol/L	0.02 mol/L
4 min	0.012 mol/L	0.011 mol/L	0.013 mol/L	0.012 mol/L	0.013 mol/L
5 min	0.009 mol/L	0.009 mol/L	0.009 mol/L	0.009 mol/L	0.009 mol/L
6 min	0.006 mol/L	0.006 mol/L	0.007 mol/L	0.006 mol/L	0.006 mol/L
7 min	0.004 mol/L	0.003 mol/L	0.004 mol/L	0.004 mol/L	0.004 mol/L
8 min	0.003 mol/L	0.003 mol/L	0.003 mol/L	0.003 mol/L	0.003 mol/L
9 min	0.003 mol/L	0.003 mol/L	0.003 mol/L	0.003 mol/L	0.003 mol/L
10min	0.003 mol/L	0.003 mol/L	0.003 mol/L	0.003 mol/L	0.003 mol/L
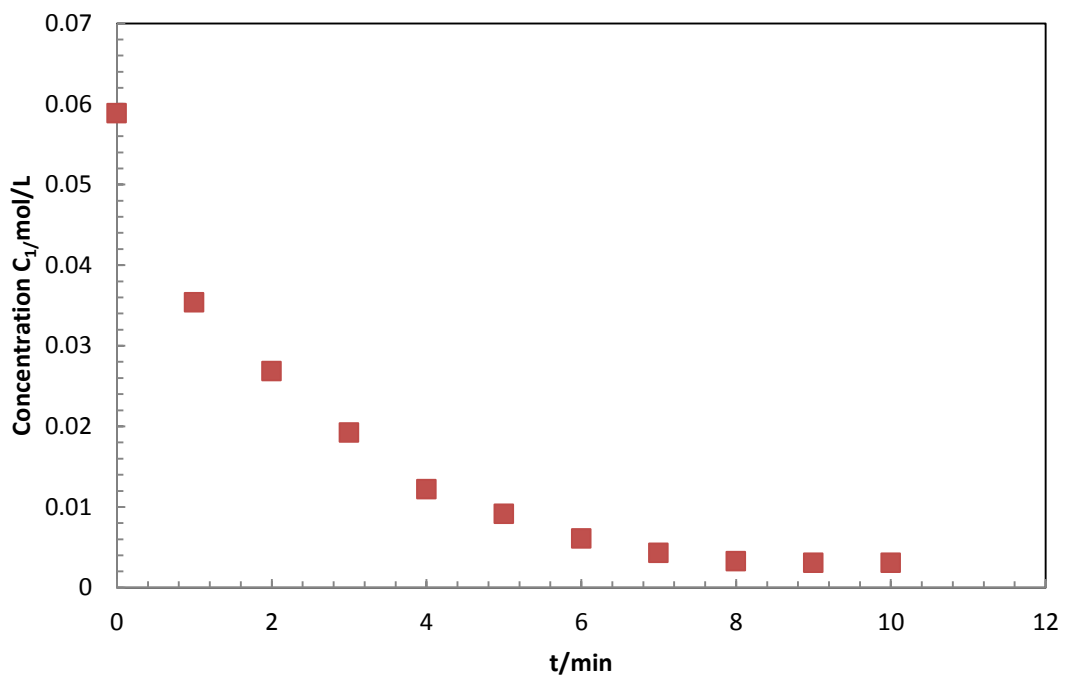
Figure 8.3 Mean concentration curve of acid cefuroxime (C_1) during the reaction crystallization process measured by ultraviolet–visible spectrometer for residence time determination.
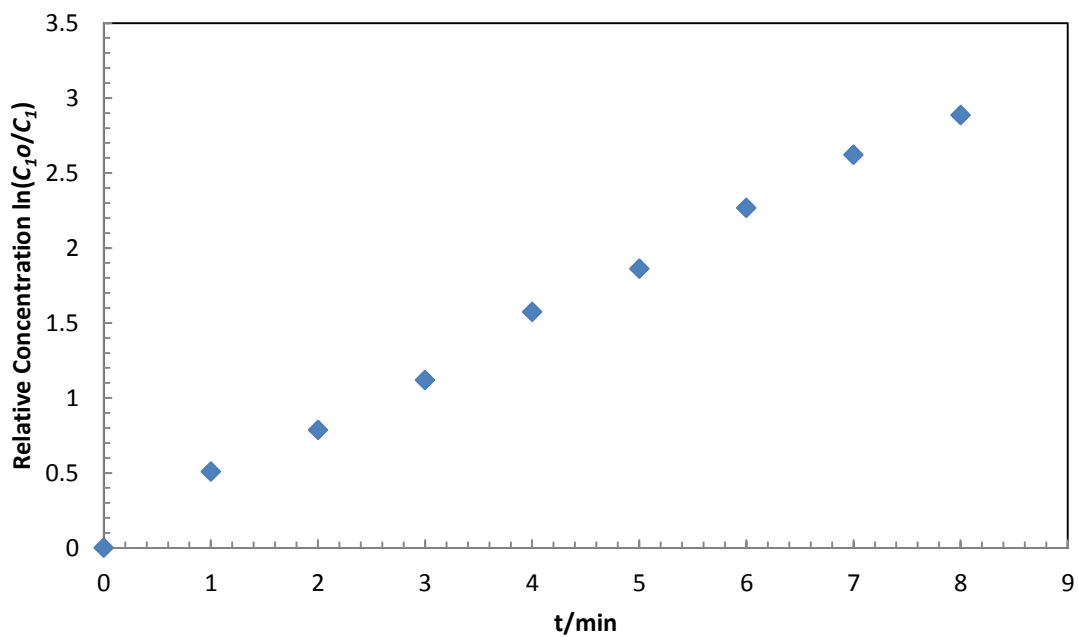
Figure 8.4 Relative concentration (ln (C_{10}/C_1)) curve of acid cefuroxime (C_1) during the reaction crystallization process measured by ultraviolet–visible spectrometer for reaction kinetics determination.

162

As can be seen from Figure 8.3, the reaction nearly stopped at 8 minutes. Therefore, the required residence time of the reactive crystallization process in a tank reactor (mixed flow area) should be no less than 8 minutes. As can be seen in Figure 8.4, ln (C_0/C_1) versus reaction time was a straight line. Therefore, this reaction is a first-order one with the reaction rate constant being found to be 2.688 min^{-1}.

8.3.1 FBRM Measurement for Crystal Growth

As is well known, serious aggregation is usually considered as a significant problem for pharmaceutical crystallization because of solvent and impurity. The aggregation phenomenon of sodium cefuroxime was monitored by FBRM in this study (Barrett and Glennon, 1999; Heath et al., 2002; Saleemi et al., 2012b; Saleemi et al., 2012c).

As can be seen in Figure 8.5, it was found that after all counts numbers increased for about 15 minutes, the 1-5.012 line dropped first, and the total number of particles counted reduced at almost the same time. Then the 10-23.263 line and the 29.286-85.77 line dropped one by one, only the number of the largest particles still kept increasing. Since the reaction had stopped this meant that the driving force had already disappeared, it must be the aggregation of small particles rather than the growth which made larger particles increase, which indicated that the aggregation phenomenon had happened during the synthesis process. Due to the lamellar habit, it was hard to completely avoid agglomeration during the reactive crystallization process of sodium cefuroxime, especially in the industrial manufacturing process with high initial concentration and fast feed rate. Figure 8.5 also indicated that the entire crystallization process needed about 30 minutes to finish. Since 8 minutes are required by the tank reactor, the required residence time for crystal growth in the tubular reactor (plug flow area) should be no less than 22 minutes.
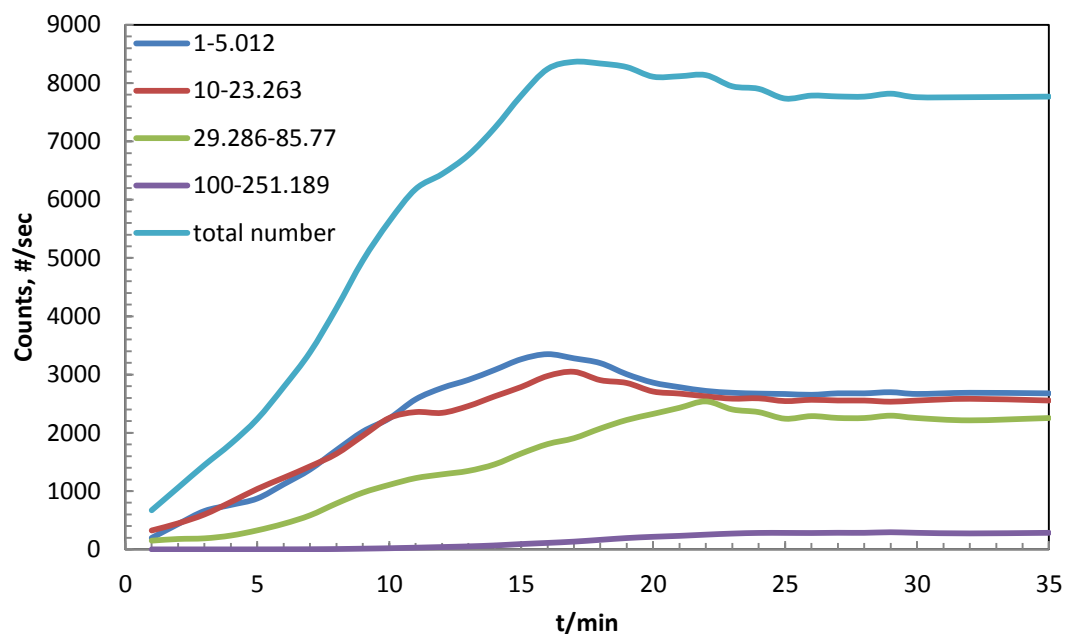
Figure 8.5 Counts curves of sodium cefuroxime during the reaction crystallization process measured by focused beam reflectance measurement (FBRM) for the mechanism of crystal growth determination.

8.3.2 CFD Simulation for Residence Time Determination

The residence time of a reactor can be measured by injecting a small amount of an inert substance into the stabile fluid within the reactor and monitoring the concentration change of this inert substance at the outlet of the reactor. However, it will waste a lot of time and solvent. So CFD (Ansys Fluent 13 software) was used to simulate this process. The reactor we simulated was the 1L tank reactor with an impinging jet mixer, which was used for optimization experiments in chapters 6 and 7 previously, and adding a tubular reactor following the outlet of the 1L tank reactor. The specific parameters can be seen in Figure 8.6.

12mm

100mm

50mm

200mm

20mm

10mm

D_1=0.065mm

D_2=0.13mm

2500mm
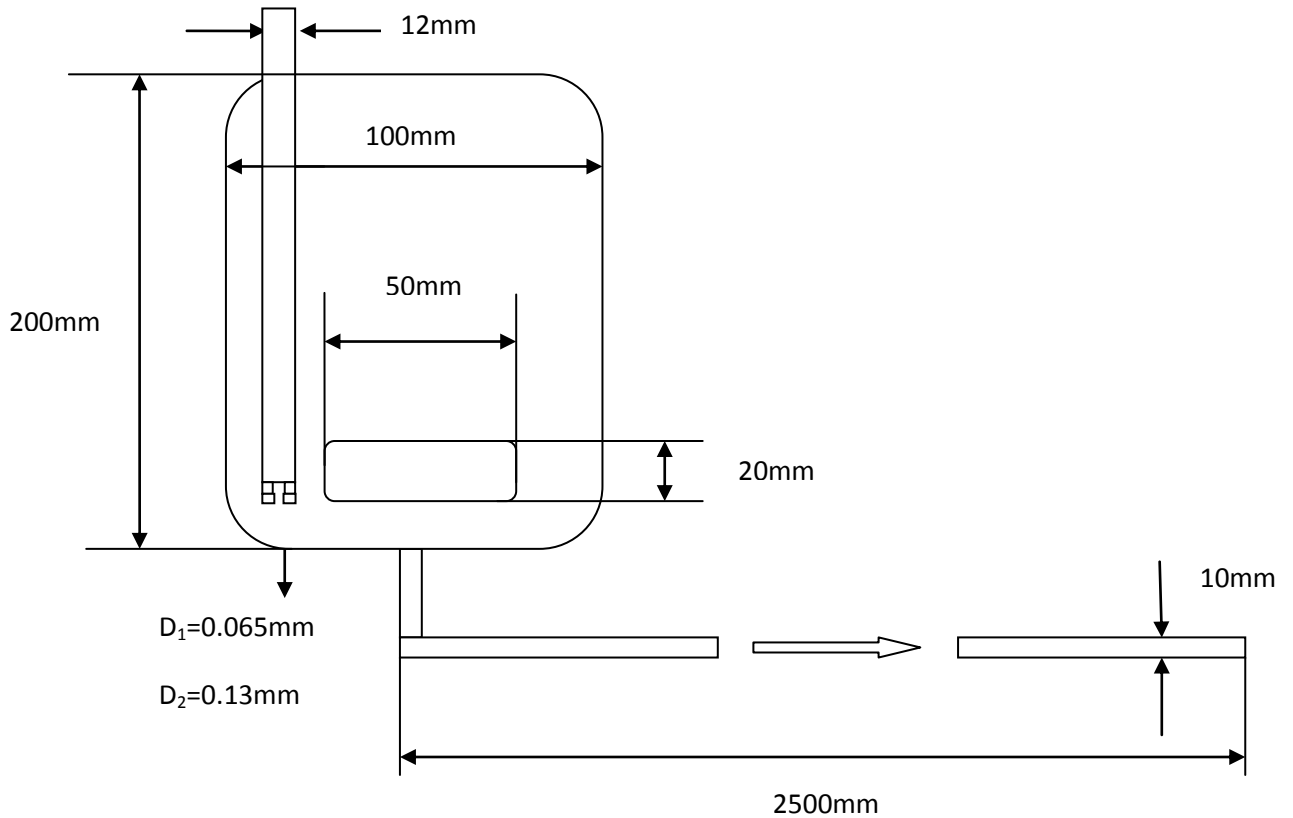
Figure 8.6 Illustration of specific parameters of 1L crystallizer for reactive crystallization of sodium cefuroxime.

8.3.3.1 Meshing

As preparatory work for the CFD simulation study, the computational domain of the reactor with discretised cells was produced by Gambit 2.4 software. Figure 8.7 shows that the computational domain involved a tank reactor with a two-impinging-jet probe for reactant feed and a stirrer for fluid mixing, also a long tubular reactor for crystal growth. Inside the tank reactor, to model the rotation of the impeller, sliding mesh was used in the mixing paddle region. Meanwhile, the setting of the interface was also used to achieve the mass and heat transfer between the mixing paddle region and the main reactor region. The entire reactor was compartmentalized by three-dimensional mesh with 255269 tetrahedral cells in total where the main reactor region contained 228142 cells and the mixing paddle region contained 27127 cells. Since the diameter of the

feed nozzle and the outlet tube was much smaller than the reactor diameter, the surface mesh construction was used first to ensure the uniformity of the grid, and then using the grid self-amplifying function, the whole mesh could be generated automatically.
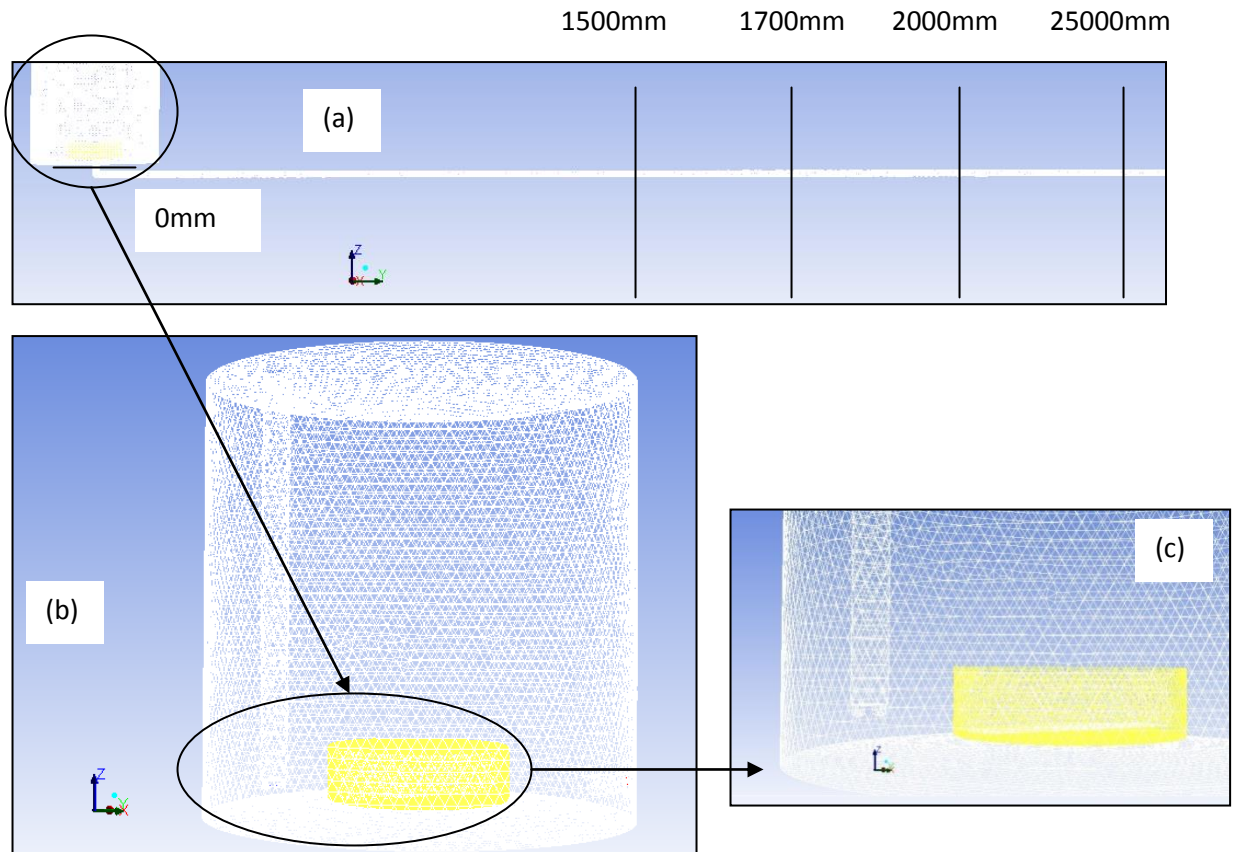
Figure 8.7 Illustration of the computational mesh of the crystallizer for computational fluid dynamic (CFD) simulation: (a) overall three-dimensional mesh in reactor region with the collection surface of residence time distribution; (b) mesh in tank reactor with impinging jet mixer probe; and (c) mesh in mixing paddle region.

8.3.3.2 Computational Details

The computational domains and meshing of the crystallizer have been described in the last section. The hydrodynamic and mixing behavior in the crystallizer systems were studied based on the optimized operating conditions (the reaction temperature, the feed rate and the stirring speed) obtained in chapters 6 and 7. The operating pressure and the inlet temperature were fixed

at 101325 Pa and 20 $^{\circ}$C. The inlet concentrations of the two solutions (acid cefuroxime solution and sodium lactate solution) were the same as those described in chapter 3. The properties of the solvent such as the density, viscosity, thermal conductivity and the specific heat could be set to the corresponding fixed value at 20 $^{\circ}$C temperatures because there was no temperature change during this reactive crystallization process. The outlet boundary was defined as the pressure outlet with a given outlet temperature of 20 $^{\circ}$C.

8.3.3.3 Solution Method

The standard SIMPLE pressure-velocity coupling was used with a first-order upwind scheme being employed for the discretization of the convection terms in the governing equations. Since the reaction is neither endothermic nor exothermic, the heat losses through the outer wall of the reactor were assumed to be negligible. Standard non-slip wall boundary conditions were applied in the studies with the standard turbulent wall function being used. Solution convergence was achieved when energy residuals were less than 1E-6 and other residuals were lower than 1E-3 for all simulation cases.

8.3.3.4 Fluid Dynamics Simulation

1. Pure single-phase flow simulation

In order to verify the independence of the mesh, pure single-phase flow simulation was carried out first, which can also help in selecting the appropriate parameter settings and give further explanation of the former conclusions in chapter 7.

Mesh independent tests were performed with the mesh size of 255269 and 378635 for the continuous crystallizer. The main objective of the simulation was to investigate the impact of the nozzles' angles on the flow state. As can been seen in Figure 8.8, the angles we chose were the same as those used in chapter 7 for impinging jet mixer optimization. From Figure 8.8, the following

conclusions can be drawn: (a) the high-speed zone in the middle of the two nozzles (Figure 8.8 (a_1) and (a_2)) indicated that 10° upward nozzles could guarantee the two reactants would produce a frontal mid-way collision. However, after collision, the rapid decline of the jet core velocities indicated that it was difficult for the mixture to leave the mixing zone (impinging jets region), which was not a desired flow state; (b) the high-speed zone moved to one side obviously (Figure 8.8 (b_1) and (b_2)) indicating that the parallel nozzles cannot guarantee the two reactants will collide in the mid-way. The collision speed was relatively lower than the other two cases (Figure 8.8 (a_1) and (a_2), (c_1) and (c_2)) indicated the mixing effect was not satisfactory. This result explained why in impinging jet mixer optimization experiments (chapter 7) the parallel nozzles always led to crystal accumulation which caused clogging of the nozzle. However, the velocity distribution of the reactants in the nucleation area was well which meant that the mixture left the mixing zone smoothly; and (c) when using the 10° downward nozzles (Figure 8.8 (c_1) and (c_2)), the advantages of the former two cases were reflected. On the one hand, the two reactants could collide in the mid-way at high speed; on the other hand, the mixture could flow into the nucleation area gradually. There was no significant difference in flow state between the two mesh sizes of 255269 and 378635. In order to save time, the mesh size of 255269 was chosen for the following Euler-Euler multi-phase flow simulation.

According to the experimental results obtained from the impinging jet mixer optimization experiments in chapter 7, which in case (c), the 10° downward nozzles, can bring the best product with satisfactory crystallinity and stability, it can be summarised that good mixing and flow conditions could improve the crystallinity of the product and the simulation results were consistent with the actual results which meant that this simulation method could be used to provide more reference data for reactor design.

(a$_1$)   (a$_2$)

(b$_1$)   (b$_2$)

(c$_1$)   (c$_2$)
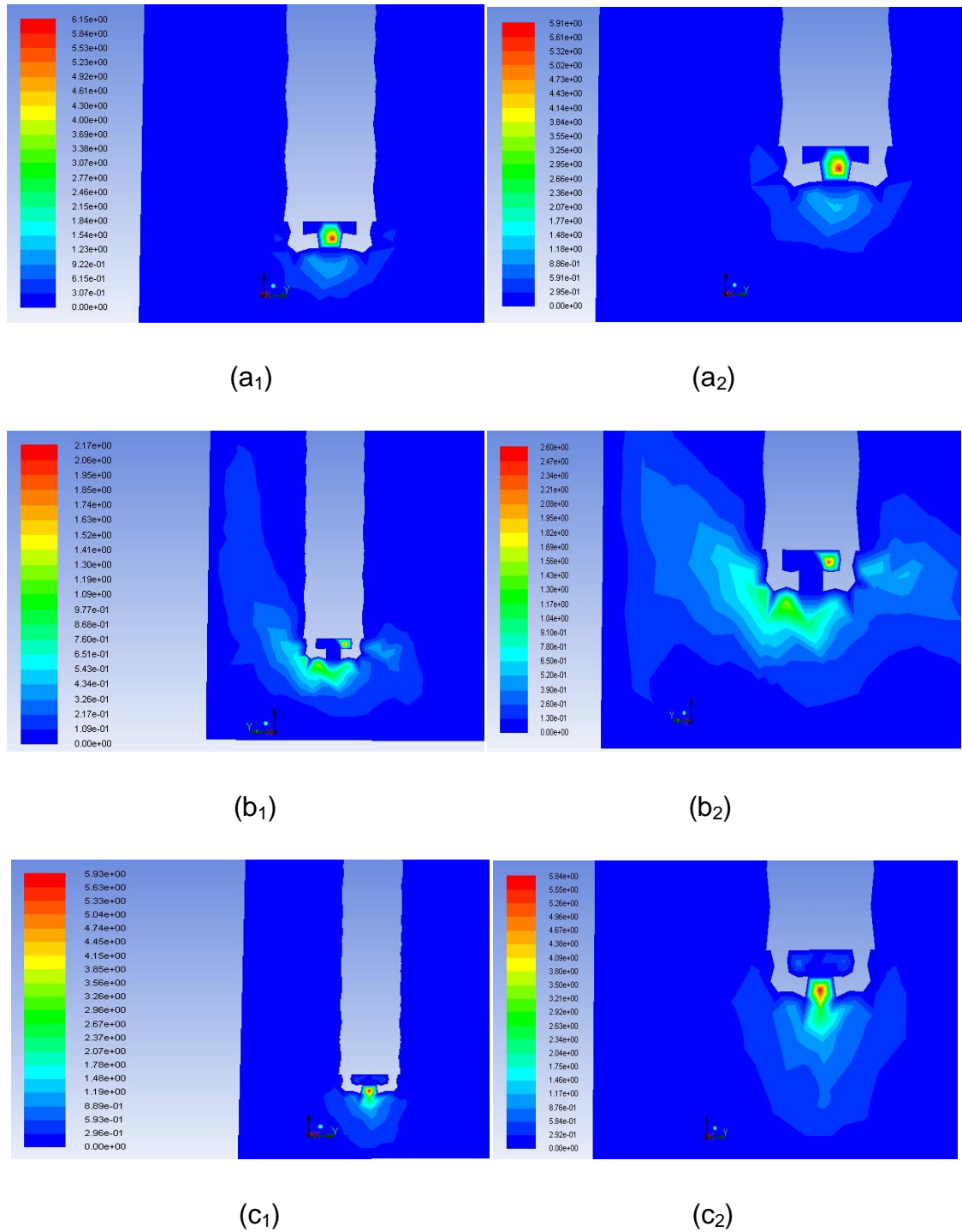
Figure 8.8 Velocity distribution (m·s^{-1}) of the impinging jet mixer probe region measured by computational fluid dynamic (CFD) single - phase flow simulation approach in the tank reactor: (a) 10° upward; (b) parallel; (c) 10° downward; 1- the mesh size of 378635; 2 - the mesh size of 255269.

2. Euler-Euler multiphase flow simulation for residence time distribution

In this section, on the basis of the single-phase flow simulation, the particle was put into the reactor so that the simulation conditions were closer to the actual situations. The mixture of sodium cefuroxime synthesis system was suspension or slurry, which meant that the flow regime of the system should be characterised as liquid-solid multiphase flow. Therefore the Euler-Euler multiphase approach was selected in this project. For this approach, the primary phase was assumed to be a mixture of sodium lactate solution and acid cefuroxime solution, whereas the particle, sodium cefuroxime, was considered as a dispersed secondary phase. The physical properties of the particle were the same as the sodium cefuroxime crystal with the uniform size of 8.5 µm.

Simulation of mixing in the CFD model was carried out by introducing an inert tracer that has the same property as the mixture of sodium lactate solution and acid cefuroxime solution into the bulk phase in the crystallizer. The tracer was treated as the secondary phase and the bulk phase was therefore considered to be the primary phase liquid. The tracer concentration and residence time distribution was solved using the Reynolds-averaged species transport equation (Ma et al., 2014):

$$\frac{\partial \rho Y_i}{\partial t} + \frac{\partial \rho u_j Y_i}{\partial x_j} = \frac{\partial}{\partial x_i}\left(\Gamma_{i,eff} \frac{\partial Y_i}{\partial x_j}\right) \tag{8.7}$$

where $\Gamma_{i,eff} = \Gamma_i + \mu_t/Sc_t$ is the effective diffusion coefficient of species i; ρ is the mixture density, kg·m^{-3}; u_i is the mixture velocity, m·s^{-1}; Y_i represents the species mass fraction, Γ_i is the species diffusion coefficient, μ_t the turbulent eddy viscosity, mPa·s; and Sc_t the turbulent Schmidt number.

The properties of the mixture used in the calculation were defined using volume/mass weighted mixing laws for mixture components and are described as follows:

$$\rho = \frac{1}{\sum_i \frac{Y_i}{\rho_i}}; \ c_p = \sum_i Y_i \, c_{p,i}; k = \sum_i Y_i k_i \, ; \ \mu = \sum_i Y_i \mu_i \tag{8.8}$$

where, Y_i, ρ_i, $c_{p,i}$, k_i, and μ_i represent the mass fraction, density (kg·m^{-3}), specific heat capacity (J/K), thermal conductivity (W/(m·K)) and viscosity (mPa·s) of species i, respectively. The diffusion coefficient of mixture was solved by a modified Chapman-Enskog equation and was dependent on the mixture temperature (Gorban and Karlin, 1991; Reinecke and Kremer, 1991; Schochet and Tadmor, 1992).

For measuring the residence time distribution in a tank reactor, an inert tracer was injected into the crystallizer from the impinging jet probe and the concentration change of this inert substance was monitored at the outlet of the reactor (0 mm in Figure 8.7). The concentration data should be normalized to obtain the function E(t). From Figure 8.9 (a), it can be seen that all cases could meet the required residence time (8 minutes) for full reaction. However, the mixing efficiency of different cases had significant variations. The results of variance σ^2 indicated that the 10° downward nozzles could provide the best mixing followed by the parallel, and the 10° upward was the worst. This conclusion was also consistent with the single-phase flow simulation results, which further illustrated the importance of mixing for the reaction process.

For measuring the residence time distribution of a tubular reactor, an inert tracer was injected into the reactor from 0 mm in Figure 8.7 and the concentration change of this inert tracer was monitored at different lengths (1500 mm, 1700 mm, 2000 mm, and 2500 mm in Figure 8.7). From Figure 8.9 (b), it can be seen that all cases could meet the required residence time (22 minutes) for the crystal growth process. However, like the tank reactor, the mixing efficiency of different cases showed significant variations. For the length of the tubular reactor, the longer the tube was, the less the mixing efficiency obtained. But considering the degradation of sodium cefuroxime, the tube could not be too long. Therefore, the 1L tank reactor with impinging jet mixer of 10° downward nozzles, and the tubular reactor with the tube length of 1500 mm, 1700 mm and 2000 mm were chosen as the experimental cases.
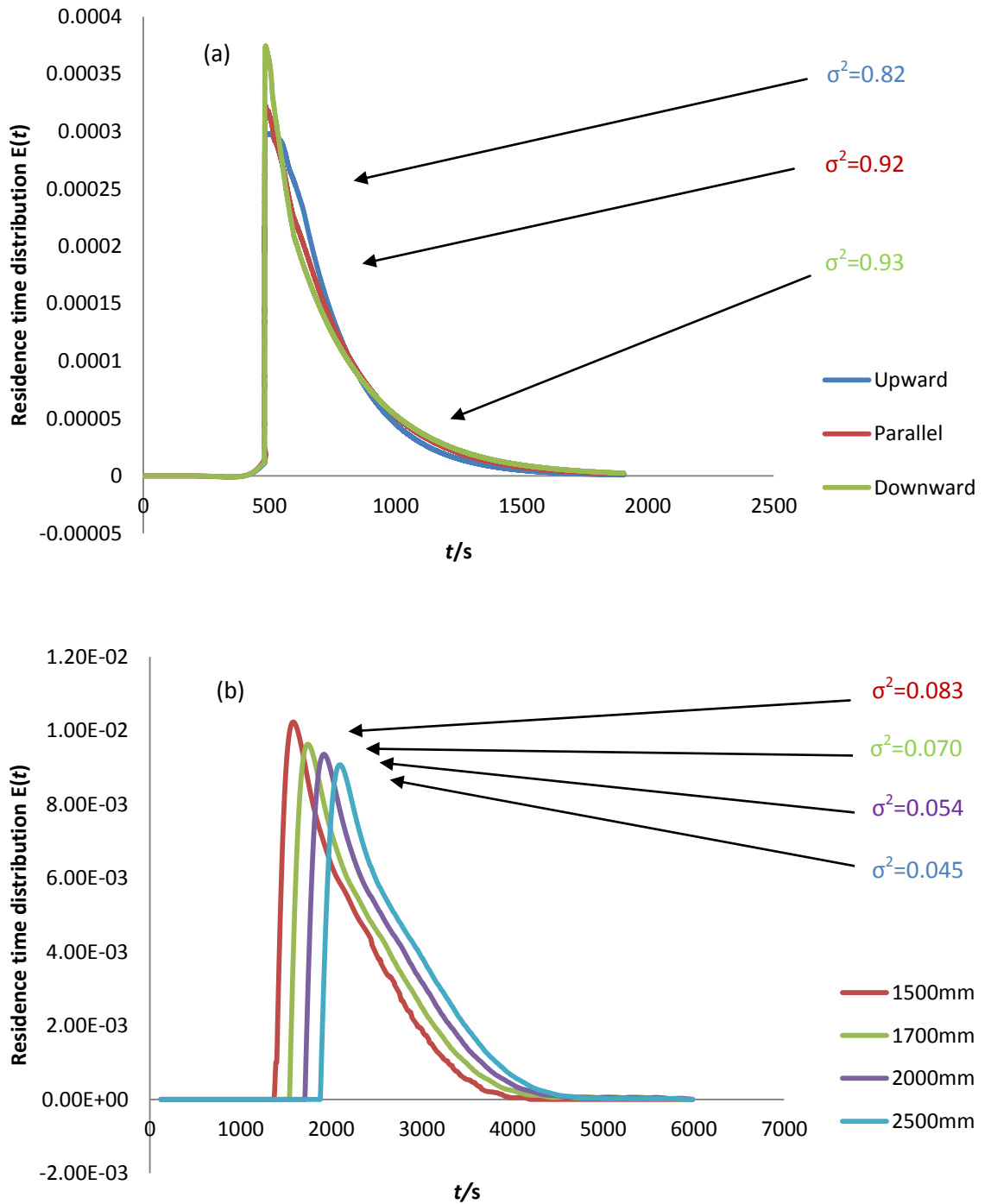
Figure 8.9 Residence time distribution monitored by computational fluid dynamic (CFD) Eulerian-Eulerian two-phase flow simulation approach for process design: (a) the tank reactor; (b) the tubular reactor.

8.4 Experimental Verification and Scale-Up

By CFD simulations, the optimal parameters of the reactor were determined. In this section, more detailed design concepts and instructions were introduced and the verification and scale-up experiments were carried out to further demonstrate the accuracy of simulations and the advantages of the reactor.

8.4.1 Detailed Description of Reactor

8.4.1.1 Impinging Jet Mixer

This crystallizer involved a tank reactor (reaction/nucleation area) with the use of impinging jet mixer with/without stirrers and baffles. One or more pairs of impinging jets could be used to mix two or more fluids. When using these pairs of jets, the two impinging jets of each pair should be substantially diametrically opposed to each other, i.e., they should be at or close to a 180 degree angle (upward or downward) to each other from an overhead view. The slight upward or downward from the horizontal of from 0 degree to about 20 degrees, but preferably >10 degrees downward from the horizontal, could prevent one of the reactants from entering the opposite nozzle, possibly causing crystallization in the jet. These pairs could be immersed in or suspended on the surface of the liquid in the tank reactor and the position of each pair could be the same or under demand. The spacing between two jets should be adjusted on the basis of the conditions, for example, generally, the spacing when the jets immersed should be larger than suspended to grantee the mixing effect.

Regardless of the number of jet pairs used, the fluid jets must impinge to create an immediate high turbulence impact. Concentric or converging jets generally could create insufficient turbulence to achieve the required mixing. The feed speed through the two jets should be no less than 5 m·s^{-1}, preferably 10 m·s^{-1} and can be increased to 20 m·s^{-1}. If the probe was operated above the liquid, the same velocity could achieve higher mixing due to the lower resistance. Theoretically, there was no upper limit of linear velocity which was only limited

by the practical difficulties involved in achieving it. However, for reactive crystallization process, the required reaction time also needed to be considered in order to prevent those excessive un-reacted reactants left the impinging jets region prematurely. If the reactants were more than two, more nozzles equal to their number should be used in coaxial converge uniformly distributed position to guarantee the mid-way collision. The feed speed, which could be controlled by many methods, such as altering the diameter of the nozzle outlet, or the strength of the external force that moved the fluid into the nozzle, of each reactant should be the same, which meant the volumetric ratio may be much different based on the chemical reaction ratio.

8.4.1.2 Tank Reactor

The tank reactor should be cylindrical in shape with a jacket to control the reaction temperature by water/oil cycle. The chamber of tank reactor should have a bottom which slopes downward in a conical shape toward the bottom's centre which was open to the tubular reactor. If the reactor scale was too large to achieve sufficient mixing of the reactants only by impinging jets, stirrers and baffles should be used. Ruston turbines, Intermig impellers, or other agitators were preferably suitable for stirring a slurry suspension. If the height of the reactor was more than twice of the width, two coaxial stirrers/multiple impellers were preferable, where one should be placed at the bottom and the other should be placed in the middle. In addition, to ensure that the mixture could leave the impinging jets region to contact the seeds, the impinging jet probes should be preferably placed near the stirrer as long as there is no effect on the performance of stirrers.

8.4.1.3 Tubular Reactor

The tubular reactor should be connected with the bottom centre of the tank reactor which slopes downward in a conical shape. The flow rate of the mixture within the tube, which could be controlled by pumps or valves, should be equal to the feed flow rate so as to ensure a constant liquid level position within the

tank reactor. The flow rate of the mixture should not be too slow to lead to crystal settlement. The flow state of flow mixture within the tube, which could be controlled by the diameter of the tube, should be kept as laminar flow so as to avoid unnecessary back mixing. In order to keep full pipe flow, the diameter of the tube should not be too large. For those crystal growth processes which required a relatively long residence time, a longer tube length was needed, resulting in placement difficulties in the actual operating conditions. Therefore, in addition to the horizontal position, the tubular reactor could also be placed vertically or spirally.

8.4.2 Experiments in a 1L Crystallizer

8.4.2.3 Length of Tubular Reactor

As mentioned previously, 1500 mm, 1700 mm and 2000 mm were chosen as the experimental length. From the XRD pattern in Figure 8.10, it can be seen that the high main peak intensity of the product can be obtained from the tubular reactor lengths of 1700 mm and 2000 mm. As the mean sizes and size distributions of the products (Figure 8.11) with these two lengths were almost the same, the tubular reactor with a length of 1700 mm was chosen to be the most suitable length. Then, using this 1L crystallizer, four experiments (Sample 2, Sample 3, Sample 4, and Sample 5) were repeated (Table 8.3) and the same good quality of products was obtained (Figure 8.12). From the stability test results in Table 8.4, it can be seen that the products obtained from this crystallizer were more stable (improved about three color grades) than the product obtained from the conventional crystallizer with optimized operating parameters (Sample 1), which meant a longer shelf-life.

Table 8.3 The operating conditions of samples in 1L continuous crystallizer.

Batch No	Operating Conditions
Sample 1	Temperature: 20 - 25 °C, The feed rate: 4 mL·min^{-1}, The stirring speed: 80-100 rpm, no seed, conventional crystallizer
Sample 2	Temperature: 20 - 25 °C, The feed rate: 4 mL·min^{-1}, Feed speed: 10 m·s^{-1}, The stirring speed: 80-100 rpm, no seed, with impinging jet probe, continuous process
Sample 3	Temperature: 20 - 25 °C, The feed rate: 4 mL·min^{-1}, Feed speed: 10 m·s^{-1}, The stirring speed: 80-100 rpm, no seed, with impinging jet probe, continuous process
Sample 4	Temperature: 20 - 25 °C, The feed rate: 4 mL·min^{-1}, Feed speed: 10 m·s^{-1}, The stirring speed: 80-100 rpm, no seed, with impinging jet probe, continuous process
Sample 5	Temperature: 20 - 25 °C, The feed rate: 4 mL·min^{-1}, Feed speed: 10 m·s^{-1}, The stirring speed: 80-100 rpm, no seed, with impinging jet probe, continuous process

Peak intensity: 35407
Peak width at half height: 0.118°

Peak intensity: 35314
Peak width at half height: 0.119°

Peak intensity: 30664
Peak width at half height: 0.136°
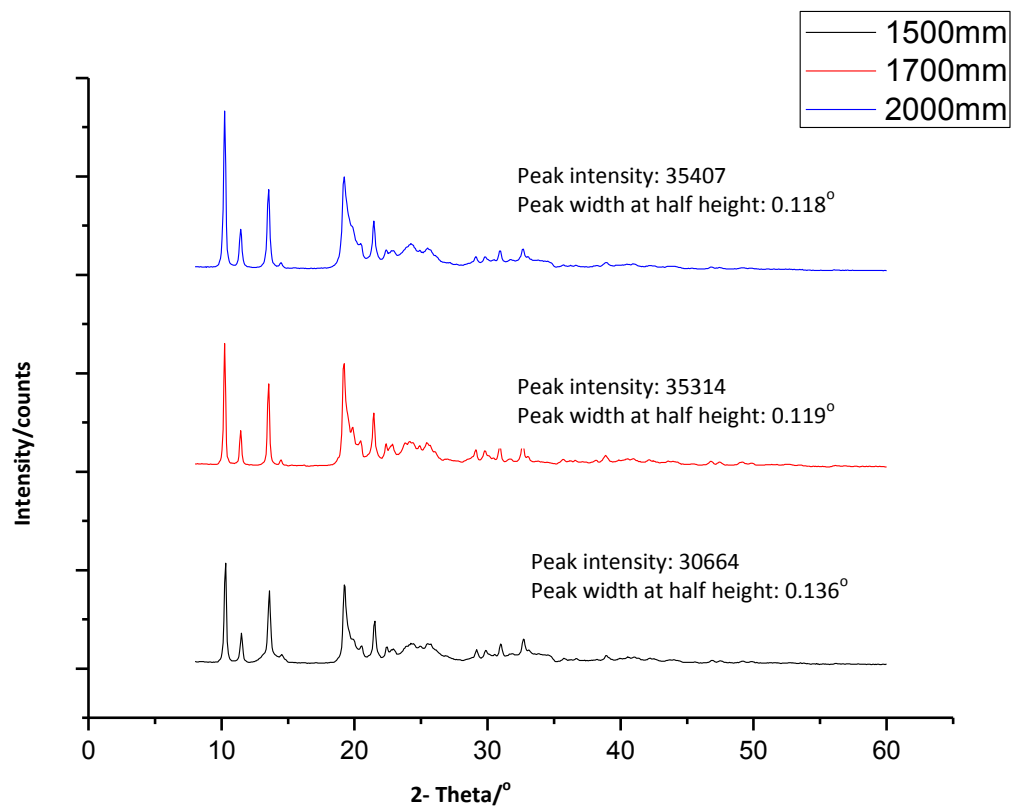
Figure 8.10 The XRD pattern of sodium cefuroxime obtained from 1L experiments (peak intensity and peak width at half height of peak between 9° to 10.5° were chosen to present the crystallinity).
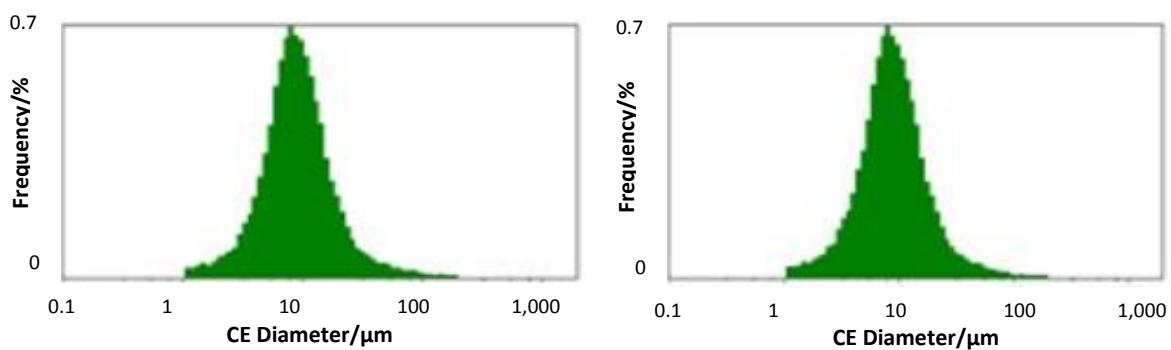
(a) 1700 mm (8.4 μm)

(b) 2000 mm (8.5 μm)

Figure 8.11 The *Morphologi* G3 results of sodium cefuroxime obtained from 1L crystallizer: (a) 1700 mm; (b) 2000 mm.
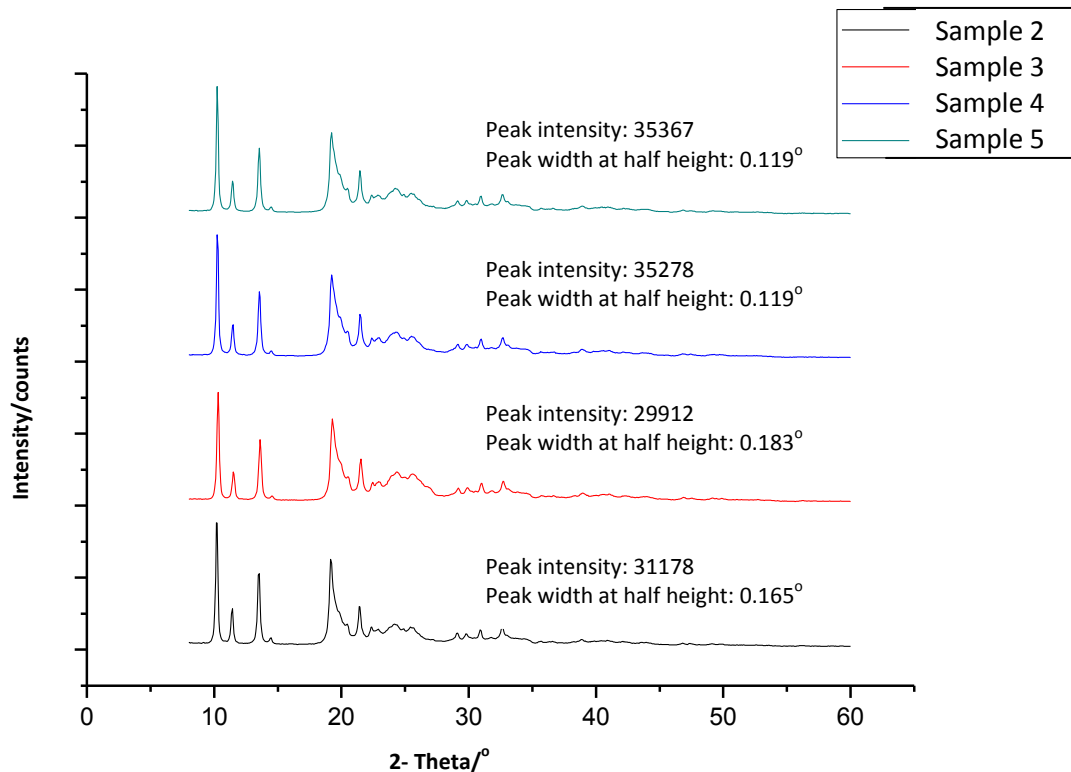
Figure 8.12 The XRD pattern of sodium cefuroxime obtained from 1L four repeat experiments (peak intensity and peak width at half height of peak between 9° to 10.5° were chosen to present the crystallinity).

Table 8.4 Stability Test Data of Sodium Cefuroxime Obtained from 1L Crystallizer.*

Batch No.	Color Grade (60 °C)			
	0 day	5 days	7 days	10 days
Sample 1	<Y-2#	<Y-5#	<Y-7#	<Y-9#
Sample 2	<Y-2#	<Y-3#	<Y-5#	<Y-6#
Sample 3	<Y-2#	<Y-3#	<Y-4#	<Y-5#
Sample 4	<Y-2#	<Y-3#	<Y-4#	<Y-5#
Sample 5	<Y-2#	<Y-3#	<Y-5#	<Y-6#

* Y means the color grade yellow.

8.4.3 Scale-up Experiment in a 50L Crystallizer

The scale-up was based on the same feed velocity (10 m·s^{-1}) in the 1L crystallizer with a volumetric scaling-up factor of 50 while keeping all other operating parameters the same. 50L scale-up experiment parameters:

- Feed velocity: 10 m·s^{-1} (the same as the 1L crystallizer)
- Probe: 10° downward and 6.78 mm spacing (the same as 1L crystallizer)
- Stirring speed: 50 rpm
- Length of the tubular reactor: 5.0 m
- Diameter of the tubular reactor: 5.6 cm
- The reactant ratio was enlarged 50 times.

8.4.3.2 50L Results

Four repeated experiments (Sample 7, Sample 8, Sample 9, and Sample 10) were carried out (Table 8.5). As can been seen from the XRD pattern in Figure 8.13, the crystallinity of products obtained from the 50L crystallizer were almost the same as that from the 1L crystallizer. It can be seen from the *Morphologi* G3 results in Figure 8.14, the crystal size distribution of products obtained from the 50L crystallizer were much better than the ones obtained from the conventional crystallizer (Sample 6). The mean size was uniform and there was no bi-modal phenomenon. As can be seen from the stability results (Table 8.6), the color grades of the 50L scale-up samples were almost the same as that from the 1L crystallizer, higher than the products obtained from the conventional crystallizer (Sample 6) by three color grades under 60 ^{o}C. The batch-to-batch variation was also reduced.

Table 8.5 The operating conditions of samples in 50L crystallizer.

Batch No	Operating Conditions
Sample 6	Temperature: 20 - 25 °C, The feed rate: 200 mL·min^{-1}, The stirring speed: 50 rpm, no seed, conventional crystallizer
Sample 7	Temperature: 20 - 25 °C, The feed rate: 200 mL·min^{-1}, Feed speed: 10 m·s^{-1}, The stirring speed: 50 rpm, no seed, with impinging jet probe, continuous process
Sample 8	Temperature: 20 - 25 °C, The feed rate: 200 mL·min^{-1}, Feed speed: 10 m·s^{-1}, The stirring speed: 50 rpm, no seed, with impinging jet probe, continuous process
Sample 9	Temperature: 20 - 25 °C, The feed rate: 200 mL·min^{-1}, Feed speed: 10 m·s^{-1}, The stirring speed: 50 rpm, no seed, with impinging jet probe, continuous process
Sample 10	Temperature: 20 - 25 °C, The feed rate: 200 mL·min^{-1}, Feed speed: 10 m·s^{-1}, The stirring speed: 50 rpm, no seed, with impinging jet probe, continuous process

Peak intensity: 31092
Peak width at half height: 0.135°

Peak intensity: 31172
Peak width at half height: 0.135°

Peak intensity: 25731
Peak width at half height: 0.194°

Peak intensity: 24296
Peak width at half height: 0.199°
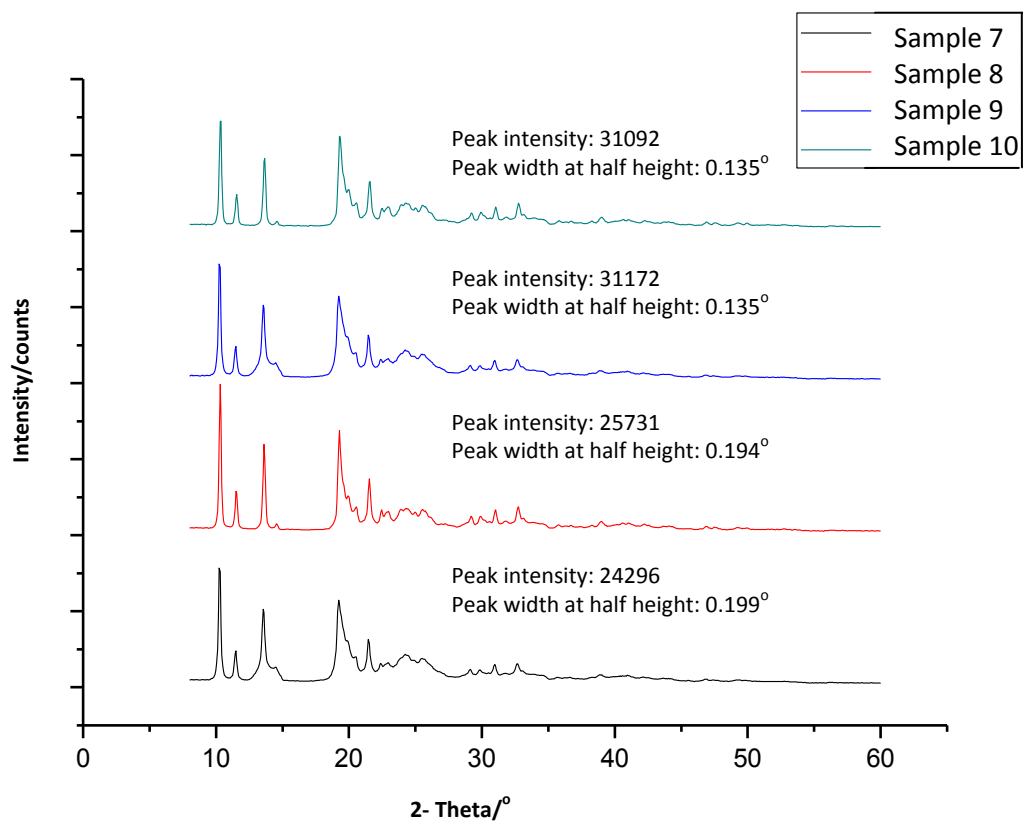
Figure 8.13 The XRD pattern of sodium cefuroxime obtained from 50L scale-up experiments (peak intensity and peak width at half height of peak between 9° to 10.5° were chosen to present the crystallinity).
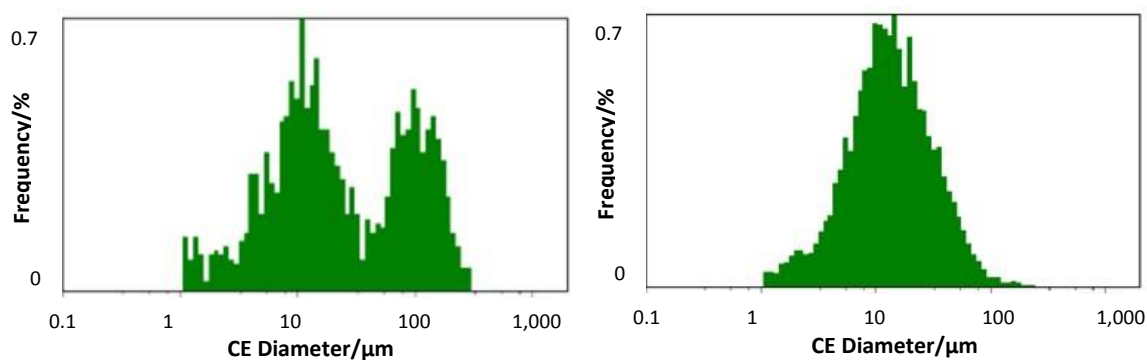
(a) Sample 6 (18.6 μm)   (b) Sample 7 (8.6 μm)

Figure 8.14 The *Morphologi* G3 results of sodium cefuroxime obtained from 50L scale-up experiments: (a) Product obtained from the conventional crystallizer Sample 6; (b) Sample 7.

Table 8.6 Stability Test Data of Sodium Cefuroxime Obtained from 50L Scale-Up Experiments.*

Batch No.	Color grade (60 ^{o}C)					
	0 day	5 days	7 days	10 days	14 days	20 days
Sample 6	<Y-2#	<Y-5#	<Y-7#	<Y-9#	<Y-9#	<Y-10#
Sample 7	<Y-2#	<Y-3#	<Y-4#	<Y-6#	<Y-6#	<Y-7#
Sample 8	<Y-2#	<Y-3#	<Y-5#	<Y-5#	<Y-6#	<Y-7#
Sample 9	<Y-2#	<Y-3#	<Y-4#	<Y-5#	<Y-6#	<Y-7#
Sample 10	<Y-2#	<Y-2#	<Y-4#	<Y-5#	<Y-6#	<Y-7#

* Y means the color grade yellow.

8.5 Optimization of Industrial-Scale Reactors

Using the impinging jet mixer and the continuous process to the industrial-scale reactor directly is complex. On the one hand, normal production cannot be terminated randomly; on the other hand, other instruments including the feed pumps and the downstream processing equipment such as the oven for drying are difficult to enhance simultaneously. However, there are still rooms to improve. Tank reactors are widely used in industrial production. Based on the conclusions obtained from the previous studies, the increase of the mixing effectiveness can improve the crystallinity of the product. Therefore, in this section, the CFD simulation method was used to improve the conventional reactor design by adding stirrers and baffles.

8.5.1 Industrial-scale Reactor Simulation

The parameters and the mesh of a 3000L tank reactor for industrial production can be seen in Figure 8.15. The height of the tank reactor was 2000 mm, and the diameter was 1400 mm. The height of the stirrer was 600 mm, the width was 1300 mm, and thickness was 20 mm. The stirring speed was 62 rpm. The

entire reactor was compartmentalized by three-dimensional mesh with 210617 tetrahedral cells in total where the main reactor region contains 153467 cells and the mixing paddle region contains 57150 cells. As in the 1L tank reactor, to achieve the impeller rotation, sliding mesh was used in the mixing paddle region. Meanwhile, the setting of the interface was used to achieve the mass and heat transfer between the mixing paddle region and the main reactor region.
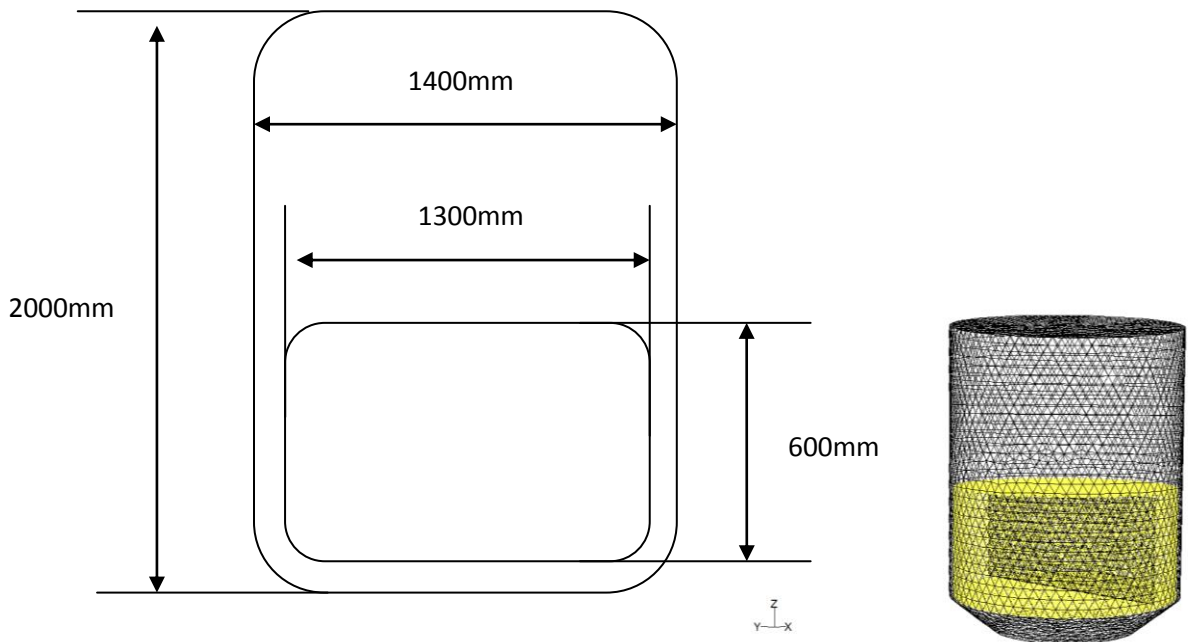
Figure 8.15 The industrial-scale reactor simulation meth diagram.

Firstly, a simulation study of the original structure was conducted. It can be seen from Figure 8.16 that the highest velocity of the fluid in the reactor was 5.0214 m·s^{-1}, and the lowest was 0.00913 m·s^{-1}. In and around the stirrer area, the velocity of the fluid was higher than in other parts of the reactor. However, away from the stirrer area (the upper part of the reactor, which was the feed position), the local fluid velocity was slower.
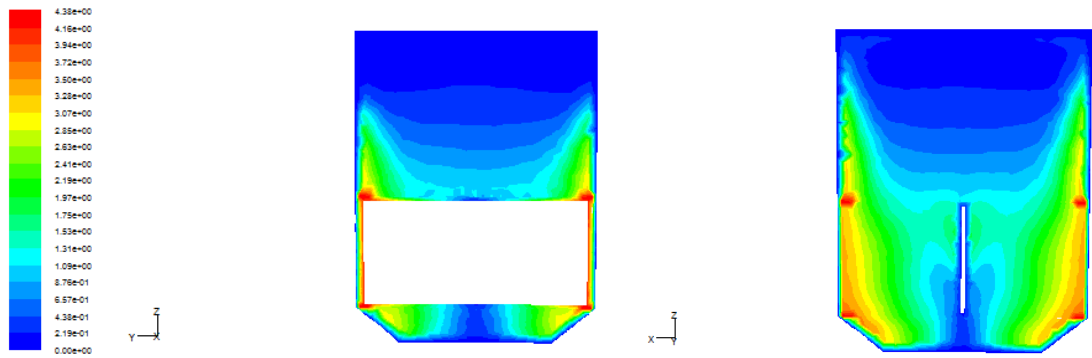
Figure 8.16 Speed contours of the parallel and vertical sections of the stirrer in the 3000L industrial-scale reactor.

From Figure 8.17, it can be seen that the fluid from the upper part of the reactor, where the acid cefuroxime dropped into the reactor, was not well mixed with the sodium lactate (the lower part of the reactor) at the central mixing region, so it was very unfavourable to the reaction. Therefore, the mixing effectiveness of the reactor should be enhanced.
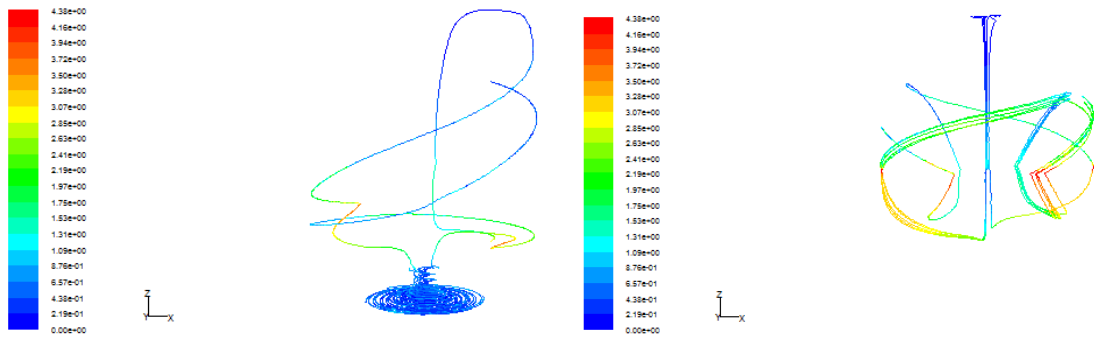
(a) Lower part   (b) Upper part
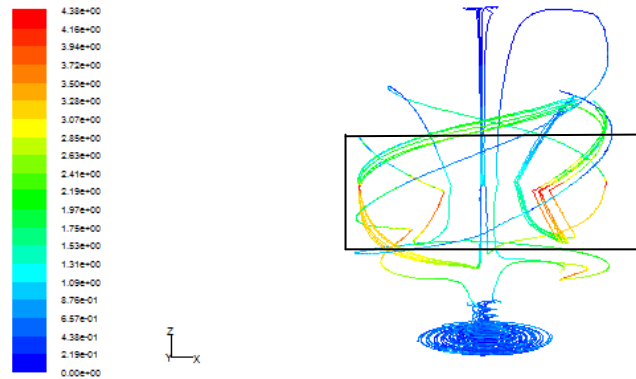
(c) Central mixing region

Figure 8.17 The diagram of the fluid pathline in the 3000L industrial-scale reactor.

8.5.1.1 The Impact of Baffles on Flow State

The reactor was modified by adding four baffles with a height of 600 mm, and width of 200 mm and a thickness of 20 mm can be seen in Figure 8.18. The entire reactor was compartmentalized by three-dimensional mesh with 210388 tetrahedral cells in total where the main reactor region contained 153347 cells and the mixing paddle region contained 57041 cells. We also tried: a) adding three baffles with a height of 600 mm, a width of 300 mm and a thickness of 20 mm; b) adding four baffles with a height of 600 mm, a width of 300 mm and a thickness of 20 mm; c) adding three baffles with a height of 600 mm, a width of 200 mm and a thickness of 20 mm. However, those three cases did not show as good a result as the first one.

H=20 mm

L=600 mm

D=200 mm
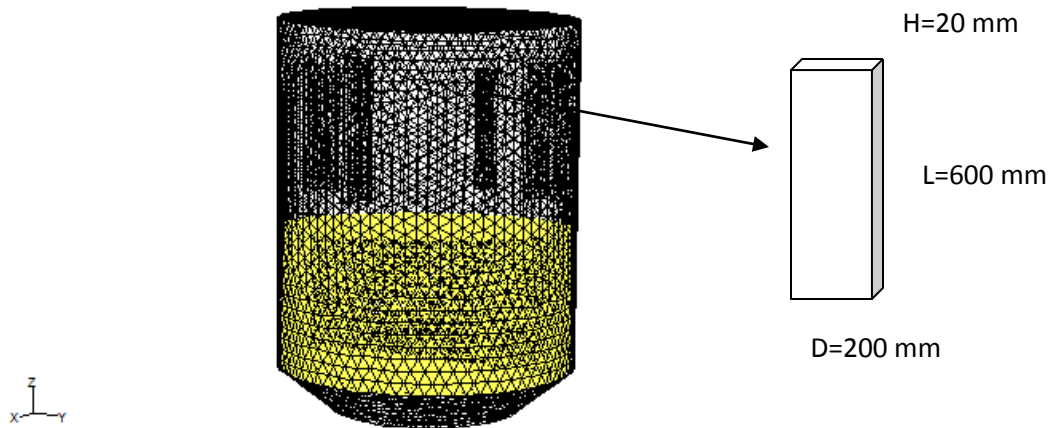
Figure 8.18 The 3000L industrial-scale reactor with four baffles simulation meth diagram.

It can be seen from Figure 8.19, that the highest velocity of the fluid in the reactor was 4.16 m·s^{-1}, and the lowest was 0.00947 m·s^{-1}. The velocity distribution in the reactor changed with the effect of the baffles. The fluid in the upper part, where the original velocity was low, produced a higher velocity. From Figure 8.20, it can be seen that adding the baffles had less effect on the flow in the lower part of the reactor. But the impact on the upper part of the reactor was very clear, which enhanced the mixing effectiveness of the upper part and the central mixing region of the reactor.
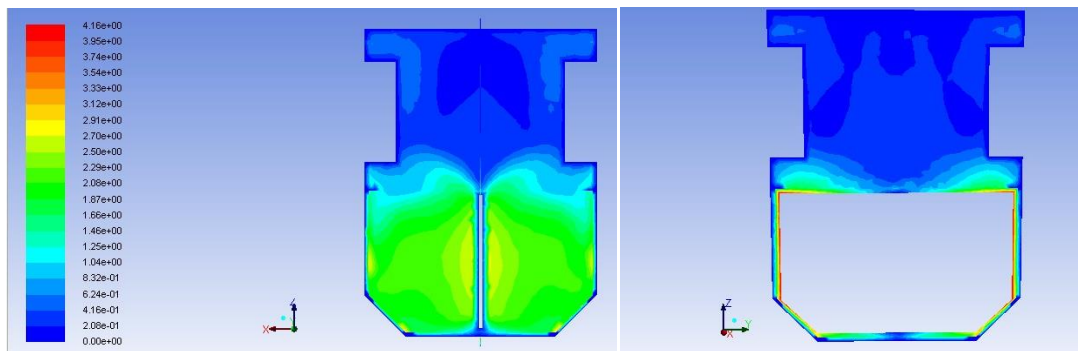
Figure 8.19 Speed contours of the parallel and vertical sections of the stirrer in the 3000L industrial-scale reactor with four baffles.

(a) Lower part   (b) Upper part

(c) Central mixing region
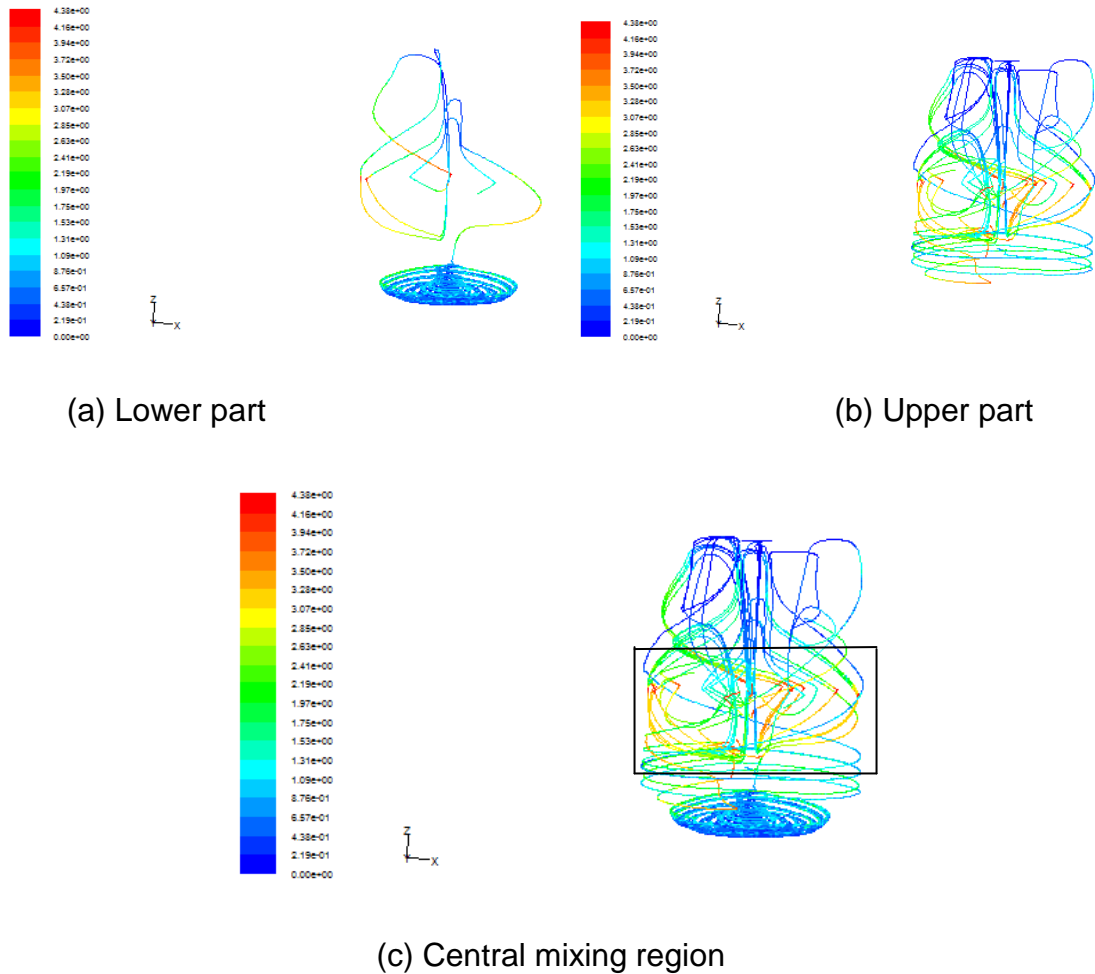
Figure 8.20 The diagram of fluid pathline in the 3000L industrial-scale reactor with four baffles.

8.5.1.2 The Impact of Stirrers on Flow State

To further enhance the mixing, on the basis of the same size as the original reactor, adding three baffles with a height of 1800 mm, a width of 200 mm and a thickness of 20 mm, and two stirrers with a height of 300 mm, a width of 800 mm, a thickness of 20 mm and a tilt angle of 45° formed another modified reactor (Figure 8.21).
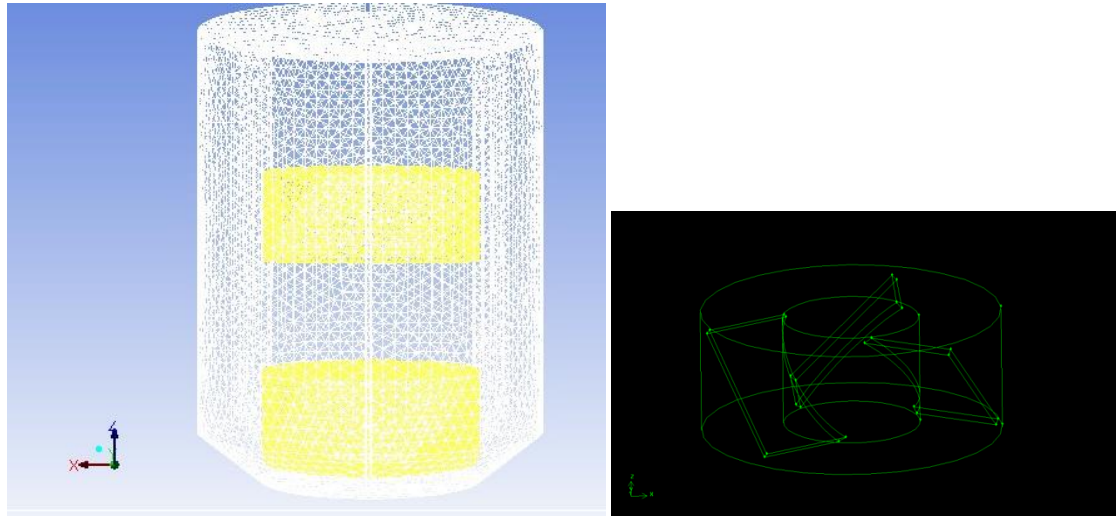
Figure 8.16 The industrial-scale reactor with three baffles and two stirrers' simulation meth diagram.

It can be seen from Figure 8.22, that the highest velocity of the fluid in the reactor was 2.854 m·s^{-1}, and the lowest was 0.00976 m·s^{-1}. The biggest advantage of this new structure was that, under the same stirring speed, it can reduce the speed gap between the fluid in the upper and lower part of the reactor. On the one hand, this can make the supersaturation distribution in the reactor become more uniform, thus preventing local supersaturation becoming too high. On the other hand, the smaller speed gap can reduce the risk of the breakage of crystals.

From Figure 8.23, it can be seen that the fluid from the lower part of the reactor went up along the middle of the reactor, while the fluid from the upper part of the reactor dropped along the wall and rose in the central mixing region. This whole disturbance fully enhanced mixing effectiveness between the reactants, resulting in more uniform crystal size distribution.
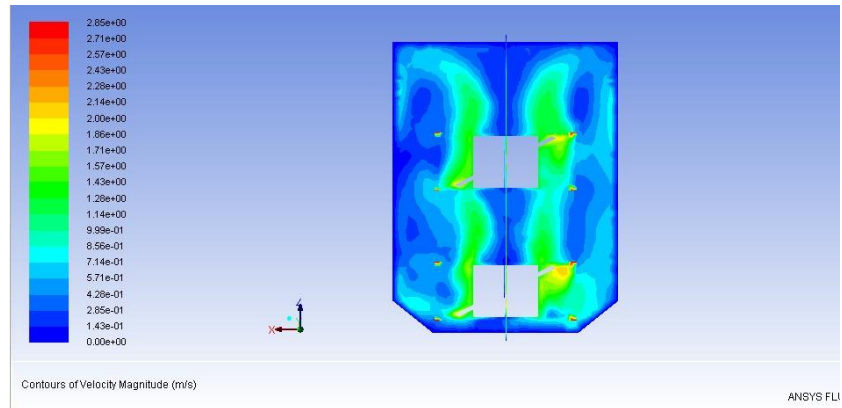
Figure 8.17 Speed contours of the 3000L industrial-scale reactor with three baffles and two stirrers.
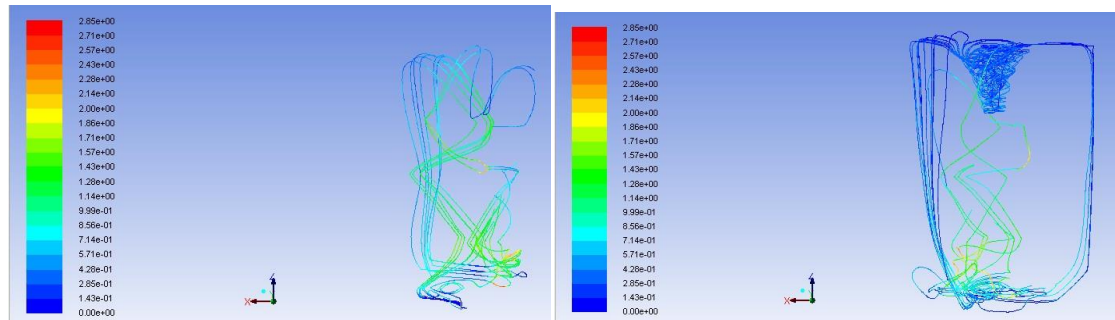
(a) Lower part

(b) Upper part
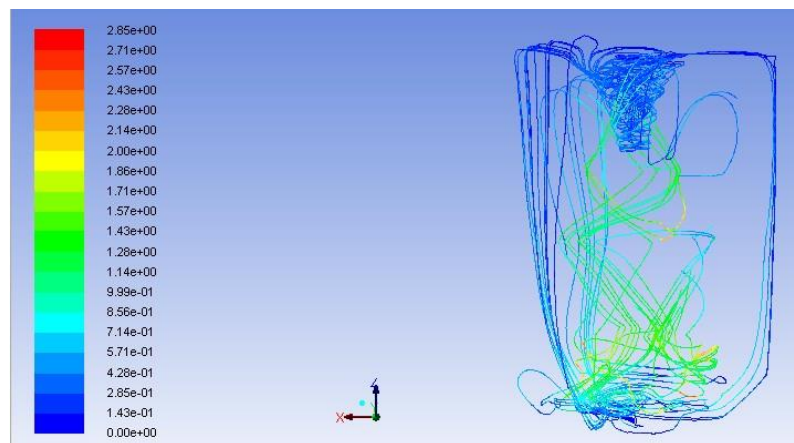
(c) Central mixing region

Figure 8.18 The diagram of fluid pathline in the 3000L industrial-scale reactor with three baffles and two stirrers.

8.5.2 Reactor Design for Industrialization

This calculation was based on the operating time and product handling capacity of a 3000L conventional batch reactor used in industrial production. It was also an embodiment of this crystallizer which has been chosen for the purposes of describing the feasibility and advantages when industrialized.

In industrial production, the completion of one production cycle required approximately 10 hours. As can be seen in Table 8.7, if the filtration process cannot be finished continuously with the reaction process, this reactive crystallization process needed to be done within two hours. So it needed four 50L crystallizers to replace the old 3000L conventional batch reactor. But if the filtration process can be finished continuously with the reaction process, it needs only one 50L crystallizer to achieve the product handling capacity of the 3000L conventional batch reactor. This crystallizer can achieve the same product handling capacity with a smaller volume, in other words, it can achieve a greater amount of product handling with the same volume.

Table 8.7 Reactor design for industrialization

Operation time	2h	10h
Flow rate	1500L/h	300L/h
Tank volume	200L (4*50L)	40L (1*50L)
Tube volume	550L	110L
Tube Radius (length)	6.6cm (10m)	5.9cm (10m)
	4.6cm (20m)	4.2cm (20m)

8.6 Final Remarks

1. The structural parameters of the crystallizer proposed in this study were only an example. The residence time in the tank reactor should be determined by reaction kinetics and adapted by flow rate and the scale of the tank reactor. Besides, the scale of the tank reactor also needed to be designed based on production requirements. If necessary, multiple tanks can be used in parallel. The flow rate of the mixture within the crystallizer, which can be controlled by pumps or valves, should be equal to the feed flow rate so as to ensure a constant liquid level position within the tank reactor. For those crystal growth processes which require a relatively long residence time, the scale of the tank reactor can be larger and the tubular reactor can also be placed vertically or spirally. One or more pairs of impinging jets can be used to mix two or more fluids.

2. Manual seeding can be done at any point in the system, such as in the tank reactor, the tubular reactor or through the jet fluid itself. In some situations, this continuous process may be self-seeding, for example, the first crystals to form inside the tank reactor can serve as seed for the material that flows through thereafter. When using this process, the reactants should be soluble in all the solvents used and the reaction product needs to be highly insoluble in these solvents. The solvent acts as both the solvent and anti-solvent for the reactive crystallization process.

3. Changing the structure and number of the stirrers and join baffles is another method to improve the mixing of the reactor. On the one hand, this can make the supersaturation distribution in the reactor more uniform. On the other hand, the smaller speed gap can reduce the risk of the crystal breakage.

Chapter 9
Conclusions and Future Work

This chapter gives an overview of the main conclusions drawn from the work presented in this thesis and some suggestions for future research direction.

9.1 Conclusions

1. In Chapter 5, the solubility of sodium cefuroxime in water, ethanol, and the mixture of water and ethanol was measured at various temperatures and *pH* values, and was correlated in models. The derived solubility models were applied together with an on-line ATR-FTIR probe to monitor in real-time the supersaturation during the re-crystallization process of cefuroxime sodium. This provided a means for studying the effect of operating parameters on the crystal quality. It was found that the anti-solvent flow rate of 2 mL·min^{-1} can be considered as the optimum value. Re-crystallization under the optimised operational condition has improved crystallinity as characterised by XRD pattern. The positive relationship between the stability of sodium cefuroxime and the crystallinity was also observed.

2. In Chapter 6, process analytical technology (PAT) including focused beam reflectance measurement (FBRM) was used to optimize the operating conditions including reaction temperature, feed rate, stirring speed, and seed loadings for the reactive synthesis of sodium cefuroxime. The optimized operating parameters were: 20 – 25 ^{o}C for reaction temperature, 4 mL·min^{-1} for feed rate, 80 – 100 rpm for stirring speed, and 0.407 g for the amount of seeds in the 1L crystallizer; 20 – 25 ^{o}C for reaction temperature, 4 mL·min^{-1} for feed rate, 50 rpm for stirring speed, and 4.07 g for the amount of seeds in the 10L crystallizer.

3. In Chapter 7, reactive crystallization of sodium cefuroxime was examined and found to have three main features: rapid reaction, very low solubility of sodium cefuroxime in the solvent, and as a result huge supersaturation. Based on the mechanistic understanding, the process was designed to have an impinging jet mixer submerged in the solution of a stirred tank crystallizer, putting the jet nozzles as close as possible to the stirrer. The thinking was that the impinging jet mixer achieved high intensity micromixing of fluids so as to form a homogeneous compound prior to the start of nucleation, and that the formed nuclei or the small particles were immediately dispersed in the slurries of the stirred tank crystallizer where crystals were growing so that these nuclei, or small particles leaving the jet nozzles, would move to and grow on the surfaces of the growing crystals, rather than the nuclei and small particles themselves being further aggregated. The stirred tank crystallizer allowed the mixture to have sufficient residence time in the tank to undergo growing (or aggregates) to larger high quality crystals. The feed speed, angle and spacing of nozzles were also optimised based on the performance of the product. The diameters of the two nozzles were 0.13 mm and 0.065 mm in the 1L crystallizer, 0.3 mm and 0.15 mm in the 10L crystallizer. The experimental results indicated that both 1L and 10L crystallizers provided high quality products. Both 1L and 10L crystallizers produced crystals of higher crystallinity (XRD pattern), narrow size distribution (*Morphologi* G3), high stability (stability test), and purity (HPLC).

4. In Chapter 8, a continuous process for organic reactive crystallization synthesis was designed and scaled up by process analytical technology (PAT) and the computational fluid dynamics (CFD) simulation method. It provided two reactors, a tank reactor and a tubular reactor, in series for conducting a rapid reactive crystallization process of pharmaceutical compounds. This process separated the reaction and crystal growth processes with the tank reactor (reaction/nucleation area) and the tubular reactor (crystal growth area) in series based on their respective characteristics, hence achieving a continuous operation. Impinging jet mixers were used in the tank reactor to mix the

reactants sufficiently and quickly before nucleation. The crystals obtained from this process had uniform size distribution, great stability, and longer shelf-life both in 1L and 50L crystallizers. The high stability products produced by this process also perform superior crystal structure when compared with product formed by the batch process which used the same quality and kind of reactants. Moreover, the continuous process design could achieve a greater amount of product handling and reduce the batch-to-batch variation.

In summary, this work first optimized the anti-solvent re-crystallization process for seed preparation and the operating parameters for the reactive crystallization process, reactive synthesis of sodium cefuroxime, and then designed a continuous crystallization process with impinging jet mixer for this process based on the PAT, modelling and simulation method, and finally scaled it up successfully.

9.2 Suggestions for Future Work

Although interesting and promising results were found in this study, more challenges than addressed in this work need to be considered in order to further understanding and optimize the reactive crystallization process. Below is a summary of the suggestions for future work.

1. More methods of adding seeds can be used for further optimization of the reactive crystallization process. In this study, the anti-solvent re-crystallization process was used for seed preparation (Chapter 5), and the seeds obtained from this process were directly added into the reactor with a small amount of solvent mixture before the reactants were added into the reactor (before the reaction started) for the seeded experiments in Chapters 6 and 7.

For the continuous crystallization process (Chapter 8), self-seeding was used which means that there was no adding of seeds. In fact, using seeds may further improve the quality of the product obtained from the continuous crystallization process. The original design was putting seeds in one reactant

solution so that the concentration of the seeds could stay the same during the entire continuous crystallization process. However, due to the pumps not being able to transport particles this method of adding seeds could not be achieved. Besides, there are other methods of adding seeds, for example, the seeds can be added in batches, in a tubular reactor or at any point in this system.

2. In this study, we assumed that the crystal growth was likely to follow an aggregation mechanism rather than a surface growth model or a combination of the two mechanisms. Based on these considerations, the design of a combination of an impinging jet mixer and a stirred tank crystallizer was proposed and optimized. Although from the SEM, *Morphologi* G3 and FBRM results, this assumption was evidenced and reasonable, it was merely a qualitative analysis. More instruments, such as dynamic light scattering (DLS), could be used for further studying the aggregation mechanism. Besides, due to the rapid reaction, it was hard to catch the on-line nucleation and growth process of sodium cefuroxime by the camera in our laboratory. If some high-speed imaging technologies, such as a high speed camera can be used, the reactive crystallization process would be further understood and even the relationship between the stability and the aggregation would be uncovered. As a result, without the judgement of the off-line stability test, the quality of the drug can be controlled on-line.

3. The CFD simulation work for determination of the residence time distribution in the crystallizer (Chapter 8) was carried out based on the Euler-Euler multi-phase approach without the reaction. The sodium cefuroxime crystal used in this simulation work was a uniform size without considering the size distribution. Although the simulation work in this study was merely the preliminary work for design, it would be worthwhile to develop a more accurate approach which could be applied to other processes by adding the reaction model for the concentration changes or the population balance (PB) model for the particle size distribution.

4. Some valuable designs and suggestions for the improvement of the industrial equipment has been proposed in Chapter 8 based on the CFD simulation results. The industrial application could be carried out. And the industrial application of the continuous crystallizer could also be carried out.

Reference

Abbasi, M., Abduli, M.A., Omidvar, B., Baghvand, A., 2013. Forecasting municipal solid waste generation by hybrid support vector machine and partial least square model. International Journal of Environmental Research 7, 27-38.

Acree, W.E., 1992. Mathematical representation of thermodynamic properties: Part 2. Derivation of the combined nearly ideal binary solvent (NIBS)/Redlich-Kister mathematical representation from a two-body and three-body interactional mixing model. Thermochimica Acta 198, 71-79.

Adams, E., 1969. Effect of organic matter and increased inoculum size on minimum inhibitory concentration of crystal violet towards staphylococcus aureus at various ph values. Journal of Pharmacy and Pharmacology S 21, S182-183.

Adnadjevic, B., Vukicevic, J., Filipovicrojka, Z., Markovic, V., 1990. The influence of nax zeolite particle-size on crystallinity measured by the xrd method. Zeolites 10, 699-702.

Akindeju, M.K., Pareek, V.K., Tade, M.O., Rohl, A.L., 2010. A novel spinning disc continuous stir tank and settler reactor (SDCSTR) model for continuous synthesis of Titania: a phenomenological model. Chemical Engineering Communications 198, 73-84.

Alatalo, H., Hatakka, H., Kohonen, J., Reinikainen, S.-p., Louhi-kultanen, M., 2010a. Process control and monitoring of reactive crystallization of l-glutamic acid. Aiche Journal 56, 2063-2076.

Alatalo, H., Kohonen, J., Qu, H., Hatakka, H., Reinikainen, S.-P., Louhi-Kultanen, M., Kallas, J., 2008. In-line monitoring of reactive crystallization process based on ATR-FTIR and Raman spectroscopy. Journal of Chemometrics 22, 644-652.

Alatalo, H.M., Hatakka, H., Louhi-Kultanen, M., Kohonen, J., Reinikainen, S.-P., 2010b. Closed-loop control of reactive crystallization. Part I: Supersaturation-controlled crystallization of L-Glutamic acid. Chemical Engineering & Technology 33, 743-750.

Anderson, B.D., Wygant, M.B., Xiang, T.X., Waugh, W.A., Stella, V.J., 1988. Preformulation solubility and kinetic-studies of 2',3'-dideoxypurine nucleosides - potential anti-aids agents. International Journal of Pharmaceutics 45, 27-37.

Barrett, P., Glennon, B., 1999. In-line FBRM monitoring of particle size in dilute agitated suspensions. Particle & Particle Systems Characterization 16, 207-211.

Barus, C., 1902. On spontaneous nucleation and on nuclei produced by shaking solutions. Philosophical Magazine 4, 262-269.

Beggs, H.D., Parker, J.D., 1971. Determination of pressure drop optimum pipe size for 2 phase slug flow in an inclined pipe. Journal of Engineering for Industry 93, 763-764.

Berry, D.A., Ng, K.M., 1997. Synthesis of reactive crystallization processes. Aiche Journal 43, 1737-1750.

Benedict, U., Dufour, C., Mayne, K., 1979. Low-temperature xrd study of actinide metals and compounds. Journal De Physique 40, 103-105.

Birch, M., Fussell, S.J., Higginson, P.D., McDowall, N., Marziano, I., 2005. Towards a PAT-Based strategy for crystallization development. Organic Process Research & Development 9, 360-364.

Bocek, M., Kratochvil, P., Lukac, P., 1962. The effect of impurities on the critical resolved shear stress of zinc single crystals. Physica Status Solidi 2, 1221-1224.

Borissova, A., Khan, S., Mahmud, T., Roberts, K.J., Andrews, J., Dallin, P., Chen, Z.-P., Morris, J., 2009. In Situ Measurement of Solution Concentration during the Batch Cooling Crystallization of L-Glutamic Acid using ATR-FTIR

Spectroscopy Coupled with Chemometrics. Crystal Growth & Design 9, 692-706.

Boswell, M.C., Iler, R.K., 1936. Nickel catalysts. I. The effect of the temperature of preparation on the crystal size and composition of nickel oxide. Journal of the American Chemical Society 58, 924-928.

Bragg, W.H., 1912. On the direct or indirect nature of the ionization by X-rays. Philosophical Magazine 23, 647-650.

Bridgman, P.W., 1933. The effect of pressure on the electrical resistance of single metal crystals at low temperature. Proceedings of the American Academy of Arts and Sciences 68, 95-123.

Brodersen, R., 1947. Inactivation of penicillin-g by acids - a reaction-kinetic investigation. Transactions of the Faraday Society 43, 351-355.

Brugel, W., 1965a. Chemical applications of infrared spectroscopy. Angewandte Chemie-International Edition 4, 377-378.

Brugel, W., 1965b. Theory of electronic spectra of organic molecules. Angewandte Chemie-International Edition 4, 269-270.

Bube, R.H., Thomsen, S.M., 1955. Photoconductivity and crystal imperfections in cadmium sulfide crystals .1. effect of impurities. Journal of Chemical Physics 23, 15-17.

Buckle, E.R., 1961. Studies on freezing of pure liquids .2. kinetics of homogeneous nucleation in supercooled liquids. Proceedings of the Royal Society of London Series a-Mathematical and Physical Sciences 261, 189-190.

Bunn, C.W., Emmett, H., 1949. Crystal growth from solution .1. layer formation on crystal faces. Discussions of the Faraday Society, 119-120.

Burshtei.Ai, Tsvetkov, Y.D., 1974. Diffusion-controlled recombination of radicals in molecular-crystals. Doklady Akademii Nauk Sssr 214, 369-372.

Brusewitz, A.M., 1982. A filtering device for oriented xrd mounts. Clay Minerals 17, 263-264.

Burton, A.A., Chiswell, E.B., Claussen, W.H., Huey, C.S., Senger, J.F., 1948. Reactor design for manufacture of toluene by catalytic reforming. Chemical Engineering Progress 44, 195-200.

Cabri, W., Siviero, E., Daverio, P.L., Cristiano, T., Felisi, C., Longoni, D., 2003. Process for the synthesis of beta-Lactam derivatives, US 6,642,378 B1.

Cai, Z.W., Li, M.C., Yang, J., 2007. The synthesis process of cefuroxime sodium, CN 101054386 A.

Careno, S., Boutin, O., Badens, E., 2012. Drug recrystallization using supercritical anti-solvent (SAS) process with impinging jets: Effect of process parameters. Journal of Crystal Growth 342, 34-41.

Castle, E.S., 1934. The spiral growth of single cells. Science 80, 362-363.

Chen, M., Ma, C.Y., Mahmud, T., Darr, J.A., Wang, X.Z., 2011. Modelling and simulation of continuous hydrothermal flow synthesis process for nano-materials manufacture. Journal of Supercritical Fluids 59, 131-139.

Chen, P.C., Chen, C.C., Fun, M.H., Liao, O.Y., Jiang, J.J., Wang, Y.S., Chen, C.S., 2004. Mixing and crystallization kinetics in gas-liquid reactive crystallization. Chemical Engineering & Technology 27, 519-528.

Chen, Q., Yin, F., Zheng, L., Xiao, X., Lin, J., 2013. Crystallization behavior of polypropylene-graft-cardanol prepared by reactive extrusion. International Polymer Processing 28, 43-48.

Chigrinov, V.G., Grebenkin, M.F., 1975. Determination of elastic-constants k11 and k33 and viscosity factor, gamma-1, of nematic liquid-crystals from orientational electrooptical effects. Kristallografiya 20, 1240-1244.

Choo, Y.J., Kang, B.S., 2007. The effect of jet velocity profile on the characteristics of thickness and velocity of the liquid sheet formed by two impinging jets. Physics of Fluids 19.

Cohen, E.R., 1954. The role of exponential experiments in reactor design. Chemical Engineering Progress Symposium Series 50, 72-81.

Cook, M.C., Gregory, G.I., Bradshaw, J., 1976a. 7-hydrocarbonoxyimino-acetamido-3-carbamoyloxymethylceph-3-em-4-carboxylic acids. Glaxo Laboratories Limited, Greenford, England, US 3,974,153.

Cook, M.C., Gregory, G.I., Bradshaw, J., 1976b. 7-β-acylamido-3-carbamoyloxymethylceph-3-em-4-carboxylic acids and salts thereof. Glaxo Laboratories Limited, Greenford, England, US 3,966,717.

Crisp, H.A., Clayton, J.C., Elliott, L.G., Wilson, E.M., 1991a. Process for preparing cefuroxime axetil, US 5,013,833.

Crisp, H.A., Clayton, J.C., Wilson, E.M., 1991b. Process for preparation of cefuroxime axetil, US 4,994,567.

Danckwerts, P.V., 1953. Continuous flow systems - distribution of residence times. Chemical Engineering Science 2, 1-13.

Danckwerts, P.V., 1958. Local residence-times in continuous-flow systems. Chemical Engineering Science 9, 78-79.

Danckwerts, P.V., Jenkins, J.W., Place, G., 1954. The distribution of residence-times in an industrial fluidised reactor. Chemical Engineering Science 3, 26-35.

David J. Am Ende, Thomas C. Crawford, Weston, N.P., 2003. Reactive crystallization method to improve particle size, US 6,558,435 B2.

Debaun, R.M., Katz, S., 1961. Approximations to residence time distributions in mixing systems and some applications thereof. Chemical Engineering Science 16, 97-104.

Dehkordi, A.M., Ebrahimi, A.A., 2009. Catalytic Wet Peroxide Oxidation of Phenol in a New Two-Impinging-Jets Reactor. Industrial & Engineering Chemistry Research 48, 10619-10626.

Dehkordi, A.M., Safari, I., Ebrahimi, A.A., 2009. Solid-Liquid Catalytic Reactions in a New Two-Impinging-Jets Reactor: Experiment and Modeling. Industrial & Engineering Chemistry Research 48, 2861-2869.

Desikan, S., Anderson, S.R., Meenan, P.A., Toma, P.H., 2000. Crystallization challenges in drug development: scale-up from laboratory to pilot plant and beyond. Current opinion in drug discovery & development 3, 723-733.

Devilliers, M.M., Vanderwatt, J.G., Lotter, A.P., 1992. Kinetic-study of the solid-state photolytic degradation of 2 polymorphic forms of furosemide. International Journal of Pharmaceutics 88, 275-283.

Doki, N., Yokota, M., Sasaki, S., Kubota, N., 2004. Simultaneous crystallization of D- and L-asparagines in the presence of a tailor-made additive by natural cooling combined with pulse heating. Crystal Growth & Design 4, 1359-1363.

Dunuwila, D.D., Berglund, K.A., 1997. ATR FTIR spectroscopy for in situ measurement of supersaturation. Journal of Crystal Growth 179, 185-193.

Ebian, A.R., Moustafa, M.A., Khalil, S.A., Motawi, M.M., 1975. Succinylsulfathiazole crystal forms .2. effect of additives on kinetics of interconversion. Journal of Pharmaceutical Sciences 64, 1481-1484.

Edwards, L.J., 1950. The hydrolysis of aspirin - a determination of the thermodynamic dissociation constant and a study of the reaction kinetics by ultra-violet spectrophotometry. Transactions of the Faraday Society 46, 723-724.

Elert, J., Karlsson, S., Gerdle, B., 1998. One-year reproducibility and stability of the signal amplitude ratio and other variables of the electromyogram: test-retest of a shoulder forward flexion test in female workers with neck and shoulder problems. Clinical Physiology 18, 529-538.

Ellin, R.I., Wills, J.H., 1964. Oximes antagonistic to inhibitors of cholinesterase .1. Journal of Pharmaceutical Sciences 53, 995-996.

Fairclough, R.A., Hinshelwood, C.N., 1937. The functional relation between the constants of the Arrhenius equation. Journal of the Chemical Society, 538-546.

Falco, J.W., Walker, R.D., Shah, D.O., 1974. Effect of phase-volume ratio and phase-inversion on viscosity of microemulsions and liquid-crystals. Aiche Journal 20, 510-514.

Felipe Soares, F.L., Carneiro, R.L., 2014. Evaluation of analytical tools and multivariate methods for quantification of co-former crystals in ibuprofen-nicotinamide co-crystals. Journal of Pharmaceutical and Biomedical Analysis 89, 166-175.

Fitzgerald, F.J., 1902. The conversion of amorphous carbon to graphite. Journal of the Franklin Institute 154, 321-348.

Fleischmann, P., Michaelis, L., 1907. The formulation of precipitation reaction following Hamburger and Arrhenius. Biochemische Zeitschrift 3, 425-430.

Foner, H.A., Adan, N., 1983. The characterization of papers by X-ray-diffraction (XRD) - measurement of cellulose crystallinity and determination of mineral-composition. Journal of the Forensic Science Society 23, 313-321.

Fu, G.Q., Zhou, Z.J., Dong, Q.B., Long., W.G., 2010. Preparation of cefuroxime sodium, CN 101906109 A.

Garrett, E.R., 1957. The Kinetics of Solvolysis of acyl esters of salicyclic acid. Journal of the American Chemical Society 79, 3401-3408.

Garside, J., Tavare, N.S., 1985. Mixing, reaction and precipitation - limits of micromixing in an msmpr crystallizer. Chemical Engineering Science 40, 1485-1493.

Goldstein, S., Rosenhead, L., 1936. Boundary layer growth. Proceedings of the Cambridge Philosophical Society 32, 392-401.

Gorban, A.N., Karlin, I.V., 1991. The structure and approximations of Chapman-EnsKog expanding for the grad linearized equations. Zhurnal Eksperimentalnoi I Teoreticheskoi Fiziki 100, 1153-1161.

Gosselin, G., Girardet, J.L., Perigaud, C., Benzaria, S., Lefebvre, I., Schlienger, N., Pompon, A., Imbach, J.L., 1996a. New insights regarding the potential of the pronucleotide approach in antiviral chemotherapy. Acta Biochimica Polonica 43, 196-208.

Gosselin, G., Girardet, J.L., Perigaud, C., Benzaria, S., Lefebvre, I., Schlienger, N., Pompon, A., Imbach, J.L., 1996b. New insights regarding the potential of the pronucleotide approach in antiviral chemotherapy. Acta Biochimica Polonica 43, 195-208.

Gower, P.E., Dash, C.H., 1977. Pharmacokinetics of cefuroxime after intravenous-injection. European Journal of Clinical Pharmacology 12, 221-227.

Greenwood, D., Pearson, N.J., O'Grady, F., 1976. Cefuroxime a new cephalosporin antibiotic with enhanced stability to enterobacterial beta lactamases. Journal of Antimicrobial Chemotherapy 2, 337-343.

Groen, H., Roberts, K.J., 1999. Application of ATR FTIR spectroscopy for on-line determination of solute concentration and solution supersaturation, Proceedings of the 14th international symposium on industrial crystallization, Cambridge.

Gundy, L., 1987. Effect of detrital muscovite on illite crystallinity measurement by X-ray-diffraction (XRD). Aapg Bulletin-American Association of Petroleum Geologists 71, 1007-1007.

Guo, Z., Jones, A.G., Li, N., 2006. The effect of ultrasound on the homogeneous nucleation of BaSO4 during reactive crystallization. Chemical Engineering Science 61, 1617-1626.

Hacherl, J.M., Paul, E.L., Buettner, H.M., 2003. Investigation of impinging-jet crystallization with a calcium oxalate model system. Aiche Journal 49, 2352-2362.

Hatakka, H., Alatalo, H., Louhi-Kultanen, M., Lassila, I., Haeggstrom, E., 2010. Closed-Loop Control of Reactive Crystallization PART II: Polymorphism Control of L-Glutamic Acid by Sonocrystallization and Seeding. Chemical Engineering & Technology 33, 751-756.

Heath, A.R., Fawell, P.D., Bahri, P.A., Swift, J.D., 2002. Estimating average particle size by focused beam reflectance measurement (FBRM). Particle & Particle Systems Characterization 19, 84-95.

Hempel, W., von, H., 1900. The formation of amorphous silicon, silicon sulphide, silicon chloride and of sulpho silicates. Zeitschrift Fur Anorganische Chemie 23, 32-42.

Hermanto, M.W., Chow, P.S., Tan, R.B.H., 2010. Implementation of Focused Beam Reflectance Measurement (FBRM) in Antisolvent Crystallization to Achieve Consistent Product Quality. Crystal Growth & Design 10, 3668-3674.

Higuchi, T., Havinga, A., Busse, L.W., 1950. The kinetics of the hydrolysis of procaine. Journal of the American Pharmaceutical Association-Scientific Edition 39, 405-410.

Hirasawa, I., Nakagawa, H., Yosikawa, O., Itoh, M., 1997. Phosphate recovery by reactive crystallization of magnesium ammonium phosphate: Application to wastewater, in: Botsaris, G.D., Toyokura, K. (Eds.), Separation and Purification by Crystallization, pp. 267-276.

Hiwalea, P., Amin, A., Patel, S., Bansal, A.K., 2009. Variables affecting reconstitution behavior of cefuroxime sodium for injection. Reconstitution of cefuroxime sodium injection/Asian Journal of Pharmaceutical Sciences 4, 23-31.

Hoener, B.A., Sokolosk.Td, Mitscher, L.A., Malspeis, L., 1974. Kinetics of dehydration of epitetracycline in solution. Journal of Pharmaceutical Sciences 63, 1901-1904.

Huang, S.T., Lu, P.Q., Zhang, X.L., Qiu, G.C., 1981. XPS and XRD study of thermal-oxidation and decomposition of poly(vinylferrocene). Acta Chimica Sinica 39, 512-519.

Hubbard, C.R., Robbins, C.R., Snyder, R.L., 1983. XRD quantitative phase-analysis using the nbs quant82 system. Advances in X-Ray Analysis 26, 149-156.

Hu, Y.R., Wang, G.S., Hu, L.M., Tan, Q.Z., Dong, W.C., Wang, C.J., 2011. Recrystallization of cefuroxime sodium, CN 101967156 A.

Humber, D.C., Laing, S.B., Weingarten, G.G., 1981. .Process for preparing 3-carbamoyloxymethylcephalosporins. Glaxo Group Limited, London, England, US 4,284,767.

Inoue, M., Shima, K., Inazu, K., 1984. Crystal-growth of cephalothin sodium in frozen solution .2. effects of amount of seed, concentration, and temperature. Yakugaku Zasshi-Journal of the Pharmaceutical Society of Japan 104, 1268-1274.

Inoue, M., Hirasawa, I., 2013. The relationship between crystal morphology and XRD peak intensity on CaSO4 center dot 2H(2)O. Journal of Crystal Growth 380, 169-175.

Johnson, M.D., May, S.A., Calvin, J.R., Remacle, J., Stout, J.R., Diseroad, W.D., Zaborenko, N., Haeberle, B.D., Sun, W.-M., Miller, M.T., Brennan, J., 2012. Development and Scale-Up of a Continuous, High-Pressure, Asymmetric

Hydrogenation Reaction, Workup, and Isolation. Organic Process Research & Development 16, 1017-1038.

Johnston, W.G., 1962. Effect of impurities on flow stress of lif crystals. Journal of Applied Physics 33, 2050-2051.

Jouyban, A., Acree, W.E., 2006. In silico prediction of drug solubility in water-ethanol mixtures using Jouyban-Acree model. J Pharm Pharmaceut Sci 9, 262-269.

Juttner, F., 1909. Reaction kinetics and diffusion. Zeitschrift Fur Physikalische Chemie--Stochiometrie Und Verwandtschaftslehre 65, 595-623.

Kelkar, V.V., Ng, K.M., 1999. Design of reactive crystallization systems incorporating kinetics and mass-transfer effects. Aiche Journal 45, 69-81.

Kisbye, J., Schou, S.A., 1951. Studies on the stability of drugs. 3. Racemization of adrenaline. Dansk tidsskrift for farmaci 25, 185-197.

Kitamura, M., Konno, H., Yasui, A., Masuoka, H., 2002. Controlling factors and mechanism of reactive crystallization of calcium carbonate polymorphs from calcium hydroxide suspensions. Journal of Crystal Growth 236, 323-332.

Kossel, W., 1934. The energetics of surface procedures. Annalen Der Physik 21, 457-480.

Kruger, F., 1904. Quartz glass. Physikalische Zeitschrift 5, 391-392.

Kunchur, N.R., 1965. Effect of environment on orientation of nitrate ions in crystals. Nature 208, 778-779.

Lasko, W.R., 1961. The effect of environment on the crystal morphology of copper oxide as observed by high magnification electron microscopy. Journal of Electron Microscopy 10, 222-232.

Leaf, W., 1908. Drifted ice-crystals. Nature 77, 271-271.

Lehmann, O., 1900. Structure, system and magnetic behaviour of liquid crystals and their miscibility with the solid ones. Annalen Der Physik 2, 649-705.

Lehmann, O., 1915. Solution and precipitation of substances, in particular of liquid crystals. Annalen Der Physik 47, 832-852.

Leubner, I.H., 1998. A new crystal nucleation theory for continuous precipitation of silver halides. Journal of Imaging Science and Technology 42, 355-364.

Lewiner, F., Klein, J.P., Puel, F., Fevotte, G., 2001. On-line ATR FTIR measurement of supersaturation during solution crystallization processes. Calibration and applications on three solute/solvent systems. Chemical Engineering Science 56, 2069-2084.

Li, R., Ashgriz, N., 2007. Edge instability and velocity of liquid sheets formed by two impinging jets. Atomization and Sprays 17, 71-97.

Liebig, B., 1846. On Amorphous Quinine As It Exists in the Substance Known in Commerce As Quinoidine. Provincial medical & surgical journal 10, 265-267.

Lindrud, M.D., Kim, S., Wei, C., 2001. Sonic impinging jet crystallization apparatus and process, US 6,302,958 B1.

Liu, P.D., M. Futran, M. Midler, Paul, E.L., 1990. Particle size design of pharmaceuticals by continuously impinging jets precipitation. AIChE Meeting, Chicago.

Liu, W.J., Ma, C.Y., Feng, S.X., Wang, X.Z., 2014. Solubility measurement and stability study of sodium cefuroxime. Journal of Chemical & Engineering Data 59, 807-816.

Lu, J., Wang, J.K., 2006. Agglomeration, breakage, population balance, and crystallization kinetics of reactive precipitation process. Chemical Engineering Communications 193, 891-902.

Lucas, B., Seavey, K.C., Liu, Y.A., 2007. Steady-state and dynamic modeling for new product design for the solid-state polymerization of poly(ethylene terephthalate). Industrial & Engineering Chemistry Research 46, 190-202.

Luckhaus, S., Modica, L., 1989. The gibbs-thompson relation within the gradient theory of phase-transitions. Archive for Rational Mechanics and Analysis 107, 71-83.

Lunde, G., 1926. The formation of mixed crystals through precipitation. Berichte Der Deutschen Chemischen Gesellschaft 59, 2784-2786.

Luo, Y.-H., Tu, Y.-R., Ge, J.-L., Sun, B.-W., 2013. Monitoring the Crystallization Process of Methylprednisolone Hemisuccinate (MPHS) from Ethanol Solution by Combined ATR-FTIR- FBRM- PVM. Separation Science and Technology 48, 1881-1890.

Lusena, C.V., Cook, W.H., 1954. Ice propagation in systems of biological interest .2. effect of solutes at rapid cooling rates. Archives of Biochemistry and Biophysics 50, 243-251.

M. J. Pikal, A. L. Lukes, John E. Lang, Gaines, K., 1978. Quantitative crystallinity determinations for β-lactam antibiotics by solution calorimetry: Correlations with stability. Journal of Pharmaceutical Sciences 67, 767-773.

Ma, C.Y., Chen, M., Wang, X.Z., 2014. Modelling and simulation of counter-current and confined-jet reactors for hydrothermal synthesis of nano-materials. Chemical Engineering Science 109, 26-37.

Ma, C.Y., Wang, X.Z., 2012. Closed-loop control of crystal shape in cooling crystallization of L-glutamic acid. Journal of Process Control 22, 72-81.

Ma, C., 2010. Particle shape distribution control in crystallization processes. University of Leeds.

Mahajan, A.J., Kirwan, D.J., 1996. Micromixing effects in a two-impinging-jets precipitator. Aiche Journal 42, 1801-1814.

Mandare, P.N., Pangarkar, V.G., 2003. Semi-batch reactive crystallization of sodium perborate tetrahydrate: effect of mixing parameters on crystal size. Chemical Engineering Science 58, 1125-1133.

Marcus, A.D., Baron, S., 1959. A comparison of the kinetics of the acid catalyzed hydrolyses of procainamide, procaine, and benzocaine. Journal of the American Pharmaceutical Association 48, 85-90.

Matsuda, Y., Akazawa, R., Teraoka, R., Otsuka, M., 1994. Pharmaceutical evaluation of carbamazepine modifications - comparative-study for photostability of carbamazepine polymorphs by using fourier-transformed reflection-absorption infrared-spectroscopy and colorimetric measurement. Journal of Pharmacy and Pharmacology 46, 162-167.

McComas, S.T., Eckert, E.R.G., 1965. Laminar pressure drop associated with continuum entrance region and for slip flow in a circular tube. Journal of Applied Mechanics 32, 765-766.

Michell, R.M., Muller, A.J., Boschetti-de-Fierro, A., Fierro, D., Lison, V., Raquez, J.M., Dubois, P., 2012. Novel poly(ester-urethane)s based on polylactide: From reactive extrusion to crystallization and thermal properties. Polymer 53, 5657-5665.

Midler, M., E. L. Paul, Whittington, E.F., 1989. Production of high purity, high surface area crystalline solids by turbulent contacting and controlled secondary nucleation. Engineering Foundation Conf. on Mixing, Potosi, Mo.

Midler, M., Paul, E.L., Whittington, E.F., Futran, M., Liu, P.D., Hsu, J., Pan, S.-H., 1994. Crystallization method to improve crystal structure and size, U.S.

Mitrevej, A., Hollenbeck, R.G., 1983. Influence of hydrophilic excipients on the interaction of aspirin and water. International Journal of Pharmaceutics 14, 243-250.

Momonaga, M., Yazawa, H., Kagara, K., 1992. Reactive crystallization of methyl alpha-methoxyimino acetoacetate. Journal of Chemical Engineering of Japan 25, 237-242.

Morgan, N., Wells, C., Kraft, M., Wagner, W., 2005. Modelling nanoparticle dynamics: coagulation, sintering, particle inception and surface growth. Combustion Theory and Modelling 9, 449-461.

Moustafa, M.A., Ebian, A.R., Khalil, S.A., Motawi, M.M., 1975. SUCCINYLSULFATHIAZOLE CRYSTAL FORMS .3. CRYSTAL-GROWTH STUDIES. Journal of Pharmaceutical Sciences 64, 1485-1489.

Munson, J., Stanfield, C.F., Gujral, B., 2006. A review of process analytical technology (PAT) in the US pharmaceutical industry. Current Pharmaceutical Analysis 2, 405-414.

Nielsen, A.E., 1959. The kinetics of crystal growth in barium sulfate precipitation .3. mixed surface reaction and diffusion controlled rate of growth. Acta Chemica Scandinavica 13, 1680-1686.

Nightingale, C.H., 1976. Bioavailability monograph - erythromycin. Journal of the American Pharmaceutical Association 16, 203-206.

Okamura, M., Hanano, M., Awazu, S., 1980. Relationship between the morphological character of 5-nitroacetylsalicylic acid crystals and the decomposition rate in a humid environment. Chemical & Pharmaceutical Bulletin 28, 578-584.

Orloff, G., 1912. The kinetics of chemical reactions. Zeitschrift Fur Physikalische Chemie--Stochiometrie Und Verwandtschaftslehre 80, 280-298.

Parvov, V.F., Shubniko.Av, 1964. Faces of zero growth rate on a crystal of $K_2Cr_2O_7$. Soviet Physics Crystallography, Ussr 9, 361-362.

Pavlow, P., 1904. On several properties of crystals from a thermodynamical point of view. Zeitschrift Fur Krystallographie Und Mineralogie 40, 189-205.

Pikal, M.J., Lukes, A.L., Lang, J.E., Gaines, K., 1978. Quantitative crystallinity determinations for β-lactam antibiotics by solution calorimetry: Correlations with stability. J. Pharm. Sci. 67, 767-773.

Pierron, E.D., Rashkin, J.A., Roth, J.F., 1967. COPPER OXIDE ON ALUMINA .I. XRD STUDIES OF CATALYST COMPOSITION DURING AIR OXIDATION OF CARBON MONOXIDE. Journal of Catalysis 9, 38-39.

Pishch, I.V., Rotman, Romanenko, Z.A., 1986. Feldspar-based ceramic pigments. Glass and Ceramics 43, 125-127.

Pohorecki, R., Baldyga, J., 1983. The use of a new model of micromixing for determination of crystal size in precipitation. Chemical Engineering Science 38, 79-83.

Polissar, M.J., 1932. The relation between the two constants of the arrhenius equation. Journal of the American Chemical Society 54, 3105-3111.

Pollanen, K., Hakkinen, A., Reinikainen, S.P., Louhi-Kultanen, M., Nystrom, L., 2005. ATR-FTIR in monitoring of crystallization processes: comparison of indirect and direct OSC methods. Chemometrics and Intelligent Laboratory Systems 76, 25-35.

Preston, R.D., 1948. Spiral growth and spiral structure .1. spiral growth in sporangiophores of phycomyces. Biochimica Et Biophysica Acta 2, 155-166.

Purwins, M., Enderle, R., Schmid, M., Berwian, P., Mueller, G., Hergert, F., Jost, S., Hock, R., 2007. Phase relations in the ternary Cu-Ga-In system. Thin Solid Films 515, 5895-5898.

Purwins, M., Weber, A., Berwian, P., Muller, G., Hergert, F., Jost, S., Hock, R., 2006. Kinetics of the reactive crystallization of CuInSe2 and CuGaSe2 chalcopyrite films for solar cell applications. Journal of Crystal Growth 287, 408-413.

Rakowski, A., 1906. Kinetics of the consequential reaction of the first order. Zeitschrift Fur Physikalische Chemie--Stochiometrie Und Verwandtschaftslehre 57, 321-340.

Reinecke, S., Kremer, G.M., 1991. A generalization of the Chapman-EnsKog and grad methods. Continuum Mechanics and Thermodynamics 3, 155-167.

Richard, J.A., Kelly, I., Marion, D., Auger, M., Pezolet, M., 2005. Structure of beta-purothionin in membranes: A two-dimensional infrared correlation spectroscopy study. Biochemistry 44, 52-61.

Riecke, E., 1900. Interdependency and balance of triagonal polisystems, an article on the theory of crystal structure. Annalen Der Physik 3, 545-577.

Rietema, K., 1958. Heterogeneous reactions in the liquid phase - influence of residence time distribution and interaction in the dispersed phase. Chemical Engineering Science 8, 103-112.

Rodebush, W.H., Clarke, J.V., 1958. Spontaneous nucleation in supersaturated vapors. Proceedings of the National Academy of Sciences of the United States of America 44, 536-540.

Ruf, A., Worlitschek, J., Mazzotti, M., 2000. Modeling and experimental analysis of PSD measurements through FBRM. Particle & Particle Systems Characterization 17, 167-179.

Saien, J., Moradi, V., 2012. Low interfacial tension liquid-liquid extraction with impinging-jets contacting method: Influencing parameters and relationship. Journal of Industrial and Engineering Chemistry 18, 1293-1300.

Saleemi, A., Rielly, C., Nagy, Z.K., 2012a. Automated direct nucleation control for in situ dynamic fines removal in batch cooling crystallization. Crystengcomm 14, 2196-2203.

Saleemi, A.N., Rielly, C.D., Nagy, Z.K., 2012b. Comparative investigation of supersaturation and automated direct nucleation control of crystal size distributions using ATR-UV/vis spectroscopy and FBRM. Crystal Growth & Design 12, 1792-1807.

Saleemi, A.N., Rielly, C.D., Nagy, Z.K., 2012c. Monitoring of the combined cooling and antisolvent crystallisation of mixtures of aminobenzoic acid isomers using ATR-UV/vis spectroscopy and FBRM. Chemical Engineering Science 77, 122-129.

Sargent, G.A., Conrad, H., Keshavan, M.K., 1979. Structural characterization of the surface damage of metals due to erosion with solid particles by SEM, TEM, XRD and auger-electron spectroscopy. Journal of Metals 31, 109-109.

Sarkar, D., Rohani, S., Jutan, A., 2007. Multiobjective optimization of semibatch reactive crystallization processes. Aiche Journal 53, 1164-1177.

Schmidt, L.D., Dauenhauer, P.J., 2007. Chemical engineering - Hybrid routes to biofuels. Nature 447, 914-915.

Schumann, D., Nagel, U., 1982. APPENDIX .1. Sediment xrd data, LEG-64. Initial Reports of the Deep Sea Drilling Project 64, 1297-1301.

Schleicher, A., 1923. Diamond-structure and graphite structure in organic compounds. Journal Fur Praktische Chemie-Leipzig 105, 350-354.

Schochet, S., Tadmor, E., 1992. The regularized Chapman-EnsKog expansion for scalar conservation-laws. Archive for Rational Mechanics and Analysis 119, 95-107.

Schoenecker, P.M., Belancik, G.A., Grabicka, B.E., Walton, K.S., 2013. Kinetics Study and Crystallization Process Design for Scale-Up of UiO-66-NH2 Synthesis. Aiche Journal 59, 1255-1262.

Schou, S.A., 1951. Studies on the stability of drugs. I. Processes of fundamental importance to the stability of galenicals. Dansk tidsskrift for farmaci 25, 153-173.

Schou, S.A., Rhodes, J.M., 1951a. Studies on stability of drugs. 5. Shift in pH in sodium pyrosulfite solutions in autoclaving. Dansk tidsskrift for farmaci 25, 365-371.

Schou, S.A., Rhodes, J.M., 1951b. Studies on the stability of drugs. 4. Preparation and stability of metaoxedrine solution for injection. Dansk tidsskrift for farmaci 25, 350-364.

Sear, R.P., 2007. Nucleation: theory and applications to protein solutions and colloidal suspensions. Journal of Physics-Condensed Matter 19.

Seligman, G., 1937. Snow crystal or snowflake. Nature 140, 730-730.

Shan, G., Igarashi, K., Noda, H., Ooshima, H., 2002. Control of solvent-mediated transformation of crystal polymorphs using a newly developed batch crystallizer (WWDJ-crystallizer). Chemical Engineering Journal 85, 169-176.

Shimizu, Y., Hirasawa, I., 2013. Creation of controlled manganese and Zinc compounds by reactive crystallization. Journal of Chemical Engineering of Japan 46, 342-346.

Sholl, C.A., Fletcher, N.H., 1970. Decoration criteria for surface steps. Acta Metallurgica 18, 1083-1084.

Simpson, G.C., 1937. Snow crystal or snowflake. Nature 140, 729-730.

Siviero, E., Cabri, W., Terrassan, D.M., 2002. Process for the preparation of β-lactam derivatives. Antibiotics S.p.A., Rodano (IT), US 6,458,558 B1.

Smith, A., Holmes, W.B., 1902. Amorphous sulphur. Berichte Der Deutschen Chemischen Gesellschaft 35, 2992-2994.

Smythe, B.M., 1967. Sucrose crystal growth .3. relative growth rates of faces and their effect on sucrose crystal shape. Australian Journal of Chemistry 20, 1115-1116.

Sokoloski, T.D., Mitscher, L.A., Yuen, P.H., Juvarkar, J.V., Hoener, B., 1977. Rate and proposed mechanism of anhydrotetracycline epimerization in acid-solution. Journal of Pharmaceutical Sciences 66, 1159-1165.

Spalding, D.B., 1958. A note on mean residence-times in steady flows of arbitrary complexity. Chemical Engineering Science 9, 74-77.

Steele, M.L., Wertz, D.L., 1977. XRD Studies of concentrates ndcl3 solutions. Abstracts of Papers of the American Chemical Society 173, 8-8.

Stables, H.C., 1981. Crystallization process. Glaxo Group Limited, England, US 4,298,732.

Stahl, P.H., Wermuth, C.G., 2002. Handbook of pharmaceutical salts : properties, selection, and use. Weinheim ; Chichester : Wiley-VCH, c2002., Germany.

Steyer, C., Mangold, M., Sundmacher, K., 2010. Modeling of Particle Size Distribution for Semibatch Precipitation of Barium Sulfate Using Different Activity Coefficient Models. Industrial & Engineering Chemistry Research 49, 2456-2468.

Stoller, M., Bravi, M., Chianese, A., 2005. The effect of scaling on the performances of a DTB crystallizer by means of a compartmental simulation model. Chemical Engineering Research & Design 83, 126-132.

Tamir, A., Kitron, A., 1987. Applications of impinging-streams in chemical-engineering processes - review. Chemical Engineering Communications 50, 241-330.

Tavare, N.S., 1994. Mixing, reaction and precipitation: An interplay in continuous crystallizers. Chemical Engineering Science 49, 5193-5201.

Tavare, N.S., 2000. Mixing, reaction and precipitation: An interplay in continuous crystallizers with unpremixed feeds.

Teeaar, R., Serimaa, R., Paakkari, T., 1987. Crystallinity of cellulose, as determined by cp/mas nmr and xrd methods. Polymer Bulletin 17, 231-237.

Thiessen, P.A., 1929. Spontaneous nucleation in diluted, highly oversaturated gold solutions. Zeitschrift Fur Anorganische Und Allgemeine Chemie 180, 57-64.

Thompson, E., Baalham, C.J., 1981. Preparation of sodium cefuroxime. Glaxo Group Limited, England, US 4,277,601.

Tiselius, H.G., 1981. The effect of ph on the urinary inhibition of calcium-oxalate crystal-growth. British Journal of Urology 53, 470-474.

Tsuge, H., Kotaki, Y., Hibino, S., 1987. Reactive crystallization of calcium-carbonate by liquid-liquid reaction. Journal of Chemical Engineering of Japan 20, 374-379.

Tsuge, H., Yoshizawa, S., Tsuzuki, M., 1996. Reactive crystallization of calcium phosphate. Chemical Engineering Research & Design 74, 797-802.

Tsuruta, K., 1900. Some thermal properties of crystal. Physikalische Zeitschrift 2, 112-112.

Valeton, J.J.P., 1923. Growth and dissolution of crystals. I. Zeitschrift Fur Kristallographie 59, 135-169.

Valeton, J.J.P., 1924a. Growth and dissolution of crystals. II. Zeitschrift Fur Kristallographie 59, 335-365.

Valeton, J.J.P., 1924b. Growth and dissolution of crystals. III. Zeitschrift Fur Kristallographie 60, 1-38.

van Uven, M.J., 1914. The theory of Bravis (on errors in space) for polydimensional space, with applications to correlation. Proceedings of the Koninklijke Akademie Van Wetenschappen Te Amsterdam 17, 150-156.

Vancampen, L., Amidon, G.L., Zografi, G., 1983a. Moisture sorption kinetics for water-soluble substances .1. theoretical considerations of heat-transport control. Journal of Pharmaceutical Sciences 72, 1381-1388.

Vancampen, L., Amidon, G.L., Zografi, G., 1983b. Moisture sorption kinetics for water-soluble substances .2. experimental-verification of heat-transport control. Journal of Pharmaceutical Sciences 72, 1388-1393.

Vancampen, L., Amidon, G.L., Zografi, G., 1983c. Moisture sorption kinetics for water-soluble substances .3. theoretical and experimental studies in air. Journal of Pharmaceutical Sciences 72, 1394-1398.

Vandevusse, J.G., 1959. Residence times and distribution of residence times in dispersed flow systems. Chemical Engineering Science 10, 229-233.

Vogel, R., Tammann, G., 1909. The conversion of diamond in graphite. Zeitschrift Fur Physikalische Chemie--Stochiometrie Und Verwandtschaftslehre 69, 598-602.

Voigt, W., 1902. Articles on the explanation of the properties of pleochroic crystals. Annalen Der Physik 9, 367-416.

Wang, D., Li, Z., 2012. Gas-liquid reactive crystallization kinetics of hydromagnesite in the $MgCl_2$-CO_2-NH_3-H_2O system: its potential in CO_2 sequestration. Industrial & Engineering Chemistry Research 51, 16299-16310.

Wang, I.C., Lee, M.J., Sim, S.J., Kim, W.S., Chun, N.-H., Choi, G.J., 2013. Anti-solvent co-crystallization of carbamazepine and saccharin. International Journal of Pharmaceutics 450, 311-322.

Wang, X., Liu, W., Liu, J., 2014. A continuous crystallizer for rapid reactive crystallization process, CN201320685656.2.

White, H.J., Eastlick, D.T., Oughton, J.F., 1988. Process for preparing sodium cefuroxime. Glaxo Group Limited, London, England, US 4,775,750.

Woo, X.Y., Tan, R.B.H., Braatz, R.D., 2009. Modeling and computational fluid dynamics-population balance equation-micromixing simulation of impinging jet crystallizers. Crystal Growth & Design 9, 156-164.

Wong, E.R., Yeko, J., Engler, P., Gerron, R.A., 1983. SCRIP - fortran-iv software for quantitative XRD. Advances in X-Ray Analysis 26, 157-162.

Woo, X.Y., Tan, R.B.H., Braatz, R.D., 2011. Precise tailoring of the crystal size distribution by controlled growth and continuous seeding from impinging jet crystallizers. Crystengcomm 13, 2006-2014.

Wood, T., 1962. A note concerning residence time distribution in a cylindrical vessel. Chemical Engineering Science 17, 391-392.

Wozniak, T.J., Hicks, J.R., 1991. Analytical profile of cefuroxime sodium. Analytical profiles of drug substances 20, 209-236.

Wulff, G., 1901a. Examinations in the field of optical properties of isomorphic crystals. Zeitschrift Fur Krystallographie Und Mineralogie 36, 1-28.

Wulff, G., 1901b. On the question of speed of growth and dissolution of crystal surfaces. Zeitschrift Fur Krystallographie Und Mineralogie 34, 449-530.

Yagi, S., Kunii, D., 1961. Fluidized-solids reactors with continuous solids feed .1. residence time of particles in fluidized beds. Chemical Engineering Science 16, 364-371.

Yin, Q.X., Wang, J.K., Xu, Z., Li, G.Z., 2000. Analysis of concentration multiplicity patterns of continuous isothermal mixed suspension-mixed product removal reactive precipitators. Industrial & Engineering Chemistry Research 39, 1437-1442.

Yin, Q.X., Wang, J.K., Zhang, M.J., Wang, Y.L., 2001. Influence of nucleation mechanisms on the multiplicity patterns of agglomeration-controlled crystallization. Industrial & Engineering Chemistry Research 40, 6221-6227.

Yoshioka, S., Stella, V.J., 2002. Stability of drugs and dosage forms. Kluwer Academic, New York, Boston, Dordrecht, London, Moscow.

Yu, L.X., Lionberger, R.A., Raw, A.S., D'Costa, R., Wu, H.Q., Hussain, A.S., 2004. Applicatlons of process analytical technology to crystallization processes. Advanced Drug Delivery Reviews 56, 349-369.

Yu, Z.Q., Chow, P.S., Tan, R.B.H., 2008. Interpretation of focused beam reflectance measurement (FBRM) data via simulated crystallization. Organic Process Research & Development 12, 646-654.

Zhai, Y.F., Cui, L.J., Zhou, X., Gao, Y., Fei, T., Gao, W.X., 2013. Estimation of nitrogen, phosphorus, and potassium contents in the leaves of different plants using laboratory-based visible and near-infrared reflectance spectroscopy: comparison of partial least-square regression and support vector machine regression methods. International Journal of Remote Sensing 34, 2502-2518.

Zhang, C.T., Wang, H.R., Wang, Y.L., 2010. Internally generated seeding policy in anti-solvent crystallization of ceftriaxone sodium. Chemical Engineering and Processing 49, 396-401.

Zhang, M., Karjala, T.W., Jain, P., Villa, C., 2013. Theoretical Modeling of Average Block Structure in Chain-Shuttling alpha-Olefin Copolymerization Using Dual Catalysts. Macromolecules 46, 4847-4853.

Zhao, Y.Y., Hou, B.H., Jiang, X.B., Liu, C., Wang, J.K., 2012. Determination of thermodynamics in various solvents and kinetics of cefuroxime sodium during antisolvent crystallization. Journal of Chemical and Engineering Data 57, 952-956.

Zhao, Y.Y., Jiang, X.B., Hou, B.H., 2013. Measurement and correlation of solubility of cefuroxime acid in pure and binary solvents at various temperatures. Journal of Chemical and Engineering Data 55, 3369-3372.

Zheng, Y.L., Li, J.W., Guan, H.Y., Xue, M.H., Qin, J., 2011. Preparation of cefuroxime sodium, CN 101812076 A.

Zhou, Z.J., Fu, G.Q., 2010. Preparation of cefuroxime sodium, CN 101955492 A.